Time-Resolved Spectroscopy and Near Infrared Imaging for Prostate Cancer Detection: Receptor-targeted and Native Biomarker

by

Yang Pu

A dissertation submitted to the Graduate Faculty in Electrical Engineering

in partial fulfillment of the requirements for the degree of Doctor of

Philosophy, The City University of New York

2011

This manuscript has been read and accepted for the Graduate Faculty in Electrical Engineering in satisfaction of the dissertation requirement for the degree of Doctor of Philosophy

Date	**Professor: R. R. Alfano** **Chair of Examining Committee**
Date	**Professor: Mumtaz Kassir** **Executive Officer**

Supervisory Committee:

Dr. Wubao Wang (IUSL)

Prof. S. K. Gayen (Physics)

Prof. Ping-Pei Ho (Electrical Engineering)

Prof. Roger Dorsinville (Electrical Engineering)

Dr. Wei Cai (IUSL)

THE CITY UNIVERSITY OF NEW YORK

Abstract

TIME-RESOLVED SPECTROSCOPY AND NEAR INFRARED IMAGING FOR PROSTATE CANCER DETECTION: RECEPTOR-TARGETED AND NATIVE BIOMARKER

by

Yang Pu

Adviser: Professor R. R. Alfano
Co-Adviser: Dr. W. B. Wang

Optical spectroscopy and imaging using near-infrared (NIR) light provides powerful tools for non-invasive detection of cancer in tissue. Optical techniques are capable of quantitative reconstructions maps of tissue absorption and scattering properties, thus can map *in vivo* the differences in the content of certain marker chromophores and/or fluorophores in normal and cancerous tissues (for example: water, tryptophan, collagen and NADH contents). Potential clinical applications of optical spectroscopy and imaging include functional tumor detection and photothermal therapeutics.

Optical spectroscopy and imaging apply contrasts from intrinsic tissue chromophores such as water, collagen and NADH, and extrinsic optical contrast agents such as Indocyanine Green (ICG) to distinguish disease tissue from the normal one. Fluorescence spectroscopy and imaging also gives high sensitivity and specificity for biomedical diagnosis. Recent developments on specific-targeting fluorophores such as small receptor-targeted dye-peptide conjugate contrast agent offer high contrast between normal and cancerous tissues hence provide promising future for early tumour detection.

This thesis focus on a study to distinguish the cancerous prostate tissue from the normal prostate tissues with enhancement of specific receptor-targeted prostate cancer contrast agents using optical spectroscopy and imaging techniques. The scattering and absorption coefficients,

and anisotropy factor of cancerous and normal prostate tissues were investigated first as the basis for the biomedical diagnostic and optical imaging. Understanding the receptors over-expressed prostate cancer cells and molecular target mechanism of ligand, two small ICG-derivative dye-peptides, namely Cypate-Bombesin Peptide Analogue Conjugate (Cybesin) and Cypate-Octreotate Peptide Conjugate (Cytate), were applied to study their clinical potential for human prostate cancer detection.

In this work, the steady-state and time-resolved fluorescence spectroscopy of Cybesin (Cytate) in solution, and in cancerous and normal prostate tissues were studied. It was found that more Cybesin (Cytate) was uptaken in the cancerous prostate tissue than those in the normal tissue. The preferential uptake of Cybesin (Cytate) in cancerous tissue was used to image and distinguish cancerous areas from the normal tissue. To investigate rotational dynamics and fluorescence polarization anisotropy of the contrast agents in prostate tissues, an analytical model was used to extract the rotational times and polarization anisotropies, which were observed for higher values of Cybesin (Cytate)-stained cancerous prostate tissue in comparison with the normal tissue. These reflect changes of microstructures of cancerous and normal tissues and their different binding affinity with contrast agents.

The results indicate that the use of optical spectroscopy and imaging combined with receptor-targeted contrast agents is a valuable tool to study microenvironmental changes of tissue, and detect prostate cancer in early stage.

献给我的父亲和母亲
普治海和杨会英
这个世界上最爱我的人

献给我的亲爱的儿子
普天一(Gordon St. Clair Pu)
这个世界上我最爱的人

Acknowledgments

I would like to gratefully thank my mentor: Prof. R. R. Alfano, Distinguished Professor of Science and Engineering, for his excellent supervision, continuous insight guidance, and support throughout the work of my thesis. In particular, I appreciate him to give me the opportunity to work directly with him and the independence to pursue this thesis and other topics. He has motivated me to my highest level, inspiring me that we can do frontier works with the best researchers in the world. My further education in the research ways would not have been imaginative and enthralling without having the fortune to work with him. His professional knowledge, sense, especially his passion and ideas on science and technology has been the greatest help in the preparation of this thesis and wealth of knowledge for my future career.

I'm extremely grateful to my co-thesis advisor, Dr. W. Wang, for his supervision, training, advice, discussions, encouragement, support and teaching me many experimental techniques in the thesis work. I deeply appreciate my advisors patience on my acquiring the needed skills to do my thesis work.

Many thanks to Prof. S. K. Gayen, Prof. R. Dorsinville, Prof. Ping-Pei Ho and Dr. Wei Cai for serving on my thesis committee and reviewing the thesis.

I could not have been fulfilled in pursuing this work without support of Prof. S. Achilefu, at Washington University School of Medicine at St. Louis for providing the target contrast agents.

It is with deep sadness that we have lost wonderful colleague: Mr. Fanan Zeng, my countryman who graduated from the same high school as mine. His uncertain death is a great loss to science.

To my colleagues at the Institute of Ultrafast Spectroscopy and Lasers (IUSL), thank all of you for the help and advice. Special thanks go to Mr. Gui-Cheng Tang and Mr. Y. Budansky for

the long time we spent on the NIR optical scanning imaging system and for their valuable help with constructing and testing this system.

I want to thank the people that trust me in the field: Prof. Min Xu for the fruitful discussion and help in the theoretical physics of light scattering in highly scattering media. My acknowledgment is extended to my friends, my teammates and my colleagues: Dr. Chun Wang, Ms. C-H. Liu, Dr. S-K. Zhang, Ms. X-C Liang, Dr. M. Sharanov, Dr. Z. Manuel, Dr. B. B. Das, Dr. M. Abu-Ammouneh, Dr. H. Sztul, Mr. Giovanni Milione, Dr. T. Myint, Ms. A. Alimova, Dr. Bykov and Mr. M. Jeanty for their help and support in many aspects of my research. I want to thank deeply Dr. K. Sutkus, Ms. Lauren Gohara, Ms. Joan Brijlall and Ms. M. Gibbs, at administration of IUSL for their help and support during my thesis work.

I also want to acknowledge the help from Hackensack University Medical Centre (HUMC) for providing normal and cancer prostate tissue samples for the measurements, in particular, to Dr. J. H. Vitenson (M.D), Dr. I. Sawczuk (M.D), Dr. S. Peters (M.D), Dr. J. M. Lombardo (M.D) and Ms. Alexandra T. Sawczuk.

This work was possible with the financial support and help from the IUSL, U. S. Army Medical Research and Materiel Command grant numbered DAMD17-01-1-0084 (CUNY RF 47462-00-01) and W81XWH-08-1-0717 (CUNY RF 47170-00-01).

Finally, I would like to thank my parents: Zhihai Pu and Huiying Yang, who love me the most, my sisters and brothers: Yan Pu, Tao Pu and Yin Pu for their constant support, encouragement, and endless love throughout my studies, and my son, Gordon St. Clair Pu, whom I love the most in the world.

Time-resolved Spectroscopy and Near Infrared Imaging for Prostate Cancer Detection: Receptor-targeted and Native Biomarker

Table of Contents

List of Figures

Chapter 1

Chapter 2

Chapter 3

Chapter 4

Chapter 5

Chapter 6

List of Tables

Chapter 2

Chapter 3

Chapter 1
Introduction and thesis statement

1.1. Background

In my thesis, I would like to present the various applications of near-infrared (NIR) optical spectroscopy, backscattering imaging techniques and time-resolved fluorescence polarization kinetics in prostate cancer detection. Although light has been used to image surface structures for the last 100 years, its use to measuring large organs and probing internal structures has been limited mainly due to the absorption in visible and high scattering that tissue exhibits in the visible and NIR region. The multiple scattering nature of the biological tissue demands for development of sensitive instrumentation and sophisticated physical model to qualitatively, semi-quantitatively or quantitatively understand the underlying physiological events. In the late 1980's, photon propagation in tissue was modeled with a simple differential equation, the diffusion equation. The field of backscattering optical imaging has been continuously developed since the 1980s owing to the advances in laser technologies, sensitive photon detectors, high density CCD cameras and mathematical algorithms. This thesis work reflects the past 8 years of exciting research I have undertaken in the Institute for Ultrafast Spectroscopy and Lasers (IUSL) at the City University of New York.

Prostate cancer has a high incidence and mortality rate for men. In 2009, nearly 192,280 new prostate cancer cases were diagnosed, and about 27,360 deaths were caused by prostate cancer in the U. S. [1]. The region of the highest incidence is in the western world, where there are 10–11% chances for a man to develop prostate cancer, and 3–4% chances of dying from the disease [1]. The common screening techniques for detection of prostate cancer diagnosis are digital rectal examination (DRE), the serum tumor marker prostate specific antigen (PSA) tests and the

transrectal ultrasound (TRUS) imaging. TRUS is no longer considered a first-line screening test for prostate cancer because of its poor spatial resolution and contrast, but does play a role in the biopsy of patients with abnormal DRE or PSA [2].

Both PSA and DRE can detect occult prostate cancer. A PSA value greater than 4.0 ng/ml is the accepted threshold for further diagnostic evaluation, but some studies report a much lower value of sensitivity of 29%-35% [3]. DRE has a reported the values of sensitivity as low as 18%-22% [3]. Combining PSA and DRE increases the positive predictive value to 49% [3]. The confirmation of prostate cancer finally needs a needle biopsy of the prostate. In the biopsy, a number of cores of prostate tissue are taken with a small diameter needle guided into selected regions of the prostate with ultrasound imaging [4]. But, the fine-needle biopsies may miss cancerous lesions and it is an invasive method.

The early detection and treatment of prostate cancer are crucial for reducing mortality. However, conventional oncology imaging methods for prostate cancer diagnosis depend on bulk physical properties of cancer tissue and are not effective for early-stage primary tumors [5]. Since the conventional methods: TRUS has poor spatial resolution and contrast, PSA and DRE have limited accuracy, and the needle biopsy is invasive, better methods are needed to develop high resolution and noninvasive techniques to detect early small prostate cancers.

1. 2. Optical methods and intrinsic contrasts

Compared with other modalities, the optical methods have the merits of high sensitivity and biochemical specificity. The spectral window in the far-red to NIR range (650nm – 1,000nm), corresponding to lower absorption from major tissue chromophores such as water and blood, allows light to penetrate deep into the tissue up to several centimeters [6]. The deep penetration of NIR light makes optical imaging possible for detecting abnormalities in the host tissue. The

light propagation in the turbid media (such as human prostate tissue) can be well modeled by the diffusion or Monte Carlo theory, and the photons undergoing different scattering events can be recorded by a high sensitive CCD camera. The optical imaging has been applied to prostate cancer detection and shows great promise for indentifying prostate cancer [7].

The principal chromophores that account for absorption in prostate tissues are water (H_2O) [7], oxygenated and deoxygenated hemoglobin (HbO_2 and Hb) and lipids [8]. The concentration of each component can be derived through the absorption spectrum analysis using certain wavelengths which correspond to the absorption fingerprints of chromophores. From optical density measurements or determination of the attenuation coefficient, the relative water content can be determined in both cancer and normal tissues. It was reported that there is a lack of water in neoplastic tissues in comparison to surrounding normal tissues. The difference of water absorption was observed between cancerous and normal human prostate tissues by means of transmittance spectroscopy in visible and NIR spectral range [7].

The fluorescence spectroscopy of intrinsic fluorophores can also be used to differentiate diseased tissue from healthy tissue. Since the fluorescence of most known fluorophores is in ultraviolet and visible range, they are not in the NIR “tissue optical window” [6]. Major advancement occurred when the behavior of Spectral Wing (SW) in far-red and NIR from cancerous and normal human breast and prostate tissues was investigated in IUSL [9]. The characteristics of the NIR SW emission of human native tissue were shown to be different for different types of tissues, such as normal and cancerous tissue in both time-resolved and steady-state spectroscopy. Although the model for far-red to NIR emission wing from biomedical samples are still under the development, the differences can be applied to image and distinguish malignant human prostate tissue from non-malignant human prostate tissue [9].

The scattering properties of tissue also contain important information for lesion diagnosis. The *in vivo* measurements show that scattering coefficients are wavelength dependent and related to the tissue structure and concentration or size of organelles [10]. The well-known five Gleason Grades [11], which describe evolution of malignant prostate tumor and reveal the change of the contributors for scattering of tissue. The pattern of Gleason Grade 1 (corresponding to early stage) consists of evenly placed uniform gland cells supported by a highly structured network of collagen fiber [12]. With grade advances, the cancer cells proliferate, the cell density increases, the cellular nuclei become non-uniform and content of collagen decreases [13]. This phenomenon appears at Grade 3 and is obvious at Grade 5 [12]. The different micro-structures between cancerous and normal prostate tissues maybe cause the difference of the scattering coefficients between these two types of tissues and can be measured using transmittance and reflectance spectroscopy, which will be presented in Chapter 4.

1.3. Extrinsic contrasts

Contrast enhancement through contrast agents, either for absorption or fluorescence, have shown great promise for using improving the sensitivity and specificity of cancer detection [14]. The use of extrinsic contrasts to gain a better understanding of the physiological process has been an active field of research in the past years [14].

1.3.1. Non-specific contrast agents

The most commonly used contrast agent in the NIR spectral “tissue optical window” is Indocyanine Green (ICG). ICG is an FDA (Food and Drug Administration) approved fluorescent dye for imaging of retinal vasculature and hepatic function [14, 15]. The absorption contrast provided by ICG mainly probes the permeability and vascularization [15] of tissue blood vessels. ICG has been applied in human subjects clinically. Figs. 1-1 (a) and (b) show the measured

absorption and fluorescence spectra of ICG, respectively. The absorption band of ICG ranges from ~650 nm to ~830 nm with a strong peak at ~780 nm. The fluorescence spectrum covers from ~790 nm to 900 nm with a main peak at ~820 nm. Researchers are interested in ICG because their emission range of 700 nm to 900 nm is in the "tissue optical window" [6].

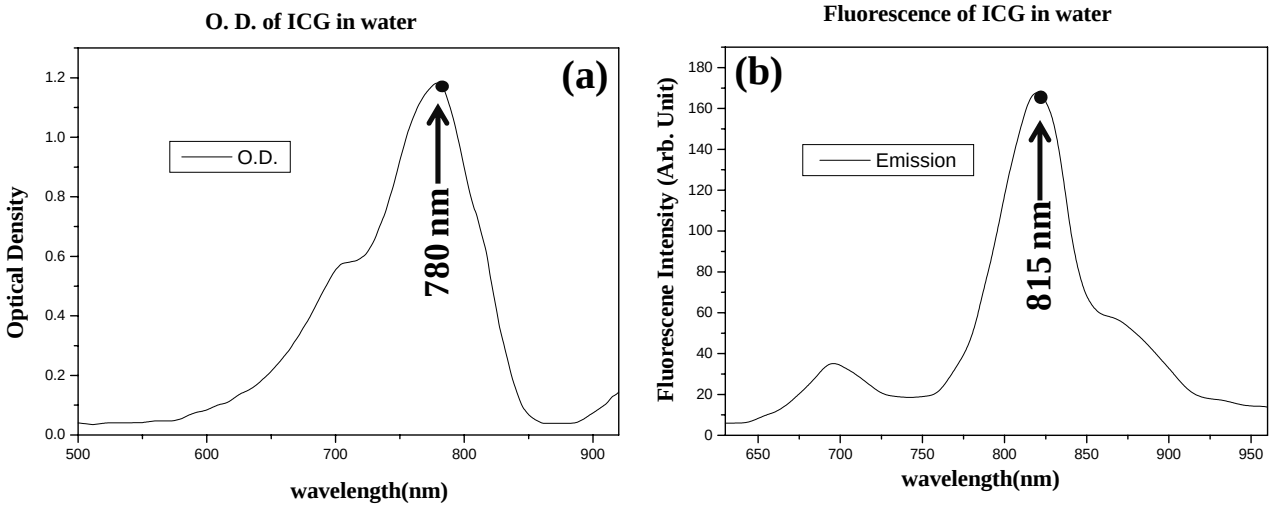

Fig. 1-1 The measured (a) absorption and (b) fluorescence spectra of Indocyanine Green in water.

Although ICG is not designed for specific target of cancer cells, the effect of contrast enhancement for tumor detection has been reported by several groups [15-16] especially in mammary tumor with both animal and human model. Licha *et al* detected the fluorescence signal from a low dose ICG (~ 80 μg/kg body weight) injection into the rat model with a subcutaneous mammary tumor. They reported a contrast around 2.5 between the fluorescence intensities of the tumor and control tissues [16]. Ebert *et al* reported a 6:1 tumor-to-tissue contrast ratio in fluorescent imaging of a highly hydrophilic cyanine dye derivative [16]. Using intensity-modulated frequency-domain imaging with a gain-modulated image-intensified CCD camera, Reynolds *et al* located the canine spontaneous mammary tumor *in-vivo* from the ICG distribution [16]. With a similar instrumentation and animal model, Gurfinkel *et al* tracked the pharmacokinetics of ICG using a double-exponential model. They mapped the fluorescence

intensity of the dye during the uptake (wash-in) and release (wash-out) through the tissue, and observed a delayed wash-out of ICG up to 72 hours [15]. Reports of Chance's group at University of Pennsylvania [16] suggest that the ICG in breast cancer detection has been shown to be capable of localizing and quantifying enhancing lesion *in-vivo* with human model.

The ICG-enhanced optical images combined with fluorescence polarization difference imaging (FPDI) techniques have been investigated in IUSL [17]. Our primary results show that the ICG stained prostate dot tissue with a diameter of ~1 mm embedded in human prostate tissue at 8.5 mm can be distinguished under a weak illumination power of ~ 50 $\mu w/cm^2$ [17]. This indicates that ICG or ICG-derivative dye have a promising sensitivity and resolution than conventional oncology imaging methods [17].

1. 3. 2. Molecular specific contrast agents

While ICG is mainly a blood-pooling agent and is cleared out by the liver rapidly, numerous efforts have been invested to improve the affinity and the retention time of contrast agents in the tumor cells, including the increasing of the hydrophilicity and binding to macromolecules [16]. To further improve the performance of contrast agents, target-specific conjugates have been developed to study the molecular specificity [18]. Advances in biology have shown that many tumors over-expressed specific receptors that could be used to differentiate them for normal cells [15, 18]. Therefore, ligands for such receptors can be used as delivery vehicles to enhance tumor specificity [15, 18]. Hence, a useful strategy involves conjugating a dye to carriers that can target the over-expressed receptors on tumor cells to enhance specificity [15]. It has been reported the feasibility by conjugating fluorescein or carbocyanine with antibody or other large biomolecules of targeting tumor receptor [15, 18]. However, targeting of tumor receptors with antibodies or large biomolecules is hampered by many factors, including low diffusion rates into tumors, rapid

uptake by the liver, and the potential to elicit adverse immunogentic reactions [18]. Besides biocompatibility, high molar absorptivity and fluorescent yield, ideal properties for optical contrast gents should absorb and emit in NIR region to enhance the depth of tissue penetration of light [15, 18].

Recent progresses in nuclear medicine have shown that attachment of the optical contrast agents possessing desirable wavelengths (for instance, ICG) to small molecular peptides can be used to target the over-expressed receptors on certain tumor without loss of receptor affinity of the peptide [15]. This approach has several advantages with respect to either the nonspecific contrast agents or the conjugation of the probes to large biomolecules. Such advantages include enhance localization in tumors, rapid clearance from the non-target (normal) tissue, possibilities of preparing a library of peptides for rapid identification of bioactive molecules [15] and preservation of the spectral advantages in the NIR range of the "tissue optical window".

Over the past decade, several groups designed and synthesized novel specific contrast agents in order to achieve these goals. For instance, Zheng *et al* [19] have targeted one kind of receptor, Low-Density Lipoprotein receptors (LDLr), which tends to over-express on several types of tumor cells. They incorporated tricarbocyanine cholesteryl laurate within the lipid core of LDL that could be internalized by tumor cells via LDLr-mediated endocytosis. Another interesting type of molecular fluorescent markers has been developed by Weissleder et al [20]. They use the protease-activated probes containing auto-quenched fluorescent molecules through fluorescence resonance energy transfer (FRET) that can be cleaved by tumor-specific proteases and then fluoresce [20]. Through this kind of approach, the high fluorescent contrast (12 folds) has been demonstrated in the tumor. Achilefu *et al* [15, 18] have developed two kinds of small ICG-derivative dye-peptide: Cypate-Octreote Peptide Analogue Conjugate (Cytate) and Cypate-

Bombesin Peptide Analogue Conjugate (Cybesin). Cytate has a highly affinity to somatostatin receptor (SSTR) to image the tumor that tends to over-express the SST Receptor, and Cybesin is indicated to be preferentially localized for over 24 hours in tumors known to over-express bombesin receptors both in animal model.

Prostate is a highly hormone-sensitive organ. Numerous studies have investigated the regulatory role of hormones, chiefly androgens, estrogens, and Prolactin (PRL), on prostatic cell growth and differentiation. At a higher hierarchical level, somatostatin was implicated directly or indirectly in the regulation of prostate function [21]. Somatostatin is a small cyclic peptide. It is formed by proteolytic processing of larger precursor molecules: prepro-somatostatin and pro-somatostatin. This peptide was detected accidentally during studies of the distribution of growth hormone-releasing factor in the hypothalamus of rats [21]. In addition to playing an important regulatory role of hormones, this peptide controls cell proliferation in cancerous and normal tissues [21]. Therefore, tumors arising from somatostatin-target tissue frequently express a high density of somatostatin receptors [21, 22]. Somatostatin receptors, which have five subtypes, are known to be over-expressed in a large number of human tumors [22] including human prostate tumor. So they can represent the basis for *in-vivo* tumor targeting. As expected previously, several control experiments were carried out to determine that expression of somatostatin receptors is up-regulated in prostate malignant cells [22]. J. Hansson *et al* report, for the first time, tissue localization of somatostatin receptor subtype 2 (SSTR2) and subtype 4 (SSTR4) in benign prostatic hyperplasia (BPH) and malignant cells of human prostate [22]. Furthermore, the staining intensity for SSTR2 and SSTR4 is stronger in malignant cells compared with adjacent BPH epithelium, which suggests that SSTR2 and SSTR4 are over-expressed in prostate cancerous cells [22]. J. C. Reubi *et al* have also studied SSTR in a selection of prostate and

prostate cancer tissue and found that the SSTR subtype preferentially expressed by the eight tested prostate cancers was SSTRl [21]. Besides Somatostatin, Bombesin-like peptides can function as autocrine or paracrine growth factors and stimulate the growth of some cancer cells, including human prostate cancer [23]. Bombesin belongs to a family of brain-gut peptides that play an important role in cancer development [21]. It was observed that human primary tumors can synthesize bombesin [24]. Bombesin is potent neuropeptides expressed by prostate cancer neuroendocrine cells and are related to the progression of this malignancy [22]. There are three bombesin receptor subtypes, termed gastrin-releasing peptide receptor (GRPR), neuromedin B receptor (NMBR), and bombesin receptor subtype 3 (BRS-3) [22]. The experimental results of B. Sun *et al* detecting the distribution of bombesin/GRP receptors in human prostate carcinomas support the view that they may be involved in modulation of tumor progression [23]. Their data suggest that of the 22 prostate cancer specimens analyzed, 20 (91%) over-expressed GRPR, one subtype of bombesin receptor [23]. J. C. Reubi *et al* reported that cancer cell lines as well as primary human tumors can synthesize bombesin and GRP [24]. These peptides probably act in an autocrine fashion to stimulate the growth of the tumor cells they originate from, through bombesin receptors over-expressed on the membranes of these cells [24]. More recently, it has been shown that the GRP receptor proteins can be over-expressed in a large variety of human tumors, including prostate and breast cancer [24].

The combination of molecular probes and optical imaging techniques will yield the high sensitivity and specificity for cancer detection. The successful detection of tumor over-expressing somatostatin receptors and bombesin receptors in animal model using Cytate and Cybesin, respectively, motivated us to apply these two kinds of contrast agents for detection of human prostate cancer, which over-expresses somatostatin and bombesin receptors.

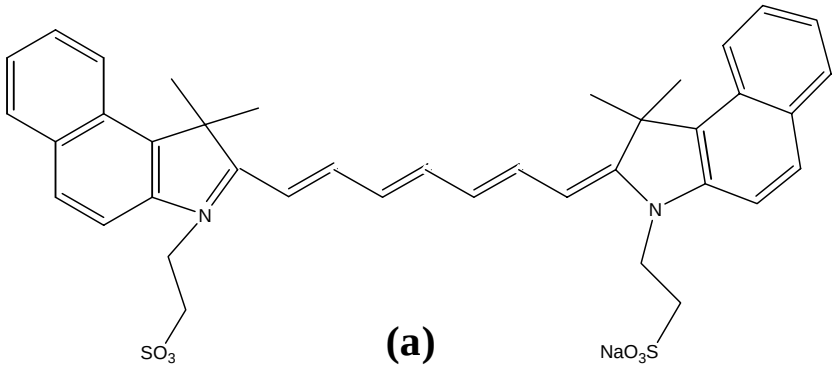

(a)

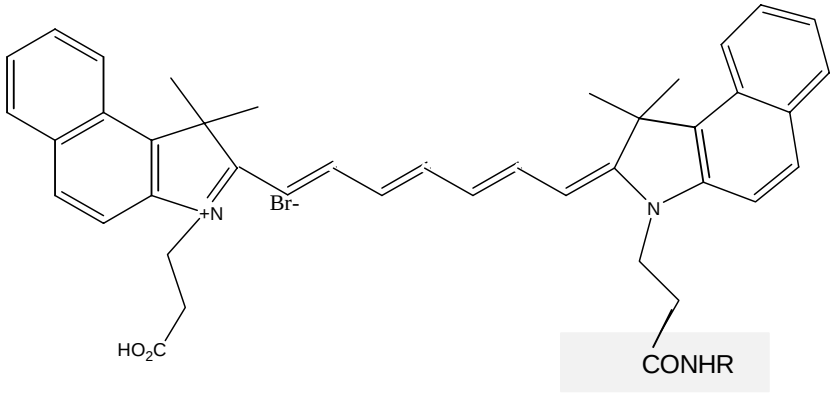

R=Dphe-Cys-Tyr-DTrp-Lys-Thr-Cys-Thr-OH

S S

(Cytate, Octreotate derivative)

(b)

R=Gly-Ser-Gly-Gln-Trp-Val-Ala-Gly-His-Leu-Met-NH_2

(Cybesin, Bombesin derivative)

(c)

Fig. 1-2 The molecular structure of (a) Indocyanine Green (ICG), (b) peptide-dye conjugate Cytate, and (c) peptide-dye conjugate Cybesin.

As a small ICG-derivative dye-peptide, both Cytate and Cybesin keep respective receptor affinity, thus would enhance localization of prostate tumors [14]. The molecular structures of ICG, Cytate and Cybesin are shown in Figs. 1-2(a), (b) and (c), respectively. For the optical

properties, both Cytate and Cybesin possess the spectral advantages of ICG that the fluorescence and the absorption ranges are in the NIR “tissue optical window”. We will discuss their optical properties including spectral and time-resolved elaborately in the following chapter.

1. 4. Thesis statement and organization

The theme of this thesis is to study the endogenous fluorophores and the contrast agent enhancement in NIR optical spectroscopy, backscattering imaging and time-resolved fluorescence polarization kinetics. Contrast is important in differentiating the targeted object (for instance, the tumor) from the background (normal tissue). The intrinsic optical contrast between tumor and normal tissue can be used to differentiate diseased tissues from healthy tissues. Furthermore, the new kind of extrinsic contrast enhancement lies in the recent advances in the molecular specific, receptor-targeted fluorescent contrast agents. These novel probes will yield elevated tumor-to-normal contrast through various biological principles, and enhance the sensitivity and specificity in tumor detection.

The contents of this thesis are organized as follows:

Chapter 1 presents the introduction and motivation for investigation of optical spectroscopy and backscattering image techniques for early prostate cancer detection, and briefly reviews the exciting advances in the molecular targeting contrast agents.

Chapter 2 introduces the concept of light propagation in tissue and its interaction with biological tissue, and discusses the physical processes involved in absorption, scattering and fluorescence in whole tissues. Absorption and scattering parameters of tissue are introduced and discussed. Mie scattering theory is described and used to investigate light scattering properties in tissue. The models commonly used to describe the transport of light through turbid media, namely diffusion model and Monte Carlo model are discussed.

Chapter 3 explores the difference of optical properties between cancerous and normal prostate tissue including absorption coefficient, scattering coefficient and anisotropy factor. The biological origins of the differences of optical parameters between cancerous and normal prostate tissues were studied using the fractal dimension tissue model.

Chapter 4 introduces the spectral and imaging studies on Cybesin. The absorption and fluorescence spectra of Cybesin were measured and shown to exist in the NIR tissue "optical window". Then time-resolved polarization-dependent fluorescence of Cybesin in cancerous and normal prostate tissues were measured and studied. A larger degree of fluorescence polarization preserved in the Cybesin-stained cancerous tissue than Cybesin-stained normal tissue was observed. An analytical model was developed to describe the time-resolved fluorescence kinetics and polarization anisotropy from Cybesin in human prostate tissue. The spectral and image results can be explained by the mechanism of preferential uptake of Cybesin in human prostate cancerous tissue. The spectral polarization imaging of Cybesin-stained cancerous and normal prostate tissues shows that cancerous prostate tissue takes-up more Cybesin than that of prostate normal tissue. This makes Cybesin a potential fluorescence contrast agent for prostate cancer.

Chapter 5 introduces the studies on Cytate. The absorption and fluorescence spectra of Cytate were measured and shown to exist in the NIR tissue "optical window". The spectral polarization imaging of Cytate-stained prostate cancerous and normal tissues was used to study preferential uptake of Cytate in prostate cancerous tissue. The fluorescence kinetics of Cytate in both solution and in prostate tissue was also studied using the analytical model.

Chapter 6 presents the studies of the time-resolved polarization kinetics of near infrared spectral wing emission from human cancerous and normal prostate tissues. These differences

between cancerous and normal tissues were used to image and identify cancerous areas from the surrounding normal tissue.

Chapter 7 concludes the current work and discusses the future studies in cancer detection (and other biomedical applications) based on the thesis work.

1. 5. References:

1. American Cancer Society. "Cancer facts and figures"' *American Cancer Society, Atlanta* (2009).
2. Rebecca Ferrini, Steven H. Woolf, "Screening for prostate cancer in American men", http://www.acpm.org/prostate.htm, *American College of Preventive Medicine - Practice Policy Statement.*
3. W. J. Catalona, J. P. Richie, F. R. Ahmann, *et al*. "Comparison of digital rectal examination and serum prostate specific antigen in the early detection of prostate cancer: results of a multi-center clinical trial of 6,630 men", *J. Urol.*, 151, 1283-1290 (1994).
4. D. J. Tindall and P. T. Scardino, "Defeating prostate cancer: crucial direction for research --- except from the report of the Prostate Cancer Progress Review Group (Review)", *Prostate,* 38(2), 166-171 (1999).
5. David A. Benaron, "The future of cancer imaging". *Cancer and Metast. Rev.*, 21, 45–78 (2002).
6. R. R. Anderson and J. A. Parrish, "The optics of human skin", *J. Invest. Dermatol*., 77, 13–19 (1981).
7. J. H. Ali, W. B. Wang, M. Zevallos, R. R. Alfano, "Near infrared spectroscopy and imaging to probe differences in water content in normal and cancer human prostate tissues", *Technol. Cancer Res. Treat.*, 3, 491-497 (2004).
8. T. O. McBride, B. W. Pogue, E. D. Gerety, S. P. Poplack, U. L. Osterberg and K. D. Paulsen, "Spectroscopic diffuse optical tomography for the quantitative assessment of hemoglobin concentration and oxygen saturation in breast tissue", *Appl. Opt.*, 38, 5480-5490 (1999).

9. G. Zhang, S. G. Demos and R. R. Alfano, “Far-red and NIR spectral wing emission from tissues under 532 and 632 nm photo-excitation”, *Laser Life Sci.*, 9, 1-16 (1999); and Y. Pu, W. B. Wang, B. B. Das, and R. R. Alfano, “Differences of time-resolved near infrared spectral wing emission and imaging of human cancerous and normal prostate tissues”, *Opt. Commun.*, 282, 4308–4314 (2009).
10. V. Ntziachristos and B. Chance, “Probing physiology and molecular function using optical imaging: applications to breast cancer”, *Breast Cancer Res.*, 3, 41-46 (2001).
11. D. F. Gleason and G. T. Mellinger, “Prediction of prognosis for prostate adenocarcinoma by combined histological and clinical”, *J. Urol.*, 111, 58-64 (1974).
12. C. Morrison, J. Thornhill and E. Gaffney, “The connective tissue framework in the normal prostate, BPH and prostate cancer: analysis by scanning electron microscopy after cellular digestion”, *Urol. Res*., 28, 304-307 (2000).
13. Rodolfo Montironi, Adhemar Longatto Filho, Alfredo Santinelli, Roberta Mazzucchelli, Roberto Pomante, Paola Colanzi and Marina Scarpelli, “Nuclear changes in the normal-looking columnar epithelium adjacent to and distant from prostatic intraepithelial neoplasia and prostate cancer”, *Virchow Arch*., 437, 625-634 (2000).
14. Y. Pu, W. B. Wang, B. B. Das, S. Achilefu, and R. R. Alfano, “Time-resolved fluorescence polarization dynamics and optical Imaging of Cytate: a prostate cancer receptor-targeted contrast agent”, *Appl. Opt.*, 47, 2281-2289 (2008).
15. J. E. Bugaj, S. Achilefu, R. B. Dorshow and R. Rajagopalan, “Novel fluorescent contrast agents for optical imaging of *in vivo* tumor based on a receptor-targeted dye-peptide conjugate platform”, *J. Biomed. Opt.*, 6(2), 122-133 (2001).

16. V. Ntziachristos, A. G. Yodh, M. Schnall and B. Chance, "Concurrent MRI and diffuse optical tomography of breast after Indocyanine Green enhancement", *Proc. Natl. Acad. Sci. USA*, 97, 2767-2772 (2000).
17. Wubao Wang, Jamal H. Ali, J. H. Vitenson, J. M. Lombardo and R. R. Alfano, "Spectral polarization imaging of human prostate tissues", *Optical Biopsy III, Proceeding of SPIE*, 3917, 75-78 (2000).
18. S. Achilefu, R. B. Dorshow, J. E. Bugaj and R. Rajagopalan, "Novel receptor-targeted fluorescence contrast agent for *in vivo* tumor imaging", *Invest. Radiol.*, 35, 479-485 (2000).
19. G. Zheng, H. Li, K. Yang, D. Blessington, K. Licha, S. Lund-Katz, B. Chance and J. D. Glickson, "Tricarbocyanine cholesteryl laurates labeled LDL: New near infrared fluorescent probes (NIRFs) for monitoring tumors and gene therapy of Familial hypercholesterolemia", *Bioorg. Med. Chem. Lett.*, 12, 1485-1488 (2002).
20. R. Weissleder, C. H. Tung, U. Mahmood and A. Bogdanov, "*In vivo* imaging of tumors with protease-activated near-infrared fluorescent probes", *Nat. Biotechnol.*, 17, 375-378 (1999).
21. J. C. Reubi, B. Waser, J. C. Schaer and R. Markwalder, "Somatostatin receptors in human prostate and prostate cancer", *J. Clin. Endocrinol. Metab*., 80, 2806-2814 (1995).
22. J. Hansson, A. Bjartell, V. Gadaleanu, N. Dizeyi and P. A. Abrahamsson, "Expression of somatostatin receptor subtypes 2 and 4 in human benign prostatic hyperplasia and prostatic cancer." *Prostate*, 53(4), 50-59 (2002).
23. B. Sun, G. Halmos, A. V. Schally, X. Wang and M. Martinez "Presence of receptors for bombesin/gastrin-releasing peptide and mRNA for three receptor subtypes in human prostate cancers", *Prostate* 42(4), 295-303 (2000).

24. Jean Claude Reubi, Sandra Wenger, Jacqueline Schmuckli-Maurer, Jean-Claude Schaer, and Mathias Gugger, “Bombesin receptor subtypes in human cancers: detection with the universal radioligand ^{125}I-[D-TYR^{6}, β-ALA^{11}, PHE^{13}, NLE^{14}] bombesin(6-14)”, *Clin. Cancer Res.*, 8, 1139–1146 (2002).

Chapter 2
Light propagation in tissue

In order to discuss the NIR tissue spectroscopy and imaging techniques in more detail, it is important to establish an understanding of light propagation through biological tissue. This chapter serves as the background of tissue optics. At the beginning of the chapter, optical properties of the tissue will be introduced. The measured optical properties of tissue will be characterized in the near-infrared (NIR) region [1], and the fluorescence properties of tissue will be discussed. Some optical diagnostic methods for cancer detection will be described by absorption and fluorescence contrast between normal and cancerous tissues. It is followed by a discussion of physics of light scattering: its origins and theoretical aspects of multiple scattering in tissue. The discussion will be concluded with a highlight of the two kinds of models (diffusion and Monte Carlo) commonly used to model the transport of light through turbid media.

2. 1. Optical characteristics of tissue

Tissues are an impressive complex creation comprised of a vast of assortment of molecules, structures and functional units. Despite this overwhelming complexity, we may still discuss average optical properties as long as we realize the limitations involved. There are five independent macroscopic parameters that are believed to characterize light propagation in tissue: the index of refraction (n), the absorption coefficient (μ_a), the scattering coefficient (μ_s), and the scattering anisotropy (g). These parameters are defined in Table: 2-1.

The definition of *mean free path (mfp)* is the mean distance that a photon travels in the medium of tissue before it is absorbed, (absorption *mfp*: l_a) or scattered (scattering *mfp*: l_s) [1]. Inverses of *mfp* are convenient manner in which to describe the absorption and scattering coefficients ($\mu_a=1/l_a$, and $\mu_s=1/l_s$). The anisotropy factor g is defined as:

$$g = < \cos\theta > = \int_0^{\pi} p(\theta)\cos\theta 2\pi \sin\theta d\theta , \tag{2.1}$$

where $\int_0^{\pi} p(\theta)2\pi \sin\theta d\theta = 1$, and $p(\theta)$ is the distribution pattern of deflection angle of a photon scattered by a particle. These optical parameters should provide some information about the biomedical properties as well as the morphological and structural configurations of tissue. The reduced scattering coefficient μ_s' is not independent from other parameters in Table 2. 1, and defined as:

$$\mu_s' \equiv \mu_s (1 - g) . \tag{2.2}$$

Table 2-1 Optical coefficients of interest in tissue

Parameter	Symbol	Definition
index of refraction	n	ratio of speed of light in vacuum to that in the medium
absorption coefficient (cm^{-1})	μ_a	absorption mean free path $\equiv \mu_a^{-1}$
scattering coefficient (cm^{-1})	μ_s	single scattering mean free path $\equiv \mu_s^{-1}$
scattering anisotropy	g	average cosin of the scattering angle (Equation (3.1))
reduced scattering coefficient (cm^{-1})	μ_s'	approximate inverse scale of isotropic scattering (Equation (3.2))
transport attenuation coefficient (cm^{-1})	μ_t	transport mean free path $\equiv (\mu_a + \mu_s')^{-1}$

The parameter μ_s' is presented indivaualy since so far no physical model can determines μ_s independently from g [2]. It is believed by most researchers that μ_s and g somehow depend on each other [3]. The physical meaning of the reduced scattering coefficient represents a length scale where a photon looses all memory of its initial direction in tissue so that the reciprocal of

μ_s' provides a scale for isotropic-scattering events [4]. From the definition of μ_s', follows the expression for the transport attenuation coefficient: $\mu_t \equiv \mu_a + \mu_s'$, and its reciprocal, $\mu_t'^{-1}$, the transport mean free path. In NIR range, since $\mu_s' \rangle\rangle \mu_a$, usually it is set that $\mu_t = \mu_s'$.

Generally we are forced to assume that the parameters in Table 2.1 are macroscopically homogeneous throughout the tissue volume, although this is not a rigorous description of tissue. Despite this simplified vision, for many cases of interest it will be sufficient.

2. 2. Light absorption in prostate tissue

The absorption coefficient (μ_a) describes the effectiveness of light absorbed by certain chromophore. When light radiation is incident on matter composed of discrete electrical charges, the charges are forced to oscillate at the frequency of the incident electric field. When infrared radiation is incident on a system of matter, resonance will occur, whereby energy is transferred from the incident field to the system and its amplitude of vibration is greatly increased. The excited state of the atoms or molecules usually lose their energy by colliding with one another within 10^{-12} seconds, thereby raising the kinetic energy of the other particles involved in the collisions. Hence, the energy associated with the incident field is most often dissipated as heat within the medium. This process is known as absorption.

The overall effect of absorption is a reduction in the intensity of the light beam travelling the medium. A relationship between the absorption of light in a purely absorbing medium and the thickness of the medium was first determined as the Beer-Lambert law [5, 6]

$$I = I_0 e^{-\alpha c l} = I_0 e^{-\mu_a l} \text{ in base of } e, \text{ or } I = I_0 10^{-\varepsilon c l} = I_0 10^{-K l} \text{ in base of 10,} \qquad (2.3)$$

where α and ε is known as the specific absorption coefficient for base of e and 10, respectively, and c is the concentration of a compound diluted in a non-absorbing medium. Beer-Lambert law determined that the absorption coefficient of a solution is linearly related to its concentration c.

In actual measurement, "optical density" (O.D.) is the unit usually used to describe the absorption property. O.D. is obtained by $O.D.=\log_{10}(I_0/I)$. In a solution containing a mixture of n pure absorbing compounds, the total O.D. is the sum of the individual absorption coefficients for base 10 (K_n) multiplied by the distance l:

$$O.D. = (K_1 + K_2 + \cdots + K_n)l = (\varepsilon_1 c_1 + \varepsilon_2 c_2 + \cdots + \varepsilon_n c_n)l. \quad (2.4)$$

There are many compounds in biological tissue which absorbs light radiation known as tissue chromophores, each of which has its own unique spectrum. Beer-Lambert law provides us a probability that theoretically the concentration of each chromophore can be obtained from the O.D. spectra of given type of tissue by the inverse model of equation (2.4) if specific absorption coefficient of each chromophore is known prior. Two main reasons make it fail when dealing with real measurements and processes: (1) the absorption coefficients of most chromophores keep little varies in NIR range and there are too many glaring discrepancies appeared in these measured coefficients because of different sample preparation protocols and varied measurement techniques; (2) the dominant scattering over the absorption of NIR range in the tissue. The O.D. spectra measurements of different types of tissue are valuable in tissue optics technique to differ diseased tissue from the normal tissues.

The spectra of major absorbing components of many soft tissues from UV to NIR are presented in Fig. 2-1 (a). Fig. 2-1(b) shows a pair of typical O.D. spectra of normal and cancer prostate tissues with ~100 μm thickness in the spectral range of 400 to 2400 nm. It can be seen from Fig. 2-1 that most of the absorption spectra of these chromophores are in the UV and the visible light range such as Tryptophan, Tyrosine, NADH, flavin and oxygenated hemoglobin (HbO_2). Hemoglobin is the strongest absorber of photon within ~500nm to ~900nm range and water is highly absorbing at the IR. In the far-red and near infrared spectral range (650 ~1000

nm), the intrinsic chromophore components are of very low absorption factor in soft tissues. We know this as the "optical window" to obtain the information inside of the human body.

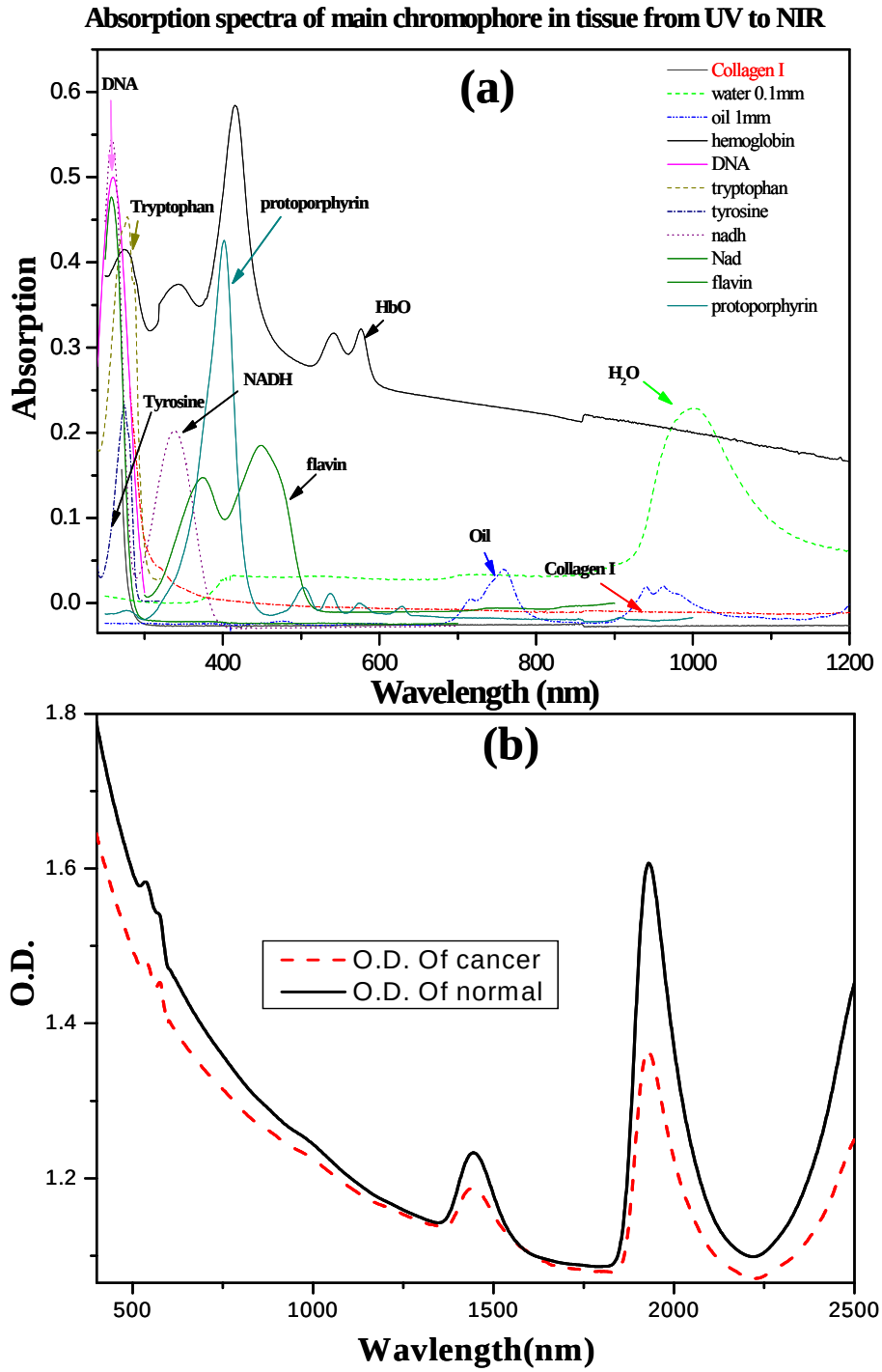

Fig. 2-1 (a) Absorption spectra of main chromophores in soft tissue from UV to NIR spectral region [Absorption is high in spectral range of UV, near visible, but low in red and NIR (650 nm ≤ λ ≤ 1,100 nm)]; (b) A pair of typical O.D. spectra of normal and cancer prostate tissues with ~100 μm thickness between 400 and 2400 nm.

As shown in Fig. 2-1(b), the profiles of major chromophores can be recognized in O.D. measurements of prostate tissue are water and HbO_2. This distinctive absorption of hemoglobin provides excellent contrast for hemoglobin concentration detection via absorption spectroscopy, which has given the biochemical specificity in breast cancer diagnosis [7]. For prostate cancer detection, the key spectra fingerprints of water were successfully used to distinguish different water contents in normal and cancerous prostate tissues [8].

2. 3. Fluorescence parameters of interest

Fluorescence occurs when a molecule, atom or nanostructure relaxes to its ground state after being electrically excited. Excitation is expressed as: $S_0 + h\nu \rightarrow S_1$ and fluorescence (emission): $S_1 \rightarrow S_0 + h\nu + heat$, where $h\nu$ is a generic term for photon energy with h = Planck's constant and ν = frequency of light (The specific frequencies of exciting and emitted light are dependent on the particular system). State S_0 is called the ground state of the fluorophore (fluorescent molecule) and S_1 is its first (electronically) excited state. There are three fluorescence parameters of interest we may concern in tissue optics: the fluorescence lifetime (τ), the fluorescence quantum yield (Φ) and the fluorescence emission peak (λ_{max}). Fluorescence lifetime refers to the average time the fluorophore spends in its excited state before emitting a photon. Fluorescence typically follows first-order kinetics: $[S_1] = [S_1]_0 e^{-t/\tau}$, where $[S_1]$ is the concentration of excited state molecules at time t, $[S_1]_0$ is the initial concentration at time t_0. At low concentrations the fluorescence intensity will generally be proportional to the concentration of the fluorophore.

The fluorescence emission peak (λ_{max}) is essential for each certain fluorophore therefore it can be identified and quantified on the basis of emission spectroscopy. The emission spectra are determined by measuring the variation in emission intensity wavelength for a fixed excitation

wavelength while the excitation spectra are determined by measuring the emission intensity at a fixed wavelength, while varying the excitation wavelength.

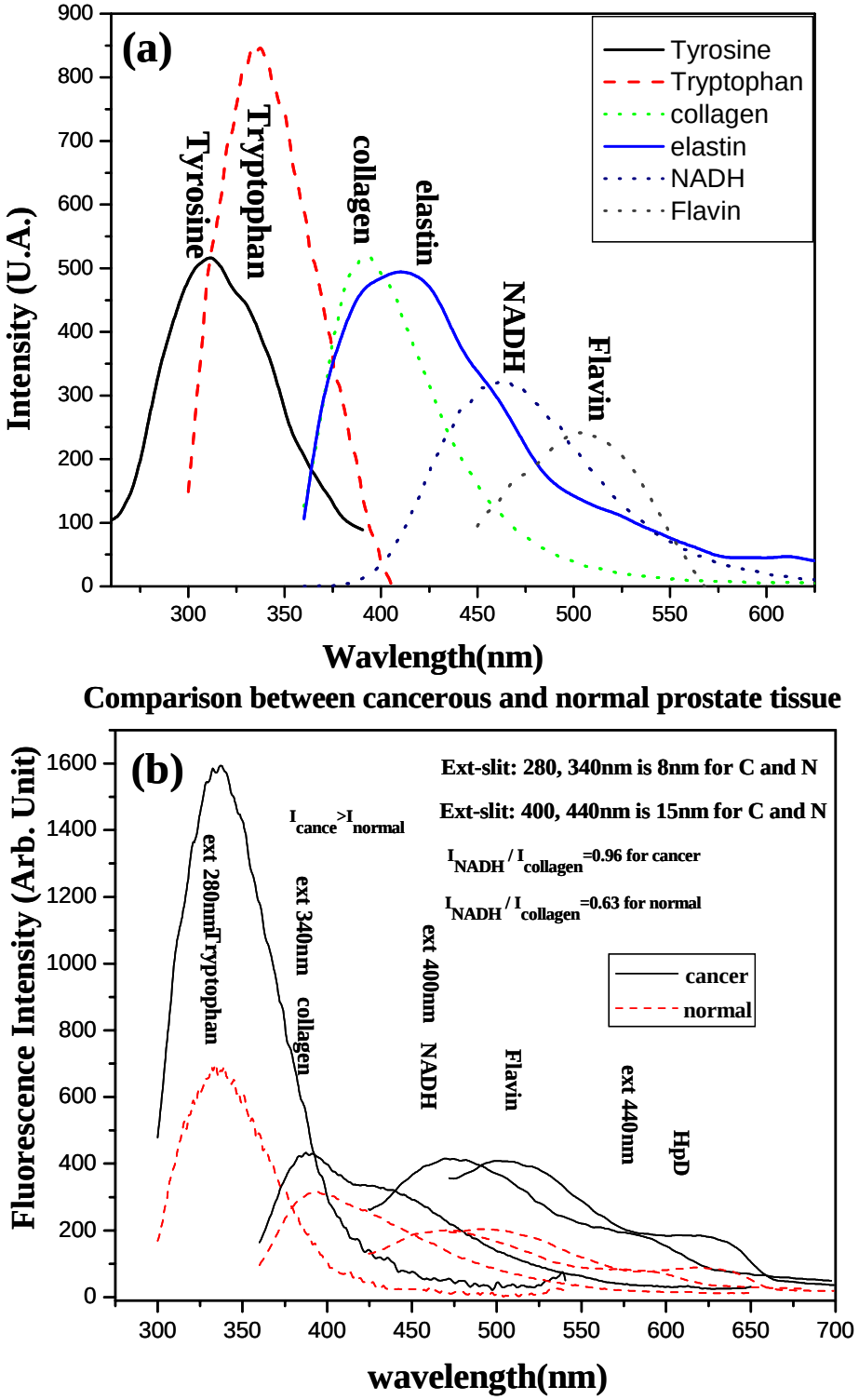

Fig. 2-2 (a) Fluorescence spectra of major intrinsic fluorophores in tissues, which emission ranges are most in UV to visible, not in NIR "optical window"; (b) Fluorescence emission spectra of cancerous and normal tissue in UV and visible range.

Fig. 2-2(a) shows the emission spectra of most auto-fluorescence fluorophores in soft tissue. Their pumping wavelength are mostly in ultraviolet (UV) and emission is limited from UV to visible [9], which are not in the tissue "optical window" [10]. However, the use of the intrinsic fluorescent biochemicals to differentiate the optical properties of diseased and healthy human prostate tissues is of the researcher's consideration because of its minimal yield of toxicity. Areas of interest include both biological fluorescence spectroscopy (steady-state and time-resolved) and imaging of endogenous fluorophores. The critical endogenous prostate fluorophores (including tryptophan, collagen, NADH, flavin and HpD) can be identified from the emission spectra of cancerous and normal prostate tissues as shown in Fig. 2-2 (b). The intrinsic fluorophores for prostate detection may be applied by stronger intensity from cancerous tissue in comparison with that of normal tissue indicated by Fig. 2-2 (b) [11]. Reproducible differences of the emission spectra profile between the cancerous and normal tissues were observed in the range from ~ 360nm to ~580nm excited by 340nm. Such alterations exposed by the tissue fluorescence are caused by both tissue biochemistry [11] and morphology [12] during tumor evolution.

2. 4. Light scattering in tissues

Scattering of light occurs in media which contains fluctuations in the refractive index n, whether such fluctuations are discrete particles or more continuous variations in n. Elastic scattering of light happens when charged particles in a medium are set into oscillatory motion by the electric field of the incident wave, and re-emit (as opposed to absorb) light of the same frequency as the primary wave. The light scattered by tissue interact with the ultrastructure of the tissue. Tissue ultrastructure extends from membranes to membrane aggregates to collagen fibers to nuclei to cells. Photons are most strongly scattered by those structures whose size matches the photon wavelength.

2. 4. 1. Scattering parameters of interest

The scattering coefficient μ_s [cm^{-1}] describes a medium containing many scattering particles at a concentration described as a volume density ρ_s [cm^3]. The scattering coefficient is essentially the cross-sectional area per unit volume of medium expressed by $\mu_s = \rho_s \cdot \sigma_s$ where σ_s is called the effective cross-section [cm^2]. The effective cross-section is related by the proportionality constant called the scattering efficiency Q_s (dimensionless): $\sigma_s = Q_s \cdot A_s$ where A_s is the geometrical size of the scattering particle [cm^2]. The scattering efficiency Q_s can be calculated using Mie theory [13].

The anisotropy factor, g (dimensionless), is a measure of the amount of forward direction retained after a single scattering event defined as equation 2.1. In equation 2.1., the angular dependence of scattering is called the scattering phase function, $p(\theta)$, which has units of [sr^{-1}] and describes the probability of a photon scattering into a unit solid angle oriented at an angle θ relative to the photons original trajectory. Henyey and Greenstein devised an expression which has proven to be useful in approximating the angular scattering dependence of single scattering events in biological tissues. The Henyey-Greenstein function allows the anisotropy factor g to specify $p(\theta)$ such that calculation of the expectation value for $\cos(\theta)$ returns exactly the same value g. The Henyey-Greenstein function is:

$$p(\theta) = \frac{1}{4\pi} \frac{1 - g^2}{(1 + g^2 - 2g\cos\theta)^{3/2}}. \qquad (2.5)$$

A series of Henyey-Greenstein functions are shown in Fig. 2-3. The forward direction along the original photon trajectory is 0°. Scattering in the backward direction is 180°. The curve for $g = 0$ has a constant value of $1/4\pi$.

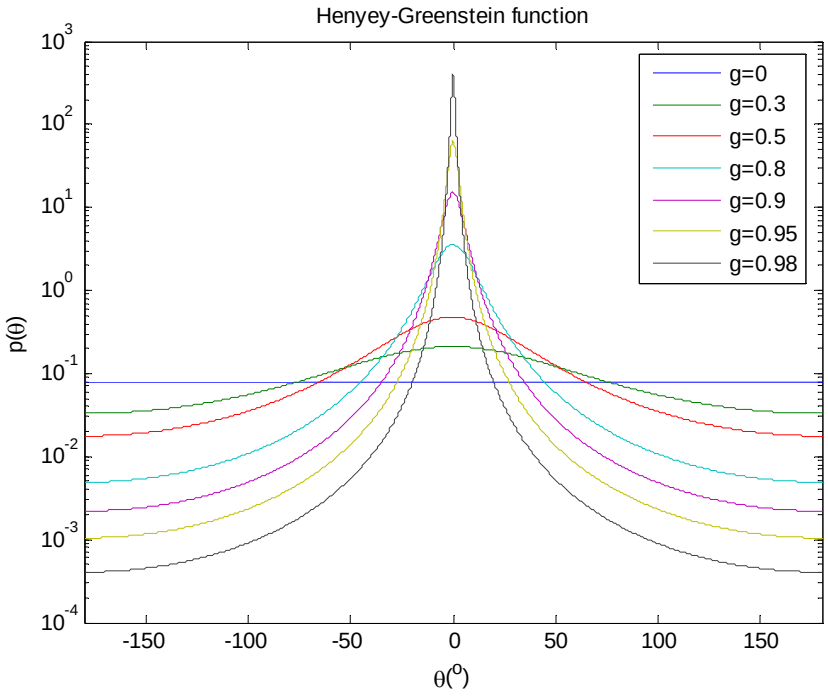

Fig. 2-3 Scattering phase function p(θ) simulated using Henyey-Greenstein function corresponding to different anisotropy factor g.

The reduced scattering coefficient is a lumped property incorporating the scattering coefficient μ_s and the anisotropy g defined as equation 2.2. The purpose of using μ_s' is to describe the diffusion of photons in a random walk of step size of $1/\mu_s'$ (cm) where each step involves isotropic scattering. If there are many scattering events before an absorption event, *i.e.*, $\mu_a \langle\langle \mu_s'$, this situation of scattering-dominated light transport is called the diffusion regime and μ_s' is useful in the diffusion regime which is commonly encountered when treating how visible and near-infrared light propagates through biological tissues.

2. 4. 2. Mie theory model for tissue optical properties

Mie theory deals with analytical solution of Maxwell's equations for the scattering of electromagnetic radiation by spherical particles of any size (also called Mie scattering). Mie's classical solution is described in terms of two parameters: (1) m, the magnitude of refractive index mismatch between particle and medium expressed as the ratio of the n of particle to that of

medium: $m = n_p / n_{med}$; (2) x: the size parameter, which is the ratio of the circumference of the sphere (2πa, where radius = a) to the wavelength (λ/n_{med}) of light in the medium, $x = 2\pi a / (\lambda/n_{med})$. Among tons of textbooks and research papers, excellent descriptions of Mie scattering were given by Bohren and Huffman (BH) [13]. The computation of these parameters has been involved spherical Bessel functions.

The Mie theory calculation yields two sets of descriptors of scattering: angular scattering pattern of polarized light and efficiencies of scattering and absorption. The angular scattering pattern is used to compute the scattered intensities of polarized light, phase function $p(\theta)$ and the anisotropy factor g. The efficiencies Q_s and Q_a of scattering and absorption can be used to calculate the scattering coefficient μ_s and the absorption coefficient μ_a given particle number density ρ_s. (The absorption coefficient is essentially the cross-sectional area per unit volume of medium expressed by $\mu_a = \rho_a \cdot \sigma_a$ where σ_a is called the effective cross-section [cm^2]. The effective cross-section is related by the proportionality constant called the absorption efficiency Q_a (dimensionless): $\sigma_a = Q_a \cdot A_a$ where A_a is the geometrical size of the absorption particle [cm^2].)

A set of Matlab functions has been developed to compute the coefficients of extinction, scattering, backscattering, absorption and the anisotropy factor and simulate the scattering pattern for sphere and cylinder using BH Mie algorithm [13]. In order to study the NIR light property in prostate tissue, the simulation and calculation were performed by taking refractive index of particle and medium as 1.46 and 1.35 since n of nuclei of prostate tissue cell is reported to be ~1.46, and that of surrounding cytoplasm to be ~1.35 for prostate tissue [14]. The total volume fraction of all scatters T_v was set to 0.02 [15]. The scattering particles are treated as spheres and the above parameters are applied in the following simulation or calculation if there are no other statements.

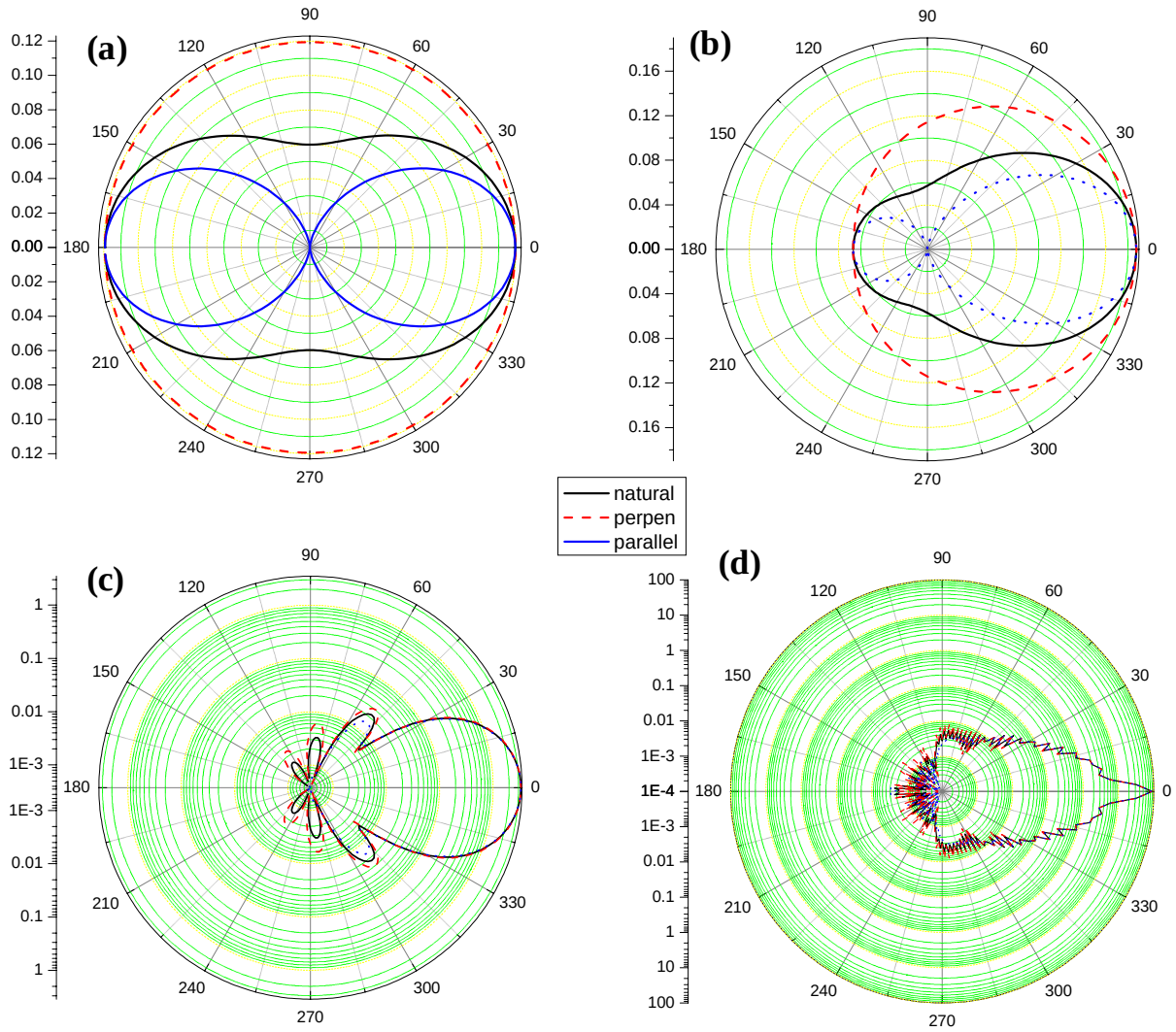

Fig. 2-4 Mie simulation of the angular dependence of the intensities for parallel (dot), perpendicular (dash) orientations of polarized source vs. detector pairs and the intensities of total nature light (solid) in medium as prostate cytoplasm irradiated by 780 nm NIR laser diode scattered by particle diameters of (a) 11nm, (b) 200nm, (c) 1.2 μm and (d) 9.3 μm.

The angular patterns of Mie scattering are studied. Consider four different diameters of the particles, 11nm ribosome, 200 nm centriole [16], 1.2 μm normal prostate nucleolar [17] and 9.3 μm cancerous prostate nuclei [18], in medium as prostate cytoplasm irradiated by 780 nm NIR laser diode. Fig. 2-4 describes the angular dependence of the intensities of scattering for parallel, perpendicular orientations of polarized source vs. detector pairs, and the intensities of total nature light. The salient features of Fig. 2-4 are that scattering intensity is isotropy when particle size is much smaller than the incident wavelength as shown in Fig.2-4 (a). This range, $x \langle\langle \lambda_i$, is

also know as Reyleiy scattering range. With particle size increasing, light prefer more and more forward scattering, which are indicated by (b) to (d).

The wavelength and particle size dependence of μ_s and g were studied using Mie theory. Fig. 2-5 exhibits the profiles of μ_s and g of the three kinds of particles changing with incident wavelength from 300 to 1,200nm. For both large and small scattering particles, Mie theory predicts that μ_s and g decrease when wavelength increases from UV to NIR.

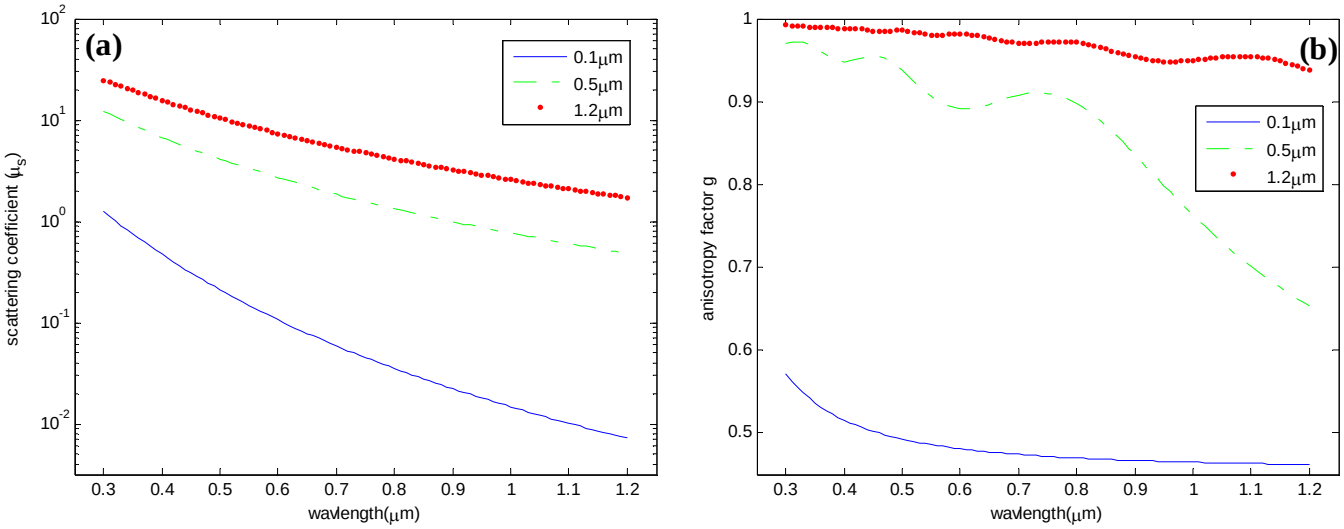

Fig. 2-5 Wavelength dependence of (a) scattering coefficients μ_s and (b) anisotropy factor g

The diameter dependence of scattering coefficients μ_s and anisotropy factor g irradiated by three laser of 632.8nm, 780 nm and 1.6 μm are shown as Fig. 2-6.

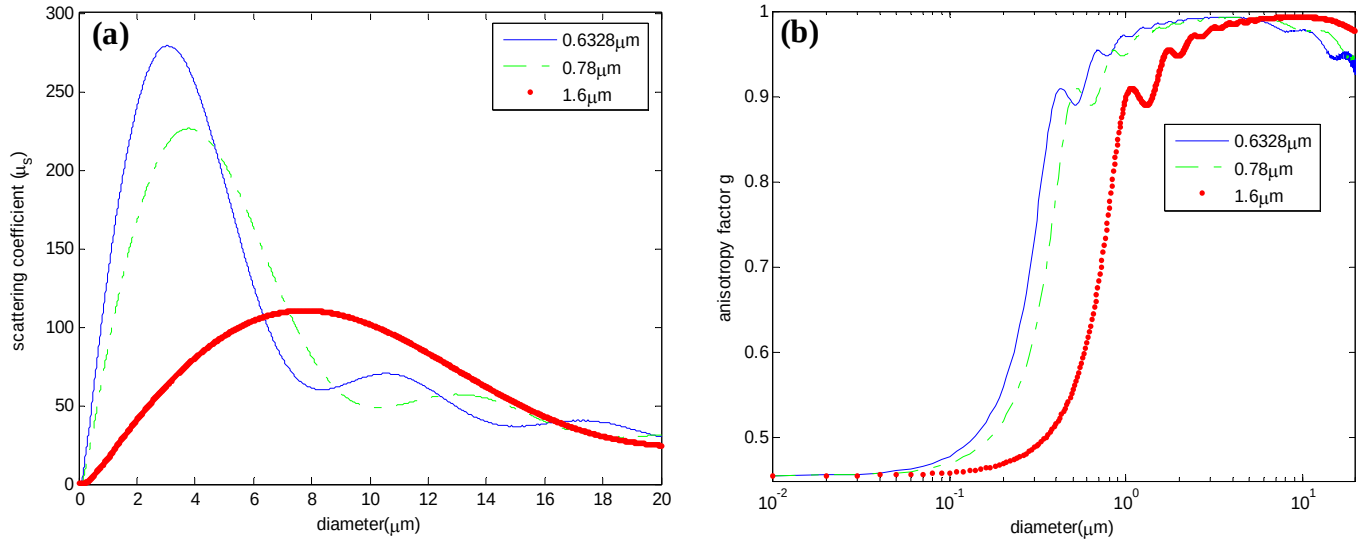

Fig. 2-6 (a) Scattering coefficients μ_s and (b) anisotropy factor g vs different diameters of particle

When particle size is very small, both μ_s and g increased with the increasing of particle diameters. After certain critical value, they somehow fluctuate. However, the fluctuation of g is very small and always larger than 0.9 indicating strong forward scattering for larger particle.

Besides scattering sphere, Mie theory also provides excellent analytical solution for cylindrical scatters. In biological tissue, collagen varies from 0.1 μm-diameter fibrils to 8 μm-diameter fiber bundles and can be modeled as cylindrical scatters. Assuming that the incident light is oriented perpendicular to the long axis of the fiber cylinders and each fiber cylinder scatters light independently, ignoring any interference effects from closely spaced fibers, Mie theory simulates collagen fiber scattering in dermis shown as Fig. 2-7. The n_{med} of the dermal ground substance is reported as 1.350, and the n_p of the collagen fiber bundles is 1.389 [14].

The Mie theory gives excellent prediction for the scattering and absorption coefficients if the distribution function of particle size and relative refractive index are known. Because of the irregular shape and varying density of scatters in tissue, and conflict report about the refractive index of tissue medium, the scattering and absorption coefficients are mainly obtained from experimental measurements [19]. There are two methods based on Mie theory, which can be used to deal with a few real world problems. One is the discrete particle model [20] and another is fractal dimension model [21, 22]. The fractal dimension model, developed by M. Xu and R. R. Alfano, treats the irregular shape of a scatter as fractal dimension thus does not require such accurate information of the distribution function of particle size as the discrete model. The application of fractal dimension model for differentiation of optical properties between cancerous and normal prostate tissues will be introduced in chapter 3.

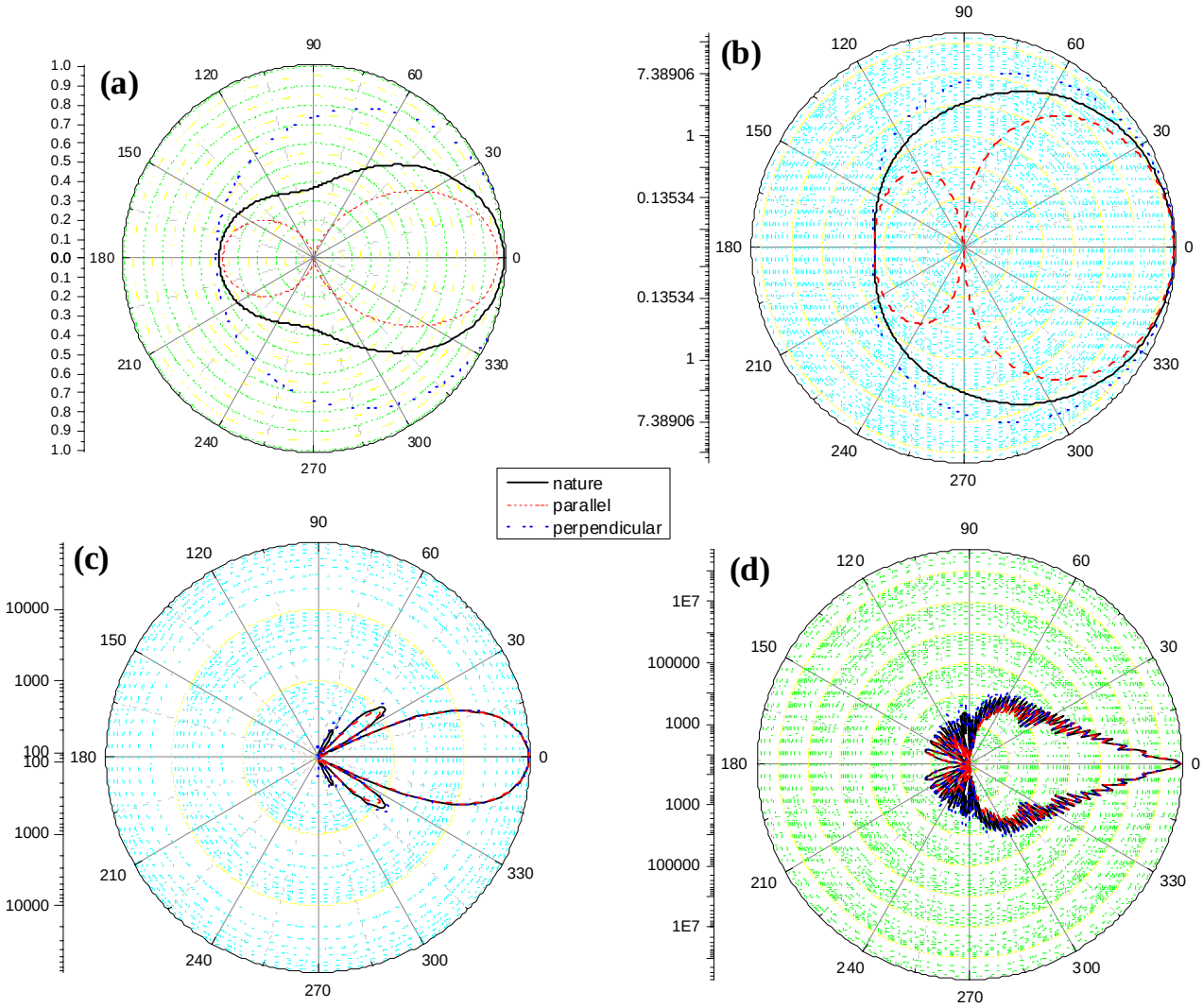

Fig. 2-7. Mie simulation of the angular dependence of the intensities for parallel (dot), perpendicular (dash) orientations of polarized source vs detector pairs and the intensities of total nature light (solid) in medium as dermis irradiated by 780 nm NIR laser diode scattered by collagen fiber of diameters of (a) 0.1 μm, (b) 0.2 μm, (c) 1 μm and (d) 8 μm.

2. 5. Models of Light Propagation in Turbid Media

The previous sections have discussed the physical basis for the absorption, emission and scattering of light radiation, and the components in biological tissue responsible for these. The theories discussed in Section 2.3 can describe light propagation by both large and small particles (relative to the wavelength of the incident light) assuming a small enough collection of particles, or one in which the particles are far enough apart, such that their individual scattered fields do

not significantly perturb each other. In biological tissue, however, the scattering particle density is such that the interaction of scattered waves between neighboring particles cannot be ignored and multiple scattering is hard to occur. This section will discuss models of light propagation that are frequently used to describe absorption and scattering in turbid media such as tissue.

It is possible to describe light transport in a regime where multiple scattering dominates using Maxwell's electromagnetic theory [13]. It has been noted, however, that solutions to multiple scattering theory will be highly complex [23], and therefore not practical for the applications associated with clinical NIR range. A more suitable description is one in which the wavelike behavior of light is ignored and the transport of individual photons, which can be absorbed or scattered, is considered. This is known as radiative transfer theory. The radiative transfer equation (RTE) is written as:

$$\frac{1}{v}\cdot\frac{\partial}{\partial t}I(\mathbf{r},t,\hat{s})+\hat{s}\cdot\nabla L(\mathbf{r},t,\hat{s})=-(\mu_a+\mu_s)I(\mathbf{r},t,\hat{s})+\mu_s\int_{4\pi}p(\hat{s},\hat{s}')d^2\hat{s}'+\varepsilon(\mathbf{r},t,\hat{s}) \qquad (2.6)$$

which describes the behavior of the energy radiance $L(\mathbf{r},t,\hat{s})$ in the medium, i.e. the energy at position **r** moving in the direction $\hat{s}$ per unit of solid angle, per unit of time *t* and per unit of area normal to the $\hat{s}$ direction. The other parameters in the equation are *v*, the velocity of the light in the medium, μ_a and μ_s, the absorption and scattering coefficients, *p*, the scattering phase function and $\varepsilon(\mathbf{r},t,\hat{s})$, the radiation source term. Analytical solutions to the RTE that describe photon migration explicitly can be obtained by introducing further approximations. One of the most popular models used in the field of tissue optics is the diffusion approximation, the theory of which will be discussed in Section 2. 4. 1. A stochastic approach to modeling light propagation can also be taken, again based on radiative transfer theory, and one such technique, the Monte Carlo (MC) method, will be discussed in Section 2. 4. 2.

2. 5. 1. The Diffusion Approximation

The RTE can be reduced to a set of coupled differential equations by approximating the angular dependence of the radiance by a spherical harmonic expansion of the energy radiance and source terms, $L(\mathbf{r},t,\hat{s})$ and $\varepsilon(\mathbf{r},t,\hat{s})$, in Equation 2. 6. The diffusion approximation is the first-order approximation of the spherical harmonic expansion, also known as the P_1 approximation, which gives a set of differential equations from which the diffusion equation can be derived. The assumptions made in the derivation of the diffusion equation are that the source is an isotropic point source and scattering within the medium is (approximately) isotropic. The time-dependent diffusion equation is given by [23]:

$$\frac{1}{v}\cdot\frac{\partial F(r,t)}{\partial t} - D\nabla^2 F(r,t) + \mu_a F(r,t) = \varepsilon_0(r,t)\,, \tag{2.7}$$

where F is the photon density or fluence rate, related to the energy radiance as follows:

$$F(\mathbf{r},t) = \int_{4\pi} L(\mathbf{r},t,\hat{s})d\hat{s}\,, \tag{2.8}$$

ε_0 is the isotropic source term and D is the diffusion coefficient, given by

$$D = \frac{1}{\mu_a + 3(1-g)\mu_s} = \frac{1}{\mu_a + 3\mu_s'}\,, \tag{2.9}$$

where μ_s' is the reduced scattering coefficient, and g is the anisotropy factor defined before. The reduced scattering coefficient μ_s', also called transport scattering coefficient, takes account of the anisotropy of the scattering in an essentially isotropic model. Therefore, μ_s' effectively represents the isotropic medium, with g = 0, that gives an equivalent light distribution to an anisotropic medium of scattering coefficient μ_s and anisotropy factor g. Hence, by incorporating g in this way the diffusion approximation can model a 'linear anisotropy' that is suitable for biological media.

The solution to diffusion equation by using Fick's 2nd Law for the case of a point source of energy, ε_0 [units], deposited at zero time ($t = 0$) at the origin ($r = 0$) is $\varepsilon(\mathbf{r},t)$ [14]:

$$\varepsilon(\mathbf{r},t) = \varepsilon_0 \frac{\exp(-\frac{r^2}{4\chi t})}{(4\pi\chi t)^{3/2}}. \qquad (2.10)$$

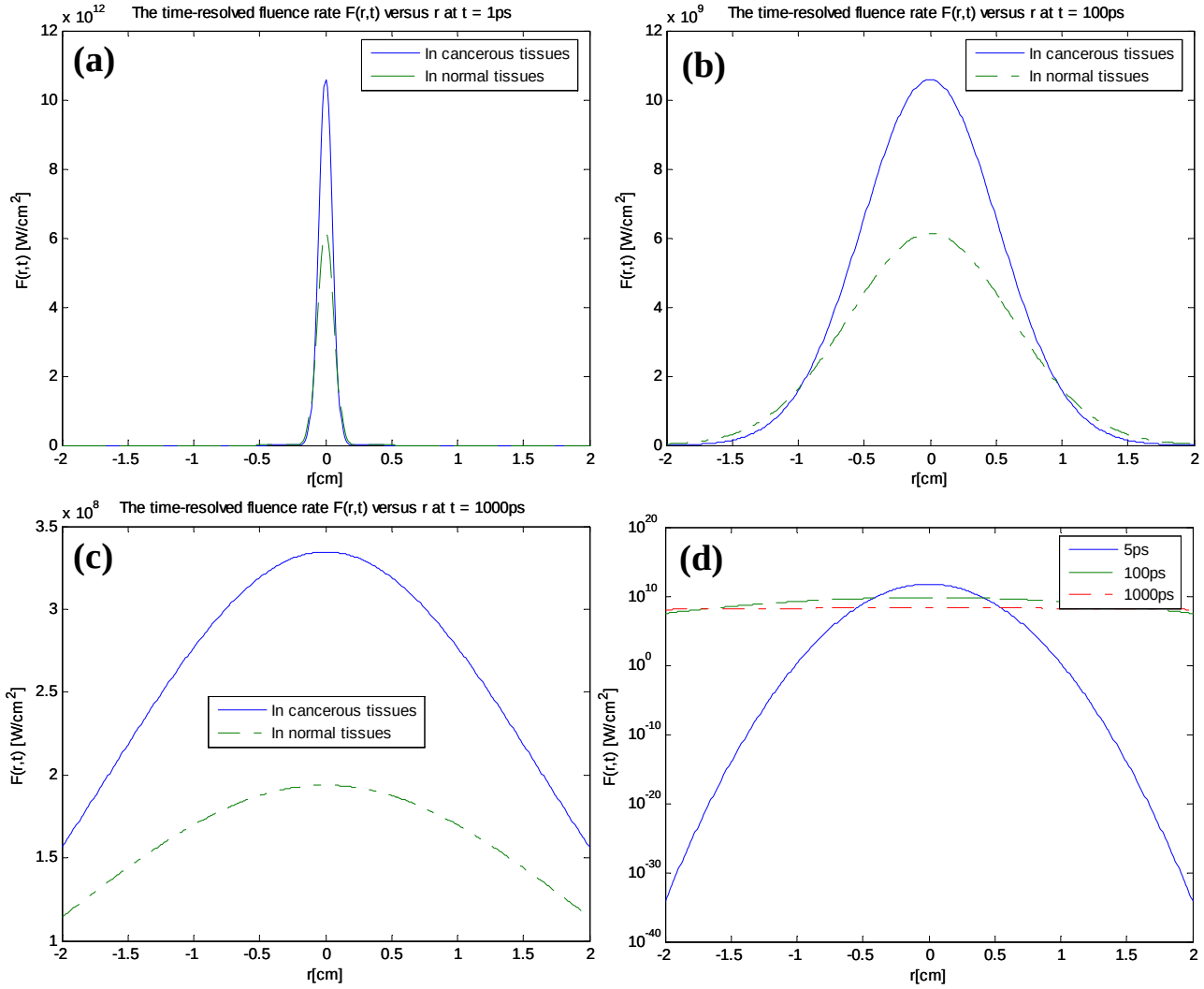

Fig. 2-8 The time-resolved fluence rates $F(r,t)$ simulated within medium of optical properties as cancerous (solid) and normal (dash-dot) prostate tissues plotted versus r at three time points: (a) 5ps; (b) 100ps; and (c) 1000ps; (d) $F(r,t)$ within medium of optical properties as cancerous prostate tissues at 5ps (solid), 100ps (dash) and 1000ps (dash-dot).

For the case of optical diffusion, $F = c\varepsilon$ and $\chi = cD$ since the diffusivity χ is proportional to the coefficient D (cm) and the speed of light c. Let the point source be an impulse of energy ε_o [J]. The expression for fluence rate $F(\mathbf{r},t)$ (W/cm^2) becomes [14]:

$$F(\mathbf{r},t) = c\varepsilon_0 \frac{\exp(-\frac{r^2}{4cDt})}{(4\pi cDt)^{3/2}}. \quad (2.11)$$

The Fig. 2-8 illustrate the time-resolved transport of light from an impulse isotropic point source of energy within a homogeneous unbounded medium with similar absorption and scattering properties as cancerous and normal prostate tissues. The optical coefficients are taken as n=1.35, g=0.94, μ_a = 0.82 cm^{-1} and μ_s = 95cm^{-1} for simulating scattering medium as cancerous prostate tissue and g=0.97, μ_a = 1.71 cm^{-1} and μ_s = 131cm^{-1} as normal prostate tissue [24]. All following simulation will be taken as the above parameter if there are no other statements. The impulse energy: ε_0 = 1 J.

The time-resolved fluence rate $F(r,t)$ (W/cm^2) in response to an impulse of energy U_o (J) while the steady-state fluence rate $F_{ss}(r)$ (W/cm^2) in response to an isotropic point source of continuous power P_o (W) are summarized:

$$F_{ss}(r) = P_0 T_{ss}(r). \quad (2.12)$$

The above expression for $T_{ss}(r)$ can be obtained by integrating $T(r,t)\exp(-c\mu_a t)$ over all time to yield the total accumulated amount of photon transport to each position r

$$T_{ss}(r) = \int_0^\infty T(r,t)\exp(-c\mu_a t)dt = \frac{\exp(-r\sqrt{\mu_a / D})}{4\pi Dr}. \quad (2.13)$$

By defining optical penetration depth δ as:

$$\delta = \frac{1}{\sqrt{\mu_a / D}}. \quad (2.14)$$

The physical meaning of δ is the incremental distance from the source that causes $F_{ss}(r)$ to decrease to 1/e its initial value. Substituting δ into equation 2.13, then put it into equation 3.11, the steady-state fluence rate $F_{ss}(r)$ can be obtained:

$$F_{ss}(r) = P_0 \frac{\exp(-r\sqrt{\mu_a / D})}{4\pi D r} = P_0 \frac{e^{-r/\delta}}{4\pi\mu_a \delta^2 r}. \quad (2.15)$$

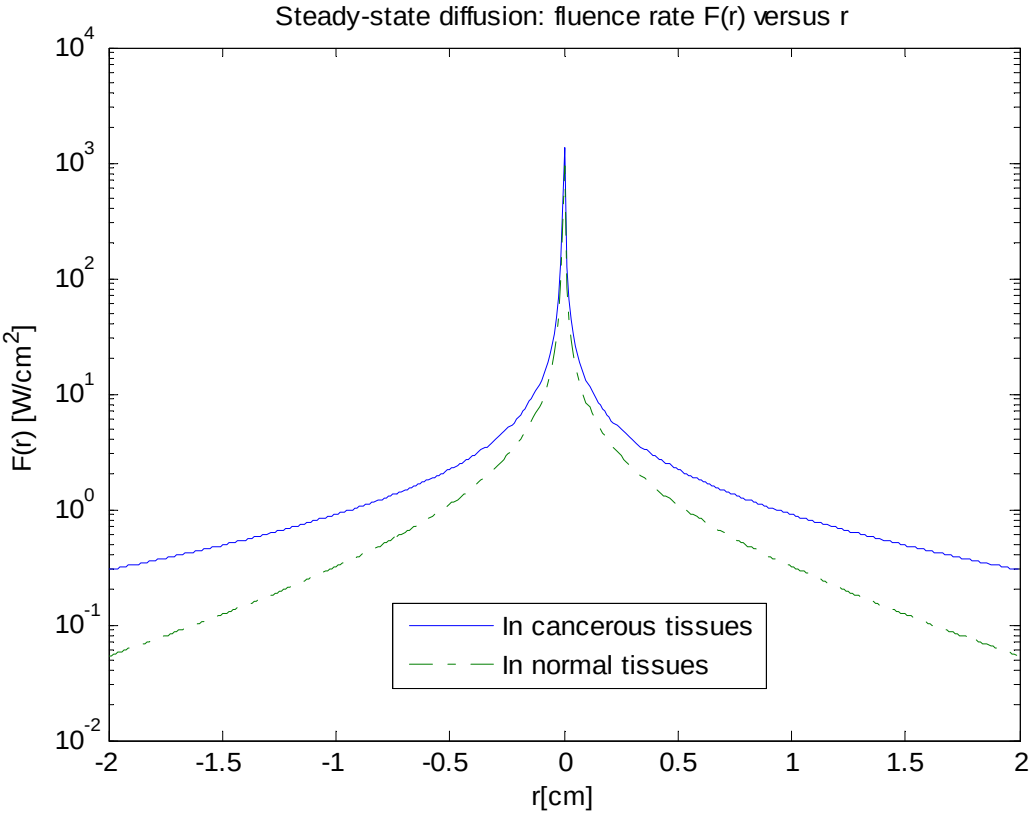

Fig. 2-9 The simulation of the transport of light from a steady-state isotropic point source of power within a homogeneous unbounded medium with same absorption and scattering properties as cancerous (solid) and normal (dash-dot) prostate tissues.

The Fig. 2-9 illustrates the transport of light from a steady-state isotropic point source of power within a medium with similar absorption and scattering properties as cancerous and normal prostate tissues. The impulse power: $P_0 = 1$ W.

A light source can be also modulated sinusoidally to yield a sinusoidally varying fluence rate distribution at a distant observation point within a medium. Such a modulated concentration will propagate in the medium and is often called a photon density wave. Considering a point source S_0(W) which is modulated sinusoidally by a modulation factor $M_0\sin(\omega t)$, where $0 < M_0 < 1$:

(2.16)

$$S(t) = S_0(1 + M_0 \sin(\omega t)) = S_0(1 + M_0 e^{i\omega t}),$$

where $\omega = 2\pi f$ (radians/s) is the angular frequency of modulation, and the modulation frequency f is in hertz. The position of observation r is located a distance r from the source. The above equation shows two ways to express $S(t)$, one using a sine function and the other using the equivalent and well-known convention of an exponential with an imaginary exponent. In response to this modulated source, the modulated fluence rate $F(r,t)$ at r is described:

$$F_{ss}(r) = P_0 \frac{\exp(-r\sqrt{\mu_a / D})}{4\pi D r} = P_0 \frac{e^{-r/\delta}}{4\pi\mu_a \delta^2 r} = S_0 T_{ss}(r)(1 + M_0 \exp(-rk'' - r/\delta)\sin(\omega t - k'r)),$$
$$F_{ss}(r) = S_0 T_{ss}(r)(1 + M_0 \exp(-rk'' - r/\delta)\exp[i(\omega t - k'r)]), \quad (2.17)$$

where $T_{ss}(r)$ is the steady-state transport, k'' is the imaginary wavenumber describing the attenuation of the photon density wave and k' is the real wavenumber describing the phase lag of the observed photon density wave. $T_{ss}(r)$ is expressed by equation 2. 13, k'' and k' are:

$$k'' = \frac{1}{\delta}\sqrt[4]{1 + [\omega/(\mu_a c)]^2}\,\sin(\theta/2) = \frac{1}{\delta\sqrt{2}}\sqrt{1 + \sqrt{1 + [\omega/(\mu_a c)]^2}}, \quad (2.18)$$
$$k' = \frac{1}{\delta}\sqrt[4]{1 + [\omega/(\mu_a c)]^2}\,\cos(\theta/2) = \frac{1}{\delta\sqrt{2}}\sqrt{-1 + \sqrt{1 + [\omega/(\mu_a c)]^2}},$$

where $\theta = \tan^{-1}[\omega/(\mu_a c)]$.

At observation point, the persistence of source modulation is called modulation, M, and is often described in the literature as $[(AC)_{out}/(DC)_{out}]/[(AC)_{in}/(DC)_{in})]$ which equals: $M = \exp[-r(k''-1/\delta)]$. The phase of the signal lags the phase of the source by an angle called the phase lag, ϕ (radians), which equals: $\phi = rk'$.

The Fig. 2-10 illustrates the frequency domain signal $F(r,t)$ in the medium with optical properties same as cancerous tissue (dash) and that as normal tissue (dot). The source $S(t)$ is also plotted as reference. Source: f = 400 MHz, S_0 = 1W, M_0 = 1. Note that the greatly decreased F_{ss}, the slightly decreased modulation M, and the phase lag ϕ at the observation point.

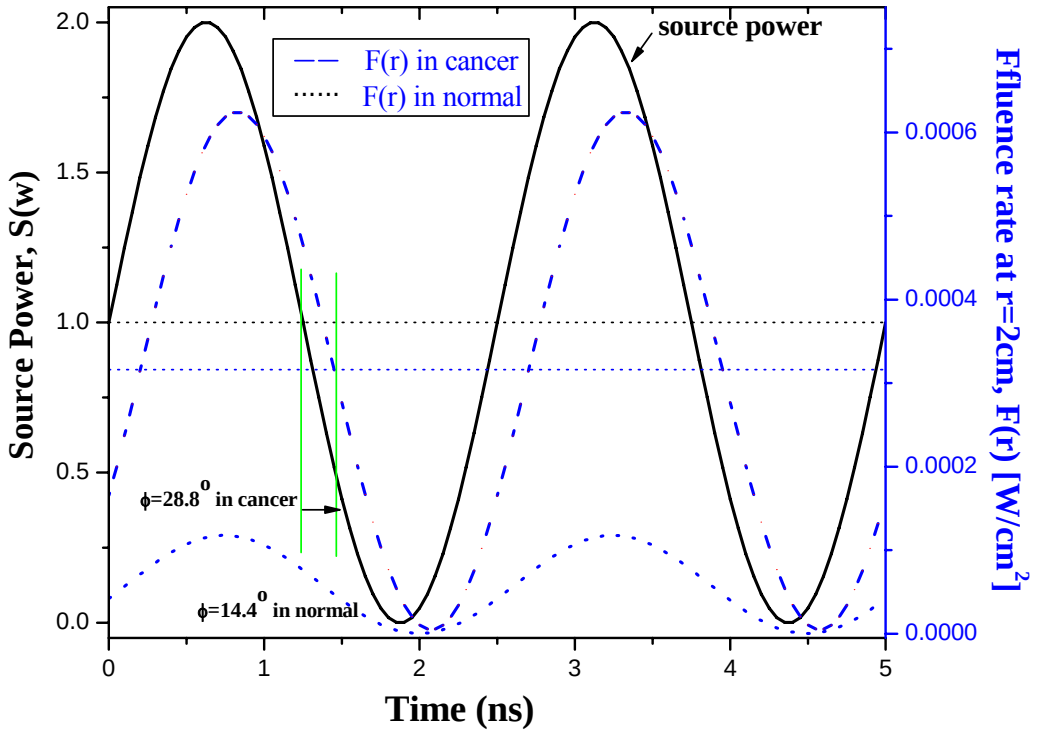

Fig. 2-10 Frequency domain signal fluence rates F(r,t) in the medium with optical properties same as cancerous tissue (dash) normal tissue (dot) at distance r=2cm of source.

The Fig. 2-11 exhibits factor $M\sin(-\phi)$ is plotted versus position r by taking same parameters values as those for Fig. 2-10.

Fig. 2-11 (a) show that light intensities in cancerous tissues decay faster than that in normal, illustrating that lower absorption yields a longer photon lifetime which allows smearing of the spatial resolution of the modulation which attenuates the modulation [14] since $\mu_a^{cancer}(0.82\text{cm}^{-1})$ $\langle\ \mu_a^{normal}(1.71\text{cm}^{-1})$ is taken in our simulation. Fig. 2-11 (b) shows the fluence rate $F(r,t)$ is versus position r for a specific time t = 0s. $F(r,t)$ falls very quickly which makes the modulation difficult to see, especially on a logarithmic scale.

There are several situations, however, in which the diffusion approximation is not valid. Due to the highly forward-directed nature of scattering in most tissues, the light close to the boundaries and the illuminating source is far from diffuse and the assumption of isotropy is

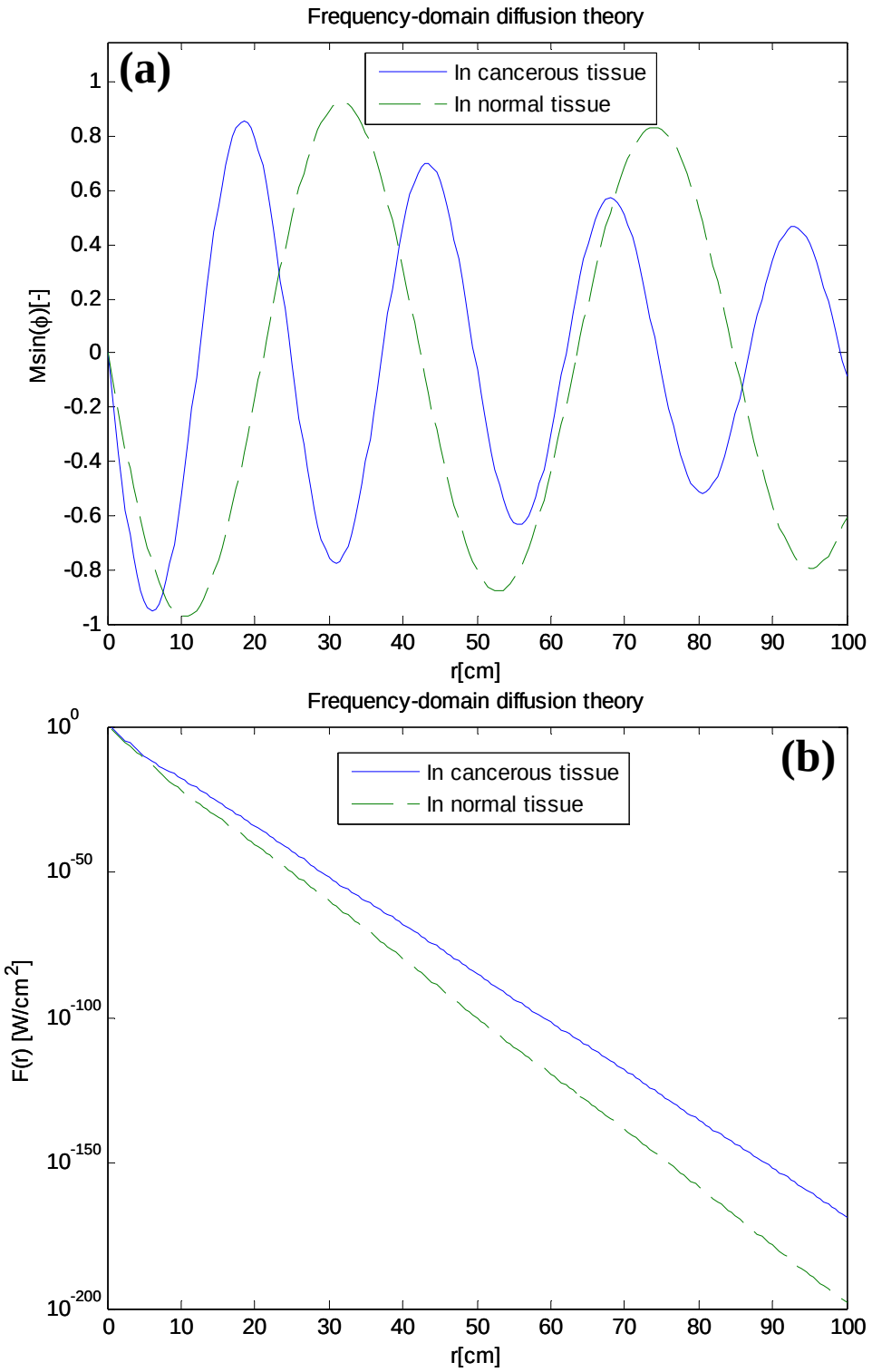

Fig. 2-11 (a) $M\sin(-\phi)$ versus position r. The light intensities in cancerous tissues (solid) decay faster than that in normal (dash). (b) The fluence rate transport in cancerous (solid) and normal (dash) tissue versus position r for a specific time t = 0s.

therefore completely invalid. A further condition of the diffusion approximation is that μ_s is much greater than μ_a. If μ_a is comparable to or larger than μ_s, then the light will not deviate sufficiently from the forward-direction, even at depth, for it to be considered diffuse. In most tissues, μ_s is greater than μ_a by one to two orders of magnitude [14], due to the low absorption by water in the NIR [14].

2. 5. 2. The Monte Carlo Method

The Monte Carlo (MC) method, as applied to the transport of light radiation, is based on the RTE and involves computer-simulated calculations of photon propagation in scattering media. As with radiative transfer theory, MC simulations treat the photons as particles, ignoring their wave-like nature. Therefore, parameters such as the phase and polarization of the light are usually discounted. Wang and Jacques [25] argue that this is justifiable since, due to the multiple scattering of the photons, these properties are quickly randomized. In the simplest of MC simulations photons are injected into a medium individually and their paths traced until they are either absorbed or permanently scattered out of the region of interest. The rules of photon propagation are expressed as probability distributions, which are based on the geometry and optical properties of the medium. The advantages over the diffusion approximation are that MC simulations do not require that μ_s and μ_a, accurate results can be obtained close to sources and boundaries [25]. In addition, complicated geometries and multi-layered tissues in which the optical properties vary spatially can be modeled easily [14, 25]. However, although potentially highly accurate, the simulations can be expensive due to the long computational times required to achieve such accuracy.

A basic method for MC simulation, developed by Prahl and coded by Wang and Jacques, will be outlined here [25]:

1. The photon is incident on the tissue boundary at an angle of α and with a weight of $W = 1$;

2. The photon weight is reduced by an amount equivalent to the reflected component at the boundary: ΔW;

3. The new direction of the photon is calculated from the incident angle$\alpha$and the refractive index at the tissue boundary;

4. The photon step size l is calculated as follows:

$$l = \frac{\ln(\xi)}{\mu_t},$$

where ξ is a randomly generated number between 0 and 1 and μ_t is the total attenuation coefficient. It can be shown that on average the step size l is equal to the mean free path, μ_t^{-1} as expected [25];

5. The photon weight is reduced again, due to absorption, by an amount:

$$\Delta w = w\frac{\mu_a}{\mu_t},$$

where W is now the weight at the end of step 2;

6. A random number, 0 or 1, is then generated to determine if the photon will be scattered. If the number generated is 0 then no scatter occurs and the procedure is repeated from step 3. For a value of 1 the photon is scattered;

7. The new direction of the scattered photon is calculated using two angles: the deflection angle θ, which has values between 0 and π, and the azimuthal angle φ with values between 0 and 2π. The deflection angle is calculated from the normalised, cumulatively integrated scattering phase function using ξ. The azimuthal angle is uniformly distributed over the interval 0 to 2π and is therefore calculated by $\varphi = 2\pi\xi$.

Steps 3–6 are repeated for the desired number of photons. If the simulation involves more complex heterogeneous model the process returns to step 1 when a tissue boundary is reached, proceeding in the same manner but using the optical properties for the new region.

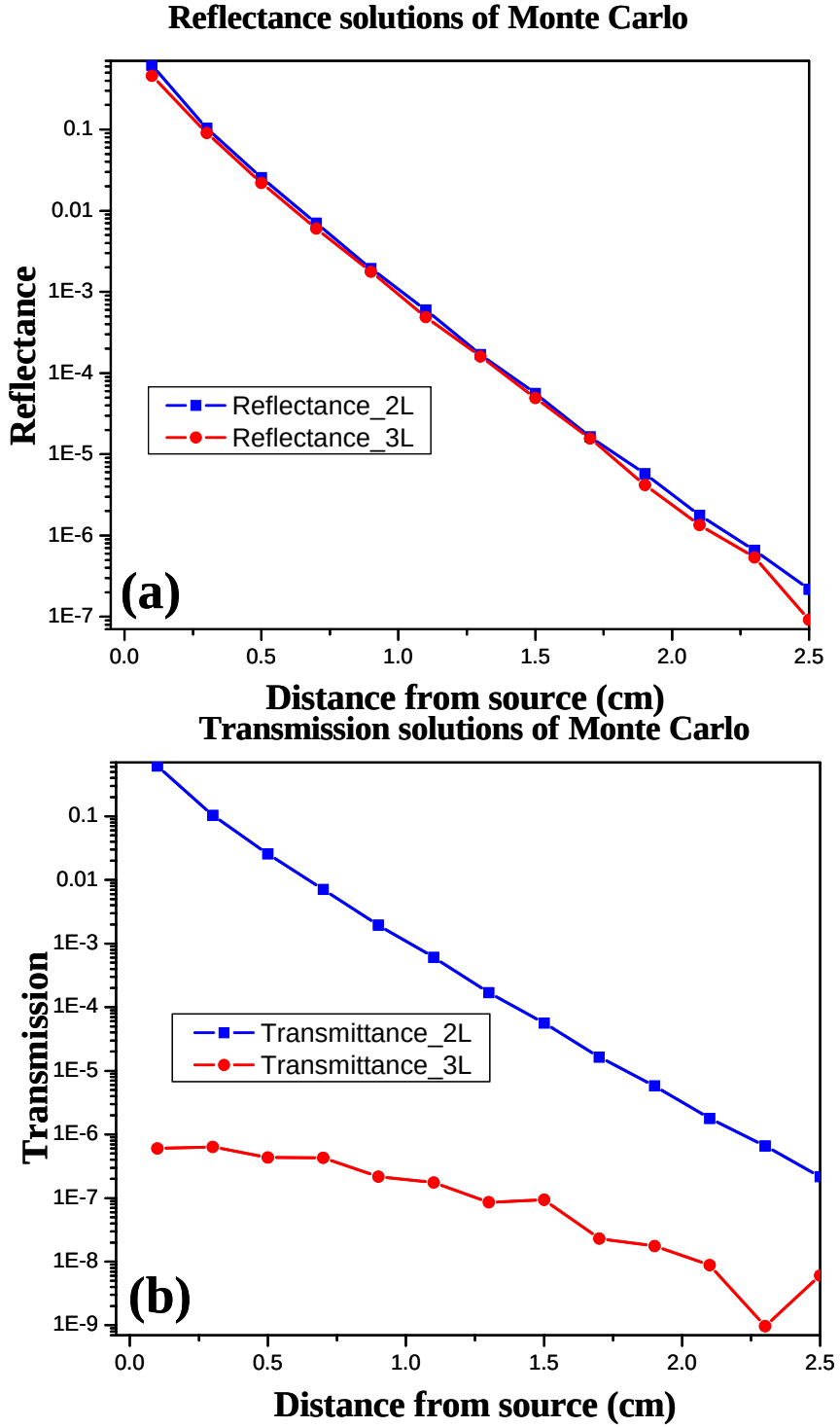

Fig. 2-12 (a) Reflectance and (b) transmittance as a function of distance from light source calculated with MC simulations for 2-layer (square) and 3-layer (circle) with same total thickness.

A set of Monte Carlo (MC) simulation matlabe code was developed to model light transport in turbid media within same optical properties as prostate tissue. The code is based on previous MC program [25], which was written in C. However, it has been adapted and truncated just for basic needs to study spatially-resolved purpose. Figs. 2-12 show the results of the spatially-resolved reflectance and transmittance of light transport in 2 layers [cancer(01.cm)-normal(2.5cm) tissue] and 3 layer [normal(0.1cm)-cancer(01.cm)-normal(2.5cm) tissue].

2. 6. Chapter summary

This chapter was started in section 2.1 with the optical coefficients, which illustrate the complex nature of light transporting in biological tissue. In section 2.2, the concept of light absorption pertaining to the NIR region of the spectrum was described and definitions relevant to its quantification and measurements were introduced. This section also presents the constituents of biological tissue responsible for the absorption of NIR light, highlighting the important features of their absorption spectra. In Section 2.3, the fluorescence spectroscopy and its application in tissue were reviewed. Then, basic theory behind light scattering and the parameters used to describing scattering are emphasized. The biological particles that give rise to scattering in tissue are studied and identified using Mie scattering. Section 2.4 discusses the models commonly used to describe the transport of light through turbid media, i.e. those in which multiple scattering occurs. In particular, the discussion of both experimental measurements and simulations in this chapter concentrates on the assumptions and approximations from the optical parameters of cancerous and/or normal prostate tissue. Therefore, the experiments and models somehow reflect their validity in 'real' situations.

2. 7. References

1. B. B. Das, Feng Liu and R. R. Alfano, "Time-resolved fluorescence and photon migration studies in biomedical and model random media", *Rep. Prog. Phys*. 60, 227–292 (1997).
2. C. F. Bohren and D. R. Huffman, "Absorption and scattering of light by small particles". First edition, New York: John Wiley and Sons, (1983).
3. M. Xu, M. Alrubaue, S. K. Gayen and R. R. Alfano, "Determination of light absorption, scattering and anisotropy factor of a highly scattering medium using backscattered circularly polarized light", *Optical interaction with tissue and cells XVIII, Proc. Of SPIE* 6435, 64350J1-6 (2007).
4. G. Zaccanti, E. Battistelli, P. Bruscaglioni and Q. Wei, "Ananlytic relationships for the statistical moments of scattering point coordinates for photon migration in a scattering medium", *Pure & Appl. Opt*, 3(5), 897-905 (1994).
5. J. H. Lambert, "Photometria, sive de mensura et gradibus luminis, colorum et umbrae" , Augsburg, (1760).
6. A. Beer, "Bestimmung der Absorption des rothen Lichts in farbigen Fl¨ussigketiten", *Ann Physik Chem*, 86(5), 78–88 (1852).
7. B. J. Tromberg, N. Shah, R. Lanning, A. Cerussi, J. Espinoza, T. Pham, L. Svaasand and J. Butler, "Non-invasive in vivo characterization of breast tumors using photon migration spectroscopy", *Neoplasia*, 2, 26-40 (2000).
8. J. H. Ali, W. B. Wang, M. Zevallos, R. R. Alfano, "Near Infrared Spectroscopy and Imaging to Probe Differences in Water Content in Normal and Cancer Human Prostate Tissues", *Technol. Cancer Res. Treat.*, Volume 3 491-497 (2004).
9. Kendric C. Smith, "The science of photobiology", 2nd edition, Plenum press, (1989).

10. Donna J. Dean and Brenda J. Korte, "Biomedical Imaging and Bioengineering", *Optics & Photonics News,* October 2003, http://ultra.bu.edu/papers/2003_10_OPN.pdf.
11. Irene Georgakoudi, Brian C. Jacobson, Markus G. Mu¨ ller, Ellen E. Sheets, Kamran Badizadegan, David L. Carr-Locke, Christopher P. Crum, Charles W. Boone, Ramachandra R. Dasari, Jacques Van Dam and Michael S. Feld, "NAD(P)H and Collagen as *in Vivo* Quantitative Fluorescent Biomarkers of Epithelial Precancerous Changes" *Can. Res.* 62, 682–687 (2002).
12. C. Morrison, J. Thornhill and E. Gaffney, "The connective tissue framework in the normal prostate, BPH and prostate cancer: analysis by scanning electron microscopy after cellular digestion", *Urol. Res*, 28(5), 304-7 (2000).
13. C. F. Bohren and D. R. Huffman, "Absorption and scattering of light by small particles", Wiley, New York, (1983).
14. Steven L. Jacques and Scott A. Prahl, "Introduction to tissue optics", http://omlc.ogi.edu/classroom/ece532/index.html
15. J. R. Mourant, T. Fuselier, J. Boyer, T. M. Johnson and I. J. Bigio, "Predictions and measurements of scattering and absorption over broad wavelength ranges in tissue phantoms", *Appl. Opt*. 36, 949-957 (1997).
16. Wikipedia, "Cell Biology/Introduction/Cell size", http://en.wikibooks.org/wiki/Cell_Biology/Introduction/Cell_size
17. R. Montironi, R. Mazzucchelli, A. Santinelli, M. Scarpelli, A. Beltran and D. Bostwick, "Incidentally detected prostate cancer in cystoprostatectomies: pathological and morphometric comparison with clinically detected cancer in totally embedded specimens", *Human Pathol.*, 36, 646– 654 (2005).

18. C. Morrison, J. Thornhill, E. Gaffney E, "The connective tissue framework in the normal prostate, BPH and prostate cancer: analysis by scanning electron microscopy after cellular digestion", *Urol. Res*. 28, 304-307 (2000).
19. Wai-Fung Cheong, Scott A. Prahl, and Ashley J. Welch, "A review of the optical properties of biological tissues", *IEEE J. Quant. Elec.*, 26(12), 2166-2184 (1990).
20. J. M. Schmitt and G. Kumar, "Optical Scattering Properties of Soft Tissue: A Discrete Particle Model", *Appl. Opt.*, 37(13), 2788-2797 (1998).
21. Ruikang K. Wang, "Modeling optical properties of soft tissue by fractal distribution of scatterers", *J. Mod. Opt.*, 47(1), 103-120 (2000).
22. M. Xu and R. R. Alfano, "Fractal mechanisms of light scattering in biological tissue and cells", *Opt. Lett*. 30, 3051-3053 (2005).
23. B. C. Wilson and S. L. Jacques, "Optical reflectance and transmittance of tissues: principals and applications", *IEEE J. Quant. Elec.*, 26(12), 2186–2199 (1990).
24. Y. Pu, M. Alrubaiee, W. B. Wang, S. K. Gayen, R. R. Alfano and M. Xu "Determination of optical coefficients and fractal dimensional parameters of cancerous and normal prostate tissues", to be submitted.
25. L. H. Wang and S. L. Jaques, "Monte Carlo modeling of light transport in multi-layered tissues in standard C", Anderson Cancer Center, University of Texas, (1992).

Chapter 3

Fractal dimensional parameters and optical coefficients of cancerous and normal prostate tissues

3. 1. Introduction:

The salient spectral optical coefficients of tissues are absorption, scattering coefficients and g factor. These govern the light propagation in tissues. In this part of the research, these coefficients are investigated in spectral range of 750 nm to 860 nm for prostate tissues. The well-known five Gleason Grades describe evolution of malignant prostate tumor [1]. The Gleason Grade 1 (corresponding to early stage) pattern consists of evenly placed uniform gland cells supported by a high structured network of collagen fiber [1, 2]. With grade advances, the cancer cells proliferate and begin to merge into "islands" of non-uniform swelling cellular nuclei [1, 3] accompanied by loss of collagens [1, 2]. A survey of the literatures provides evidence that the regulating the water volume within living cell might be the primary factor in carcinogenesis [4-6]. Tissue with high water content is usually related to normal tissue [5]. The different structures and chromophore compositions of cancerous and normal prostate tissues may cause different absorption [6] and scattering coefficients, thus serve as native markers for prostate cancer detection.

Light scattering in tissue is caused by the interaction of photons with ultra-structure of the tissue. The tissue ultra-structure related to light scattering extends from the membrane aggregates to collagen fibers, nuclei, and cells. Light transport is dominated by scattering in biological tissue in the far red and near infrared range, where there are no obvious absorption peaks [6]. Absorption can provide a clue as to the chemical composition of tissue, and serve as a mechanism of optical contrast during imaging. The most dominant chromophore in biological tissue, which absorbs light in the near and infrared range, is water [4-6].

A systematic investigation of the absorption coefficient (μ_a), scattering coefficient (μ_s), reduced scattering coefficient (μ_s') and anisotropy factor (g) of tissue are important since accurate models of light transport in tissue requires these optical properties [7]. The differences in the values of μ_a, μ_s, μ_s' and g between normal and cancerous tissues provide the basis for biomedical diagnostics and imaging using optical techniques. However, to the best of authors' knowledge, there has not been a systematic investigation of optical properties: μ_a, μ_s, μ_s' and g; and fractal dimensional parameters which will be illustrated in section 3. 3: fractal dimension (D_f), cutoff diameter (d_{max}) and most efficient diameter ($\langle d_m \rangle$) of prostate tissue in NIR range.

The focus of this study is to estimate the optical parameters of μ_a, μ_s, μ_s' and g of cancerous and normal prostate tissues in the spectral range of 750 nm to 860 nm using extinction and backscattered diffuse reflection spectroscopic techniques. In this chapter, the importance of matching experimental conditions with the theoretical model used to determine the optical properties is emphasized. Reliability of determination of optical properties depends on both theoretical and experimental techniques [7]. Passing through a thin ($d \langle\langle l_a$) slab of tissue, a NIR beam is attenuated exponentially by single scattering (ballistic) event following Beer's Law [8]. Therefore, scattering coefficient μ_s can be obtained using the measured light extinction data for a thin tissue slice. Under condition of thick tissue slice, measurements of diffuse reflection provide sufficient information for uniquely determining absorption (μ_a) and reduced scattering coefficients (μ_s'). Light transport in a thick tissue slice is usually modeled as a diffusion process [9]. When the light diffuses in tissue, its behavior essentially depends on the reduced scattering coefficient: $\mu_s' = \mu_s(1-g)$, but not on the scattering coefficient (μ_s) and anisotropy factor (g), separately [10]. The backscattered images are acquired using those photons surviving passage

back from the prostate tissue, which bear clues about their voyage and the optical coefficients of the tissue. Photons that penetrate deep into the tissue are multiply scattered and can either be absorbed, or transmit through tissue to be detected. So the optical properties, μ_a and μ_s', of prostate tissue can be obtained by analyzing the backscattered reflectance images of prostate tissues using diffusion model [8-10].

The optical parameters were also studied using the fractal dimension tissue model [11-14] to address the measured data meaningfully. There is growing interest in extracting microscopic properties of cancerous and normal tissues by means of their measured optical parameters due to the differences of microstructure between these two types of tissues. Richards-Kortum *et al* investigated light scattering of cervical cells throughout neoplastic progression influnced by nuclear morphology, DNA content etc [15]. Mourant *et al* proposed that small particles dominate by orders-of-magnitude more than large particles for effective scattering [16]. Wang and Sharma recognized that many biological tissues have fractal-like organization thus scattering of tissue might be studied as fractal systems [11, 12]. Min Xu and Alfano presented light-scattering properties of biological tissue by a fractal continuous random medium model [13, 14]. Furthermore, the fractal dimension D_f and the cutoff correlation length d_{max} were indicated as essential parameters characterizing the features of light scattering in tissue [14]. The analysis of the measured parameters showed that the difference of optical properties of cancerous and normal prostate tissues modeled by the fractal dimension tissues can be interpreted by the pathological and morphological changes in prostate cancer evolution [1-5].

3. 2. Experimental method and samples

Prostate tissue specimens were obtained from the National Disease Research Interchange (NDRI) and the Co-operation Human Tissue Network (CHTN) under the approval of the

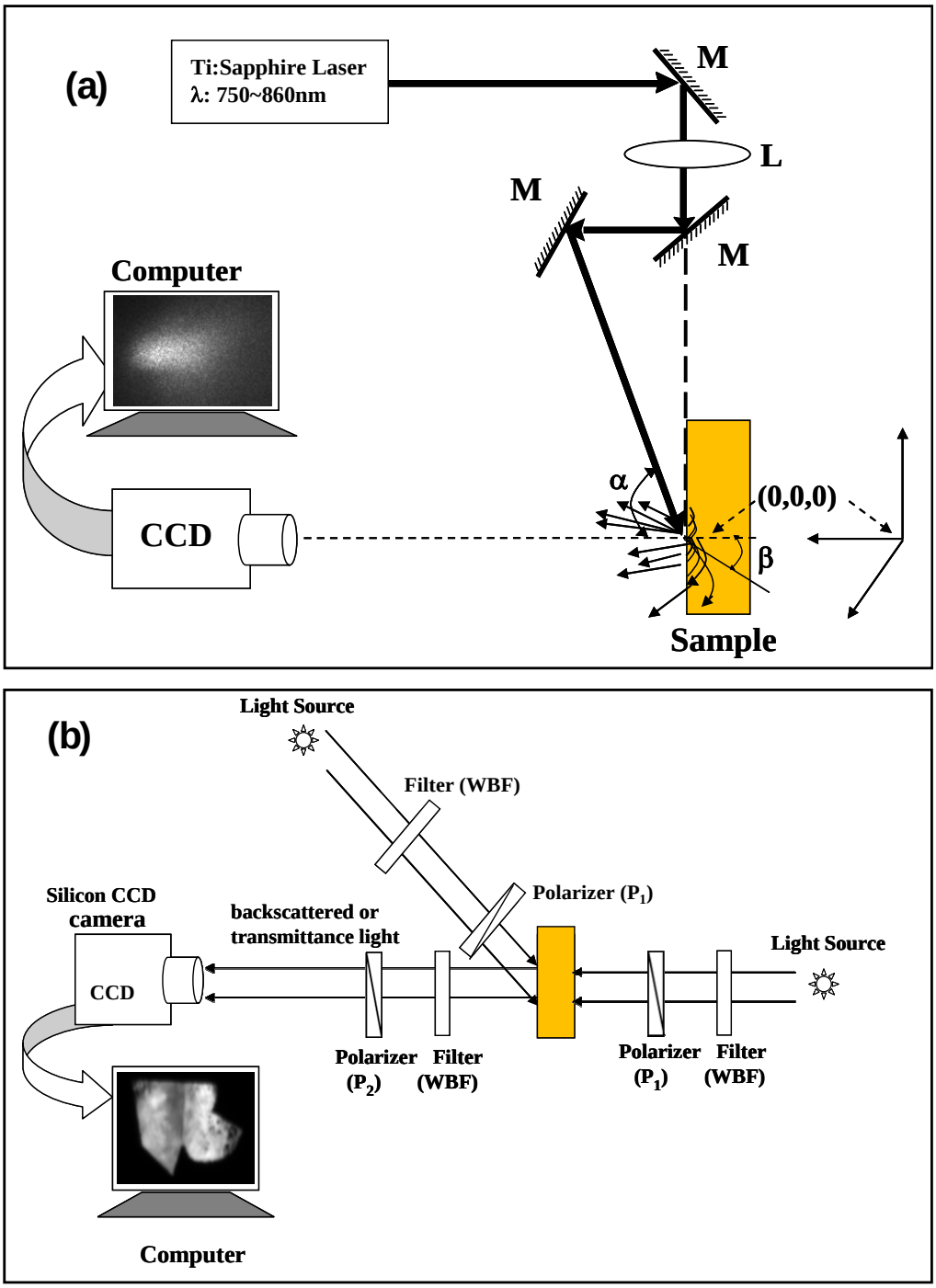

Fig.3-1. (a) Schematic diagram of the setup of diffuse reflectance imaging experiment; (b) NIR spectral polarized imaging set up for human prostate cancer detection.

Institutional Review Board (IRB) at CCNY. A pair of the normal and cancerous prostate tissues was obtained from the same patient. Samples were neither chemically treated nor were frozen

prior to the experiments. For extinction spectral measurements, the cancerous and normal prostate tissues were cut with a thickness of ~100 μm and an area of ~ 2 × 3 cm^2. The tissue samples were then put into 100 μm thick quartz cell to ensure same thickness for optical density (O.D.) measurements. The absorption spectra of normal and cancer prostate tissues were measured using a Perkin-Elmer Lambda 9 UV/VIS/NIR Spectrophotometer in NIR range.

For diffuse reflectance measurements, the cancerous and normal prostate tissue samples were cut into ~ 2cm × ~ 2cm × ~ 1.1cm. The experimental setup is shown in Fig. 3-1(a). A Ti:sapphire laser (Spectra-Physics Tsunami) beam tunable from 750 nm to 860 nm was used to illuminate the sample. The laser was operated in CW mode by turning off the acousto-modulator and had a spectral FWHM (full width at half maximum) bandwidth less than 1nm. The beam passed through a long focal length converging lens (with a focal length of 40 cm) and irradiated the sample with an incidence angle of $\alpha = 72.4^o$. Backscattered light in the direction normal to the surface of the sample is recorded by a CCD camera at wavelengths from 750nm to 860nm with a wavelength step of 10nm [10].

For transmission and backscattering imaging measurements, a spectral polarization imaging setup shown in Fig. 3-1(b) was used. A white light beam of diameter ~ 2 cm was used to illuminate the sample. Wide band filters centered at 700 nm and 800 nm with a bandwidth filter of 60 nm were used to select the desirable spectral range of the illumination and detected beams. A polarizer (P_1) is located in the incident beam pathway to obtain a linearly polarized illumination light. The second polarizer (P_2) is positioned in front of the CCD camera for selecting the detection polarization direction (parallel and perpendicular to the orientation of P_1). A cooled CCD Silicon camera (Photometric CH350, 1024 × 1024 pixels), which has spectral

response from 550 nm to 900nm and is equipped with a zoom lens of 50-mm focal length, was used to record the images in the transmission and backscattering geometries [6].

A photograph of a typical pair of human cancerous and normal prostate tissue specimen is inserted in Fig. 3-1(b). Samples were arranged such that the right hand side of the specimen was cancerous tissue, while the left hand side was normal tissue.

3. 3. Model for μ_a, μ_s, μ_s', g and D_f

3. 3. 1. Determination of μ_a, μ_s, μ_s', g and D_f

Since an optical density (O.D.) spectrum for thin prostate tissue samples is dominated by the scattering in the range of 750 nm and 860 nm [6, 7], the scattering coefficient (μ_s) can be obtained from the following Beer's equation:

$$\mu_s \cong \mu_t = O.D. * \frac{\ln(10)}{L}, \tag{3. 1}$$

where μ_t is the extinction coefficient, and L is thickness of tissue which light transport through.

Backscattered intensity values measured in diffuse reflection experiments of a 1.1 cm thick prostate tissue sample were used to extract the optical absorption and the reduced scattering coefficients because the samples is thick enough for application of diffusion model [7]. In the case of an obliquely incident pencil beam, the origin of the system co-ordinate is set as z = 0 on the surface of the prostate samples, and the light propagates in the direction of ($\sin\alpha$, *0*, - $\cos\alpha$), where α is the incidence angle (α=72.4^o in our case). The initial ballistic motion of the beam within the tissue is in the direction of ($\sin\beta$, *0*, - $\cos\beta$), where $\sin\alpha = n \bullet \sin\beta$, and n is the index of refraction of prostate tissue (n=1.35 in our case) [17]. The backscattered diffuse intensity at position (x, y, 0) on the surface recorded by the CCD camera is given by [10]:

$$I(x,y)=\frac{l_t\cos\beta}{4\pi\rho_1^3}\cdot(1+\mu_{eff}\rho_1)\cdot\exp(-\mu_{eff}\rho_1)+\frac{l_t\cos\beta+2z_e}{4\pi\rho_2^3}\cdot(1+\mu_{eff}\rho_2)\cdot\exp(-\mu_{eff}\rho_2), \quad (3.2)$$

where $\rho_1=\sqrt{(x-l_t\sin\beta)^2+y^2+l_t^2\cos^2\beta}$, $\rho_2=\sqrt{(x-l_t\sin\beta)^2+y^2+(2z_e+l_t\cos\beta)^2}$ and $\mu_{eff}=\sqrt{3\mu_a/l_t}$; l_t is transport mean free path which is approximately equal to the reciprocal of μ_s' in NIR range; z_e is the extrapolation length and dependent on mismatch of the index of refraction at the interface [18]. The extrapolation length is reported to be z_e=1.69l_t [10, 18]. Equation (3. 2) is used to fit the measured diffuse reflectance along a line in the x direction on the tissue surface to obtain μ_a and l_t ($1/\mu_s'$) [10]. The anisotropy factor g is calculated using:

$$g=1-\frac{\mu_s'}{\mu_s}, \quad (3.3)$$

which can be obtained from the values of μ_s and μ_s'.

Fractal dimension D_f was shown to be an important parameter to describe fractal system. This parameter reveals the weight for small vs. large scattering centers in the medium. Tissue with a larger value of D_f has smaller scattering centers. In the fractal continuous tissue medium model, D_f can be estimated from the wavelength dependence of μ_s' by fitting the equation of [13, 19]:

$$\mu_s'\propto\lambda^{3-D_f}. \quad (3.4)$$

3.3.2. Fractal soft tissue model for determination of cutoff diameter of scatterers

Mie theory provides analytical solution of Maxwell's equations for light scattered by homogeneous spherical particles of size comparable with the incident wavelength in terms of the scattering angle θ, wavelength λ, the particle size x, and the index of refraction m of the particle relative to the suspension medium [20]. In our study, BHMIE (Bohren and Huffman + Mie)

algorithm was applied in the Mie calculation [20]. The extinction of light is characterized by the dimensionless efficiency factor Q_s [11-12, 17, 20]:

$$Q_s = \sigma_s / G, \tag{3. 5}$$

where σ_s is the scattering cross-section and G is geometrical cross-section of the particle. Two important parameters of Mie calculation are the scatter particle size x and relative index of refraction m of the scatter system, which can be written as:

$$x = \pi * n_0 * d / \lambda, \qquad m = n_1 / n_0, \tag{3. 6}$$

where λ is the wavelength of light in vacuum, n_1 is the index of refraction of the scattering particle, and n_0 is the index of refraction of the surrounding medium. For prostate tissue, the index of refraction of nuclei is reported to be ~1.46, and that of surrounding cytoplasm to be ~1.35 [17, 21].

Scattering by fractal system has been extensively studied by several groups [10-14, 22] during the last decade. Based on the definition of a fractal, the number (n) of particles with diameter d_i in a spherical volume of diameter d_0 is given by [11, 12]:

$$n(d_i) = (d_0/d_i)^{D_f}, \tag{3. 7}$$

where D_f is the fractal dimension. If the particles are treated as spheres, the volume fraction of particles with diameter d_i is written as [11, 12]:

$$\eta(d_i) = (\pi d_i^3 / 6)\frac{n(d_i)}{\pi d_0^3 / 6} = \eta_0 d_i^{3-D_f}, \tag{3. 8}$$

where $\eta_0 = d_0^{D_f - 3}$ is a scale-dependent constant and can be determined from the total volume fraction of all particles, T_v, using equations of [11, 12]:

$$T_v = \eta_0 \int_{d_{\min}}^{d_{\max}} d_i^{3-D_f} dd_i \quad \Rightarrow \quad \eta_0 = \frac{T_v}{\int_{d_{\min}}^{d_{\max}} d_i^{3-D_f} dd_i}, \tag{3. 9}$$

where d_{min} and d_{max} are diameters of the smallest and largest particles, respectively. Using equation (8), the number of particles with diameter d_i in a spherical volume of diameter d_0 can be rewritten as:

$$n(d_i) = \frac{\eta_0 d_i^{3-Df}}{\pi d_i^3 / 6} = \frac{6\eta_0}{\pi} d_i^{-D_f} . \quad (3.10)$$

When light is scattered by particles in tissue, the overall scattering coefficient of the fractal dimensional tissue is proportional to the sum of the products of the scattering cross-section of individual particles and their number densities. Combining Mie theory [20] and the fractal soft tissue model, the total scattering coefficient can be written as [11, 12]:

$$\mu_s = \int_{d_{\min}}^{d_{\max}} \eta(d_i) \frac{\sigma_s(d_i)}{v_i} dd_i = \frac{6}{\pi} \eta_0 \int_{d_{\min}}^{d_{\max}} d_i^{-Df} \sigma_s(d_i) dd_i . \quad (3.11)$$

This equation shows that the essential features of light scattered by biological tissue can be directly determined by the fractal dimension D_f of this media and the size of the smallest and largest particles in tissues [13]. Min Xu and R. R. Alfano proposed that light scattering in tissue is due to weak random fluctuations of the dielectric permittivity, and its correlation function $R(r)$ depends on the fractal dimension D_f and the diameter of largest particles, d_{max}, which is called cutoff length or maximum correlation length [13]. They derived analytical expressions for the power law of reduced scattering coefficient, the anisotropy factor of scattering, and phase function based on the fractal continuous tissue model [13]. These expressions are shown to be in good agreement with some experimental results in NIR light scattering in biological tissues and cell suspensions [13, 14].

The fractal continuous tissue model assumes that tissue is statistically space homogeneous, and the correlation function of the random fluctuations of the dielectric permittivity is an average of exponential function weighted by the power law distribution (equation (6)) for correlation

length d (scatter's diameter). The amplitude scattering function $S(\theta)$ at the scattering angle θ is given [13]:

$$\left|S(\theta)\right|^2 = \int_{kd_{\min}}^{kd_{\max}} \frac{\varepsilon^2 \eta_0 (2k)^{Df-1} x^{6-D_f}}{2\pi[1+2(1-\cos\theta)x^2]^2} dx\,, \tag{3. 12}$$

where $\varepsilon^2=4n_0^4(m\text{-}1)^2$ and $k\equiv\pi n_0/\lambda$. The anisotropy factor (g), mean cosine of the scattering angle, was then found as [13]:

$$g = \int d\Omega \frac{(1+\cos^2\theta)\cos\theta\left|S(\theta)\right|^2}{8k^2} \Bigg/ \int d\Omega \frac{(1+\cos^2\theta)\left|S(\theta)\right|^2}{8k^2}\,, \tag{3. 13}$$

where Ω is solid angle at various scattering angles θ and $d\Omega=2\pi*\sin\theta d\theta$ [17]. Using equations (12) and (13), and the known value of d_{min}, the change of g as a function of d_{max} can be obtained and usually shown as a $g \sim d_{max}$ curve. Using the $g \sim d_{max}$ curve, the maximum correlation length d_{max} can be obtained from the determined anisotropy factor g. Before this work, the value of d_{max} was usually obtained by estimation, or guess [11, 12, 23]. This parameter is essential for determining the size distribution of scatters.

To express the contribution of scatters at certain diameter to the scattering coefficients, a parameter, namely most efficient diameter for scattering at given wavelength, is defined by:

$$\langle d_m \rangle = \frac{\int_{d_{\min}}^{d_{\max}} d_i \mu_s(d_i) dd_i}{\int_{d_{\min}}^{d_{\max}} \mu_s(d_i) dd_i}\,. \tag{3. 14}$$

Once d_{max} is determined and d_{min} is given, the most efficient diameter $\langle d_m \rangle$, which describes the size of the particles that contribute most to the scattering coefficient, can be determined using equation (3. 14) [11, 12]:

3. 4. Experimental and analysis results

3. 4. 1. Determination of optical coefficients of cancer and normal prostate tissues

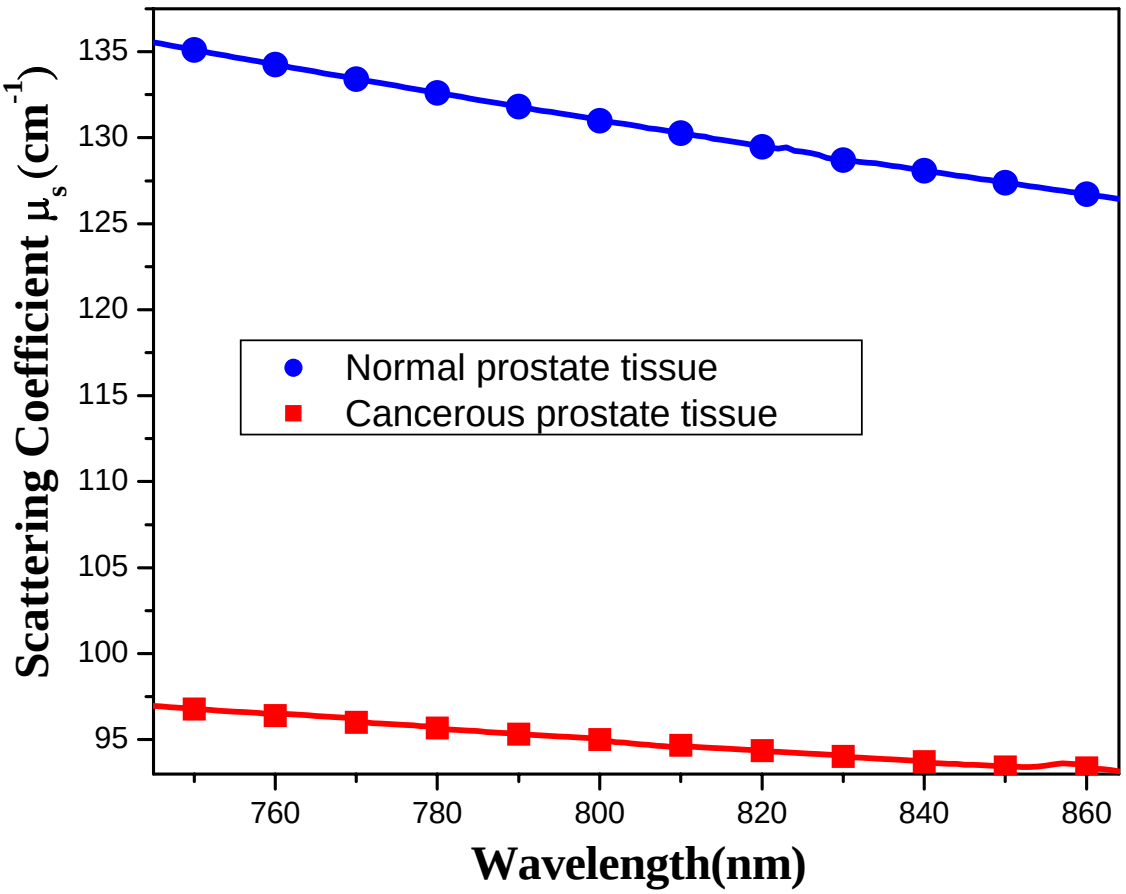

Fig. 3-2 The wavelength dependence of μ_s of cancerous (solid square) and normal (solid circle) prostate tissues extracted from the measured optical density (O.D) data in the spectral range of 750 nm to 860 nm and using equation (3. 1).

The variation of scattering coefficient (μ_s) of normal and cancerous prostate tissues, with wavelength, obtained from the measured O.D. spectra in 750 nm – 860 nm the spectral range is shown in Fig. 3-2. It can be seen that there is no obvious absorption peak in thin tissue slab. The attenuation of light transporting in tissue is usually expressed by an exponential decay (proportional to $e^{-\mu_t x}$), where μ_t is the attenuation (extinction) coefficient. Since the cancerous and normal prostate tissue samples have same thickness, the O.D. spectrum actually plots the profile of the extinction coefficient for each prostate tissue. Using equation (3. 1) and the O.D. data, the scattering coefficient μ_s can be obtained for both cancerous and normal prostate tissues

since μ_s is equal to μ_t in this NIR range for thin tissue slice. The salient feature of Fig. 3-2 is that the value of μ_s for normal prostate tissue is larger than that for cancerous prostate tissue.

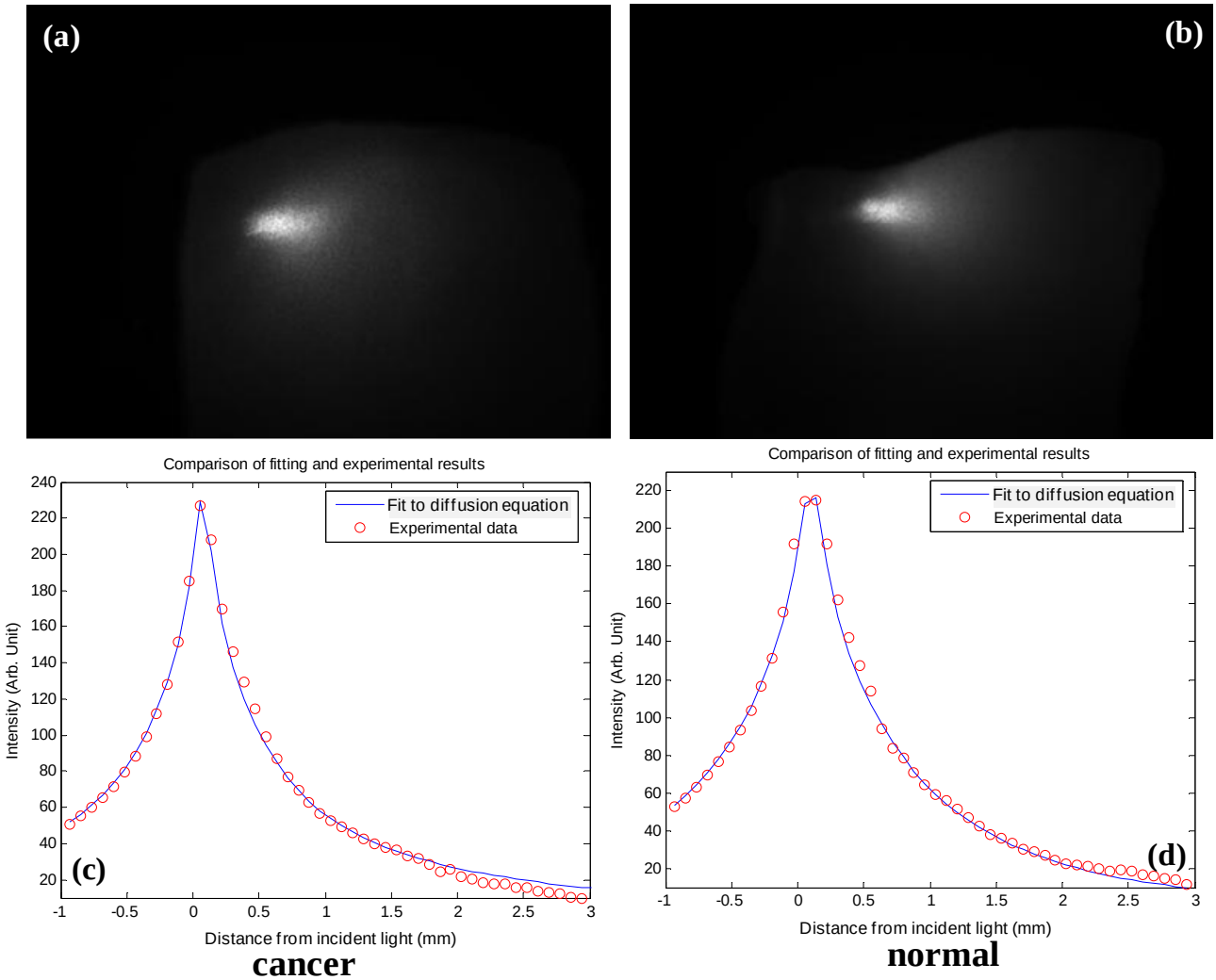

Fig. 3-3 The images of backscattered light intensities from (a) cancerous and (b) normal prostate tissues at 800 nm. The spatial intensity profiles (circle) and the fitting results (solid line) through incident light point [R(0, 0)] corresponding to (c) cancerous and (d) normal image, respectively.

Our procedure for determination of μ_a, μ_s' and g is the following. First, backscattered diffuse reflectance image of cancerous and normal prostate tissues at various wavelengths from 750 nm to 860 nm (measured with a wavelength step of 10 nm) were recorded with an obliquely incident beam using the setup described by Fig. 3-1(a). Then, diffusion model was used to analyze the 2D distribution intensity of the backscattered diffuse images to determine μ_a and μ_s'. Typical

backscattered diffuse reflectance images of cancerous and normal prostate tissues at center wavelength λ = 800 nm are shown in Figs. 3-3(a) and 3-3(b), respectively. The corresponding cross-section intensity profiles (circle) of the images of cancerous and normal tissue through the incident light point [R(0, 0)] are shown in Figs. 3-3(c) and 3-3(d), respectively. μ_a and μ_s' of cancerous and normal prostate tissues at 800 nm were obtained by fitting the measured diffuse intensity along a line crossing through [R(0, 0)] in the *x* direction using equation (3. 2). The calculated results obtained from the extracted μ_a and μ_s' and equation (3. 2) are shown as solid lines in Fig. 3-3(c) and (d). The wavelength dependence of μ_a and μ_s' in the spectral range of 750nm to 860nm can be obtained by repeating the same fitting process for each measured diffuse reflectance intensity data of images recorded at corresponding wavelengths.

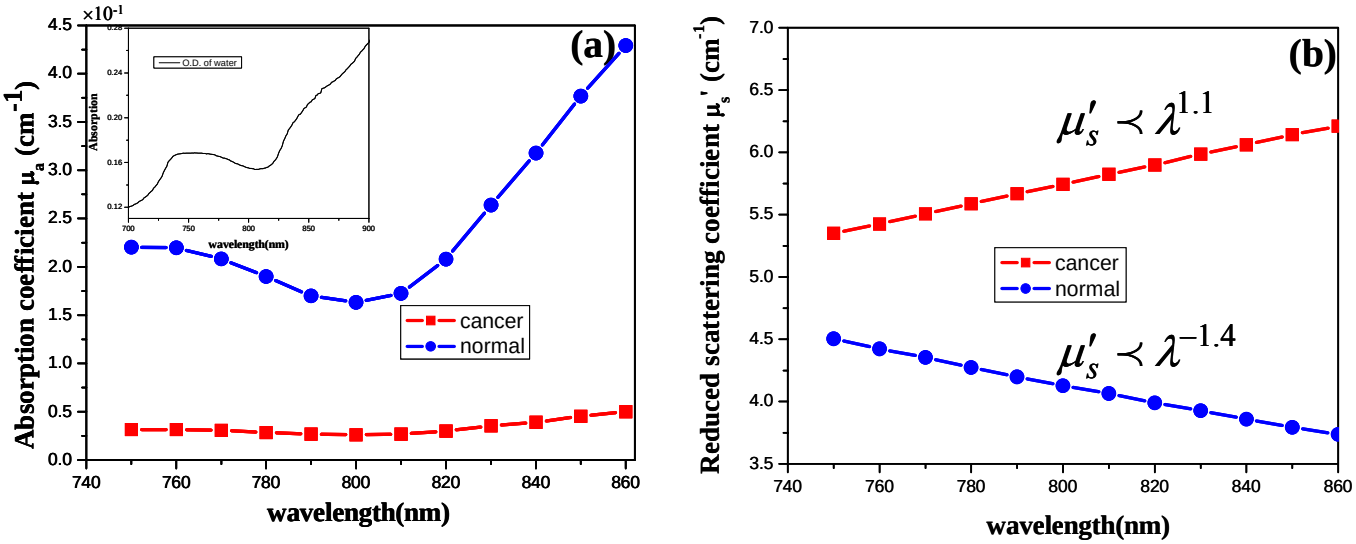

Fig. 3-4 The wavelength dependence of (a) absorption coefficient (μ_a) of cancerous (solid square) and normal (solid circle) prostate tissues; and (b) reduced coefficients (μ_s') of cancerous (solid square) and normal (solid circle) prostate tissues. The absorption spectrum of water with 2 cm thickness of 700nm – 900nm is shown at upper left of (a) as a reference.

Fig. 3-4 (a) and 3-4(b) display the wavelength dependence of μ_a and μ_s' in the spectral range of 750nm to 860nm, respectively. The salient features of Fig. 3-4(a) is that μ_a of normal prostate tissue has relative higher value at ~750nm than that at ~800nm and it goes up after ~ 800nm

while μ_a of cancerous tissue does not show any remarkable change with λ. This can be understood by lower water content in cancerous prostate tissue compared with normal tissue [5, 6]. As a reference, the absorption spectrum of water (sample thickness: 2 cm) in the spectral range of 700nm to 900nm is shown in insert of Fig. 3-4(a), indicating the 750nm absorption peak of water, which was also observed by L. Kou *et al* [24]. The μ_a curve of normal prostate tissue shown in Fig. 3-4(a) indicates its absorption profile following that of water. Therefore, this measurement refers to higher water content in normal prostate tissue and lower water content in cancerous prostate tissue [5, 6].

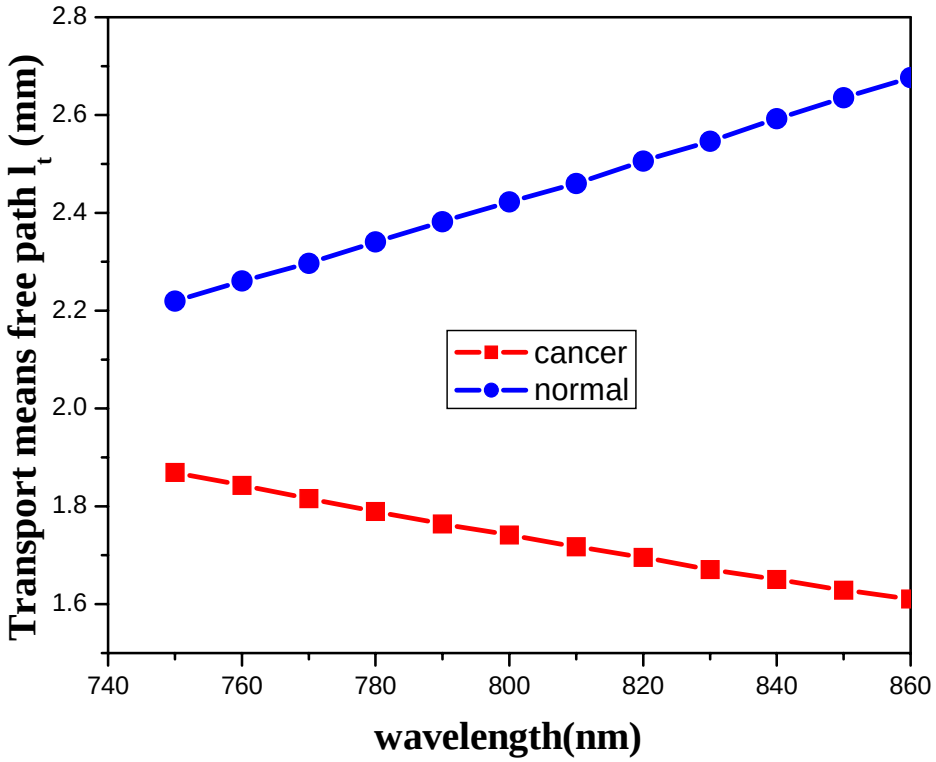

Fig. 3-5 l_t of cancerous (square) and normal (circle) prostate tissue from 750 nm to 860 nm

Transport mean free path (l_t) gives the direct impression of the distance how long photons can travel in the tissue. Fig. 3-5 presents the l_t of cancerous and normal prostate tissues in the spectral range of 750 nm to 860 nm.

Using equation (3.3) and the data of μ_s in Fig. 3-2 and μ_s' in Fig. 3-4(b), the anisotropy factors (g) of cancerous and normal prostate tissues in the spectral range of 750 nm to 860 nm were calculated and shown in Fig. 3-5. The salient feature of Fig. 3-5 is that the scattering anisotropy factor g of cancerous tissue is larger than that of normal in this spectral rang. Since μ_s, μ_s' and g depend on a number of parameters, such as index of refraction, scattering particles' size and their distribution, a detailed discussion of fractal dimension model will be given in the next section.

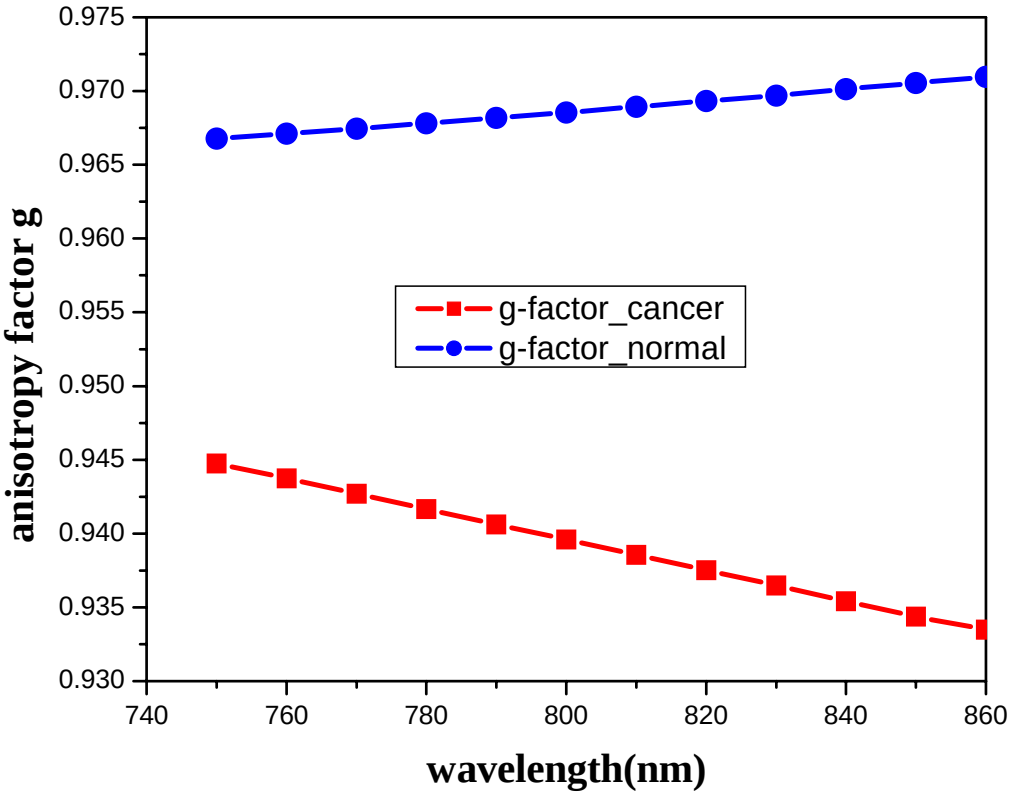

Fig. 3-6 The scattering anisotropy factor *g* of cancerous (solid square) and normal (solid circle) prostate tissues in the spectral range of 750nm - 860nm.

Table 3-1 presents the absorption and scattering coefficients for cancerous and normal prostate tissues in the spectral range of 750 nm to 860 nm obtained from our measurements and analysis.

Table 3-1: Absorption and scattering coefficients for cancerous and normal prostate tissues

μ and g / λ(nm)	μ_s(cm^{-1})		μ_a(cm^{-1})		μ_s'(cm^{-1})		g	
	cancer	normal	cancer	normal	cancer	normal	cancer	normal
750	96.8	135.1	3.15×10^{-2}	2.20×10^{-1}	5.35	4.55	0.945	0.967
760	96.4	134.3	3.14×10^{-2}	2.19×10^{-1}	5.43	4.42	0.944	0.967
770	96.0	133.4	3.07×10^{-2}	2.08×10^{-1}	5.51	4.35	0.943	0.967
780	95.7	132.6	2.84×10^{-2}	1.90×10^{-1}	5.59	4.27	0.942	0.968
790	95.3	131.8	2.69×10^{-2}	1.70×10^{-1}	5.67	4.20	0.941	0.968
800	95.0	131.0	2.61×10^{-2}	1.63×10^{-1}	5.74	4.13	0.940	0.969
810	94.7	130.3	2.69×10^{-2}	1.72×10^{-1}	5.82	4.07	0.938	0.969
820	94.4	129.5	2.99×10^{-2}	2.09×10^{-1}	5.90	3.99	0.937	0.969
830	94.0	128.7	3.53×10^{-2}	2.64×10^{-1}	5.99	3.93	0.936	0.970
840	93.7	128.1	2.91×10^{-2}	3.18×10^{-1}	6.06	3.86	0.935	0.970
850	93.4	127.4	4.53×10^{-2}	3.77×10^{-1}	6.14	3.79	0.934	0.970
860	93.4	126.7	4.99×10^{-2}	4.29×10^{-1}	6.21	3.74	0.933	0.971

Table 1 show that the reduced scattering coefficient μ_s' of cancerous prostate tissue is larger than that of normal tissue, but scattering coefficient μ_s of cancerous tissue is smaller than that of normal tissue. Comparing the values of μ_s, μ_a and μ_s' shown in Table 1, one can find that values of μ_s are higher than the value of μ_a by three orders of magnitude, and values of μ_s' larger than the value of μ_a by two orders for the cancerous prostate tissue samples.

3.4.2. Numerical evaluation of fractal dimension (D_f) and cutoff diameters of scatters of cancerous and normal prostate tissues

To study how the absorption and scattering spectra reflect microstructure properties of cancerous and normal prostate tissues, the measured scattering data of these two types of tissues are evaluated numerically using the fractal dimension soft tissue model and Mie theory discussed in section 3. 3. The following parameters were used in our simulation: (1) the value of the total volume fraction of all scatterers T_v= 0.2 [11, 12, 23], and the diameter of smallest particle d_{min} =

50 nm [11, 19]，which is in agreement with that d (<50nm) << λ (=750nm to 860nm), thus leading to a negligible contribution to the scattering; (2) the index of refraction of the host medium n_0 = 1.35 [10-14, 16, 17, 19], which was reported as the index of refraction of the surrounding cytoplasm of prostate tissue [19]; (3) the index of refraction of scatters' particle n_1 = 1.46 [12-14, 17, 19], which is reported as index of refraction of prostate cellular nuclei by *S.* Jacques *et al* [17].

To evaluate the distribution of particles in the fractal dimension soft tissue model, it is important to determine the fractal dimension D_f and cutoff correlation length d_{max} of prostate tissues [13, 14]. The wavelength dependence of μ_s' of cancerous and normal tissues actually reflects their different microscopic structures in the fractal tissue model [13, 19]. The fractal dimension of these two kinds of tissue can be obtained by fitting the data in Fig. 3-4 (b) using equation (4) [11-14, 16, 19]. The fitting results show that the wavelength dependence of the reduced scattering coefficient of cancerous and normal tissues gives $\mu_s' \propto \lambda^{1.1}$ and $\mu_s' \propto \lambda^{-1.4}$, respectively. Substituting these fitting results of $\lambda^{1.1}$ and $\lambda^{-1.4}$ into equation (4), $\mu_s' \propto \lambda^{3-Df}$, the fractal dimensions of D_f = 1.9 and D_f = 4.4 are obtained for cancerous and normal prostate tissue, respectively.

The g values of the cancerous and normal prostate tissues at 800 nm as a function of cutoff diameter d_{max} were calculated using equation (3. 12) and (3. 13), and the results are displayed as solid and dash lines, respectively, in Fig. 3-7. With the known g factors of 0.940 and 0.968 at 800nm for cancerous and normal prostate tissues, the cutoff diameters of cancerous and normal prostate tissues were determined using the data shown in Fig. 3-7 as ~ 1.42 μm for cancerous tissue, and ~6.47 μm for normal tissue.

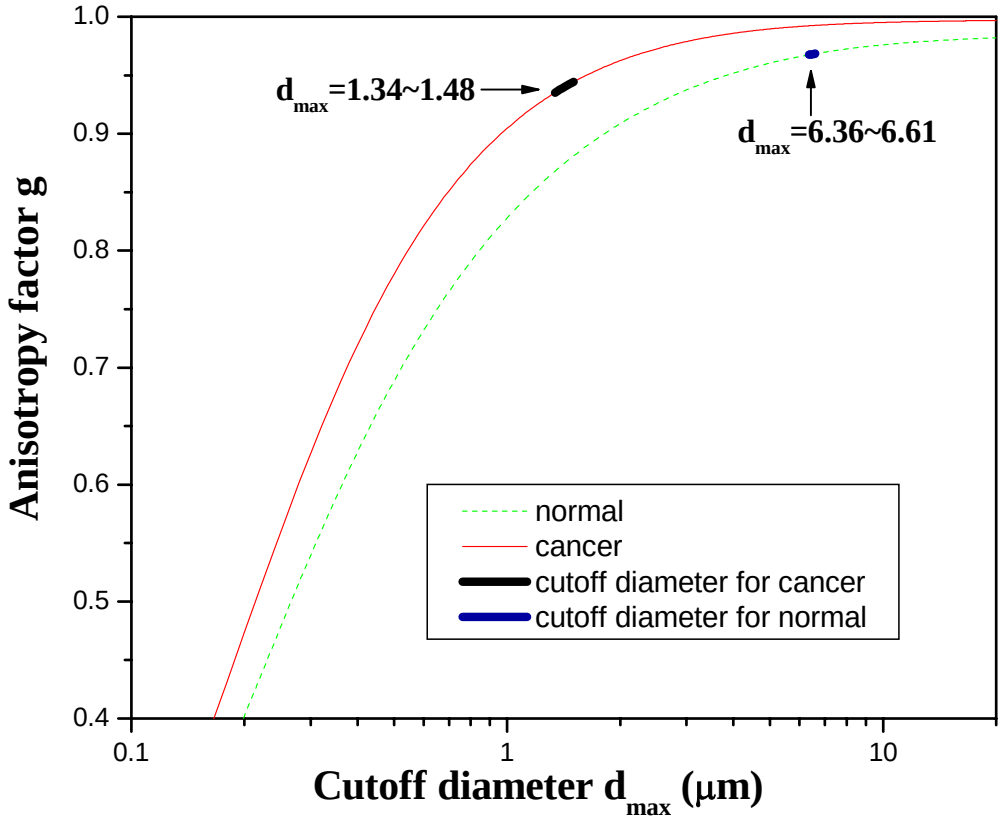

Fig. 3-7 Anisotropy factor g of the fractal continuous tissue as a function of cutoff diameter d_{max} at 800 nm evaluated by fractal tissue model. The curves standing for cancerous and normal prostate tissues are displayed as solid and dash lines, respectively.

Once the cutoff diameters of tissue are determined, the number of particles as a function of scatter diameter *d* for cancerous and normal prostate tissues can be calculated using equations (3. 9) and (3. 10). The calculated results are shown as Fig. 3-8. The most salient feature of Fig. 3-8 is that the number of particles for scatter's diameter smaller than ~ 0.46 μm in cancerous tissue is less than that of normal tissue. With scatters' diameter increasing (d>0.46μm), the number of particles in cancerous tissue becomes larger than that of normal tissue.

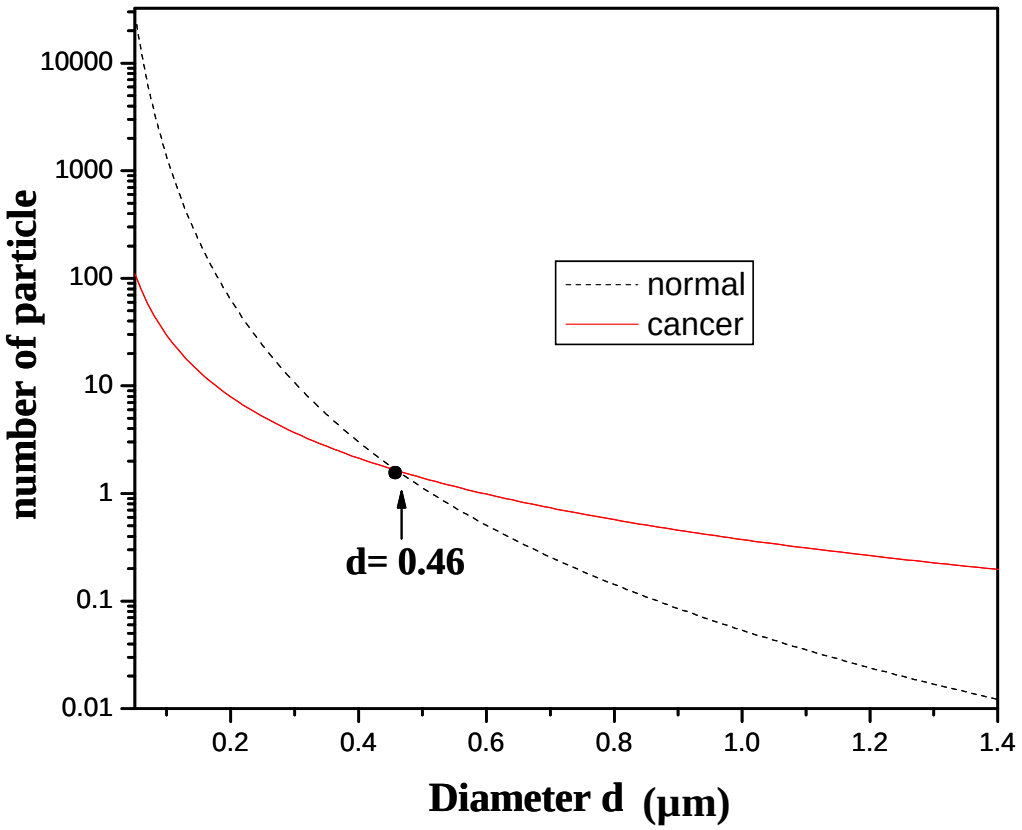

Fig. 3-8 The distribution of particle numbers with different diameters analyzed by the fractal dimension tissue model. The cancerous prostate tissue (solid line) has higher weight of larger particles than the normal prostate tissue (dash line).

The results of the above numerical evaluation using the fractal tissue model can be understood by biomedical study of prostate cancer evolutions. Normal cells, in general, are characterized by uniformity in size and shape of nuclei (round or oval) [25]. In contrast to normal and benign neoplastic cells, malignant cells are characterized by irregular morphology that is reflected in shape and size of the nucleus, the nuclear envelope, the nucleolus (which is found within the nucleus) and the chromatin [25]. The nuclei of malignant cells are usually larger than those of benign cells, and they vary in size and have irregular nuclear envelopes. Malignant cells also tend to have prominent nucleoli, meaning greater size of nucleoli. The malignant nucleoli are frequently multiple and they vary in size and shape when compared to each other [25]. They exhibit angulations and sharp corners. For chromatin, the majority of nuclei of

malignant cells are hyperchromatic, which is due to increased amount of nucleic acids and alteration of DNA. The chromatin is also irregularly distributed with areas of clumping and condensation. These chromatin clumps have sharp angles and corners, and some may be attached to the inner nuclear membrane, contributing its irregularity [25]. Richards-Kortum *et al* investigated light scattering of cervical cells throughout neoplastic progression and disclosed that light scattering is strongly influenced by the difference of morphology of nucleus and nucleolus, DNA content, and clumping and coarse chromatins [15].

Several research groups demonstrated that the cancerous and normal prostate cells reserve characteristic property in morphology described above [26-29]. A. Fischer et al show that two important cell structure changes in human prostate cancer are nucleolar enlargement and nuclear envelop irregularity [26]. M. Varma et al investigated the morphologic criteria for diagnosis of prostate adenocarcinoma in 250 consecutive cases, and observed that dysplastic nuclei have irregular size and shape, clumps of condensed chromatin, and multiple nucleoli. They suggest prominent nucleoli, marginated nucleoli (location of nucleoli is close or at the inner nuclear membrane) and multiple nucleoli are criteria having highest sensitivity and specificity for diagnosis of prostate cancer [27]. S. Bektas et al studied the relation between Gleason core and nuclear size and shape factor in malignant prostate biopsies, and conclude that nuclear size and shape irregularity increase with the Gleason score [28]. R. Montironi *et al* compared pathological and morphometric features of cancerous and normal tissue specimens for a total of 360 clinic consecutive samples [29]. They presented quantities of prostate cancer and normal nuclear and nucleolar sizes [2, 29]. The diameter of normal prostate cellular nuclei was reported as ~ 6.3 to 6.72 μm, while the diameter of cancerous nuclei is ~ 8.4 to 10.31 μm [2, 29]. The diameter of

normal prostate nucleoli was demonstrated as ~ 1.10 to 1.24 μm, while the diameter of cancerous nucleoli is ~ 1.38 to 1.96 μm [29].

We are now able to address the numerical evaluation by the fractal tissue model. The most interesting characteristics predicted by the fractal tissue model is that the cutoff diameter for cancerous tissue is in approximate agreement with the nucleolar diameter of cancerous prostate cell, and the cutoff diameter for normal tissue is in closely match with the nuclear diameter of normal prostate cell. This can be understood by the pathological and morphometric features of prostate. Since normal prostate cells are even and uniformly distributed, and optical path exists between round or oval nuclei [25, 27], scattering event is actually affected by nuclei. The smaller cutoff diameter of cancerous prostate tissues compared with the normal emphasizes the importance to consider the influence of the nuclear texture features, in addition to nuclear size [15]. Normal cells, in general, are characterized by uniformity in size and shape of nuclei (round or oval) [25]. Because of high density of malignant prostate cells [1], irregularity of nuclear envelope, clumping and condensation of the chromatin and marginated nucleoli [26-29], fractal volume of nuclei is expected. Light scattering event affected by large particle may be more influenced by marginated and multiple nucleoli [29]. Based on the evaluation of the fractal tissue model and evidence of pathological and morphologic features of cancerous and normal prostate tissue specimens, we may conclude that the largest scatter's diameter in cancerous prostate tissue is cut off by nucleolar size while the largest scatter's diameter in normal prostate tissue is cut off by nuclear size when light scattering in tissue described by this simple fractal tissue model. The results discussed above may present a potential approach that the cut off diameter predicted by the fractal tissue model may be used as one of criteria for prostate cancer detection.

Features exhibited in Fig. 3-8 can be explained by evolution of prostate cancer. Lower cell density [1] and higher water content of normal prostate tissue [5, 6] can be used to explain that the number of particles for smaller size (d<0.46μm) in cancerous tissue is less than that in normal tissue. On the other hand, the higher cell density, prominent and multiple nucleoli [1, 25-29] in cancerous prostate tissue can be used to explain that the number of particles for larger diameter (d>0.46μm) in cancerous tissue is larger than that in normal tissue. The turn over point at particle diameter of ~0.46μm somehow reflects enlarged nuclear size and prominent multiple nucleoli.

Using the determined value of d_{max} and known the value of d_{min} , the most efficient diameter $\langle d_m \rangle$ was calculated using equation (3. 14) and the results show that $\langle d_m \rangle_c$ = 1.09 μm for the cancerous tissue and $\langle d_m \rangle_n$ = 2.04 μm for the normal tissue at 800 nm.

For convenience, table 3-2 summarizes the parameters evaluated using the fractal tissue model for cancerous and normal prostate tissues at 800 nm

Table 3-2: D_f, d_{max} and $\langle d_m \rangle$ for cancerous and normal prostate tissues evaluated using the fractal tissue model

tissue type	fractal dimension (D_f)	cutoff diameter (d_{max})	most efficient diameter ($\langle d_m \rangle$)
cancer	1.9	~1.42 μm	~1.09 μm
normal	4.4	~6.47 μm	~2.05 μm

3.5. NIR optical polarized imaging

To study the potential of NIR polarized imaging for prostate cancer detection based on differences of absorption and scatter parameter of cancerous and normal prostate tissues, a prostate tissue sample of ~2cm×3cm×0.05cm consisting of a piece of cancerous tissue on the right side and a piece of normal tissue on the left side was imaged using a NIR spectral imaging system shown in Fig. 3-1(b). Figs. 3-9(a) and 3-9(b) show recorded transmission images of

normal-cancerous prostate samples at 800nm for parallel and perpendicular polarizations, respectively. It can be seen that the left piece of the specimen (mostly normal) has less transmission intensity than that on the right side (mostly cancer) for both polarization configurations. This can be understood because the extinction of normal tissues is stronger than that of cancerous tissues as shown in Fig. 3-2 [6].

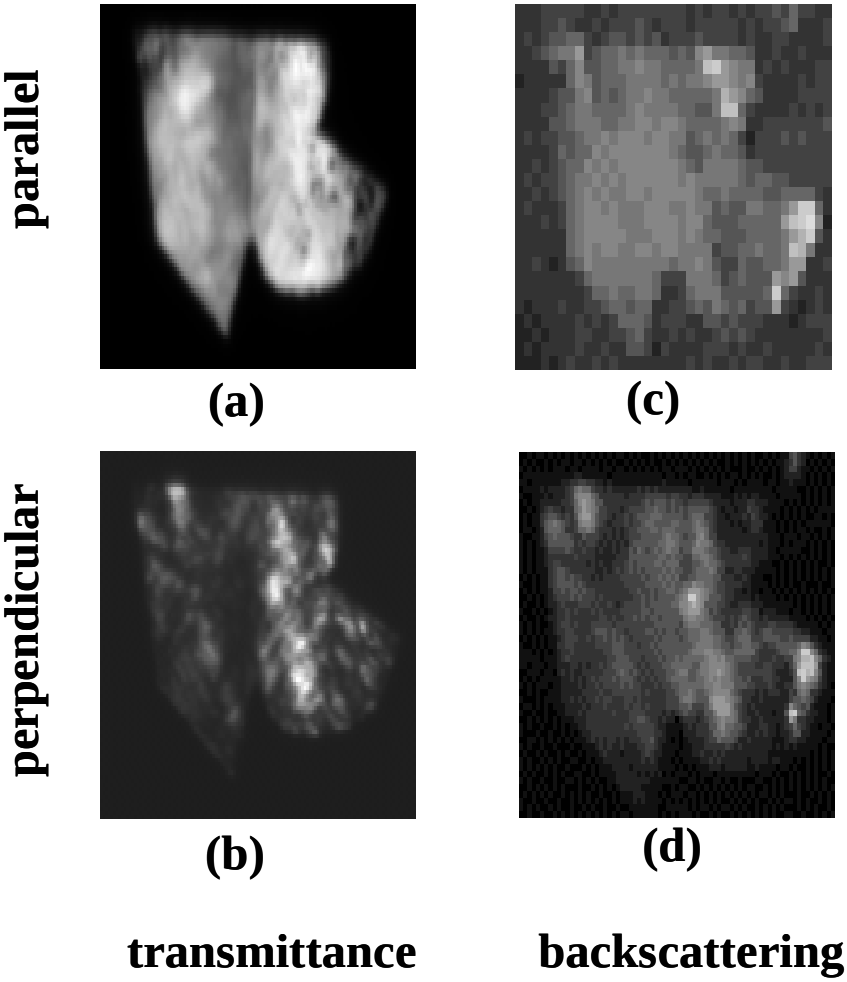

Figs. 3-9 (a)-(b) Transmission images of prostate tissue sample, normal (left) and cancer (right) at 800nm for parallel (top images) and perpendicular (bottom images) polarization configurations. (c)-(d) Backscattered images of a human prostate normal (left) and cancer (right) tissue sample at 800nm for parallel (top images) and perpendicular (bottom images) polarization configurations.

In the backscattering geometry, images as shown in Figs. 3-9(c) and 3-9(d), the light scattering from cancer tissues is stronger than that from normal tissues. This can be understood

because of larger anisotropy factor g measured in normal prostate tissue in comparison with cancerous prostate tissue at 800nm.

Digitized horizontal scans from left to right at the center of the transmission images shown in Figs. 3-9 (a) and 3-9 (b) were performed to calculate the polarization degree, defined as:

$$D = \frac{I_{\parallel} - I_{\perp}}{I_{\parallel} + I_{\perp}}. \tag{3.13}$$

The calculated degrees of polarization (D) for normal and cancerous prostate tissues at 800nm are D_{cancer} = 0.088 and D_{normal} = 0.10. The value of D for normal tissues is higher than that for cancer tissue. This is expected since cancerous prostate cells have higher cell density and irregular nuclear envelope while normal cells consist of more ordered and round nuclear [1，25，26]. It is reflected by the larger g factor of normal prostate tissue. It is well known that for a linearly polarized incident beam, its polarization depends on the single scattering by the particle and the number encountered by light when it traverses through a slab tissue. Light is less depolarized in one scattering event if light is more "forward-direction scattering", which is characterized by larger g factor. The smaller g factor for cancerous tissue indicates weaker forward scattering compared with normal tissue. This results more depolarization in cancerous tissue than that in normal tissue.

3. 6. Chapter summary:

The extinction spectra of cancerous and normal prostate tissues in the spectral range of 750 nm to 860 nm are used to derive the scattering coefficient (μ_s) in a thin tissue slab. The absorption coefficient (μ_a) and the reduced scattering coefficient (μ_s') were acquired by fitting diffuse reflectance measurements done with an obliquely incident beam using the diffusion model in a thick tissue sample. The values of μ_s' were found greater than μ_a by three orders of

magnitude for prostate tissue samples. The anisotropy factor g was calculated from μ_s and μ_s'. The values of fractal dimension (D_f) were obtained by fitting the wavelength dependence of μ_s'. Fractal dimension soft tissue model was used to study the microscopic properties of cancerous and normal prostate tissues and evaluate numerically the measured optical coefficients. The results show that the cutoff diameter of cancerous prostate tissue is approximately as nucleolar size of malignant cells while the largest scatterer in normal prostate tissues is cut off as normal nuclear size. This can be understood by pathological and morphological features of prostate cancer evolution. This study presents a potential approach that the cut off diameter d_{max} predicted by fractal tissue model may be used as one of criteria for prostate cancer detection. Furthermore, number of scattering particle as a function of particle size was investigated, and explained by the higher cell density, prominent and multiple nucleoli of cancerous prostate tissue. The most efficient diameter $\langle d_m \rangle$ was calculated, which expresses the most efficient contribution of a scatter's diameter to light scattering in prostate tissues.

3. 7. References:

1. D. F. Gleason and G. T. Mellinger, "Prediction of prognosis for prostate adenocarcinoma by combined histological and clinical", *J. Urol*, 111, 58-64 (1974).
2. C. Morrison, J. Thornhill and E. Gaffney, "The connective tissue framework in the normal prostate, BPH and prostate cancer: analysis by scanning electron microscopy after cellular digestion", *Urol. Res*. 28, 304-307 (2000).
3. R. Montironi, A. Filho, A. Santinelli, R. Mazzucchelli, R. Pomante, P. Colanzi and M. Scarpelli, "Nuclear changes in the normal-looking columnar epithelium adjacent to and distant from prostatic intraepithelial neoplasia and prostate cancer. Morphometric analysis in whole-mount sections", *Virch. Arch*., 437, 625-634 (2000).
4. Martin Chaplin, "Do we underestimate the importance of water in cell biology?", *Nat. Rev.: Mol. Cell Biol.,* 7, 861-866 (2006).
5. Pavan Atluri, Giorgos C. Karakousis, Paige M Porrett and Larry R. Kaiser, "The Surgical Review: An Integrated Basic and Clinical Science Study Guide: Chapter one: Neurosurgery", *Lippincott Williams & Wilkins, ISBN 0781756413*, P10-32 (2005).
6. J. H. Ali, W. B. Wang, M. Zevallos and R. R. Alfano, "Near Infrared Spectroscopy and Imaging to Probe Differences in Water Content in Normal and Cancer Human Prostate Tissues", *Technol. Cancer Res. Treat*., 3, 491-497 (2004).
7. Wai-fung Cheong, Scott A. Prahl, and Ashley J. Welch, "A review of the optical properties of biological tissues", *IEEE J. Quant. Elec.*, 26(12), 2166-2185 (1990).
8. L. Wang, P. P. Ho, C. Liu, G. Zhang and R. R. Alfano, "Ballistic 2-D imaging through scattering wall using an ultrafast Kerr gate", *Science*, 253, 769-771 (1991).

9. D. A. Benaron, Wai-Fung Cheong and D. K. Stevenson, “Imaging enhanced: tissue optics”, *Science*, 276(5321), 2002–2003 (1997).
10. M. Xu, M. Alrubaue, S. K. Gayen and R. R. Alfano, “Determination of light absorption, scattering and anisotropy factor of a highly scattering medium using backscattered circularly polarized light”, *Optical interaction with tissue and cells XVIII, Proc. of SPIE*, 6435, J1-6 (2007).
11. Ruikang K. Wang, "Modeling optical properties of soft tissue by fractal distribution of scatterers", *J. Mod. Opt.*, 47(1), 103-120 (2000).
12. S. K. Sharma and S. Banerjee, “Volume concentration and size dependence of diffuse reflectance in a fractal soft tissue model,” *Med. Phys.*, 32(6), 1767-1774 (2005).
13. M. Xu and R. R. Alfano, "Fractal mechanisms of light scattering in biological tissue and cells", *Opt. Lett*. 30, 3051-3053 (2005).
14. M. Xu, T. Wu and J. Y. Qu, “Unified Mie and fractal scattering by cells and experimental study on application in optical characterization of cellular and subcellular structures”, *J. Biomed. Opt*., 13, 0240151-9 (2008).
15. R. Drezek, M. Guillaud, T. Collier, I. Boiko, A. Malpica, C. Macaulay, M. Follen and Rebecca Richards-Kortum, “Light scattering from cervical cells throughout neoplastic progression: influence of nuclear morphology, DNA content, and chromatin texture”, *J. Biomed. Opt.,* 8(1) 7–16, (2003).
16. J. R. Mourant, T. M. Johnson, S. Carpenter, A. Guerra, T. Aida and J. P. Freyer, “Polarized angular dependent spectroscopy of epithelial cells and epithelial cell nuclei to determine the size scale of scattering structures”, *J. Biomed. Opt.,* 7(3), 378–387 (2002).

17. Steven L. Jacques and Scott A. Prahl, "Introduction to tissue optics", http://omlc.ogi.edu/classroom/ece532/index.html
18. J. X. Zhu, D. J. Pine and D. A. Weitz, "Internal reflection of diffusive light in random media", *Phys. Rev. A*, 44, 3948 – 3959 (1991).
19. J. R. Mourant, T. Fuselier, J. Boyer, T. M. Johnson and I. J. Bigio, "Predictions and measurements of scattering and absorption over broad wavelength ranges in tissue phantoms", *Appl. Opt*., 36, 949-957 (1997).
20. C. F. Bohren and D. R. Huffman, "Absorption and scattering of light by small particles", Wiley, New York, (1983).
21. Bausch and Lomb, "Refractive index and percent dissolved solids scale, Figure S-5195, 06075", Analytical Systems Division.
22. B. Gelebart, E. Tinet, J. M. Tualle and S. Avrillier, "Phase function simulation in tissue phantoms," *Pure Appl*. *Opt*., 5, 377–388 *(*1996).
23. J. M. Schmitt and G. Kumar, "Optical Scattering Properties of Soft Tissue: A Discrete Particle Model", *Appl. Opt.*, 37(13), 2788-2797 (1998).
24. Linhong Kou, Daniel Labrie and Peter Chylek, "Refractive indices of water and ice in the 0.65- to 2.5-gm spectral range", *Appl. Opt*., 32, 3531--3540 (1993).
25. Ibrahim Ramzy, "Clinical cytopathology and aspiration biopsy", *The McGraw-Hill Companies* copyright@2001.
26. A. Fischer, S. Bardarov Jr. and Z. Jiang, "Molecular aspects of diagnostic nucleolar and nuclear envelope changes in prostate cancer", *J. Cell. Biochem.*, 91, 170–184 (2004).
27. M. Varma, M. Lee, P. Tamboli, R. Zarbo, R. Jimenez, P. Salles and M. Amin, "Morphologic criteria for the diagnosis of prostatic adenocarcinoma in needle biopsy specimens: A study of

250 consecutive cases in a routine surgical pathology practice", *Arch. Pathol. Lab. Med.*, 126, 554-561 (2002).

28. S. Bektaş, B. Bahadir, B. Gün, G. Kertiş and Ş. Özdamar, "The relation between gleason score, and nuclear size and shape factors in prostatic adenocarcinoma", *Turk J Med Sci*, 39(3), 381-387 (2009).
29. R. Montironi, R. Mazzucchelli, A. Santinelli, M. Scarpelli, A. Beltran and D. Bostwick, "Incidentally detected prostate cancer in cystoprostatectomies: pathological and morphometric comparison with clinically detected cancer in totally embedded specimens", *Hum. Pathol.*, 36, 646– 654 (2005).

Chapter 4
Time-resolved fluorescence polarization dynamics and optical imaging of Cybesin in cancerous and normal prostate tissues

4. 1. Introduction

Over the past decade, cyanine dyes have been investigated by several groups as contrast agents for optical detection of tumors. Researchers are interested in cyanine dyes, i.e. Indocyanine Green (ICG), a clinically approved NIR dye by FDA, because its emission ranges from 700 nm to 900 nm in the tissue "optical window". As a small ICG-derivative dye-peptide, Cybesin was synthesized and used as a contrast agent to detect pancreas cancer in an animal model [1]. The prior experimental results of Cybesin for pancreas tumor detection indicated that Cybesin preferentially localized for over 24 hours in tumors known to over-express bombesin receptors in a small animal model [1]. It was observed that the bombesin receptor can be over-expressed on the membranes of human prostate cancer cells [2]. These results motivated us to apply Cybesin to human prostate cancer detection.

In this chapter, Cybesin was used to target over-expressed bombesin receptors in human prostate cancer tissue. The absorption and fluorescence spectra of Cybesin were studied in the wavelength region from 650 nm to 900 nm of NIR "tissue optical window". In order to investigate time-resolved fluorescence polarized spectroscopy of receptor-targeted contrast agents, Cybesin, bound with prostate cancer cells in prostate tissue, analytical model dealing with high viscous media need to be developed. In this chapter, an analytical model was developed based on previous works [3-7] and used to extract the rotational times and fluorescence polarization anisotropies of the contrast agents in prostate tissues from the measured data [8]. Time-resolved polarization-dependent fluorescence of Cybesin in solution and in cancerous and normal prostate tissues was measured. The polarization preservation

property of Cybesin in tissue was observed. The fluorescence intensity emitted from a Cybesin-stained cancerous tissue area was found to be much stronger than that from a Cybesin-stained normal tissue area indicating that cancerous prostate tissue takes-up more Cybesin than normal tissue [9]. The polarization anisotropy of Cybesin contained in cancerous prostate tissue was found to be larger than that of Cybesin in normal prostate tissue indicating that a larger degree of polarization was preserved in the Cybesin-stained cancerous tissue due to micro-structures. The differences of rotational times and polarization anisotropies were observed for Cybesin in cancerous and normal prostate tissues, which reflect changes of micro-structures of cancerous and normal tissues [10-12], and their different bound affinity with contrast agents. A static anisotropy component from the emission of cell-bonded Cybesin molecules in tissue and a time-dependent anisotropy component from the emission of un-bonded Cybesin molecules were determined and discussed. The static anisotropy value of Cybesin in stained cancerous tissue was found to be much larger than that in stained normal tissue. This research may be used to develop better optical methods for *in- situ* prostate cancer detection. Finally, The NIR spectral polarization imaging techniques were used to differentiate human cancerous and normal prostate using Cybesin as an optical contrast agent marker. The model prostate samples consisting of a small piece of normal prostate tissue and a small piece of prostate cancer tissues stained with Cybesin were imaged. The results indicate that this receptor-targeted Cybesin can be used as a potential fluorescent biomarker in human prostate cancer detection.

4. 2. Model of fluorescence depolarization

4.2.1. Pico-second rotational diffusion kinetic fluorescence spectroscopy of dye in solution

The time-resolved fluorescence study can be used to obtain not only the information of the intensities of fluorophores but also that of their biophysical microenvironments. The time-

resolved polarization measurements of fluorophores excited with linearly polarized light can be applied as a probe to determine the rotational (re-orientation) rate of molecules, which is a function of the viscosity of their local environment, temperature and the size of the rotating fluorophore [3]. Therefore, the ultrafast rotation of a dye can be used to extract the information about surrounding medium [3-8]. We begin with brief reviewing of the time-resolved fluorescence spectroscopy of dye in solution.

The fluorescence depolarization property is usually described by the time-resolved fluorescence polarization anisotropy defined as [3, 4]:

$$r(t) = \frac{I_{\parallel}(t) - I_{\perp}(t)}{I_{\parallel}(t) + 2I_{\perp}(t)}, \qquad (4.\ 1)$$

where $I_{\parallel}(t)$ and $I_{\perp}(t)$ are the emission intensities of the fluorescent components whose polarizations are parallel and perpendicular to the excited light, respectively [3, 4]. The decay of the parallel ($I_{\parallel}(t)$) and the perpendicular ($I_{\perp}(t)$) components of the fluorescence excited by linear polarized light can be described by [4]:

$$I_{\parallel}(t) = \frac{I_0}{3}\exp(-\frac{t}{\tau_f})\left(1 + 2r_0\exp(-\frac{t}{\tau_r})\right), \text{ and } I_{\perp}(t) = \frac{I_0}{3}\exp(-\frac{t}{\tau_f})\left(1 - r_0\exp(-\frac{t}{\tau_r})\right), \qquad (4.\ 2)$$

where I_0 is the initial emission intensity, τ_f is the fluorophore's lifetime, τ_r is re-orientation time affecting the depolarization rate of the emission of excited polarized molecules, and r_0 is anisotropy at t=0 reflecting the initial orientation of the dipoles. Substituting equations (4. 2) into (4. 1), r(t) can be written as [3]:

$$r(t) = r_0\exp(-\frac{t}{\tau_r}). \qquad (4.\ 3)$$

Theoretical calculation of r_0 is based on the physical phenomenon of photoselection: the population of excited fluorophores partially oriented along the parallel direction. The theoretical

value of r_0 was calculated and reported to be 0.4 in solution_by taking the dipoles' initial orientation as random distribution function [5, 7]. In the simple possible case where molecules undergo Brownian rotation as Einstein spheres, the rotation time is determined as Einstein-Stokes relationship [3]:

$$\tau_r = \frac{\eta V}{KT}, \tag{4. 4}$$

where k is the Boltzmann constant, and T is the absolute temperature, η is viscosity of the solvent, and V is the volume of a molecule.

Using equation (4. 2), the total fluorescence intensity I(t) can be written as:

$$I(t) = I_{\parallel}(t) + 2\, I_{\perp}(t) = I_0 \exp(-\frac{t}{\tau_f}). \tag{4. 5}$$

The factor 2 is used for counting the contribution of the perpendicular component to the whole fluorescence intensity because the dipoles' Brownian motion happens in 3D space.

4.2.2. Development of the analytical model: static and time-resolved components of anisotropy of receptor-targeted contrast agent in prostate tissues

In order to investigate time-evolution of emission from Cybesin bound with prostate cancer cells in prostate tissue, an analytical model dealing with high viscous media was developed. It is well known that property of biological living tissues are somehow similar to the behavior of liquid with very high viscosity [11, 12] and the volume of 70% to 80% of human body is water. Experimental result also indicated that that dye in tissues with high viscosity is expected to have ordered structure to cause the different distribution of the initial excited fluorescent molecules while the time-resolved fluorescence polarized spectroscopy is measured [6, 7]. The viscosities of prostate tissues were reported to be much higher than 3,000 Poise [13]. Therefore, Cybesin in prostate tissues is considered as a fluorescent contrast agent in "high viscous liquid".

After cancerous prostate tissue was soaked into the Cybesin solution and washed off using

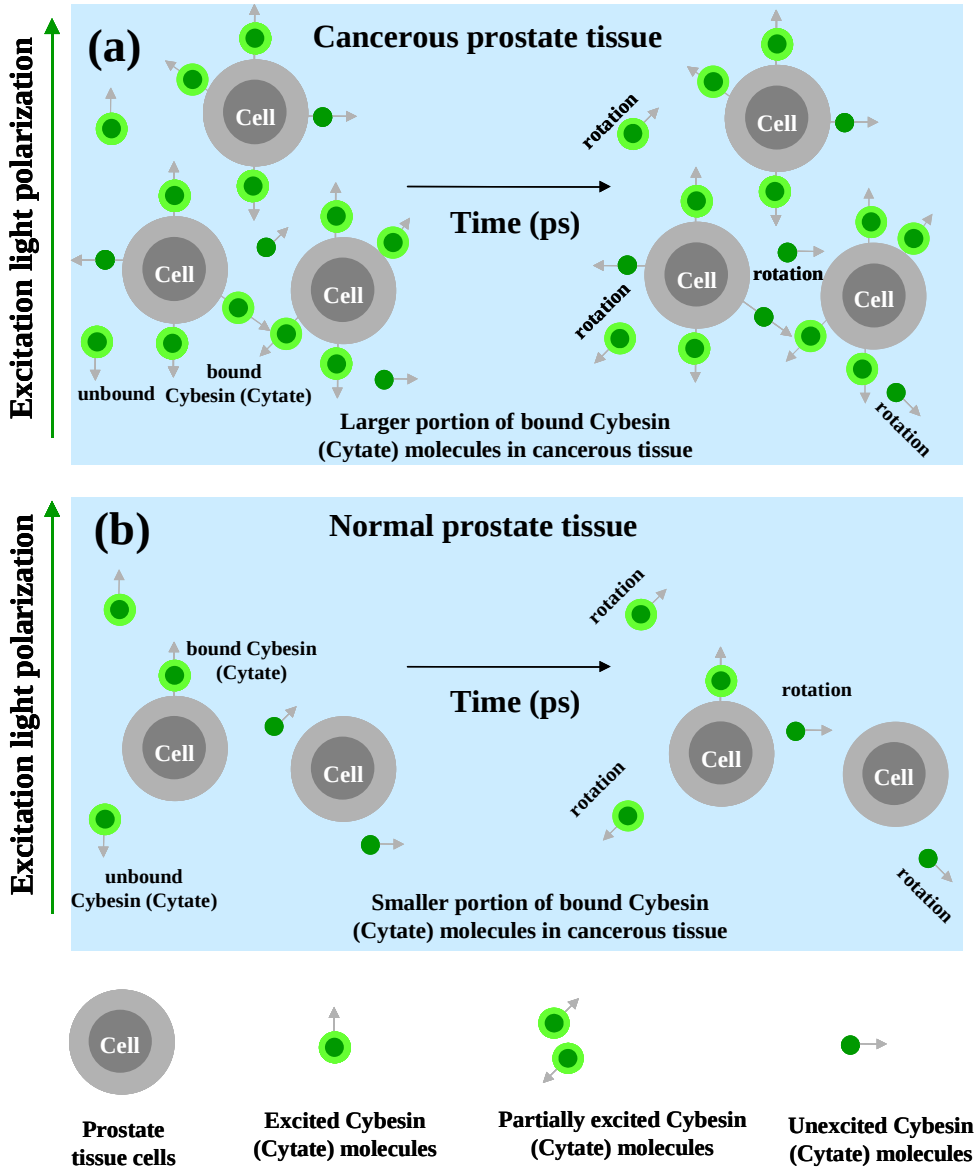

Fig. 4-1. The schematic diagrams of the cell-bound mechanism and reorientation of Cybesin in stained (a) cancerous tissue which has a higher cell density and more cell-bound Cybesin, and (b) normal tissue which has a lower cell density and less cell-bound Cybesin. Molecules with their absorption transition vectors (arrows) aligned parallel to linearly polarized pump light (for example: vertical), and those having a parallel component of other-orientated transition vectors are excited. For free molecules, the rapid rotations contribute fluorescence depolarization. In contrast, Cybesin conjugated to prostate cells show a static anisotropy component.

sodium phosphate buffer consequently, a large proportion of Cybesin was conjugated to the corresponding receptor on cells [8, 9]. Although a large amount of free Cybesin molecules in

surface and sub-surface were removed by buffer, some free contrast agents were still conserved in deep tissue. For the case of normal prostate tissue, a smaller proportion of contrast agent was conjugated to tissue cells in comparison with cancerous tissue [8, 9] and some free fluorescent molecules exist in deep tissue, too. The cell-bound mechanism and reorientation of Cybesin molecules in prostate tissues can be schematically shown in Fig. 4-1. This model describes two types of bound and rotating situations of Cybesin molecules in Cybesin-stained prostate tissues and their contributions to total fluorescence and fluorescence polarization anisotropy.

As shown in Fig. 4-1, the emission of Cybesin can be considered to be contributed from two components: (1) static component caused by cell-bound Cybesin molecules in prostate tissue; (2) the temporal component contributed by the rotation of unbound Cybesin molecules remained in the body liquid of prostate tissue. These assumptions are reasonable because the weights of tissue cells are much larger than that of Cybesin molecules and tissue cells are too huge to undergo rapid rotation. There are more cell-bound Cybesin molecules in cancerous prostate tissue than those in normal tissues as indicated in Fig. 4-1 because of the over-expressed bombesin receptors on the prostate cancer cells and high bound affinity of Cybesin to the bombesin receptors [2, 8, 9]. The free contrast agent molecules would undergo rotation while the Cybesin molecules conjugated to tissue cell would stay steady.

The following model describes a system of *n* types of non-interacting fluorophores to investigate rotational dynamics and fluorescence polarization anisotropies of the contrast agents in prostate tissues. The impulse response function of the system to the excitation pulse is given by [14]:

$$I(t) = \sum_n I^{(n)}(t) = \sum_n I_0^{(n)} \exp(-\frac{t}{\tau_f^{(n)}}) \cdot \qquad (4.\ 6)$$

For the parallel component [14]:

$$I_{\parallel}(t) = \sum_n I_{\parallel}^{(n)}(t) = \sum_{\mathrm{n}} \frac{I_0^{(n)}}{3} \exp(-\frac{t}{\tau_f^{(n)}}) \left(1 + 2r_0^{(n)} \exp(-\frac{t}{\tau_r^{(n)}})\right) \quad . \tag{4. 7}$$

There are two types of molecules (n=2) in our case: cell-bound and -unbound Cybesin molecules. They both have same fluorescence lifetime ($\tau_f^{(1)} = \tau_f^{(2)}$). The cell-bound contrast agents have infinite rotation time ($\tau_r^{(1)} \to \infty$) since they are bound with huge tissue cell, and their rotations are too slow in comparison with the rotational time ($\tau_r^{(2)}$) of unbound Cybesin, which is in the range of picoseconds. It is also reported that fluorescence intensity is proportional to the number of fluorophores in tissue and the intensity of emission from a single Cybesin molecule [15]. By taking these assumption, $I_{\parallel}(t)$ then can be written as the following equation:

$$I_{\parallel}(t) = \frac{I_0}{3} \exp(-\frac{t}{\tau_f}) \left(1 + 2r_1 + 2r_0 \exp(-\frac{t}{\tau_r})\right). \tag{4. 8}$$

Using similar procedure of derivation, the perpendicular component can be obtained as:

$$I_{\perp}(t) = \frac{I_0}{3} \exp(-\frac{t}{\tau_f}) \left(1 - r_1 - r_0 \exp(-\frac{t}{\tau_r})\right) . \tag{4. 9}$$

Substituting equations (4. 8) and (4. 9) into equation (4. 1), the time-dependent polarization anisotropy of contrast agents can be written as:

$$r(t) = r_1 + r_0 \exp(-\frac{t}{\tau_r}) \quad . \tag{4. 10}$$

Introducing equation (4. 8) and equation (4. 9) into $I(t)=I_{\parallel}(t)+2I_{\perp}(t)$, the total time-resolved fluorescence intensity can be obtained as same as equation (4. 5).

4. 3. Experimental method

The absorption spectrum of Cybesin in DMSO solution was investigated using a Perkin-Elmer Lamda 9 UV/VIS/NIR Spectrophotometer in the spectral range of 300 nm to 900 nm [9]. The fluorescence spectrum was measured using a far-red to NIR spectral setup excited by

modulated excitation with a 680 nm diode laser. Fluorescence light from the sample after passing through lenses was focused on the entrance slit of a SPEX Minimate 0.25-m monochromator (spectrometer) and detected by a Hamamatsu P394A PbS detector mounted at the exit slit of the monochromator [9].

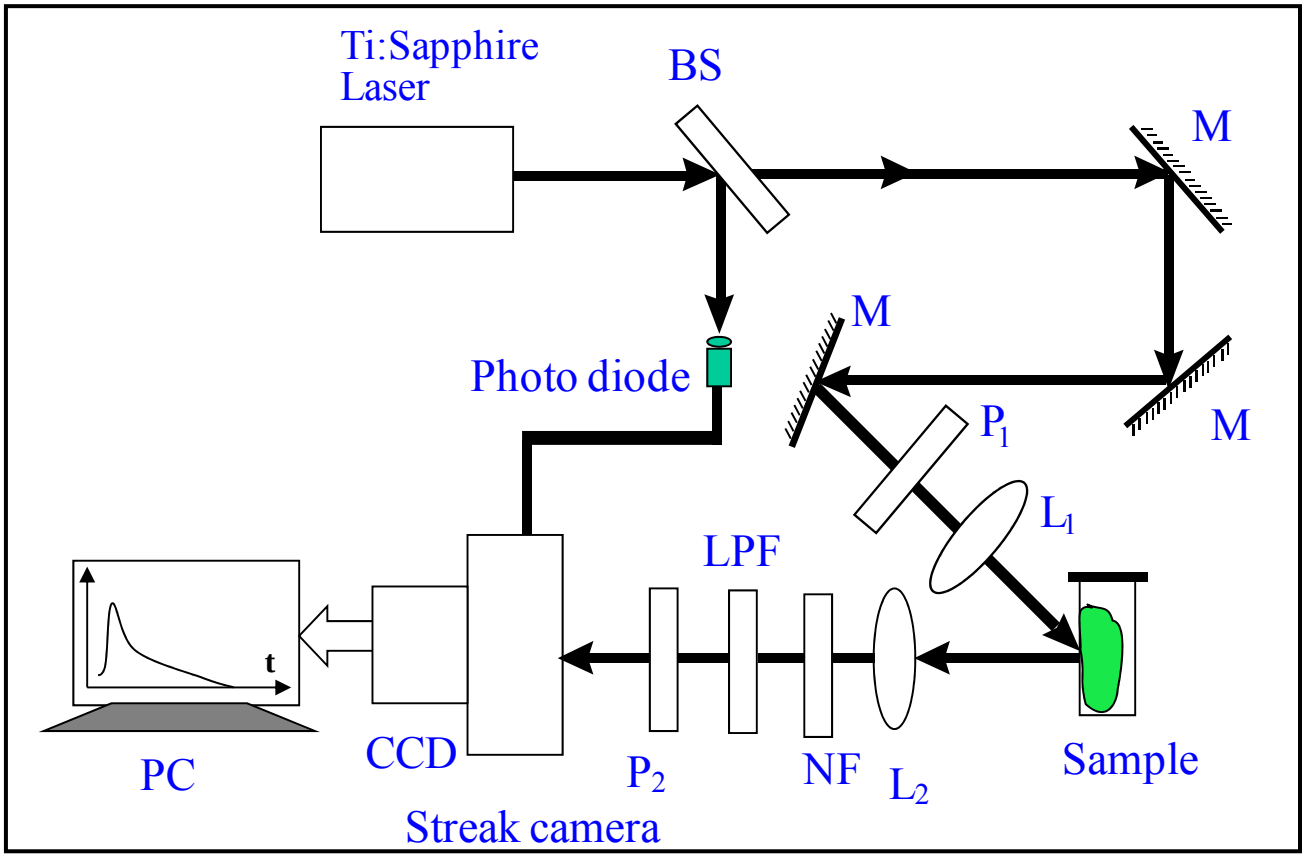

Fig. 4-2 Schematic diagrams of the experimental sets up used for time-resolved fluorescence polarized spectroscopy measurements, where P: polarizers; M: mirrors; BS: beam splitters; LPF: long pass filter; NF: Notch filter; L: lenses; CCD: charge-coupled device camera.

The experimental arrangement for the time-resolved fluorescence measurements is schematically shown in Fig. 4-2. Optical pulses of 130 fs at 800 nm with a repetition rate of 82 MHz from a Coherent Mira 900 Mode-locked Ti:Sapphire laser were used to pump the samples. The fluorescence was collected by a large diameter lens (L_2) with a focal length of 5 cm and directed onto a synchroscan streak camera with temporal resolution of 10 ps. A long pass filter

(LP) was used to block the illuminating light so that only the emission from the samples was detected. Polarizer P_1 was used to ensure the linear polarization of the input laser pulses and P_2 was used as an analyzer. The polarization of P_1 was rotated between 0^o and 90^o with respect to that of P_2 to record the intensity profiles of the parallel and perpendicular polarization components of the fluorescence. The temporal profiles of fluorescence recorded by a silicon intensified target (SIT) vidicon camera were analyzed to obtain the temporal profiles and polarization dynamics of the fluorescence [8].

The schematic diagram of the experimental set-up for our NIR spectral polarization imaging was shown as backscattered geometry of Fig. 3-1(b) in chapter 3. Light from a white light source is used to illuminate the prostate tissue sample with average power of ~ 50 $\mu W/cm^2$, which is much lower than the critical illumination level given by FDA [9].

The Cybesin used for the time-resolved fluorescence study was solvated in 20% aqueous Dimethyl Sulfoxide (DMSO). Cybesin was prepared by Professor Achilefu's group at the Washington University School of Medicine. The molecular structure the Cybesin agent has been reported shown as Fig. 1-2 (c) in Chapter 1 and the synthesis was reported elsewhere [1]. The Cybesin agent is mainly composed of ICG and the bombesin receptor ligand, which delivers the contrast agent to the corresponding receptor presented in the tumor [1, 8, 9].

Six (6) *in vitro* prostate cancer-and-normal tissue samples obtained from the National Disease Research Interchange (NDRI), the Cooperation Human Tissue Network (CHTN) and the Hackensack University Medical Center (HUMC) were used for the time-resolved fluorescence and optical imaging measurements under IRB approvals at the City College of New York. Samples were not chemically treated and they were not frozen prior to our measurements. The cancerous and normal prostate tissues used for the temporal fluorescence measurements were cut

into ~2 × ~1 × ~0.5 cm (length × width × thickness) pieces, and were soaked in the same Cybesin-DMSO (20% aqueous Dimethyl Sulfoxide) solution with a Cybesin concentration of ~3.2×10^{-6} M for the same period of time. Then the samples were put into sodium phosphate buffer (Sigma-Aldrich) to wash off and consequently reduce the amount of unbound Cybesin. All the measurements and processes were performed at room temperature.

4. 4. Experimental results and discussion

4.4.1. The absorption and fluorescence spectra of Cybesin

Figs. 4-3 (a) and 4-3 (b) show the measured absorption and fluorescence spectra of Cybesin, respectively. The absorption band of Cybesin ranges from 680 nm to 830 nm with a shoulder peak at 720 nm and a strong peak at 792 nm. The fluorescence spectrum covers from 800 nm to 950 nm with a main peak at 825 nm and a weak peak at 925 nm. Both results show that Cybesin possesses the spectral advantages of ICG that the fluorescence and the absorption ranges are in the NIR range of the "tissue optical window".

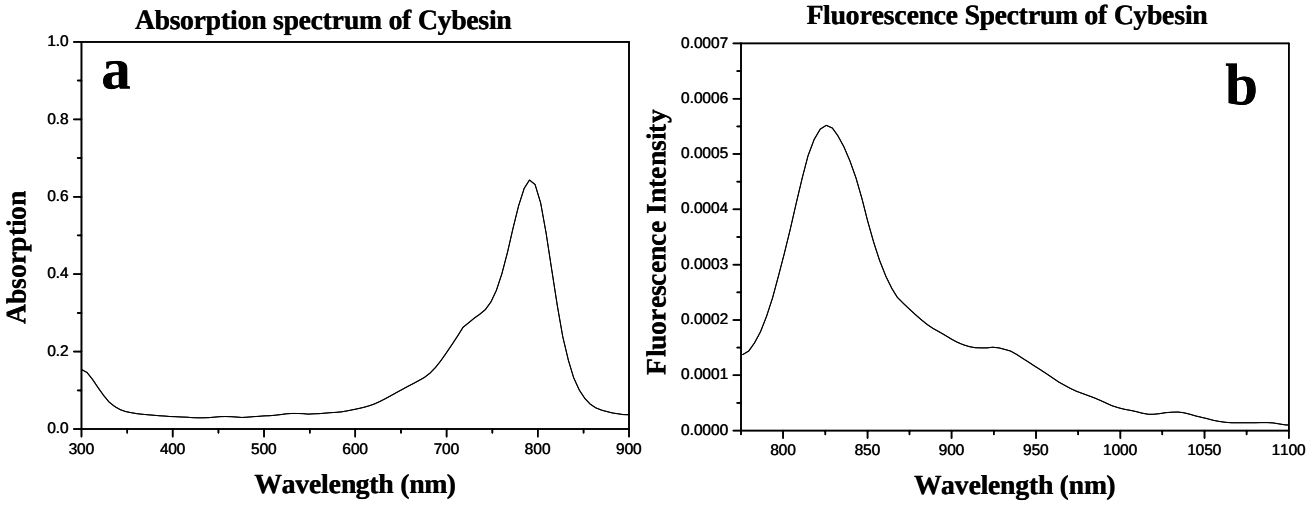

Fig. 4-3 (a) Absorption and (b) fluorescence spectra of Cybesin in 20% aqueous DMSO.

4.4.2. Time-resolved fluorescence kinetics and polarization anisotropy of Cybesin in 20% aqueous DMSO

The measured temporal profiles of the fluorescence emitted from Cybesin in solution for polarizations parallel and perpendicular to the polarization direction of the excitation at 800 nm are shown in Fig. 4-4 (a). The dash- and dot-line profiles are the parallel and the perpendicular components $I_{\parallel}(t)$ and $I_{\perp}(t)$, respectively. The main difference between these two components is that $I_{\parallel}$ is greater than $I_{\perp}$ for all of the decay times. In particular, at the peak position (t=0), the parallel component $I_{\parallel}(0)$ is almost three (3) times stronger than that of the perpendicular one $I_{\perp}(0)$. This indicates the polarization preservation nature of Cybesin.

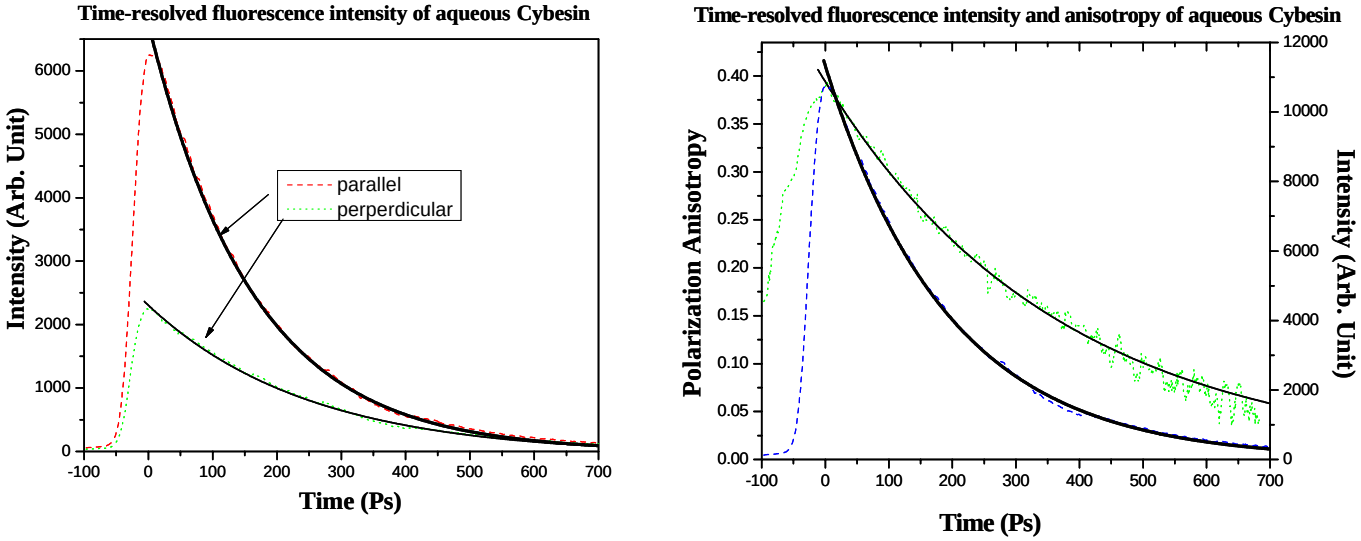

Fig. 4-4 (a) Time-resolved fluorescence polarization component of parallel (dash) and perpendicular (dot) to the polarization direction of the exciting light and the fitting curve (solid) obtained by fitting the data using equation (4. 2); (b) Time-dependent polarization anisotropy (dot) and total intensities (dash) calculated using the measured data shown in (a) with equation (4. 1) and (4. 5) in the text, respectively, and the fitting curve (thin solid) for r(t) is calculated using equation (4. 3) and fitting results (thick solid) for I(t) using equation (4. 5).

Using equation (4. 1), the calculated temporal profile of the polarization anisotropy r(t) of Cybesin in solution is shown as a dot line in Fig. 4-4 (b). The r_0 obtained from Fig. 4-4 (b) is 0.39, which is very close to the theoretical value of 0.4. This indicates that the transition dipole moments of Cybesin molecules in solution are randomly oriented and that the depolarization effects of Cybesin in 20% DMSO solvent can be confined to molecular rotations and to the trivial effect of initial randomness [3, 4]. The polarization anisotropy peak value r_0 and the

rotation time τ_r of Cybesin in solution can be obtained using equation (2) to fit the experimental data of r(t) in Fig. 4-4 (b). The fitting curve calculated using the experimental data of r(t) and equation (4. 3) is shown as thin-solid line by the thick line in Fig. 4-4 (b). Using equation (4. 5), the temporal profile of the total intensities of I(t) is shown as a dash line in Fig. 4-4(b). Equation (4.5) is used to obtain τ_f by fitting the measured data. The fitting curve calculated using the experimental data of I(t) and equation (4. 5) is shown by the thick-solid line in Fig. 4-4 (b). Substituting fitting data of r_0, τ_r and τ_f into equation (4. 2), the fitting curves of $I_{\parallel}(t)$ and $I_{\perp}(t)$ are shown as thick- and thin-solid lines, respectively in Fig. 4-4 (a). The fitting results of Cybesin solution are $r_0 = 0.39 \pm 0.02$, $\tau_r = 352 \pm 11$ ps and $\tau_f = 193 \pm 5$ ps.

4.4.3. Time-resolved fluorescence kinetics and polarization anisotropy of Cybesin contained in stained cancerous and normal prostate tissues

The time-resolved fluorescence intensity profiles of $I_{\parallel}(t)$ and $I_{\perp}(t)$ averaged over six (6) samples for the cancerous and normal prostate tissues stained with Cybesin are displayed in Figs.

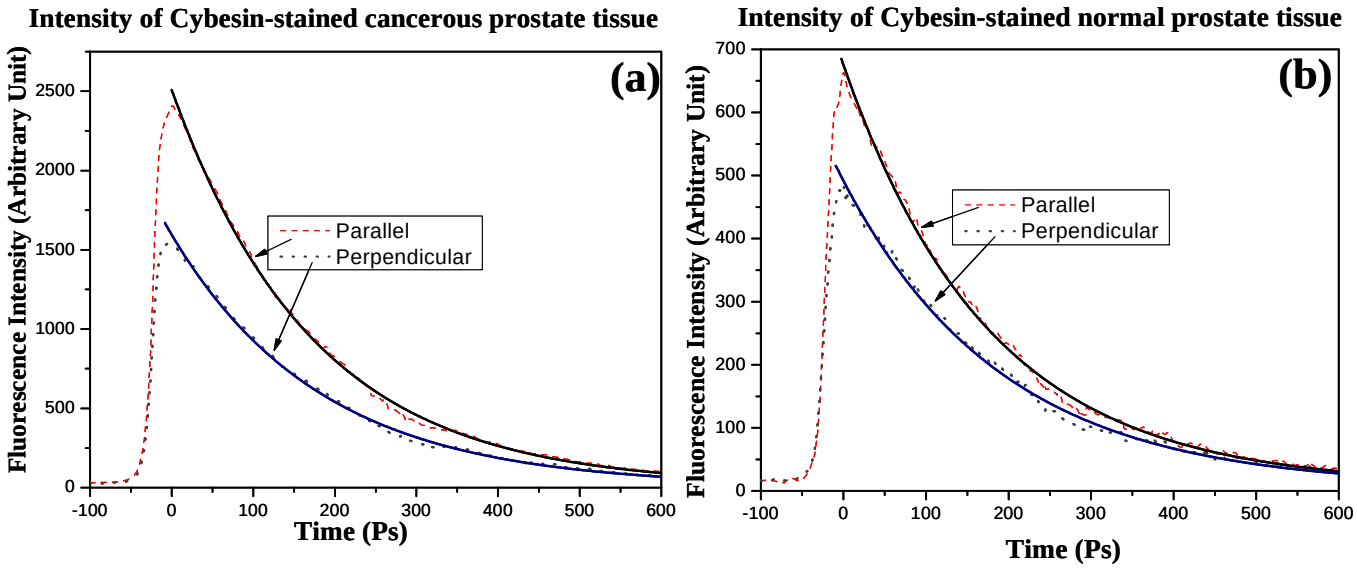

Fig. 4-5 The time-resolved polarized fluorescence intensity of light emitted from Cybesin stained (a) cancerous and (b) normal prostate tissues for linearly polarized 800nm laser excitation. The dash- and dot-line profiles display the parallel and perpendicular components emitted from stained tissue, respectively. The solid lines display the fitting curves calculated using equation (4. 8) for parallel component and equation (4. 9) for perpendicular component, respectively.

4-5(a) and 4-5(b), respectively. The thin-dash and thin-dot-line profiles are the parallel and perpendicular components emitted from Cybesin-stained cancerous and normal prostate tissue, respectively. The salient feature of Figs. 4-5(a) and 4-5(b) is that $I_{\parallel}$ is greater than $I_{\perp}$ throughout the decay period for both cancerous and normal tissues. At the peak position, $I_{\parallel}(0)$ is ~1.57 times stronger than $I_{\perp}(0)$ in cancerous tissue while this ratio is ~1.40 in normal tissue. This indicates that the fluorescence emitted from both Cybesin-stained cancerous and normal prostate tissues show the polarization preservation property [8, 15].

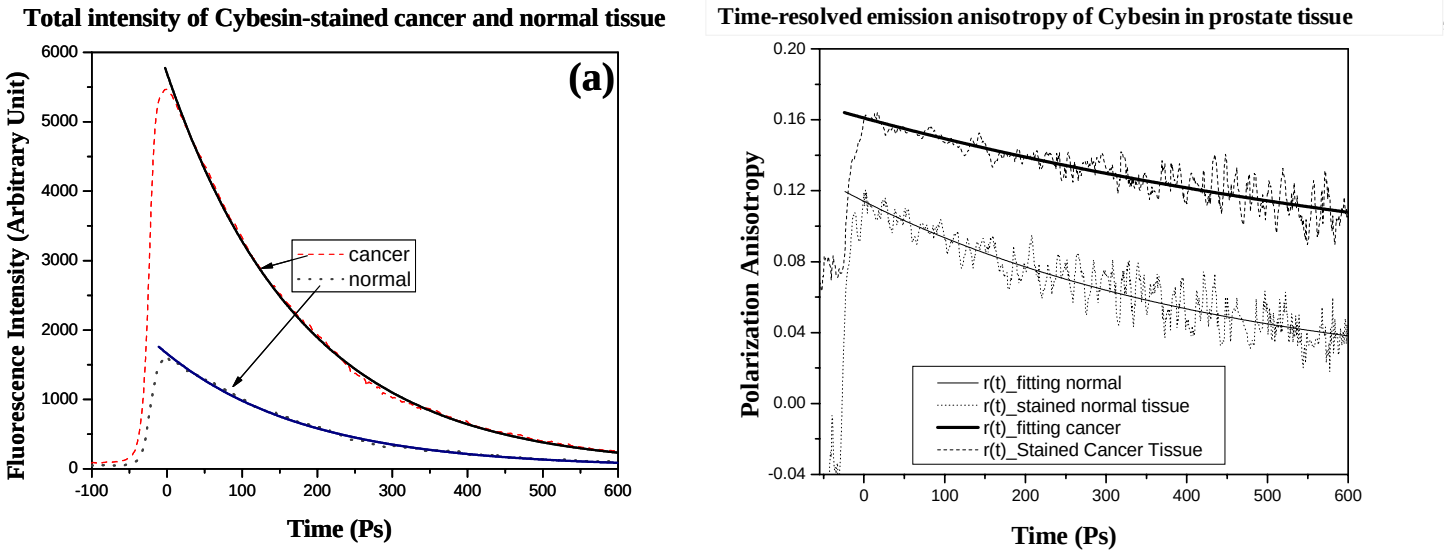

Fig. 4-6 (a) The total intensity of Cybesin-stained cancerous (dash) and normal (dot) prostate tissue obtained using the data of Figs. 4-5 (a) and (b), and equation (4. 5) in the text; (b) Time-dependent emission anisotropy of for Cybesin-stained cancerous (dash) and normal (dot) prostate tissues calculated using equation (4. 1) shown in the text and the measured data shown in Figs. 4-5 (a) and (b). The solid lines are the fitting results using the analytical model.

To extract and compare the time-resolved parameters of Cybesin in cancerous and normal prostate tissues, the total time-resolved intensities I(t) and the temporal profiles of the polarization anisotropy r(t) of Cybesin in stained prostate tissue were calculated using equations (4. 5) and (4. 10), respectively, and the results are displayed in Figs. 4-6 (a) and 4-6 (b), respectively. Fig. 4-6 (a) indicates that the emission intensity from Cybesin-stained cancerous tissue is higher than that from stained normal tissue throughout the life time of Cybesin emission.

The emission peak intensity of the Cybesin-stained cancerous tissue is much greater than that of the Cybesin-stained normal tissue. The ratio of peak fluorescence intensities of Cybesin-stained cancerous tissue to normal prostate tissues is found to be ~3.29, indicating that cancerous prostate tissue takes-up more Cybesin than normal tissue [2, 8, 9]. The interesting features of r(t) curves shown in Fig. 4-6 (b) are: (1) the values of polarization anisotropy of Cybesin in the stained cancerous tissue are always larger than that of the stained normal tissue at all the decay time; (2) The profile of r(t) for the Cybesin-stained cancerous tissue shows a little flatter decay in comparison with the normal tissue.

The depolarization property of emission form Cybesin can be studied by the time-resolved polarization spectroscopy which was developed as equations (4. 5) and (4. 8) to (4. 10). The reorientation of Cybesin molecules contributed to fluorescence will result in the decay behavior of r(t). By investigating the time-resolve spectroscopy and anisotropy of emission form Cybesin in prostate tissue, the biophysical local microenvironments of contrast agents can be studied and the results can be used to compare different types of prostate tissues. These differences can be quantified by fitting experimental data shown in Figs. 4-5 and 5-6 using our analytic model. The fluorescence lifetime (τ_f) and initial peak intensity (I_0) of Cybesin in stained cancerous and normal prostate tissues can be obtained by fitting the temporal profiles of the total emission data shown in Fig. 4-6 (a) using equation (4. 5). Equations (4. 8) to (4. 10), and the temporal profiles of the polarized fluorescence and anisotropy data shown in Figs. 4-5 and 4-6 (b) are used to obtain and compare the parameters for Cybesin in cancerous and normal prostate tissues: τ_r (the rotation time), r_1 (anisotropy of the static component) and r_0 (the value of dynamical anisotropy for the rotation dipoles at t=0). The fitting data are presented as: r_0=0.105±0.01, r_1=0.056±0.01, τ_r=850±150ps and τ_f=179±6.8ps for cancerous prostate tissues, and r_0=0.103±0.01,

r_1=0.005±0.01, τ_r=600±200ps and τ_f=189±11ps for normal prostate tissues. The fitting results are shown in Figs. 4-5 and 4-6 as solid lines for the cancerous and normal prostate tissues. The good agreement of our model fitting with the experimental data indicates that the time-resolved polarization-dependent fluorescence of the contrast agent, Cybesin in human prostate tissues can be truly considered to have two contributions from the free Cybesin molecules remained in the liquid of tissue and the static cell-bound Cybesin. The ratio of peak intensities of total fluorescence for Cybesin-stained cancerous tissue and normal tissues ($I_0^{cancer} / I_0^{normal}$) is ~3.43 [2, 8, 9]. The rotational time τ_r and static polarization anisotropy r_1 for Cybesin in cancerous tissue were found 1.4 times and ~10 times larger than those for normal prostate tissue, respectively.

The larger r_1 observed in Cybesin-stained cancerous tissue compared with that in normal tissue can be understood more uptake of Cybesin in cancerous prostate tissue. Furthermore, since the excitation wavelength of 800 nm used for pumping is close to the strong absorption peak of Cybesin [1, 8, 9], the stained cancerous tissues will absorb more photons than the stained normal, thus the Cybesin contained in the deep layer of the stained cancerous tissue will have less opportunity to be excited by the laser than those in the normal. The perpendicular component of the fluorescence emitted from the Cybesin contained in the stained tissue is more contributed by the photons undergoing multiply scattering. The light emitted from stained normal tissue undergoes more distance and more multiple scattering than that from the stained cancerous tissue, thus the r_1 values of the stained cancerous tissue are much larger than those of the stained normal tissue.

The fitting results also show $\tau_r^{cancer} > \tau_r^{normal}$. The larger decay time of free Cybesin molecules in cancerous prostate tissue indicates the higher local viscosity of cancerous prostate tissue. This can be understood because cancerous prostate tissue has a higher cell density [10], so

the rotating molecules have less "free" space. In addition, the dye crowds more in cancerous tissue due to higher adsorption of Cybesin as shown by the larger emission intensity. This increases the local viscosity, which is one of the reasons behind the larger decay time of Cybesin in cancerous prostate tissue compared to that in normal prostate tissue.

4. 5. Optical imaging and pathology study:

Optical imaging was studied for prostate cancer detection in pre-clinic application in the future. In order to obtain the optimal spectral imaging conditions, the samples were imaged at different wavelengths, polarizations, and depths in which the stained small pieces of the cancerous and normal tissues were embedded inside the normal host prostate tissue.

The contrast agent emission images of the samples were recorded at different pump and detection wavelengths varying from 650 nm to 850 nm. In order to compare images recorded at different wavelengths in the same polarization configuration, the perpendicular images were recorded. Fig. 4-7 shows perpendicular polarization images of stained cancerous and normal prostate tissue on the host normal prostate tissue recorded at different detection wavelengths of 750 nm to 850 nm. The salient features shown in Figs. 4-7 is that the dyed small pieces of cancer and normal tissues cannot be clearly distinguished from the image acquired with short pump and detection wavelengths at λ_{pump}=650 nm and $\lambda_{detection}$=750 nm, while the tumor can be recognized by the images obtained with longer pump and detection wavelengths at λ_{pump}=750 nm and $\lambda_{detection}$=850nm. The visibility of the dyed object increases with increasing wavelength. The measured results show that the optimized wavelength range is from 800 nm to 850 nm, which is exactly the strong fluorescence range of Cybesin. This indicates that the recorded images are indeed formed from the contrast agent emission, not from the tissue's native emission. It can be seen from the images that the cancerous tissue piece is much brighter than that of the normal

tissue piece indicating that the prostate cancer tissues adsorb Cybesin more than normal tissues because Cybesin targets the over-expressed bombesin receptors of human prostate cancer cells [1, 2, 8, 9]. On the other hand, since malignant tumors are more cell-packed [10], there will be

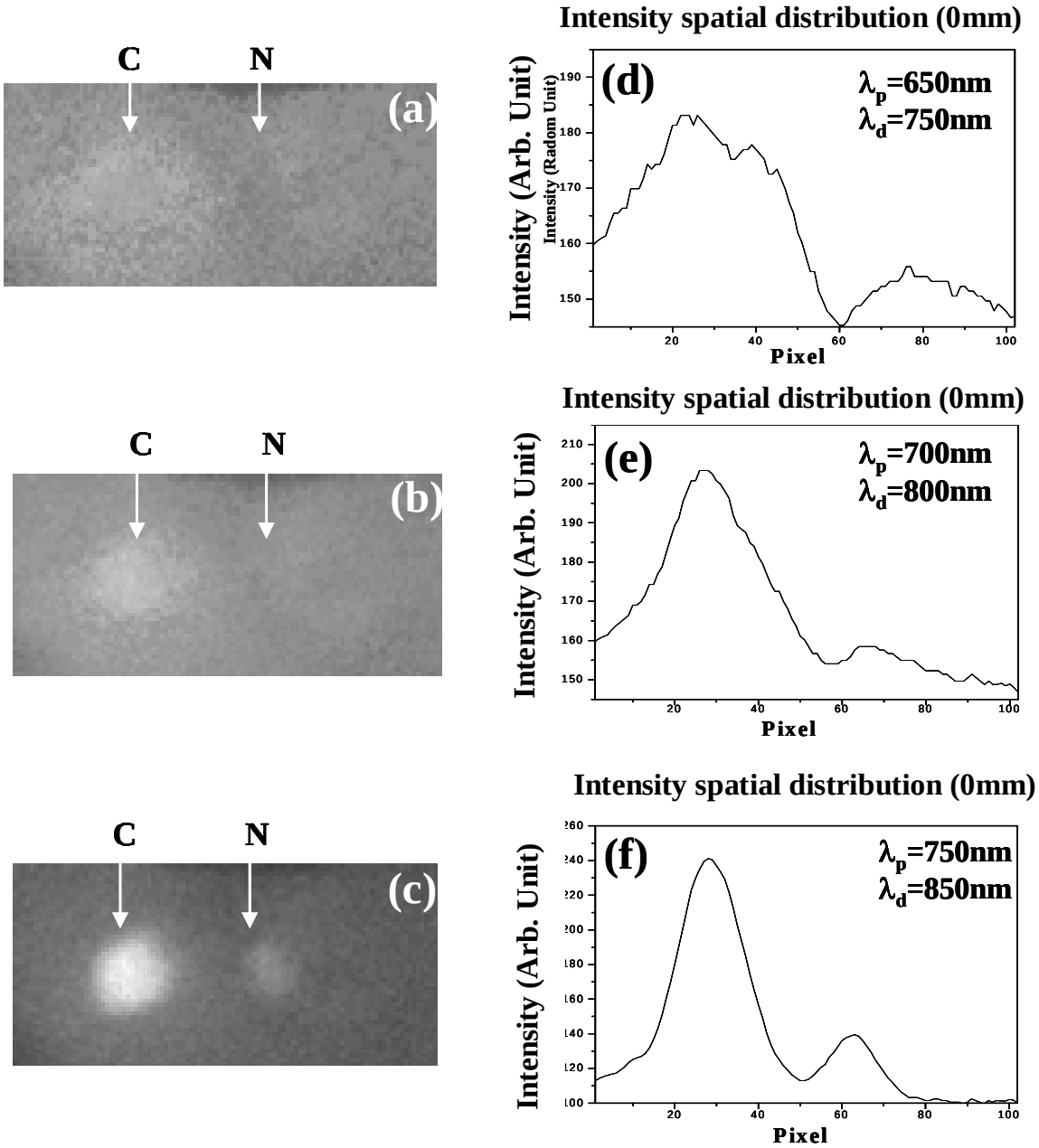

Fig. 4-7 Contrast agent emission images of a prostate cancer-and-normal tissue sample recorded at (a) λ_{pump}=650nm, $\lambda_{detection}$ =750nm, (b) λ_{pump}=700nm, $\lambda_{detection}$=800nm, and (c) λ_{pump}=750nm, $\lambda_{detection}$=850nm; (d), (e) and (f) are the cross section intensity distributions of the images of (a), (b), and (c).

more cells in cancerous area, even for same size, geometry or weight, and hence more Cybesin binding to cancerous area versus normal area. We believe that both high adsorption and density of cancer cells contribute to the large fluorescence intensity in the cancerous area, and make Cybesin a good a marker to differentiate prostate cancerous tissue from the normal tissue.

The difference between cancerous and normal tissue images can be more clearly seen from their spatial intensity distributions at the same pixel row crossing the areas of the stained cancer and normal tissues. Figs. 4-7(d), (e) and (f) show the digital spatial cross section intensity distributions of the images shown in Figs. 4-7(a), (b) and (c), respectively. The image obtained at λ_{pump}=750 nm and $\lambda_{detection}$=850 nm shows the best visibility and greatest difference between normal and cancerous tissue. Under this best imaging condition, the ratio of imaging intensity of cancerous tissue area to that of normal tissue area is found to be ~3.55.

As described in our previous study [15], the polarization preservation property of ICG and the fluorescence polarization difference imaging technique (FPDI) can be used to improve the image quality of a fluorescent object embedded in tissues. In order to determine if Cybesin has a polarization preservation property, we studied Cybesin emission images recorded at different polarization configurations. The polarization dependence of fluorescence images of the stained cancerous and normal prostate tissue surrounded by the host normal prostate tissue at λ_{pump}=750 nm and $\lambda_{detection}$=850 nm is shown in Fig. 4-8. Fig. 4-8 (a) displays the parallel image recorded when the polarization direction of P_2 in front of the CCD camera is parallel (||) to that of the illuminating beam. Fig. 4-8(b) displays the perpendicular image recorded when the polarized direction of P_2 is perpendicular ($\perp$) to that of the illuminating beam. Fig. 4-8 (c) displays the difference image obtained by subtracting the perpendicular image (Fig. 4-8 (b)) from the parallel

image (Fig. 4-8 (a)). Figs. 8-6 (d), 4-8 (e) and 4-8 (f) show the digital spatial cross section intensity distributions of the images shown in Figs. 4-8 (a), 4-8 (b) and 4-8 (c), respectively.

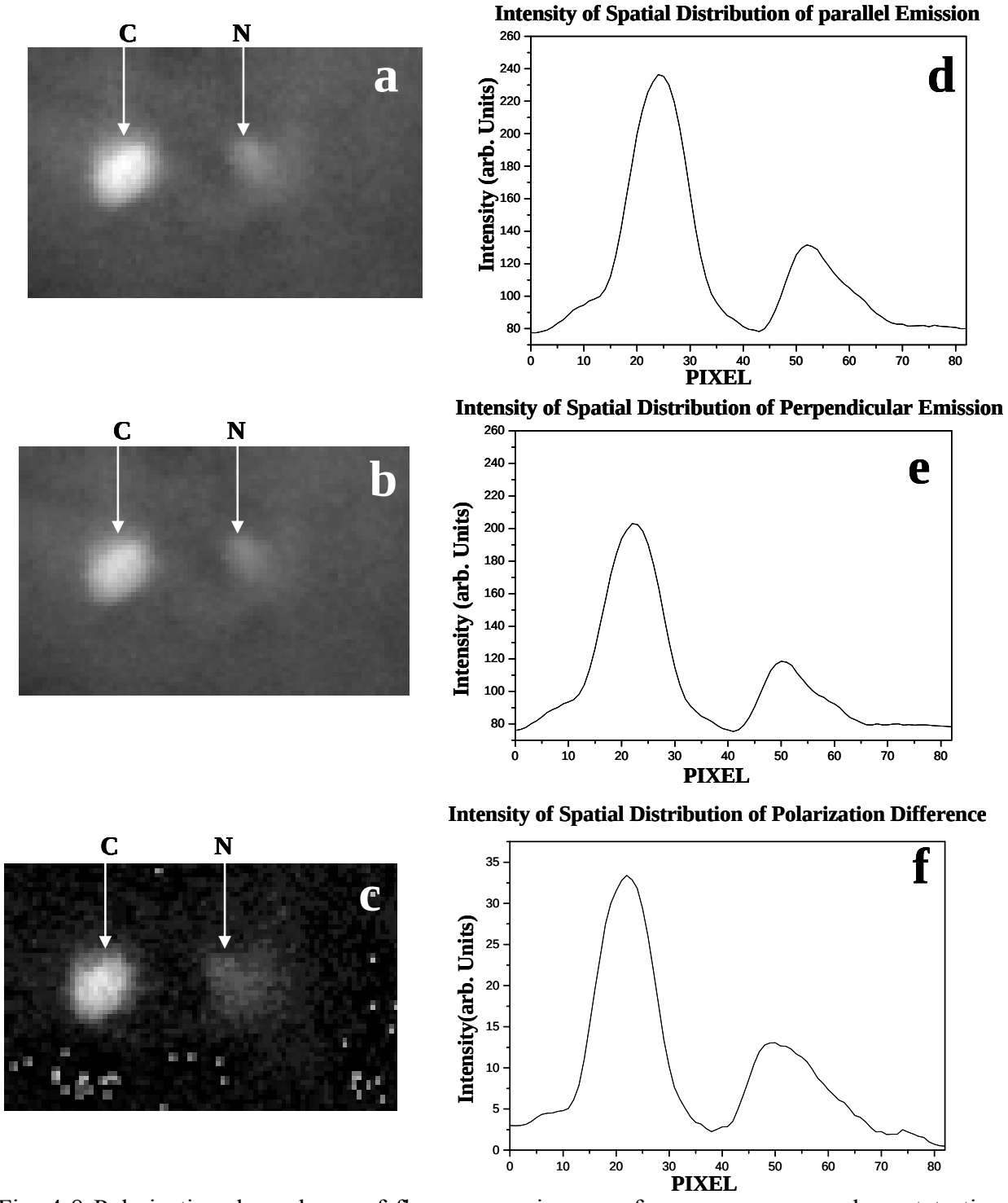

Fig. 4-8 Polarization dependence of fluorescence images of a cancerous-normal prostate tissue sample recorded at λ_{pump}=750nm, $\lambda_{detection}$=850nm when polarization direction is (a) || and (b) ⊥ to the excitation. (c) is the FPDI image obtained by subtracting (b) from (a). (d), (e) and (f) are the digital spatial cross section intensity distributions of (a), (b) and (c), respectively.

The salient features of these images and their intensity distributions are: (1) The peak intensity of the cancerous tissue of the parallel image shown in Fig. 4-8 (d) is a slight higher than that of perpendicular one shown in Fig. 4-8 (e). This difference can be explained because the light reaching the CCD camera is still partially polarized [16]. The preferred polarization direction is parallel to that of illuminating beam; and (2) the relative brightness of the stained cancerous piece in comparison with the stained normal piece for the polarization difference image shown in Fig. 4-8 (c) is obviously higher than those of the conventional polarization images shown in Figs. 4-8 (a) and 4-8 (b). To quantitatively describe the improvement of the relative brightness of the dyed cancerous area to the dyed normal tissue area for the polarization difference image, the contrasts (C) of the cancerous tissue area relative to the normal tissue area for all of the polarization and difference images were calculated. C is defined as:

$$C = (I_c - I_n) \Big/ (I_c + I_n)$$

where I_c and I_n are the local maximum values of the cancerous and normal tissue area, respectively. Using the digital data shown in Figs. 4-8 (d), (e) and (f), the contrasts for these parallel, perpendicular and polarization difference images are calculated to be 0.28, 0.26 and 0.45, respectively. These results indicate that Cybesin has a polarization preservation property similar to ICG, and the polarization difference image shown in Fig. 4-8 (c) has a better image contrast than that of the individual polarization images. The larger r_1 in Cybesin-stained cancerous tissue gives good reason for the enhancement of contrast between the cancerous and the normal area in FPDI. Due to the higher polarization anisotropy of Cybesin in cancerous tissue, the difference of $I_{\parallel}$ - $I_{\perp}$ for the Cybesin-stained cancerous tissue is larger than that in the normal tissue. Therefore, the contrast between cancerous and normal tissue areas is improved.

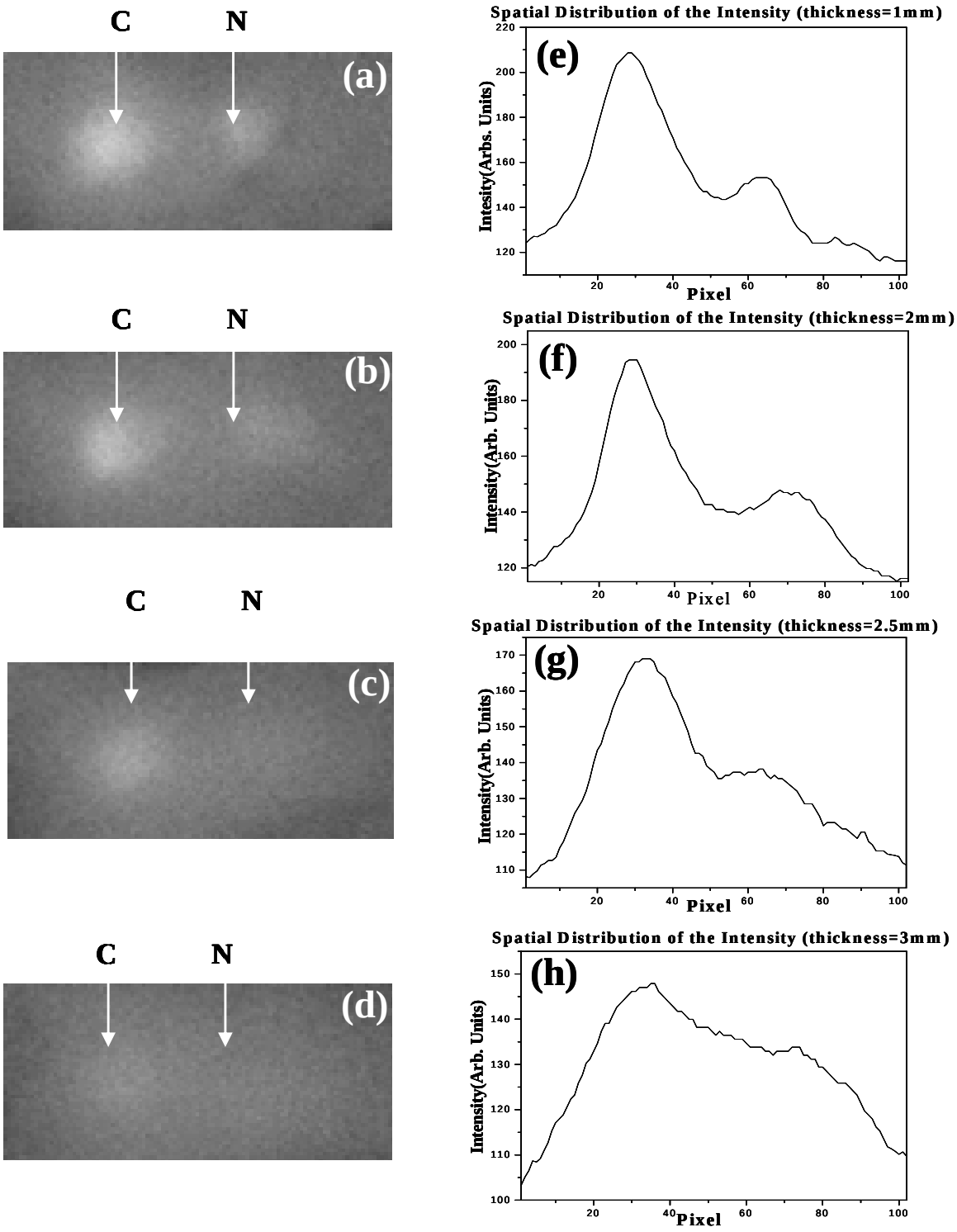

Fig 4-9 Depth-dependence of contrast agent emission images of a cancerous-normal prostate tissue sample recorded at λ_{pump}=750nm and $\lambda_{detection}$=850nm for depths of (a) ~1mm, (b) ~2mm, (c) ~2.5mm and (d) ~3 mm; (e), (f), (g) and (h) are the cross section intensity distributions of (a), (b), (c) and (d) at the same row crossing the areas.

We also investigated the depth dependence of images at λ_{pump}=750 nm and $\lambda_{detection}$=850 nm using the sandwiched structure of the prostate tissue samples. The thickness of the host normal tissue in front of the stained cancerous and normal tissue pieces was varied up to 3 mm. In order to compare images of objects at different depths in the same polarization configuration, perpendicular imaging was measured. Figs. 4-9(a) to (d) show the backscattering contrast agent emission images of the pair of stained cancerous-normal tissue pieces hidden by depths of ~1 mm, ~2 mm, ~2.5 mm and ~3 mm, respectively. Figs. 4-9 (e), (f), (g) and (h) show the spatial cross section intensity distributions of the images of Figs. 4-9(a), (b), (c) and (d), respectively. The results show that the intensity difference between normal and cancerous tissue can be clearly distinguished up to a depth of ~2.5 mm. At a depth of ~3 mm, the image is blurred, but the intensities of cancerous tissue are still stronger than that of normal tissue.

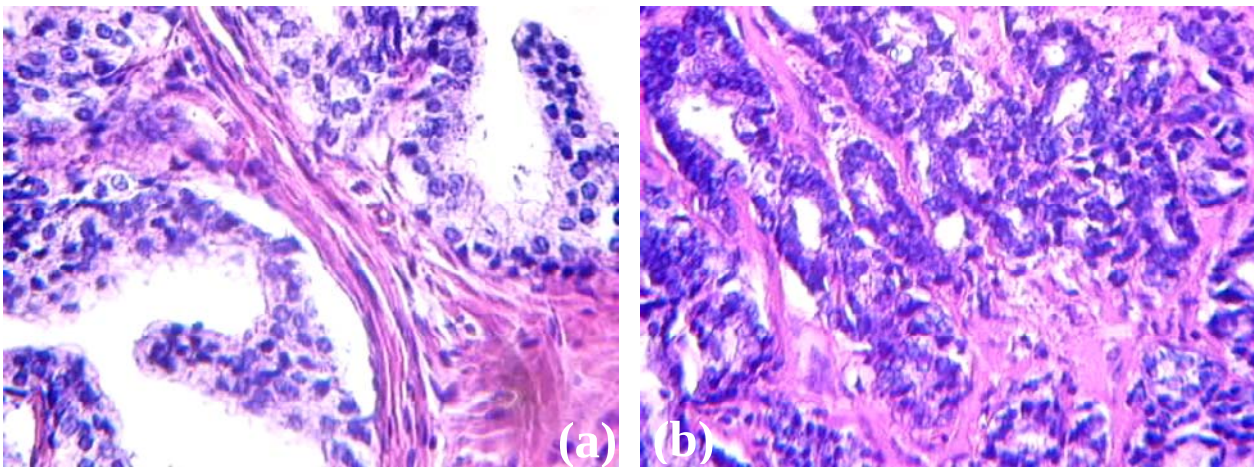

Fig. 4-10 40 times magnified microscope image of (a) the normal (b) cancerous area in a prostate tissue sample. The cancer is estimated as Gleason grade 3+4.

Pathology studies were used to verify the optical imaging measurement. The prostate tissue from which the stained normal and cancerous tissue pieces were taken was cut into a number of slides with a thickness of 250 μm at HUMC for microscopy study. The microscope images were taken using a digital electro-microscope (Mel Sobel Microscopes Ltd) and compared with the

results obtained from the optical imaging. Figs. 4-10 (a) and 4-10(b) show the low power (×40) microscope images of the normal and cancerous areas of prostate tissue, respectively.

4. 6. Chapter summary

In summary, we have developed a new time-resolved empirical analytical model to describe the emission of the receptor-targeted contrast agents, Cybesin, in prostate tissue by assuming tissue as viscous liquid. A static anisotropy component formed by the emission of prostate cell-bound Cybesin molecules (with very slow rotation), and a time-dependent anisotropy component formed by the emission of unbound Cybesin molecules (with fast rotation) were determined. This model reasonably explained the experimental results of Cybesin in cancerous and normal prostate tissues. The static anisotropy value of Cybesin in stained cancerous tissue was found to be much higher than that in stained normal tissue indicating more uptake of Cybesin in prostate cancerous tissue. The larger rotation time of Cybesin observed in cancerous tissues suggesting higher cell density in cancerous tissue compared with normal tissues. In addition, Cybesin is a sound contrast agent because it can target over-expressed bombesin receptor in cancerous tissue, and its absorption and fluorescence spectra are in the NIR "tissue optical window". Spectral imaging study of Cybesin was performed for human prostate cancerous and normal tissue. The experimental results show that prostate cancerous tissue takes up more Cybesin than normal tissue, thus Cybesin can be used as a potential marker of prostate cancer detection. The larger r_1 in Cybesin-stained cancerous tissue indicates that the fluorescence-polarization-difference-imaging (FPDI) technique was used to enhance the contrast between cancerous and normal tissue areas. Pathology studies verify the optical imaging measurement.

4.7. References

1. J. E. Bugaj, S. Achilefu, R. B. Dorshow, R. Rajagopalan, "Novel Fluorescent contrast agents for optical imaging of *in vivo* tumor based on a receptor-targeted dye-peptide conjugate platform", *J. Biomed. Opt.*, 6(2), 122-133 (2001).
2. Jean Claude Reubi, Sandra Wenger, Jacqueline Schmuckli-Maurer, Jean-Claude Schaer, and Mathias Gugger, "Bombesin receptor subtypes in human cancers: detection with the universal radioligand ^{125}I-[D-TYR^{6}, β-ALA^{11}, PHE^{13}, NLE^{14}] bombesin(6-14)", *Clin. Cancer Res.*, 8, 1139–1146 (2002).
3. G. R. Fleming, J. M. Morris and G. W. Robinson, "Direct observation of rotational diffusion by picosecond spectroscopy", *Chem. Phys.*, 17, 91-100 (1976).
4. G. Porter, P. J. Sadkowski and C. J. Tredwell, "Picosecond rotational diffusion in kinetic and steady state fluorescence spectroscopy", *Chem. Phys. Lett.*, 49, 416-420 (1977).
5. R. D. Spencer and G. Weber, "Influence of Brownian rotations and energy transfer upon the measurements of fluorescence lifetime". *J. Chem. Phys*. 52, 1654-1663 (1970).
6. F. Pellegrino, "Energy transfer in the primary stages of the photosynthetic process investigated by picosecond time resolved fluorescence spectroscopy", A dissertation thesis of the City University of New York, Chapter 9, 270-315 (1981).
7. F. Pellegrino, P. Sekuler and R. R. Alfano, "Picosecond fluorescence kinetics and polarization anisotropy from anthocyanin pigment", *Photobiol. and Photo Biophys.*, 2, 15-20 (1981).
8. Y. Pu, W. B. Wang, S. Achilefu, B. B. Das, G. C. Tang, V.Sriramoju, and R. R. Alfano "Time-resolved fluorescence polarization anisotropy and optical imaging of in cancerous and normal prostate tissues", *Opt. Commun*, 274, 260-267 (2007).

9. Y. Pu, W. B. Wang, G. C. Tang, F. Zeng, S. Achilefu, J. H. Vitenson, I. Sawczuk, S. Peters, J. M. Lombardo and R. R. Alfano, "Spectral polarization imaging of human prostate cancer tissue using a near-infrared receptor-targeted contrast agent", *Technol. Cancer Res. Treat.*, 4 429-436 (2005).
10. D. F. Gleason and G. T. Mellinger, "Prediction of prognosis for prostate adenocarcinoma by combined histological and clinical", *J. Urol*, 111, 58-64 (1974).
11. D. A. Beysens, G. Forgacs, J. A. Glazier, "Cell sorting is analogous to phase ordering in fluids", *Proc. Natl. Acad. Sci. USA.*, 97, 9467–9471 (2000).
12. Jean Paul Rieu1 and Yasuji Sawada, "Hydrodynamics and cell motion during the rounding of two dimensional hydra cell aggregates", *Eur. Phys. J. B*, 27, 167-172 (2002).
13. M. A. Dresner, P. J. Rossman, S. A. Kruse and R. L. Ehman, "MR Elastography of the Prostate", *ISMRM 99 CDs*, http://cds.ismrm.org/ismrm-1999/PDF2/526.pdf.
14. R. Cubeddu1, D. Comelli, C. D'Andrea, P. Taroni and G. Valentini, "Time-resolved fluorescence imaging in biology and medicine", *J. Phys. D: Appl. Phys.* 35, R61–R76 (2002).
15. W. B. Wang, S. G. Demos, J. Ali and R. R. Alfano, "Imaging fluorescence objects embedded inside animal tissue using a polarization difference technique", *Opt. Commun.,* 142, 161-166 (1997).
16. L. Wang, P. P. Ho, C. Liu, G. Zhang and R. R. Alfano, "Ballistic 2-D imaging through scattering wall using an ultrafast Kerr gate," *Science* 253, 769-771 (1991).

Chapter 5
Time-resolved fluorescence polarization dynamics and optical imaging of Cytate: a prostate cancer receptor-targeted contrast agent

5. 1. Introduction:

Biological studies have indicated that somatostatin receptors (SSTR), which have five subtypes, are over-expressed in human prostate tumor [1]. It was reported that each subtype of SSTRs could be identified on the basis of molecular modeling of its corresponding peptide conjugate [2]. The previous investigation showed that a small ICG-derivative dye-peptide, Cytate could be used for effectively targeting SSTR-rich kidney malignant tumor in the animal model because of the high affinity of Cytate for the SSTRs [3].

In this chapter, time-resolved fluorescence and NIR imaging studies for Cytate, an optical contrast agent for human prostate cancer detection is investigated. The absorption and fluorescence spectra of Cytate were measured in the wavelength region from 650 nm to 900 nm and 1100 nm respectively. Time-resolved fluorescence polarization measurements were performed on Cytate solution and Cytate-stained cancerous and normal prostate tissues. Fluorescence imaging of two small pieces of Cytate-stained normal and cancerous prostate tissues (one for each) sandwiched between large pieces of normal prostate tissues was accomplished. The experimental data obtained from a Cytate solution were fitted using a time-dependent fluorescence depolarization model [4-6]. The resultant parameters from Cytate fluorescence in solution and in prostate tissue were compared for understanding the effect of the rotational degree of freedom of Cytate in tissue medium. The analytical model dealing with high viscous media developed in chapter 4 was applied to describe the time-resolved fluorescence kinetics and polarization anisotropy of Cytate in human prostate tissue. The differences of

fluorescence and image intensities between Cytate-stained cancerous and normal prostate tissues showed preferential uptake of Cytate in the human cancerous prostate tissue.

5. 2. The tumor-targeted mechanism of Cytate and its absorption and fluorescence spectra

Cytate used in this study was prepared by Achilefu's group at the Washington University School of Medicine. The molecular structure of Cytate is shown in Fig. -2(b). It is mainly composed of ICG and the SSTR ligand, which delivers the ICG to the receptors presented in the tumor [3]. The synthesis of this contrast agent was reported elsewhere [3]. The advantages of this receptor-targeted peptide-dye contrast agent include enhancing localization in tumors, rapid clearance from the non-target (normal) tissue, possibility of preparing a library of peptides for rapid identification of bioactive molecules [3] and keeping the spectral advantages in the NIR "tissue optical window". It was reported that the small ICG-derivative dye-peptide, Cytate, preferentially localized for over 24 hours in tumor with over-expressed somatostatin receptors in animal model [3].

Human prostate is a highly hormone-sensitive organ. Numerous studies have found that somatostatin is directly or indirectly responsible in the regulation of prostate function [7]. Somatostatin is a small cyclic peptide. In addition to playing an important regulatory role of hormones, this peptide controls cell proliferation in cancerous tissues [1]. Therefore, tumors arising from somatostatin-needed tissues frequently express a high density of somatostatin receptors [8]. Somatostatin receptors are known for predominant expression in several human adenomas such as somatotroph and lactotroph adenomas, and neuroendocrine tumor including human prostate cancer [1, 8, 9], and can be used as a basis for *in-vivo* tumor targeting. Several control experiments were carried out to determine whether expression of somatostatin receptors is up regulated in human prostate malignant cells [10]. Among them, Hansson *et al* have found

by using fluorescing-labeled SSTR octreotide-binding probes by immunochemical analysis that SSTR2 and SSTR4 are over-expressed in human prostate cancerous cells [10]. And Bugaj *et al* have shown that the ligand of Cytate (ICG-derivative dye-peptide, Cypate-Octreote Peptide Analogue Conjugate) to target somatostatin receptors in animal model is octreotide [3]. The combination of molecular probes and optical imaging methods has the potential to provide a better cancer detection technique with high sensitivity and specificity. The successful detection of Cytate in somatostatin receptors over-expressed in tumors in animal model [3] motivated us to use Cytate to target the over-expressed specific SSTR2 and SSTR4 in human prostate cancerous cells. The basis of using Cytate as a prostate cancer contrast agent depends on two factors: (1) the high affinity of octreotide (ligand of Cytate) for the somatostatin receptors [3], and (2) the over-expression of SSTR2 and SSTR4 in human prostate cancer cells [10].

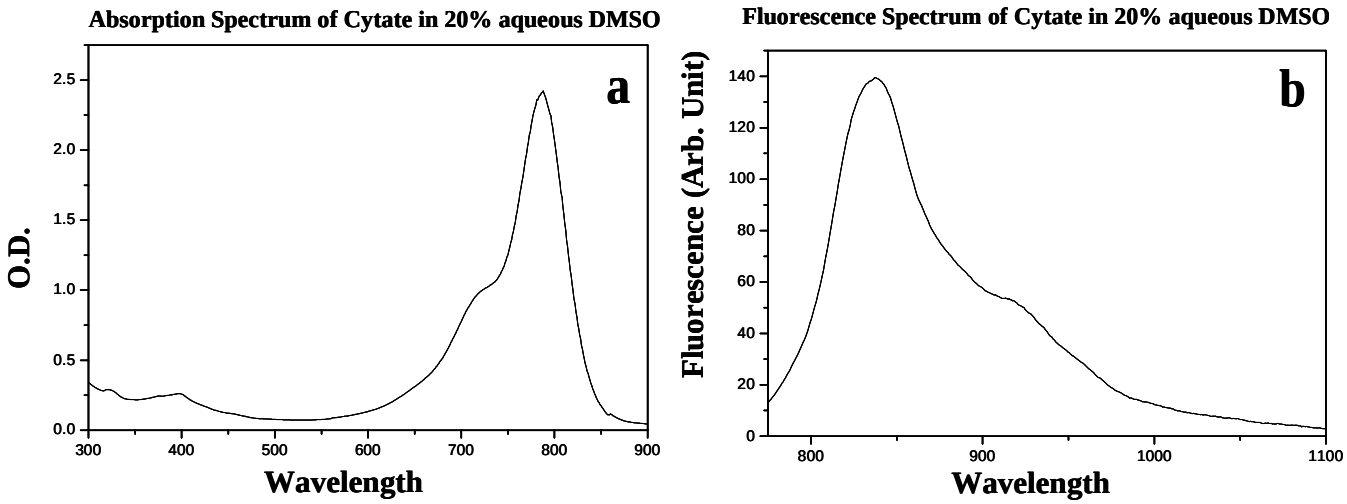

Fig. 5-1 (a) Absorption and (b) fluorescence spectra of Cytate in 20% aqueous DMSO. The fluorescence was obtained with an excitation of a 680 nm diode laser beam.

Cytate was solvated in 20% aqueous Dimethyl Sulfoxide (DMSO). The absorption spectrum of Cytate in DMSO solution was measured using a Perkin-Elmer Lambda 9 UV/VIS/NIR Spectrophotometer in the spectral range of 300 nm to 900 nm. The fluorescence spectrum of Cytate was measured using a far-red to NIR spectral setup excited by a 680 nm diode laser.

Fluorescence emission from the sample was focused on the entrance slit of a SPEX Minimate 0.25-m monochromator (spectrometer) and detected by a Hamamatsu P394A PbS detector mounted at the exit slit of the monochromator. Signals from the detector were recorded by a PAR Model HR-8 lock-in amplifier connected to a computer [11].

Figs. 5-1(a) and (b) show the measured absorption and fluorescence emission spectra of Cytate, respectively. The absorption band of Cytate ranges from 680 nm to 830 nm with a shoulder peak at ~720 nm and a strong peak at 789 nm. The fluorescence spectrum covers from 800 nm to 950 nm with a main peak at 837 nm and a weak peak at 913 nm. The results show that Cytate possesses the spectral advantages of ICG, i.e., the fluorescence and the absorption ranges are in the NIR range of the "tissue optical window" [11].

5. 3. Experimental methods for time-resolved and imaging measurements

The experimental arrangement for the time-resolved fluorescence measurements is described in our previous work in chapter 4 as Fig 4-2 [12]. Pulses of 130 fs duration at 800 nm from a Coherent Mira 900 mode-locked Ti: Sapphire laser at a repetition rate of 82 MHz were used to pump the samples (Cytate solution and Cytate-stained cancerous or normal prostate tissues). The fluorescence emission was collected by a large diameter lens with a focal length of 5 cm and directed onto the slit of a synchroscan streak camera with a temporal resolution of 10 ps. A long pass filter and an 800nm notch filter were used to cut off the excitation wavelength. Two polarizers, P_1 and P_2, were used as a polarizer and an analyzer, respectively. The polarization direction of P_2 was varied from 0^o to 90^o with respect to that of P_1 to record the intensity profiles of parallel and perpendicular polarization components of the fluorescence. The temporal profiles recorded by a silicon intensified target (SIT) of the streak camera were analyzed to obtain temporal and polarization information [12].

The Cytate solution used for time-resolved fluorescence study was prepared by adding Cytate into 20% aqueous Dimethyl Sulfoxide (DMSO). Six cancerous and six normal prostate tissue samples from six different patients obtained from the National Disease Research Interchange (NDRI) and the Co-operation Human Tissue Network (CHTN) were used for the time-resolved fluorescence and optical imaging measurements under the IRB approval at CCNY (City College of New York). Each cancerous tissue had a corresponding normal tissue sample from the same patient used for the control experiment. Samples were neither chemically treated nor were frozen prior to the experiments. Cancerous and normal prostate tissues used for the time-resolved fluorescence measurements were cut into ~2 cm × ~1 cm × ~0.5 cm (length × width × thickness) pieces. For each prostate tissue sample, measurements were performed at six different locations to get an average value. The cancerous and normal prostate tissue samples were soaked in the same Cytate-DMSO (20% aqueous Dimethyl Sulfoxide) solution with a Cytate concentration of ~3.2×10^{-6} M for fifteen minutes. Then the samples were put into sodium phosphate buffer (Sigma-Aldrich) to wash off the unbound Cytate. All the sample preparations and measurements were performed at room temperature.

The schematic diagram of the NIR optical spectral polarized imaging setup is shown as backscattered geometry of Fig. 3-1(b) of chapter 3 in our previous work [11]. Light from a white light source is used to illuminate the prostate tissue sample with average power of about 50 $\mu W/cm^2$, which is much lower than the critical illumination level given by FDA. The illumination wavelengths are selected by wide-band pass filters varying from 550 nm to 900 nm with FWHM=40 nm placed on a multiple filter wheel, which can be rotated to the desired filter position by computer control. A CCD camera records images formed by light emitted from the sample. The detection wavelength is selected by rotating a similar set of band pass filters placed

on the second multiple filter wheel located in front of the detector. Polarizer P_1 is used to ensure linear polarization of the illumination and polarizer P_2 is placed in the front of the CCD for selecting the detection polarization. For emission light imaging, the wavelengths of the band pass range of the detection (imaging) filter is longer than that of the illumination so that the pump light is blocked, and only the light emitted from the sample is collected by the CCD camera [13]. The spatial resolution of the CCD camera is 20 μm/pixel [12].

The prostate tissue samples used for the imaging measurements consisted of a small piece of cancerous prostate tissue and a small piece of normal prostate tissue. They were first soaked in the same Cytate-DMSO (20% aqueous Dimethyl Sulfoxide) solution with a Cytate concentration of ~3.2×10^{-6} M for fifteen minutes, and then put into sodium phosphate buffer to wash off the unbound Cytate. The stained cancerous and normal tissues were then covered by a large piece of ~0.5 mm thick normal prostate tissue [12].

5. 4. Experimental results and discussion

5.4.1. Time-resolved fluorescence polarization anisotropy of Cytate solution

The measured temporal profiles of the fluorescence emitted from Cytate in DMSO solution for two polarization directions, parallel and perpendicular to the polarization of the excitation at 800 nm are shown in Fig. 10-3 (a). The dash- and dot-line profiles represent the parallel [$I_{\parallel}(t)$] and perpendicular [$I_{\perp}(t)$] components, respectively. The time-dependent polarization anisotropy can be calculated using the following equations [4, 5]:

$$r(t) = \frac{I_{\parallel}(t) - I_{\perp}(t)}{I_{\parallel}(t) + 2I_{\perp}(t)}. \qquad (5.1)$$

The dot line in Fig. 5-3 (b) displays the time evolution of r(t) as calculated. The decay behavior of r(t) reflects the dipole reorientation of Cytate in solvent since the degree of

polarization of the fluorescence depends on the rotation time and fluorescence lifetime of the molecules [4, 5]. If molecular rotation is much faster compared to the florescence lifetime, the emitting molecules become randomly oriented very quickly, resulting in depolarized emission. If molecules rotate much more slowly in comparison with the fluorescence decay time, then the emission remains strongly polarized. Polarization anisotropy found in our case suggests that rotation time is on the same order as fluorescence lifetime.

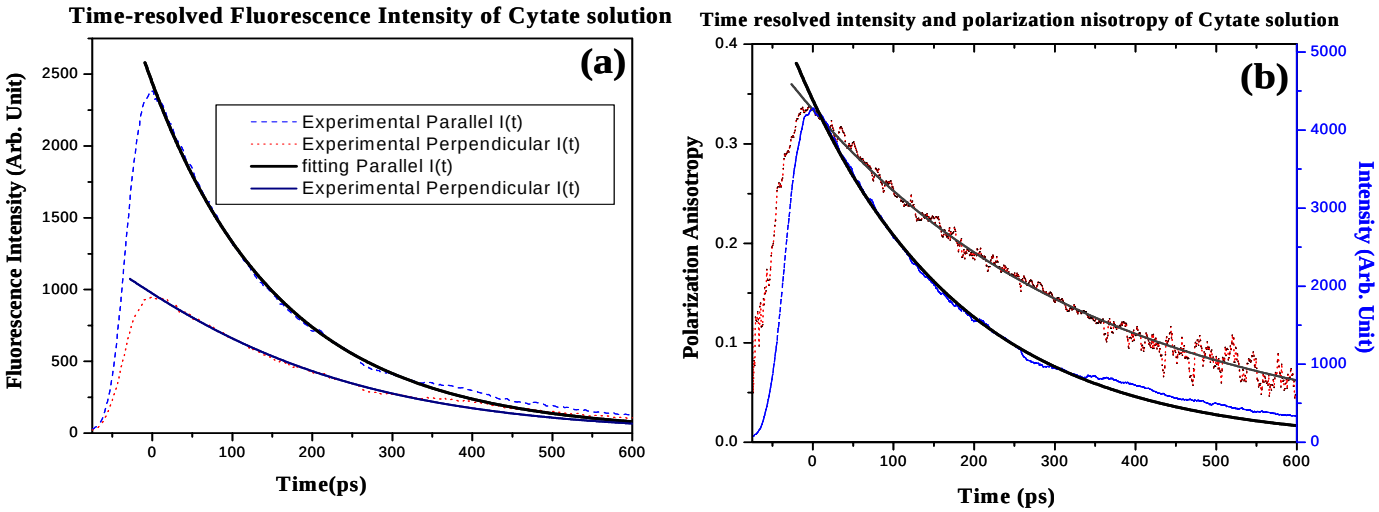

Fig. 5-2 (a) The time-resolved fluorescence components with ∥ (dash) and ⊥ (dot) to the exciting light. (b) Total intensity (dash) and polarization anisotropy (dot) calculated using the equation (5.5) and equation (5.1) shown in this chapter, respectively. All the fitting curves (solid) are calculated using the analytical model described in chapter 4 and shown as solid line.

In Fig. 5-2 (a), the main differences between parallel and perpendicular components are: (1) the intensity of $I_{\parallel}$ is greater than that of $I_{\perp}$ for all decay times. The peak intensity of the parallel component $I_{\parallel}(0)$ is almost three times stronger than that of the perpendicular component $I_{\perp}(0)$. This indicates the polarization preservation nature of Cytate. (2) There is a distinct difference between the decay slopes of the two components, which can be seen clearly by normalizing the peak of the perpendicular component to that of the parallel component as shown by the thin-dashed line in Fig. 5-2 (a). Since the rotation time and fluorescence lifetime of Cytate are on same timescale in our case, the overall decay time is affected by both re-orientation of molecules

and fluorescence decay kinetics. Since the parallel and perpendicular components emitted from Cytate have same fluorescence lifetime, the fast decay of the parallel component and slow decay of the perpendicular component are caused by the Cytate molecular rotation.

The experimental value of *r(0)* obtained from the data shown in Fig. 5-2 (b) is ~0.33, which is in reasonable agreement with the theoretical value of 0.4 [4, 5]. Flemming [4] and Porter [5], measured values of *r(0)* was always smaller than its theoretical value due to (1) the rapid internal motions of the macromolecules since the macromolecules must contain a flexible substructure that can undergo rapid depolarization rotation; (2) scattering of light in tissues; and (3) birefringence of the quartz cell containing the samples. This result indicates that the transition dipole moments of Cytate molecules in solution are randomly oriented, and the depolarization effects of Cytate in 20% aqueous DMSO solvent can be confined to molecular rotations and to the trivial effect of initial randomness [4]. The polarization anisotropy peak value, r_0, and the rotation time, τ_r of Cytate in solution can be obtained by fitting the experimental data of *r(t)* shown in Fig. 5-2 (b) using equation (4.3) in chapter 4. The fluorescence life time τ_f can be obtained fitting the experimental data of the total intensity *I(t)* shown in Fig. 5-3 (b) using equation (4.5) in chapter 4. The best fit was obtained with the parameter values of r_0=0.337±0.032 τ_f=176±7ps and τ_r=352±21ps, and the fitting curve is shown by the solid line in Fig. 5-2.

5.4.2 Time-resolved fluorescence polarization anisotropy of Cytate contained in stained cancerous and normal prostate tissues

Six Cytate-stained cancerous and six Cytate-stained normal prostate tissue samples from six patients were used for the time-resolved fluorescence measurements. For each sample, measurements were performed on six or more different locations for statistical analysis. Before

the measurements were performed, the tissue sample was carefully checked to determine the hard parts to locate the small region of the cancerous tissue. This is acknowledged to be a simple way to find the location of malignancy [14]. Two typical time-resolved fluorescence intensity profiles for the cancerous and normal prostate tissue samples stained with Cytate are displayed in Fig. 5-3 (a) and (b), respectively. The dash and dot line profiles represent the parallel and the perpendicular components of emission from stained cancerous tissue, respectively.

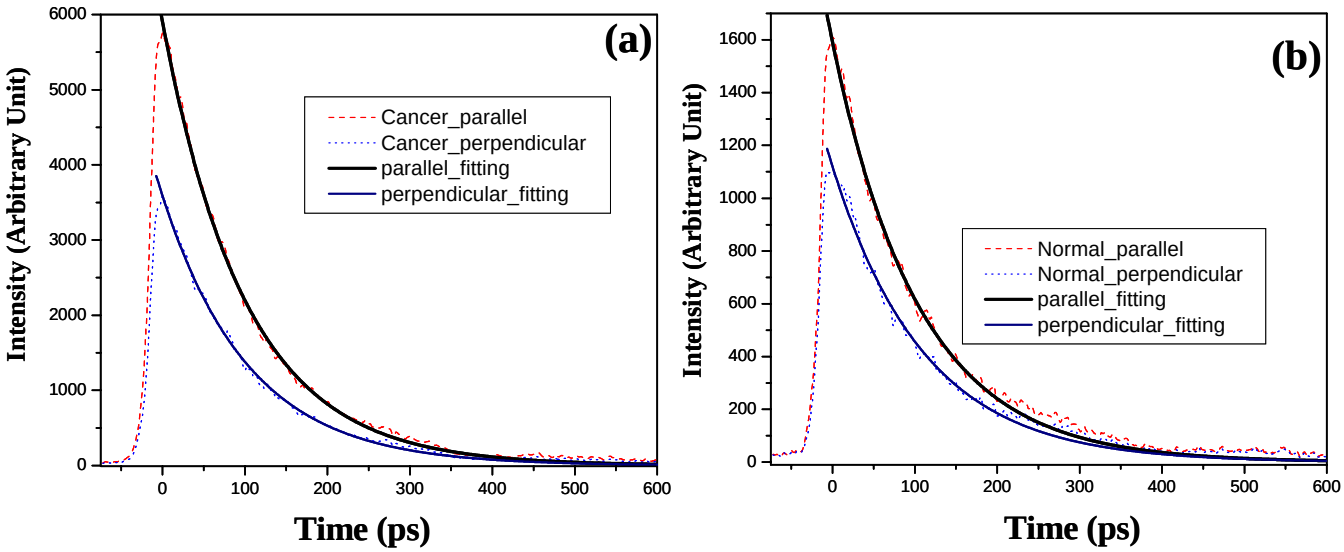

Fig. 5-3 The time-resolved polarized fluorescence intensity of light emitted from Cytate stained (a) cancerous and (b) normal prostate tissues. The dash- and dot-line profiles display the parallel and perpendicular components emitted from stained tissue, respectively. The solid lines display the fitting curves calculated using equation (5. 2) for parallel component and equation (5. 3) for perpendicular component, respectively.

One of the important features of the temporal profiles is that $I_{\parallel}$ is greater than $I_{\perp}$ throughout the decay period for both cancerous and normal tissues. At the peak position, $I_{\parallel}^{cancer}(0)$ is ~1.60 times stronger than $I_{\perp}^{cancer}(0)$, and the ratio of $I_{\parallel}^{normal}(0)$ to $I_{\perp}^{normal}(0)$ is ~1.46. This indicates that the fluorescence emitted from both Cytate-stained cancerous and normal prostate tissues show the polarization preservation property, although the ratio of $I_{\parallel}(0)/I_{\perp}(0)$ is smaller than that of Cytate solution. Another salient feature of the profiles in Fig. 5-3 is the higher emission intensity

of the stained cancerous tissue compared to the stained normal tissue throughout the Cytate emission range. Using the data in Fig. 5-3, for the parallel polarization configuration, the ratio of peak fluorescence intensity of the Cytate-stained cancerous tissue to that of the normal tissues was found to be ~3.57, while for the perpendicular configuration, the ratio was ~3.25. To illustrate the higher intensity observed in Cytate-stained cancerous prostate tissue, the total time-resolved intensities I(t) of Cytate in stained prostate tissue were calculated using equation of $I(t)=I_{\parallel}(t)+2I_{\perp}(t)$, and the results are displayed in Figs. 5-4 (a). The obviously higher intensity in Cytate-stained cancerous prostate tissue indicates that cancerous prostate tissue has higher Cytate intake than normal tissue.To extract and compare the time-resolved parameters of Cytate in cancerous and normal prostate tissues, the temporal profiles of the polarization anisotropy *r(t)* from Cytate in stained cancerous (thin-solid line) and normal (thin-dashed line) prostate tissues were calculated and the results are displayed in Fig. 5-4 (b) using equation (5. 1) and the measured values of $I_{\parallel}(t)$ and $I_{\perp}(t)$.

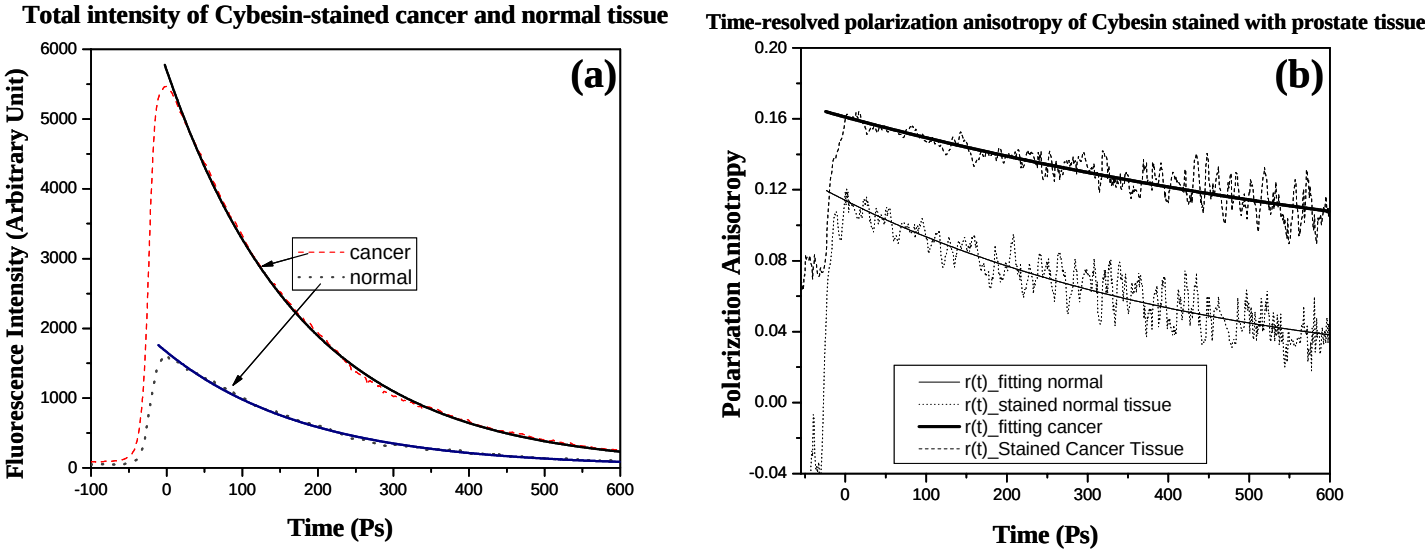

Fig. 5-4 (a) The total intensity of Cytate-stained cancerous (dash) and normal (dot) prostate tissue obtained using the data of Figs. 5-4 (a) and (b), and equation (4. 5) in the chapter 4; (b) Time-dependent emission anisotropy of for Cybtate-stained cancerous (dash) and normal (dot) prostate tissues calculated using equation (5. 1) and the measured data shown in Figs. 5-4 (a) and (b). The solid lines are the fitting results using the analytical model in chapter 4.

The interesting features of *r(t)* curves shown in Fig. 5-4 (b) are: (1) the profiles of Cytate-stained tissue show a flatter decay compared to that of Cytate solution; and (2) the values of the polarization anisotropy of Cytate in the stained cancerous tissue are always larger than that of the stained normal tissue. The peak intensity values of *r(0)* for cancerous and normal tissues were found to be: $r(0)^{cancer}=0.167\pm0.021$ and $r(0)^{normal}=0.133\pm0.011$ presented as mean values ± standard deviations. These results indicate that the Cytate-stained cancerous tissue shows a better polarization preservation property than the Cytate-stained normal prostate tissue. The polarization preservation properties of Cytate-stained prostate tissue can be used to enhance the image contrast between cancerous and normal prostate tissue areas combining with fluorescence-polarization-difference-imaging (FPDI) technique [11, 12, 15].

The value of *r(0)* for a dye solution depends on the viscosity of the solvent [16] and binding which restricts the motion.. Above a critical value of the viscosity of about 3,000 Poise, a normalized orientation distribution function was used as a model for fluorescent molecules instead of random distribution [16]. By applying this distribution function, a value of r(0)=0.1039 was calculated for the condition of the viscosity greater than 3,000 Poise [12, 16]. It was also reported that biological living tissue might mimic the behavior of viscous liquids [17]. The viscosities of biological tissues, including prostate tissue, were reported to be much higher than 3,000 Poise [18]. If the case of Cytate in prostate tissue is considered as a fluorescent dye in a "very high viscosity liquid", the anisotropy r(0) should be expected to be in the range between ~0.10 and ~0.12.

The physical model developed from our previous study in chapter 4 [12] on Cybesin (another NIR contrast agent used to target bombesin receptor that is also over-expressed in prostate tumors) suggests that the time-resolved fluorescence polarization anisotropy *r(t)* of the emission

from NIR fluorescent dye contained in stained human prostate tissues can be considered to have two components: (1) static anisotropy component caused by the emission from the tissue cell-bonded Cytate molecules without rotation; (2) a time-dependent anisotropy component formed by the emission from the un-bound Cytate molecules with rotation in the body fluid of prostate tissue [12]. These assumptions are reasonable because a tissue cell is too massive to rotate compared to a Cytate molecule. This empirical model was developed to describe the time-resolved fluorescence kinetics and polarization anisotropy emitted from contrast agent stained tissues [12]. Using this model, the temporal polarized fluorescence parallel and perpendicular component can be described as:

$$I_{\parallel}(t) = \frac{I_0}{3}\exp(-\frac{t}{\tau_f})\left(1+2r_1+2r_0\exp(-\frac{t}{\tau_r})\right), \quad (5.\ 2)$$

$$I_{\perp}(t) = \frac{I_0}{3}\exp(-\frac{t}{\tau_f})\left(1-r_1-r_0\exp(-\frac{t}{\tau_r})\right), \quad (5.\ 3)$$

Substituting equations (5. 2) and (5. 3) into equation (5. 1), the time-dependent polarization anisotropy of contrast agents can be written as:

$$r(t) = r_1 + r_0\exp(-\frac{t}{\tau_r}) \ . \quad (5.\ 4)$$

Introducing equation (10-2) and (10-3) into $I(t)=I_{\parallel}(t)+2I_{\perp}(t)$, the total time-resolved fluorescence intensity can be obtained as:

$$I(t) = I_{\parallel}(t) + 2\,I_{\perp}(t) = I_0\exp(-\frac{t}{\tau_f}). \quad (5.\ 5)$$

where $\exp(-\frac{t}{\tau_f})$ is the temporal decay caused fluorescence dynamics of the fluorophore itself, $r_0\exp(-\frac{t}{\tau_{rot}})$ is the time-dependent portion of the polarization anisotropy induced by the "free"

Cytate molecules in the fluid of prostate tissue, τ_r is the rotation time of the "free" Cytate in prostate tissue, r_0 is the peak value of the polarization anisotropy of the "free" Cytate molecules, and r_1 is the static portion of the polarization anisotropy induced by the cell-bond Cytate molecules in prostate tissue. The fluorescence life time of Cytate: τ_f in tissue can be obtained by fitting the experimental data of I(t) shown in Fig. 10-5 (a) using equation (10-5). The three parameters of τ_{rot}, r_0 and r_1 can be obtained by fitting the experimental data of r(t) shown in Fig. 5-5 (b) using equation (5. 4).

The best fitting curves for I(t) and r(t) of Cytate-stained cancerous (thick-solid line) and normal (thin-solid line) prostate tissues are shown in Fig. 5-4 (a) and (b). The fitting results yielded the following parameters: τ_f=118±3.7ps, τ_r=900±180ps, r_0=0.115±0.012 and r_1=0.062±0.013 for Cytate in stained cancerous prostate tissue; and τ_f=123±4.9ps, τ_r=550±140ps, r_0=0.109±0.030 and r_1=0.014±0.004 for Cytate in stained normal tissue. Substituting these data into equation (5. 2) and (5. 3) of the time-resolved fluorescence polarized parallel and perpendicular component, the fitting curves of $I_{\parallel}(t)$ [thick-solid line] and $I_{\perp}(t)$ [thin-solid line] for cancerous and normal tissues are displaying Fig. 5-3 (a) and (b), respectively. These curves are in reasonable agreement with our experimental data.

The fitting results yield that $r_1^{cancer} > r_1^{normal}$. This can be understood from the fact that the perpendicular component of the fluorescence emitted from cell-bond Cytate molecules is mainly contributed by the photons undergoing multiple scattering [12, 15]. Since the excitation wavelength of 800 nm is close to the strong absorption peak of Cytate and cancerous prostate tissue has higher Cytate intake than normal tissue, the stained cancerous tissue region would absorb more photons than the stained normal tissue regions. Light from same excitation source

would go deeper in normal prostate tissue than in cancerous tissue. As a result, the fluorescence from normal prostate tissue comes from the Cytate molecules embedded in deeper tissue layers than those in the cancerous prostate tissue [12]. The light emitted from stained cancerous tissue area undergoes less multiple scattering than that from the stained normal tissue. As a result, the degree of polarization and the value of r_1 for the stained cancerous tissue region are much larger than that of the stained normal tissue region [12].

The fitting results also show that $\tau_{rot}^{cancer} > \tau_{rot}^{normal}$. The larger decay time of free Cytate molecules in cancerous prostate tissue indicates the higher local viscosity of cancerous prostate tissue due to high density and decreasing interstitial spacing between cells. The higher density of cancerous cells can be recognized by the nature of evolution of malignant tumor [14]. First tumor grows in volume; and when it reaches some kind of confining volume, the mechanical pressure increases its cell density. When the tumor cell density exceeds a certain compaction maximum, invasion starts [14, 19]. The tumor grading system for prostate cancer includes well-known five Gleason Grades, usually denoted as stages 1-5 [20]. The pattern of Gleason Grade 1 (corresponding to early stage) consists of a circumscribed mass of evenly placed uniform glands. With grade advances, the cancer cells proliferate and begin to merge into "island" [20]. This pattern appears at Grade 3 and is obvious at Grade 5 [20]. The microscopic histological images shown in our previous work [11] also indicate the "island" structure and high density of cancerous cell. The higher cell density in cancerous prostate tissue [14, 19, 20] gives the molecules less "free" rotation space [12, 14, 20]. In addition, the dye crowds more in cancerous tissue due to higher adsorption levels of bound Cytate as shown by the larger emission intensity in Fig. 5-4 (a). The crowding dye-chains form a compact or contracted coil in which the dye is embedded [21]. This effect increases the local viscosity [21], which in our view is the reason

behind the larger decay time of Cytate in cancerous prostate tissue compared to that in normal prostate tissue samples.

5. 5. Optical spectral polarized imaging

Diagnostic potential of optical spectral imaging for prostate cancer detection may be realized by making the use of the preferential uptakes of Cytate in cancerous prostate tissue. Furthermore, the polarization preservation property of Cytate in prostate tissues needs to be investigated if it can be used to enhance the imaging contrast between cancerous and normal tissue areas using fluorescence polarization difference imaging techniques (FPDI) [11, 15]. In the imaging measurements, a small piece of cancerous prostate tissue and a small piece of normal prostate tissue stained with Cytate covered by a large piece of normal prostate tissue with ~ 0.5mm thickness were investigated. The polarized fluorescence images of a Cytate-stained cancerous and a normal prostate tissue sample recorded at λ_{pump}=750 nm and $\lambda_{detection}$=850 nm are shown in Fig. 5-5. Fig. 5-5 (a) displays the parallel image recorded when the polarization direction of detection is parallel (||) to that of the illuminating beam. Fig. 5-5 (b) displays the perpendicular image recorded when the polarization direction of detection is perpendicular (⊥) to that of the illuminating beam. The FPDI technique was used to enhance the contrast between cancerous and normal tissue area. Fig. 5-5 (c) displays the difference image obtained by subtracting the perpendicular image (Fig. 5-5 (b)) from the parallel image (Fig. 5-5 (a)). Figs. 5-5 (d), (e) and (f) show the digital spatial cross section intensity distributions of the images shown in Figs. 5-5 (a), (b) and (c), respectively.

To quantify the difference, the intensity of the cancerous or normal area is defined as $I_c = I_c^{max} - I_{background}$, and $I_n = I_n^{max} - I_{background}$, respectively, where $I_{background}$ is the background

intensity data and I_c^{max} and I_n^{max} is maximum intensity of the cancerous or normal area shown in Figs. 5-5 (d) to (e).

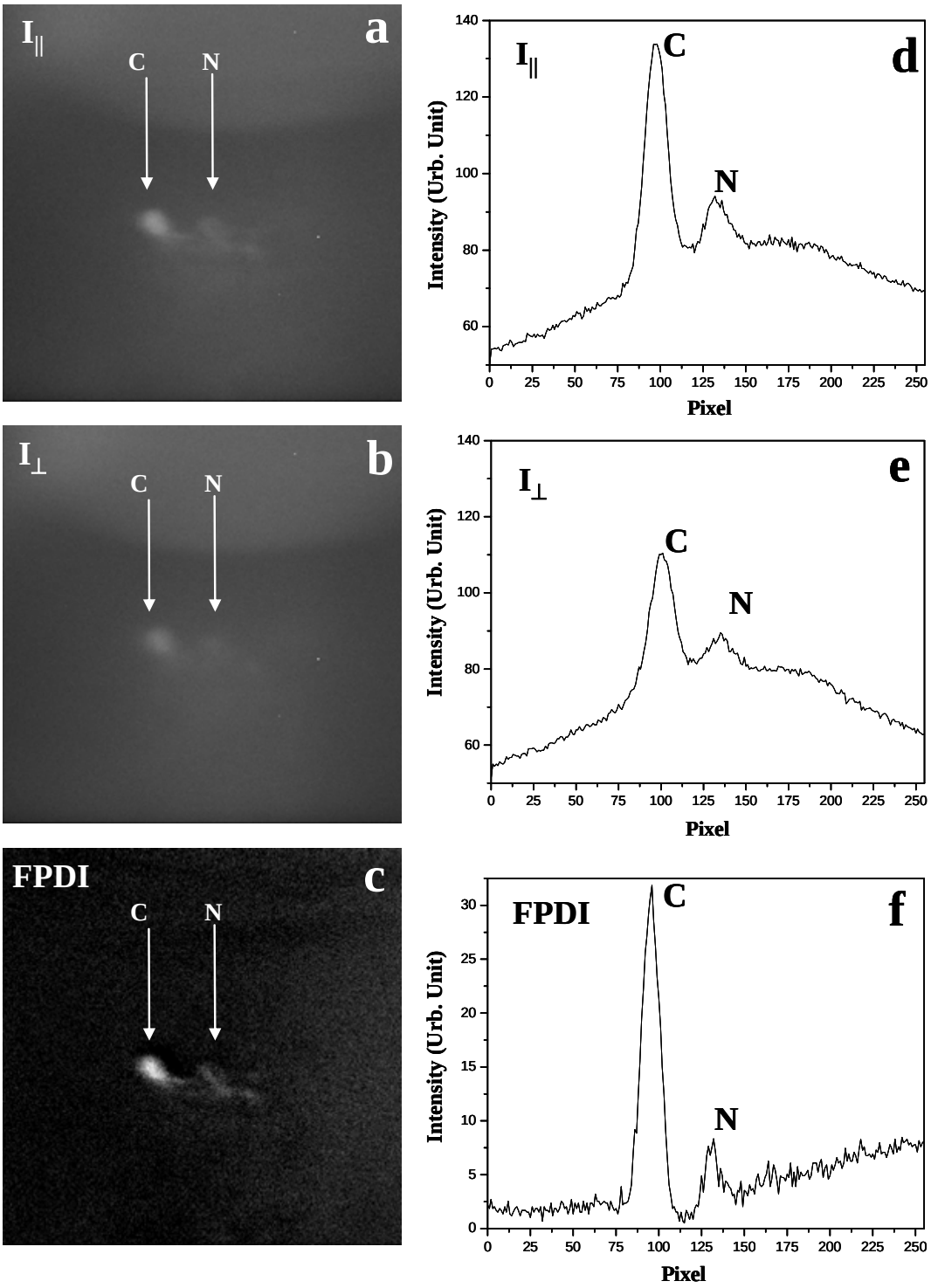

Fig. 5-5 Polarized fluorescence images of a cancerous-normal prostate tissue sample recorded at λ_{pump}=750nm, $\lambda_{detection}$=850nm when polarization direction is (a) || and (b) ⊥ to the excitation; (c) the FPDI image obtained by subtracting (b) from (a). (d), (e) and (f) are the digital spatial cross section intensity distributions of (a), (b) and (c), respectively.

It can be seen from the images that the cancerous tissue area is much brighter than that of the normal tissue area. The ratio of imaging intensity of cancerous to normal areas is calculated using the equation of $r = I_c / I_n$. Using the digital data shown in Figs. 5-5 (d) and (e), the ratio of imaging intensity of cancerous to normal areas is found to be ~3.69 under parallel polarization, and ~3.51 under perpendicular configuration. These are in good agreement with that obtained from the time-resolved fluorescence measurements.

The other salient feature is that the relative contrast of cancerous to normal areas in the polarization difference image shown in Fig. 5-5 (c) is obviously higher than those in the individual polarization images shown in Figs. 5-5 (a) and 5-5 (b) and the ratio of imaging intensity of cancerous to normal areas is found to be ~4.84 for FPDI image. The contrasts (C) of the cancerous area to the normal area for all of the images shown in Fig. 4 were calculated using

$$C = \frac{I_c - I_n}{I_c + I_n}, \qquad (5.6)$$

where I_c and I_n are the local maximum intensities of the dyed cancerous and normal tissue areas raised from the background as defined before, respectively. Using the digital data shown in Figs. 5-5 (d), (e) and (f), the contrasts for these parallel, perpendicular and polarization difference images are calculated to be 0.57, 0.54 and 0.67, respectively.

In addition, the improvement of spatial resolution of the difference image in comparison with the individual polarization image can be seen from Fig. 5-5 (d) to (f). The full width at half maximum (FWHM) for the cancerous tissue area shown in Fig. 5-5 (f) is improved by a factor of 1.9 with respect to that of the conventional image. The improvement can be understood because the fluorescence polarization difference image cancelled out the strong diffusive component and only kept ballistic photons and partial snake photons from the fluorescent objects [22]. The

contrast enhancement between cancerous and normal area is due to the higher polarization anisotropy of Cytate contained in cancerous tissue. Since the difference of $I_{\parallel} - I_{\perp}$ for the Cytate-stained cancerous tissue is larger than that in the Cytate-stained normal tissue, the contrast between cancerous and normal tissue areas is improved.

Both fluorescence intensity measurements and optical spectral imaging study show the preferential uptake of Cytate by prostate cancerous tissue. Since Hansson *et al* reported that the over-expressed SSTR2 and SSTR4 on prostate tumor cells bind octreotide [10], and the ligand of Cytate to target SSTRs in animal model is octreotide [3], we may infer that Cytate achieved targeting the over-expressed specific SSTR2 and SSTR4 in human prostate cancerous cells.

5. 6. Chapter summary

Steady-state absorption and fluorescence spectral measurements were performed on Cytate, a cancer receptor-targeted contrast agent, to study its viability in cancer detection. In addition, time-resolved fluorescence kinetics and polarization anisotropy of Cytate in solution and in stained human cancerous and normal prostate tissues were investigated. The experimental results show a larger degree of polarization preservation of fluorescence from Cytate in the stained cancerous tissue than in the stained normal tissue. The fluorescence intensity emitted from the Cytate-stained cancerous prostate tissue was found to be much stronger than that from the Cytate-stained normal prostate tissue indicating that cancerous prostate tissue has a higher Cytate intake than normal tissue. The time-resolved fluorescence intensity profile from a Cytate solution was fitted using a time-dependent fluorescence depolarization model. An empirical physical model was applied to describe the behavior of fluorescence kinetics and polarization anisotropy of Cytate in stained cancerous and normal prostate tissues. Optical imaging of cancerous and normal prostate tissues stained with Cytate was performed. The fluorescence image of the

Cytate-stained cancerous prostate tissue region was found to be much brighter than that of the Cytate-stained normal tissue region. Cytate was shown to be an excellent contrast agent because it can target over-expressed SST receptors in cancerous tissue, and its absorption and fluorescence spectra lie in the NIR "tissue optical window". Both fluorescence intensity and optical imaging studies show the potential of Cytate as a fluorescent marker in prostate cancer detection.

5. 7. References:

1. J. C. Reubi, B. Waser, J. C. Schaer and R. Markwalder, "Somatostatin receptors in human prostate and prostate Cancer", *J. Clin. Endocrinol. Metab*., 80, 2806-2814 (1995).
2. S. P. Rohrer, E. T. Birzin, R. T. Mosley and S. C. Berk *et al*, "Rapid identification of subtype-selective agonists of somatostatin receptor through combined chemistry", *Science*, 282, 737-740 (1998).
3. J. E. Bugaj, S. Achilefu, R. B. Dorshow and R. Rajagopalan, "Novel fluorescent contrast agents for optical imaging of *in vivo* tumor based on a receptor-targeted dye-peptide conjugate platform", *J. Biomed. Opt.*, 6(2), 122-133 (2001).
4. G. R. Fleming, J. M. Morris and G. W. Robinson, "Direct observation of rotational diffusion by picosecond spectroscopy", *Chem. Phys.*, 17, 91-100 (1976).
5. G. Porter, P. J. Sadkowski and C. J. Tredwell, "Picosecond rotational diffusion in kinetic and steady state fluorescence spectroscopy", *Chem. Phys. Lett.*, 49, 416-420 (1977).
6. R. D. Spencer and G. Weber, "Influence of Brownian rotations and energy transfer upon the measurements of fluorescence lifetime". *J. Chem. Phys*. 52, 1654-1663 (1970).
7. A. V. Schally, "Oncological applications of somatostatin analogs", *Can. Res., 48(24 Pt 1)*, 6977-6985 (1988).
8. L. J. Hofland and S. W. J. Lamberts, "Somatostatin subtype expression in human tumors", *Ann. of Oncol.*, 12(2), 31-36 (2001).
9. E. Thodou, G. Kontogeorgos, D. Theodossiou, M. Pateraki, "Mapping of somatostatin receptor types in GH or/and PRL producing pituitary adenomas", *J. Clin. Pathol* 59(3), 274–279 (2006).

10. Hansson J, Bjartell A, Gadaleanu V, Dizeyi N, Abrahamsson PA, "Expression of somatostatin receptor subtypes 2 and 4 in human benign prostatic hyperplasia and prostatic cancer", *Prostate*, 53(1), 50-59 (2002).
11. Y. Pu, W. B. Wang, G. C. Tang, F. Zeng, S. Achilefu, J. H. Vitenson, I. Sawczuk, S. Peters, J. M. Lombardo and R. R. Alfano, "Spectral polarization imaging of human prostate cancer tissue using a near-infrared receptor-targeted contrast agent", *Technol. Cancer Res. Treat.*, 4, 429-436 (2005).
12. Y. Pu, W. B. Wang, S. Achilefu, B. B. Das, G. C. Tang, V.Sriramoju, and R. R. Alfano "Time-resolved fluorescence polarization anisotropy and optical imaging of Cytate in cancerous and normal prostate tissues", *Opt. Commun.,* 274, 260-267 (2007).
13. Wubao Wang, Jamal H. Ali, R. R. Alfano, J. H. Vitenson and J. M. Lombardo, "Spectral Polarization Imaging of Human Rectum-Membrane-Prostate Tissues", *IEEE J. Quant. Elec.,* 9, 288-293 (2003).
14. Armin Shmilovici, "Incomplete tumor volume reduction may improve cancer prognosis", *Med. Hypoth.*, 68, 1236-1239 (2007).
15. W. B. Wang, S. G. Demos, J. Ali and R. R. Alfano, "Imaging fluorescence objects embedded inside animal tissue using a polarization difference technique", *Opt. Commun*., 142, 161-166 (1997).
16. F. Pellegrino, "Energy transfer in the primary stages of the photosynthetic process investigated by picosecond time resolved fluorescence spectroscopy", *A dissertation thesis of the City University of New York, Chapter 9*, 270-315 (1981).
17. D. A. Beysens, G. Forgacs, J. A. Glazier, "Cell sorting is analogous to phase ordering in fluids", *Proc. Natl. Acad. Sci. USA.*, 97, 9467–9471 (2000).

18. M. A. Dresner, P. J. Rossman, S. A. Kruse and R. L. Ehman, "MR Elastography of the Prostate", *ISMRM 99 CDs*, http://cds.ismrm.org/ismrm-1999/PDF2/526.pdf.

19. T. S. Deisboeck, Y. Mansury, C. Guiot, P.G. Degiorgis, P. Giorgio and P.P. Delsanto, "Insights from a novel tumor model: indications for a quantitative link between tumor growth and invasion", *Med. Hypoth.*, 65(4), 785-790 (2005).

20. D. F. Gleason and G. T. Mellinger, "Prediction of prognosis for prostatic adenocarcinoma by combined histological grading and clinical staging", *J. Urol*, 111, 58-64 (1974).

21. H. P. M. de Oliveira and M. H. Gehlen, "Time resolved fluorescence anisotropy of basic dyes bound to poly (methacrylic acid) in solution", *J. Braz. Chem. Soc*., 14(5), 738-743 (2003).

22. L. Wang, P. P. Ho, C. Liu, G. Zhang and R. R. Alfano, "Ballistic 2-D imaging through scattering wall using an ultrafast Kerr Gate", *Science*, 253, 769-771 (1991).

Chapter 6
Differences of the native time-resolved spectral wing emission kinetics and optical imaging between human cancerous and normal prostate tissues

6. 1. Introduction:

In the research shown in this chapter, time-resolved fluorescence study was performed on native tissues without dyes and used to obtain information of the location of abnormalities [1] and their biophysical microenvironments in prostate tissues. Time-resolved depolarization measurements of fluorophores excited with linearly polarized light was applied to probe the rotational (re-orientation) rate of molecules, which is a function of the viscosity of local environment, temperature and the size of the rotating fluorophore [2] thus provide more information than steady-state fluorescence techniques [3]. Although the time-resolved fluorescence anisotropy kinetics studies were relative easily applied on extrinsic contrast agents in prostate tissues [4, 5], intrinsic fluorophores, that can be used to differentiate the diseased human tissues from healthy tissues, also needs to be found since it is important to obtain minimally toxic contrast agents for human use.

Intrinsic fluorescence for diagnose applications is limited to the UV and blue excitation for most known fluorophores [6]. These excitation wavelengths are not in the NIR tissue "optical window" [7]. A major advancement occurred when the spectral wing emission in NIR from human cancerous and normal breast tissues were investigated [8]. Biological tissues excited by far-red or NIR light have strong NIR emission in that spectral range. No characteristic peaks were found for the emission from the known fluorophores [8]. This phenomenon was noted as Spectral Wing (SW) emission by Alfano's group [8]. Alfano believes the SW emission arises from quadrupole and/or octopole emission process in the ground state. The apparent differences were used to image and distinguish human malignant breast tissues from normal tissues [8].

In this chapter, I report time-resolved and spectral measurements of the SW emission from cancerous and normal prostate tissues in the spectral range of far-red to NIR without the addition of extrinsic contrast agent. The stronger intensity of the SW emission from cancerous prostate tissue was observed in comparison with normal tissue. The differences of time-resolved SW emission of cancerous and normal prostate tissues, including their profiles, decay time and polarization anisotropy were studied and explained by changes of microscopic structure of human cancerous prostate tissues as compared with the normal counter part. The stronger intensity of SW emission from cancerous prostate tissue was used to image and distinguish cancerous tissue areas surrounded by normal tissue.

6. 2. Experimental method and samples

6. 2. 1. Experimental materials

The cancerous and normal prostate tissue samples used in the experiments were provided by National Disease Research Interchange (NDRI) and the Co-operation Human Tissue Network (CHTN) under IRB approvals. Pairs of cancerous and normal prostate samples were taken from same patient and diagnosed by pathology medical doctors for the optical experiments. Samples were neither chemically treated nor were frozen prior to the experiments. Three pairs of cancerous and normal prostate tissues were cut into ~2 × ~1.5 × ~0.5 cm (length × width × thickness) pieces for the time-resolved and spectroscopy measurements of SW emission. All of the measurements were performed at room temperature.

6. 2. 2. Experimental methods

Three experimental sets up were used in this research. The experimental setup for the time-resolved spectral wing emission measurements of the human prostate tissues is schematically shown in Fig. 4-1 in chapter 4. Same model of Coherent Mode-locked Ti:Sapphire laser of 800

nm wavelength and streak camera with temporal resolution of 10ps were used to pump the tissue samples. An 830nm long pass filter and an 800nm notch filter were placed in front of the streak camera, and used to cut off the excitation wavelength. Two polarizers, P_1 and P_2, were used as the polarizer and the analyzer, respectively. The polarization of P_2 was rotated from 0^o to 90^o with respect to the polarization direction of P_1 to record the intensity profiles of parallel and perpendicular polarization components of total SW emission. The temporal profiles recorded by a CCD on the streak camera were analyzed to obtain temporal and polarization information [4].

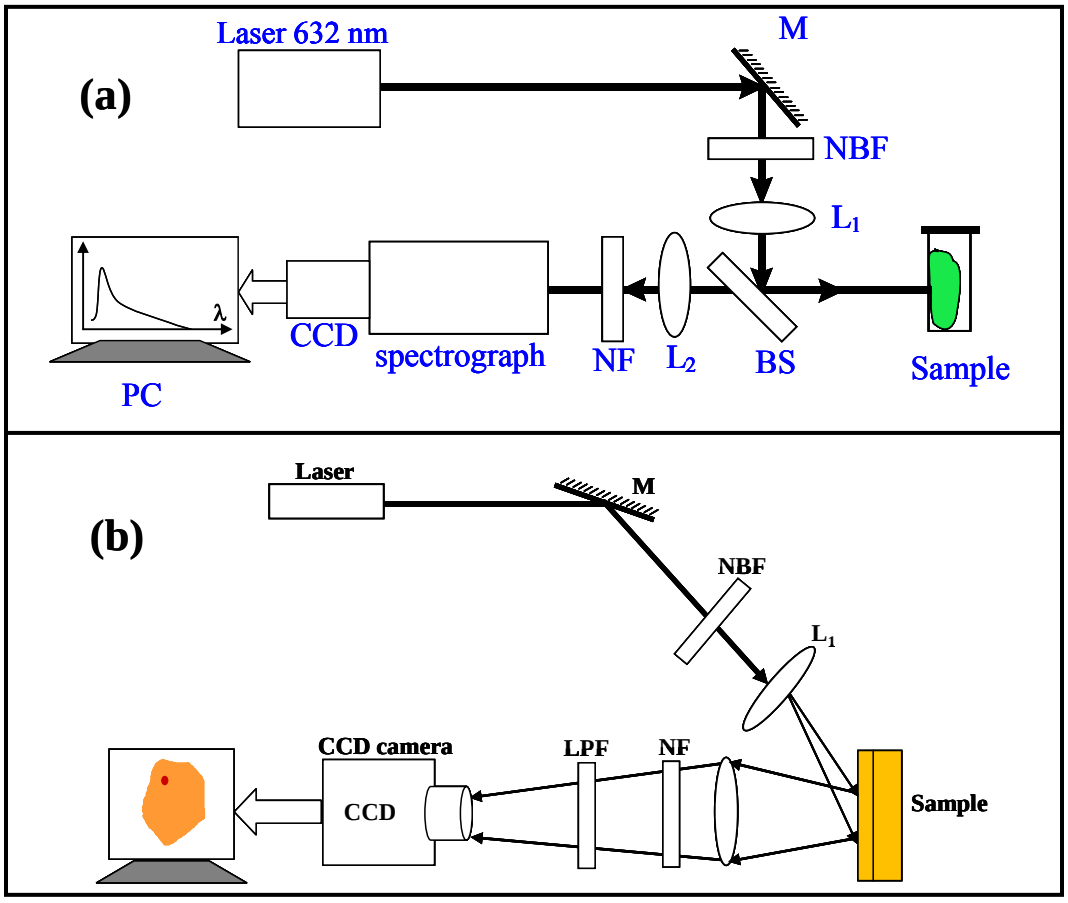

Fig. 6-1 Schematic diagrams of the experimental sets up used for (a) spectral measurements of SW emission, and (b) SW emission optical imaging measurements, where M: mirrors; BS: beam splitters; LPF: long pass filter; NBF: narrow band filter; NF: Notch filter; L: lenses; CCD: charge-coupled device camera.

The setup for the SW emission spectral measurements is schematically shown in Fig. 6-1 (a). The measurements were performed using a quarter meter spectrograph (ARC SpectroPro 275)

and a cooled CCD camera (Princeton Instrument model TE/CCD-512SF). The beam of a 633nm laser was focused by a 20cm focal length lens (L_1) onto the sample. The emitted light from tissue samples was collected with a backscattering geometry by an 85mm focal length camera lens (L_2). After passing through a notch filter (NF), the SW emission light was coupled into the 0.1mm slit of a spectrograph, spectrally analyzed and recorded by the CCD camera.

A schematic diagram for NIR optical imaging is shown in Fig 6-1(b). Prostate tissue samples consisting of a small piece of cancerous prostate tissue embedded in a larger piece of host normal prostate tissue were studied. A laser beam at 633 nm was used to illuminate the prostate tissue samples, and the emission images of the samples were recorded by a CCD camera at the far red to NIR spectral range greater than 650nm. The native SW emission light from the tissue samples is collected by a focal length of 85cm lens (L_2) into a cooled CCD camera with a the backscattering geometry for imaging. A notch filter (NF) at 633nm and a 650nm long pass filter (LPF) were used to record the images formed by the SW emission light [9]. Polarizer P_1 used to ensure the linear polarization of the illumination and polarizer P_2 is placed in the front of the CCD for selecting the detection polarizations. The spatial resolution of the CCD camera is 20 μm/pixel.

6. 3. Experimental results and discussion

6. 3. 1. Experimental results of time-resolved polarization kinetics

The temporal SW emission intensity profiles of the cancerous and normal prostate tissues under 800nm excitation are displayed in Fig. 7-2. The thick solid and thick dash line profiles display the parallel and perpendicular components emitted from cancerous prostate tissue, respectively. The thin solid and thin dash line profiles display the parallel and perpendicular components emitted from normal prostate tissue, respectively.

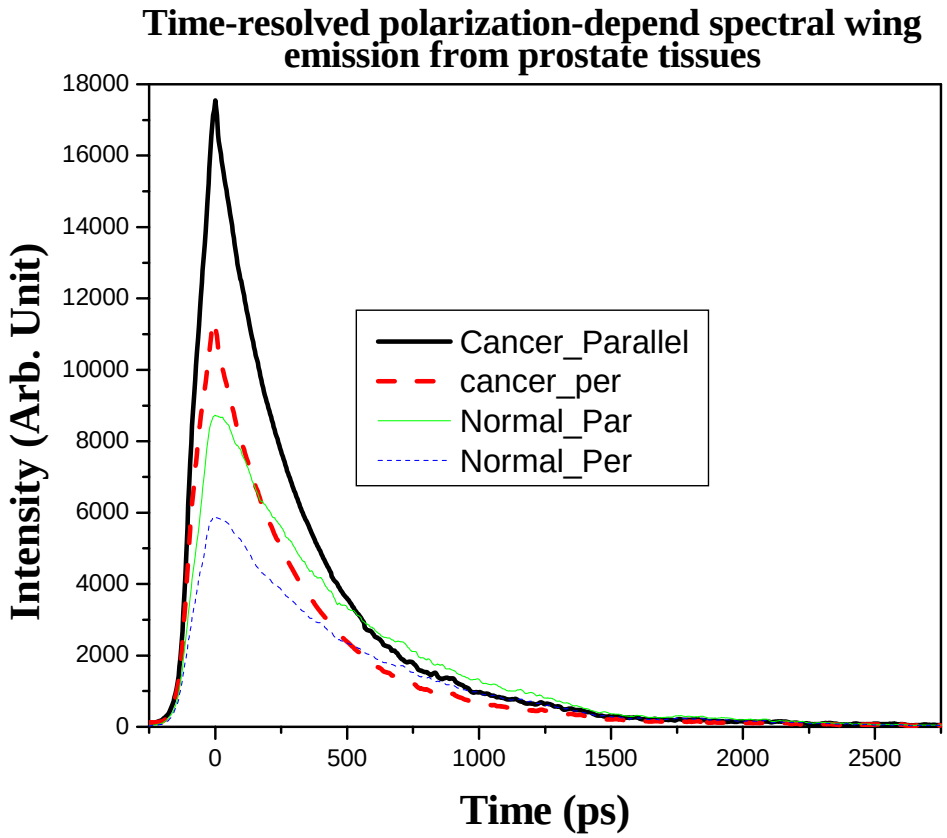

Fig. 6-2. The time-resolved intensity profiles of NIR SW emission of cancerous and normal prostate tissues with 800nm laser excitation. The thick solid and thick dash line profiles display the parallel and perpendicular components emitted from cancerous prostate tissue, respectively. The thin solid and thin dash line profiles display the parallel and perpendicular components emitted from normal prostate tissue, respectively.

The salient features of the data shown in Fig. 6-2 are that the intensities of SW emission from cancerous tissue are stronger than those of normal tissue at the peak position in both parallel and perpendicular configuration. The ratio of peak SW emission intensity of cancerous tissue to that of the normal is found to be ~2.0 for parallel configuration while the ratio is ~1.9 for the perpendicular configuration. The stronger intensity of SW emission from cancerous tissue demonstrates that optical imaging technique can be used to distinguish cancerous prostate areas from normal tissue. Another important feature shown in Fig. 6-2 is that $I_{\parallel}$ is greater than $I_{\perp}$ for both cancerous and normal tissue for all of the decay times. At the peak position, $I_{\parallel}^{cancer}(0)$ is ~1.56 times stronger than $I_{\perp}^{cancer}(0)$, and the ratio of $I_{\parallel}^{normal}(0)$ to $I_{\perp}^{normal}(0)$ is ~1.48. This indicates

that the SW emission of cancerous and normal prostate tissue shows the polarization preservation property. This property combined with optical-polarization-difference-imaging technique can be used to enhance the imaging contrast between cancerous and normal tissue areas [9].

Using the measured time-resolved polarization-dependent SW emission profiles of $I_{\parallel}(t)$ and $I_{\perp}(t)$ shown in Fig. 6-2, we can analyze the changes of fluorophores in tissue during the tumor evolution and compare the bulk feature and micro-environment of cancerous prostate tissue to that of normal prostate tissue.

6. 3. 2. Model of SW emission polarization

The time-resolved fluorescence depolarization technique was widely used as a probe for re-orientation motion of dye molecules in solution since 1970's [3]. These works have shown that time domain can be also applied to investigate the motion of bio-molecules in the tissue environment [2, 4, 5].

For an isolated fluorophore, the temporal profiles of the parallel and perpendicular components: $I_{\perp}(t)$ and $I_{\parallel}(t)$ can be expressed as we studied in chapter 4 [11]:

$$I_{\parallel}(t) = \frac{I_0}{3}\exp(-\frac{t}{\tau_f})\left(1 + 2r_0\exp(-\frac{t}{\tau_{rot}})\right), \quad (6.\ 1a)$$

$$I_{\perp}(t) = \frac{I_0}{3}\exp(-\frac{t}{\tau_f})\left(1 - r_0\exp(-\frac{t}{\tau_{rot}})\right) \quad (6.\ 1b)$$

where I_0 is the initial emission intensity, τ_f is the fluorophore's lifetime (it is called decay time for SW emission), which gives valuable insight on the binding site of the emission molecule and on other chemical and physical parameters like pH, polarity of the medium, aggregation state of the fluorophore, etc., r_0 is anisotropy value at t=0 indicating the initial distribution of the excited polarized molecules (by dipoles, quadru-pole and/or octo-pole), and τ_{rot} is re-orientation time

indicating the depolarization rate of the excited polarized molecules, which is determined by the microenvironments of medium containing the fluorophore. In the simple dye case where the fluorophore molecule undergoes Brownian rotation as an Einstein sphere, the re-orientation time τ_{rot} can be expressed in terms of the medium viscosity (η), the absolute temperature of medium (T) and the molecular volume (V) by [3, 4]:

$$\tau_{rot} = \frac{\eta V}{kT}, \tag{6. 2}$$

where k is the Boltzmann constant.

From equation (6. 1), one measures the temporal profiles of the parallel and perpendicular components of SW emission and can study both the fluorophore's decay time (τ_f) and the re-orientation time (τ_{rot}). In our investigation of the SW emission intensity and decay time of fluorophore τ_f, the total temporal SW emission intensity can be calculated using an equation of [3-5, 10]:

$$I_{total}(t) = I_{\parallel}(t) + 2I_{\perp}(t) = I_0 \exp(-\frac{t}{\tau_f}), \tag{6. 3}$$

where factor 2 is used for $I_{\perp}(t)$ since the total emission should include the component perpendicular to the plate containing the measured parallel and perpendicular directions, which can be taken approximately to be equal to the detected $I_{\perp}(t)$ [10]. Equation (6. 3) indicates that the decay time τ_f of the excited fluorophores in tissue can be obtained from a temporal profile of the total SW emission ($I_{total}(t)$). The change of the decay time may reflect the change of components of fluorophores.

In our study of re-orientation time τ_{rot}, the time-resolved polarization anisotropy of SW emission can be calculated using an equation of [3-5, 10]:

(7-4)

$$r(t) = \frac{I_{\parallel}(t) - I_{\perp}(t)}{I_{\parallel}(t) + 2I_{\perp}(t)} = r_0 \exp(-\frac{t}{\tau_{rot}}),$$

where $I_{\parallel}(t)$ and $I_{\perp}(t)$ are measured intensities of parallel and perpendicular polarization components of the SW emission, respectively [3, 9]. Equation (6. 4) indicates that the re-orientation time (τ_{rot}) can be extracted from the time-resolved polarization anisotropy (r(t)) of the SW emission.

Using equations (6. 3) and (6. 4), the decay time of the SW emission and the re-orientation time of the fluorophores in tissue can be obtained from the time-resolved total SW emission and polarization anisotropy, respectively. The intensity and decay time of SW emission are related to the bio-molecules content in tissue [12], and the re-orientation time linked to the hindered motion in micro-environment of the bio-molecules in tissue [3, 10].

6. 3. 3. Analysis of I(t)

The time-resolved total SW emission of cancerous and normal prostate tissues were calculated using equation (6. 3) and the data of $I_{\parallel}(t)$ and $I_{\perp}(t)$ shown in Fig. 6-2, and the results are shown in Fig. 6-3 (the dot and dash lines for the cancerous and normal tissues, respectively).

The salient features of Fig. 6-3 are that the higher intensity and faster decay rate of the cancerous tissue were observed compared with the normal tissue. The initial emission intensity of the cancerous tissue was found ~1.9 times stronger than the normal tissue. The decay time of SW emission of cancerous and normal prostate tissues can be obtained by fitting the temporal profiles of the total SW emission using equation (7-3). The fitting results are shown in Fig. 6-3 as thick solid line for the cancerous prostate tissue and thin solid line for the normal prostate tissue. The parameters of I_0 and τ_f obtained from the fitting are I_0= 40962±927, τ_f=311±1.9ps for cancerous tissue, and I_0= 20917±141, τ_f=517±1.2ps for the normal. Here τ_f indicates the average

decay time of different fluorophores in tissue [12]. The decay time of SW emission from the cancerous tissue is ~1.7 times shorter than the normal tissue. The almost 2 times shorter decay time of the cancerous tissue was also observed by previous experiment in animal model [2]. The faster decay rate of SW emission of cancerous prostate tissue makes I_{normal} turn over I_{cancer} at ~520ps, i.e. $I_{cancer} > I_{normal}$ when t < ~520ps and $I_{cancer} < I_{normal}$ when t > ~520ps.

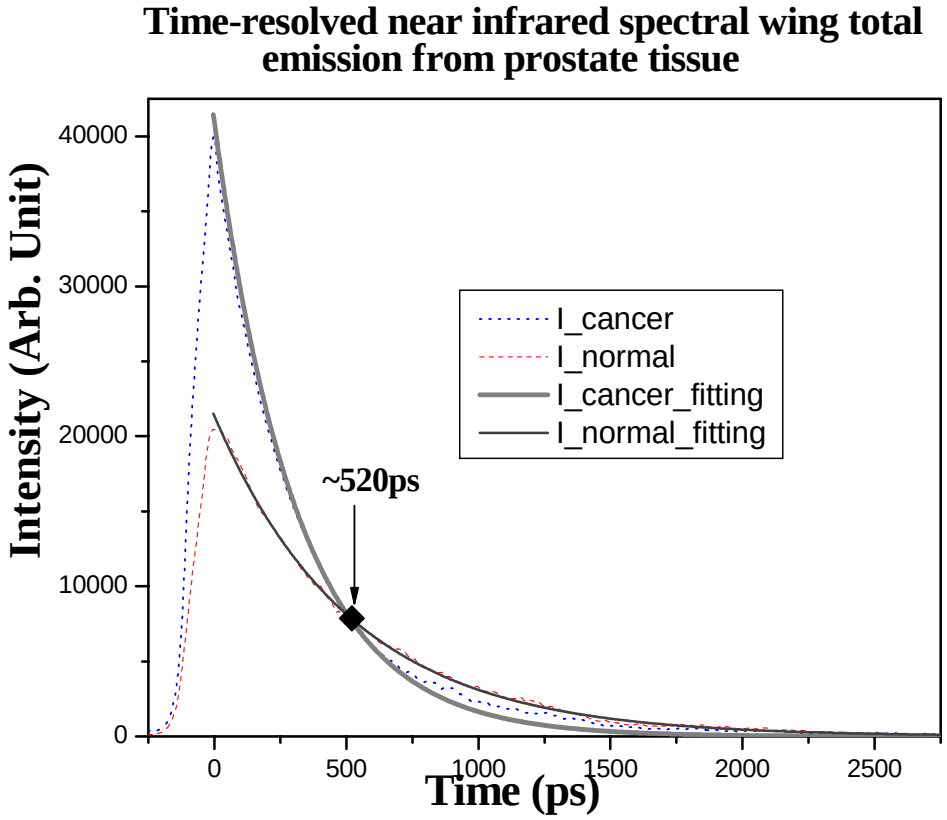

Fig.6-3 Time-dependent total NIR SW emission intensity of cancerous (dot) and normal (dash) prostate tissues calculated using equation $I_{total}(t) = I_{\parallel}(t) + 2I_{\perp}(t)$ and the data of $I_{\parallel}(t)$ and $I_{\perp}(t)$ shown in Fig. 6-2. The fitting curves are obtained using equation (6. 3).

The integrated SW emission intensities of the cancerous and normal prostate tissues is showed in Fig. 6-4(a), which were calculated using equation (6. 3) for I(t) and the equation of $I_{(\tau)}^{integ} = \int_0^{\tau} I(t)dt$. The results show that the integrated intensity of cancerous tissue (solid line) is always greater than that of normal tissue (dash line) within the whole emission time. The ratio of integrated intensity of cancerous prostate tissue over normal prostate tissue is 1.54 at ~ 310ps (τ_f

of SW emission for cancerous tissue), 1.43 at ~510ps (τ_f of SW emission normal tissue) and 1.2 at 1500 ps and later. These results show that continue wave (CW) optical imaging can be used to image and identify cancerous prostate tissue from the surrounding normal prostate tissue based on the difference of their integrated intensities of the SW emission.

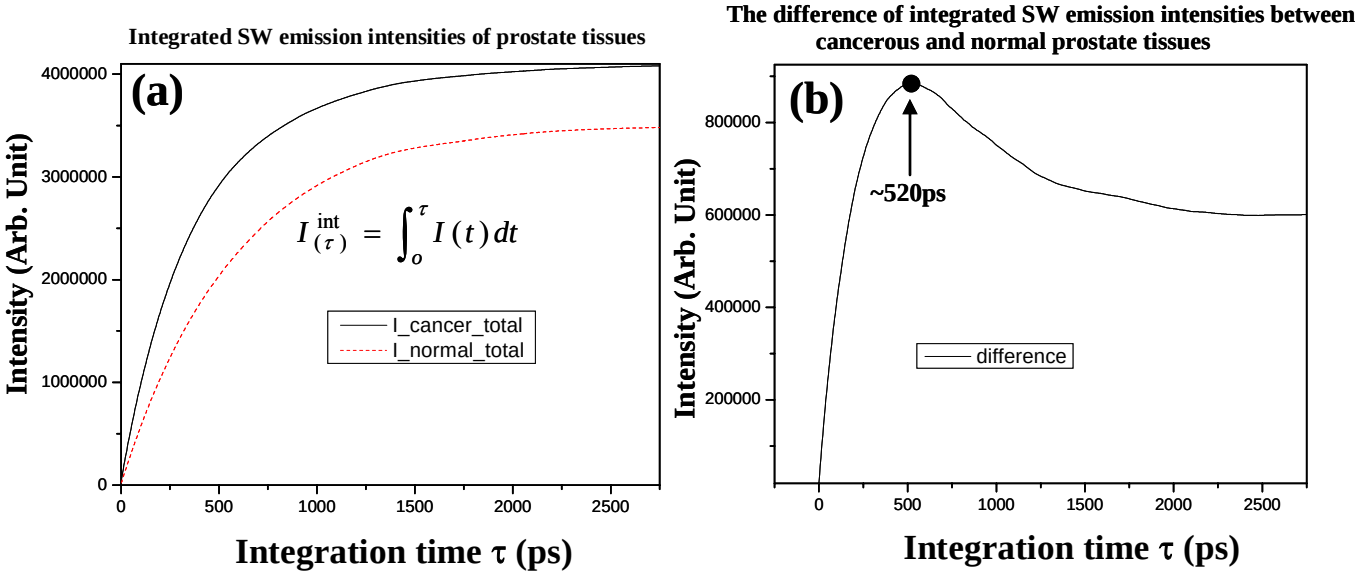

Fig. 6-4 (a) The integrated intensity of the spectral wing emission from the cancerous (solid line) and normal (dash line) prostate tissue as a function of integration time; (b) Difference of the integrated intensity of the SW emission obtained by subtracting integrated intensity of normal (dash line in Fig. 6-4(a)) prostate tissue from the cancerous (solid line in Fig. 6-4 (a)) tissue.

The difference of integrated SW emission intensities between cancerous and normal prostate tissues is shown in Fig. 6-4(b), which was obtained by subtracting the integrated SW emission intensity of normal tissue (dash line in Fig. 6- 4(a)) from that of cancerous tissue (solid-line in Fig. 6-4(a)), i.e. $I_{diff}(\tau) = I^{integ}_{cancer}(\tau) - I^{integ}_{normal}(\tau)$. Fig. 6-4(b) indicates that the maximum difference happens at ~520ps shown as the dot-point, which is corresponding to the time when the SW emission intensity of normal prostate tissue surpasses that of cancerous tissue in the decay portion of emission as shown in Fig. 6-3.

The phenomenon of higher SW emission intensity of the cancerous prostate tissue may be explained by the tumor cell evolution and the contributions of fluorophores in tissues to SW

emission. It is reasonable to assume that the SW emission intensity is proportional to the concentration of the fluorophore in the biological tissue since the fluorescent intensity is proportional to the fluorophores concentration in living tissue [13]. In a typical malignant tumor evolution, it first grows in volume until it reaches some kind of confining volume; then, the mechanical pressure increases its cell density [14]. The prostate tumor grading system known as five Gleason Grades, usually denoted as stages 1-5 [15]. The Pattern of Gleason Grade 1 (corresponding to early stage) consists of a circumscribed mass of evenly placed uniform glands. With grade advances, the cancer cells proliferate and begin to merge into "island", which appears at Grade 3 and is obvious at Grade 5 [15]. This pattern is illustrated by the microscope images of the normal and cancerous areas of prostate tissue shown as Figs. 4-10 (a) and (b) of chapter 4, respectively. The histological slides for microscope images were prepared at HUMC, and the microscope slide images of the cancerous and normal prostate tissue were taken using a digital electro-microscope (Mel Sobel Microscopes Ltd) at CCNY. The different microstructures of prostate cancerous and normal tissues corresponding to the typical normal and cancerous microstructures were observed from their microscope images (×40), and the presences of the tumor structure in cancerous tissue were identified. The microscope slide images clearly exhibit higher density and the "island" structure of the cancerous prostate tissue in comparison with the normal prostate tissue [16]. Montironi *et al* also quantified the diameter of cancerous and normal prostate cellular nuclear as: $D_{cancer} \approx 8.40 - 9.11$ μm and $D_{normal} \approx 6.30 - 7.11$ μm [17]. The higher cell density and larger cellular nuclear in cancerous prostate tissue give the more fluorophores to yield stronger intensity of spectral wing emissions.

The difference of the average SW emission decay times between cancerous and normal prostate tissues may be attributed to the changes of prostate tissue structure and the fluorophores

during cancer development. It has been shown that the scattering dominates over absorption in the NIR range [7], and light transporting in tissue essentially depends on the reduced scattering coefficient $\left[\mu_s' = \mu_s(1-g)\right]$, not on the scattering coefficient (μ_s) and anisotropy factor (g) separately [18]. It was observed by Das *et al* that the time-resolved backscattered pulses from the cancerous tissues (ductal carcinoma) were found to be much narrower than the pulses from the benign samples [19]. This difference is due to larger reduced scattering coefficient (μ_s') of cancerous tissue [19]. The increase of μ_s' indicates that higher cellular density in cancerous tissue [14, 15] increases the amount of scattering and lengthens for the reduced scattering coefficient as compared to normal tissue [19]. It is reported that the fluorescence contrast difference between cancerous and normal tissue of endogenous fluorophores are mainly caused by NADH and collagen [20, 21], and there is a reduced contribution from collagen in cancerous prostate tissues [21]. The investigations of the percentage of fluorescence emitted from NADH and collagen in cancerous and normal tissues indicate that up to 50% of fluorescence is emitted from NADH in cancerous tissue while collagen accounts for approximately 70% of the total fluorescence signal in normal tissue in visible and UV ranges [20]. The fluorescence lifetime of free NADH was reported to be ~400ps and fast component of lifetime of collagen was reported to be ~610ps [22]. Since both fluorescence and SW emission emit light with longer wavelength during certain time, (for fluorescence, lifetime, for SW, so-called "decay time"); and the fluorescence lifetime of NADH is shorter than collagen [22], it is reasonable to hypothesize that the shorter decay time of SW emission observed in cancerous tissue may be caused by greater contribution from NADH and reduced contribution from collagen.

6. 3. 4. Analysis of time-resolved anisotropy

The depolarization property of SW emission is described by the time-resolved polarization anisotropy which is defined as equation (6. 4) [3-5, 10]. The reorientation of bio-molecules contributed to SW emission will result in the decay behavior of r(t). By investigating the time-resolve anisotropy of SW emission in prostate tissue, the biophysical local microenvironments of fluorophores can be studied and the results can be used to compare different types of prostate tissues.

Using the measured values of $I_{\parallel}(t)$ and $I_{\perp}(t)$ shown in Fig. 6-2 and Equation (6. 4), the temporal profiles of the polarization anisotropy r(t) from cancerous (thin dashed line) and normal (thin dot line) prostate tissues were calculated and the result are displayed in Fig. 6-5.

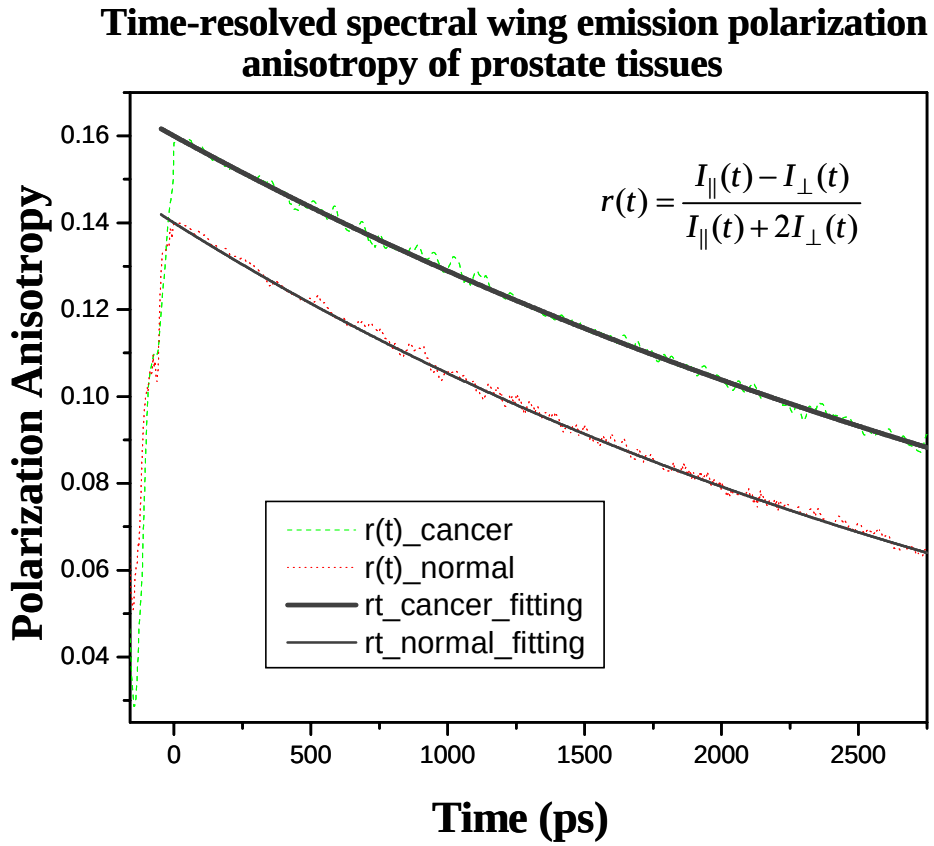

Fig. 6-5 Time-dependent polarization anisotropy calculated using equation (6. 4) and the measured data shown in Fig. 6-2. The fitting curves are obtained using equation (6. 4)

The salient features of r(t) curves shown in Fig. 6-5 are that the polarization anisotropy of SW emission of cancerous tissue are always larger than that of the normal tissue. This indicates

that the cancerous tissue shows a better polarization preservation property of SW emission than the normal prostate tissue. The time-resolved anisotropy kinetics of SW emission can be characterized by fitting the experimental data of r(t) shown in Fig. 6-5 using equation (6. 4). r(t) are denoted by a thick solid line and a thin solid line for cancerous and normal prostate tissues in Fig. 6-4, respectively. The fitting results yield the following parameters: τ_{rot}=5.0±0.12ns and r_0=0.169±0.003 for the cancerous prostate tissue; and τ_{rot}=3.5±0.05ns and r_0=0.141±0.002 for the normal tissue.

The differences of r_0 and τ_{rot} between cancerous and normal prostate tissues may be understood from changes of the cellular nuclear size during the tumor cell evolution and the hindered motion caused by different microstructures of these two types of tissues. In tissue, anisotropy r_0 is determined by initial distribution of the excited polarized molecules (dipoles, quadrapoles or octopoles) [3, 10] and is sensitive to changes of molecular weight [23]. The fitting result shows $r_0^{cancer} > r_0^{normal}$, which can be understood by the larger size of cellular nuclear in cancerous prostate tissue [14, 15]. It has been reported that increasing molecular weight of fluorescent biomolecule should increase fluorescence anisotropy [23]. It is reasonable to assume the same phenomenon happens for SW emission. Since the larger nuclear size was reported in cancerous prostate tissue [17], we believe this is why the ratio of $I_{\parallel}^{n} / I_{\perp}^{n} = 1.48$ for the normal tissue is smaller than that of $I_{\parallel}^{c} / I_{\perp}^{c} = 1.56$ for the cancerous tissue at initial time, and the polarization anisotropy of SW emission of cancerous tissue is always larger than that of the normal tissue.

The fitting shows $\tau_{rot}^{cancer} > \tau_{rot}^{normal}$. The re-orientation time of SW emission molecules is proportional to the local viscosity in the prostate tissue. The larger the re-orientation time of fluorophores contributed to SW emission for cancerous prostate tissue indicates the higher local

viscosity of cancerous prostate tissue due to larger nuclear size in cancerous prostate tissue [19] and high density which decreases interstitial spacing between cells in cancerous tissue[14, 15], thus restrict the hindered motions of the bio-molecules.

6. 3. 5. SW emission spectra and optical imaging of prostate tissues

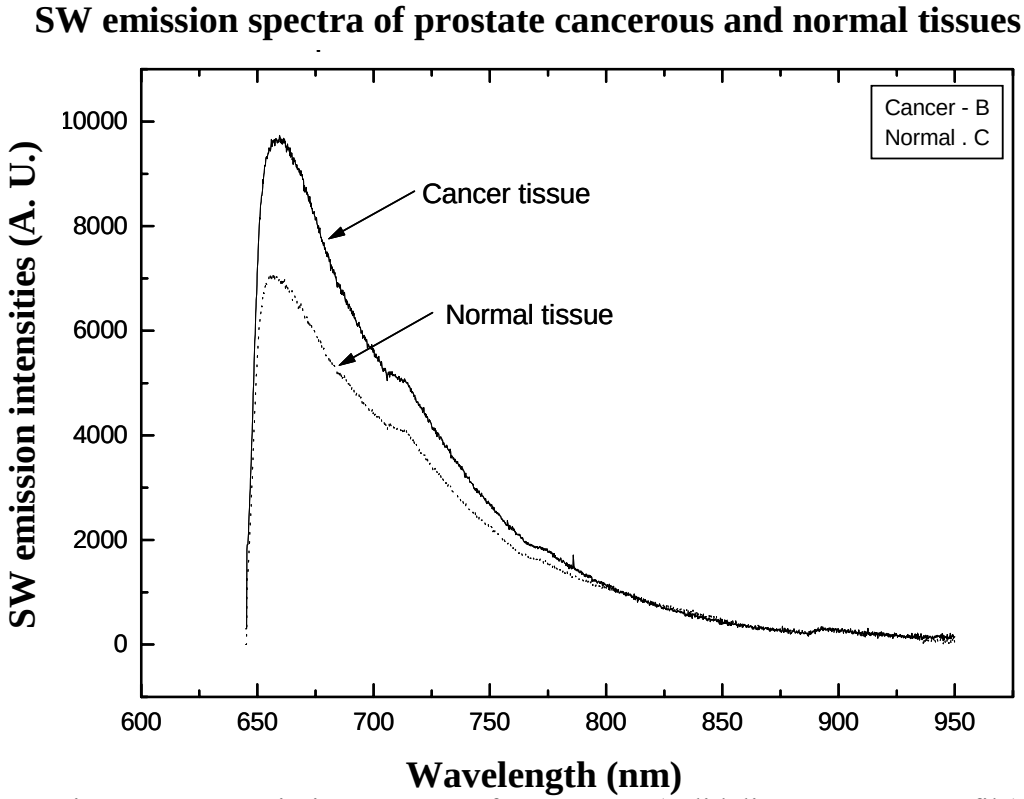

Fig. 6-6 SW emission spectra of cancerous (solid line at upper profile) and normal prostate tissues (dash line at lower profile) under 633 nm excitation.

The SW emission spectra measurements were performed on more than six different locations for statistic analysis for each cancerous or normal prostate tissue samples. A pair of typical SW emission spectra profiles for cancerous and normal prostate tissue samples excited at 633nm is shown in Fig. 6-6. The spectra show that the SW emission from the cancerous prostate tissue exhibits stronger intensity than that from the normal prostate tissue within the emission spectral range from 650nm to 800nm under identical excitation conditions. The ratio of the peak intensity of the cancerous prostate tissue over that of the normal prostate tissue has an approximate value

of 1.4, which is in reasonable agreement with the results obtained from time-resolved intensity measurements. The stronger intensity of SW emission observed in cancerous prostate tissue may be due to higher cell density [14, 15] and larger nuclear size of cancerous prostate tissue [17] in comparison with normal prostate tissue.

Diagnostic potential of optical imaging for prostate cancer detection may be realized by using of the stronger SW emission intensity of cancerous prostate tissue. The SW emission of biological tissue extends the optical imaging in visible range (using native tissue fluorescence wavelengths) to NIR range (using native SW emission), which can penetrate tissue more deeply.

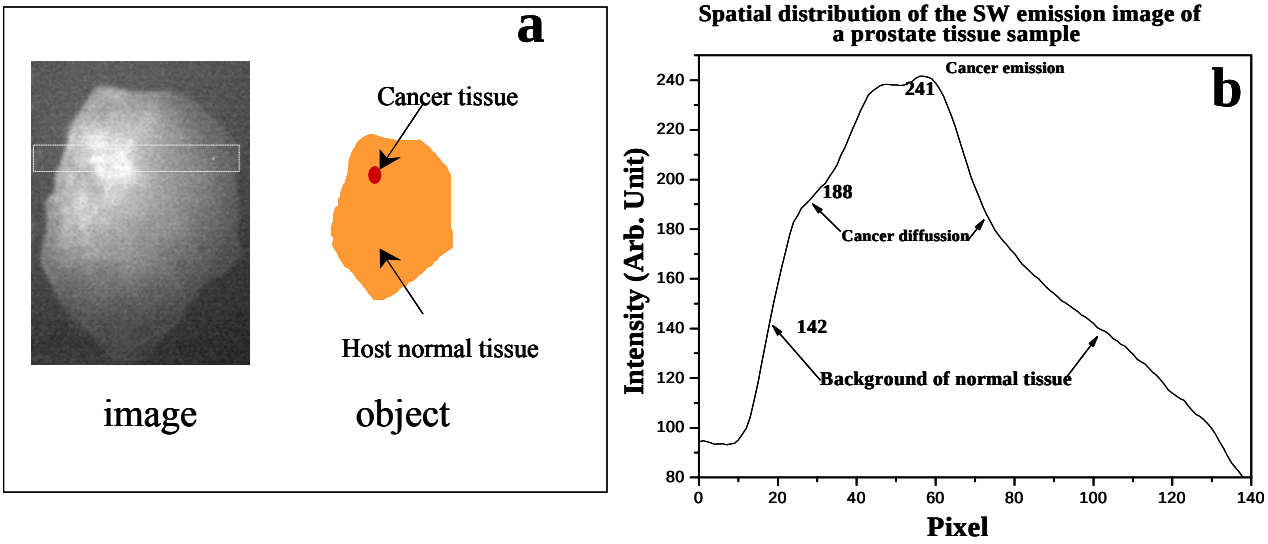

Fig. 6-7 (a) Spectral wing emission image (the left side of Fig. 6-7(a)) of a small piece of cancerous prostate tissue embedded in a large piece (~15mm × ~20 mm) of the host normal prostate tissue at depth of 1.5 mm. The cancerous tissue is located at the upper left area as shown on the right-side of Fig. 6-7(a). Fig. 6-7(b) shows the digital spatial cross section intensity distribution of the image shown in Fig. 6-7(a).

Fig. 6-7 (a) shows an optical image of a small piece of cancerous prostate tissue (2×3 mm) embedded in a larger piece (~15 × 20 mm) of normal prostate tissue at depth of ~1.5 mm. The cancerous tissue is located at the upper left area as shown in the schematic diagram on the right-side. The salient feature of the image is that the cancerous tissue appears much brighter on the upper left side. The NIR SW emission image also show the structure of the cancer: it does not

have regular smooth surface but diffused to the neighborhood normal tissues. The corresponding spatial intensity profiles of the image obtained by integrating the horizontal area over the box shown by the dash line are displayed in Fig. 6-7 (b). The brighter cancerous area can be more clearly verified from the ratio of imaging intensity of cancerous area to that of normal tissue area, which is found to be ~1.7. This result demonstrates that the difference of the SW emission intensities between cancerous and normal prostate tissues may provide a distinguishable fingerprint for the optical imaging for prostate cancer diagnosis through the rectum.

6. 4. Chapter summary

Time-resolved SW emission profiles and polarization anisotropy kinetics of Native human cancerous and normal prostate tissues were investigated. The stronger intensity and shorter decay time of SW emission of cancerous prostate tissue were observed in comparison with normal prostate tissue. A mono-exponential decay for total intensity was used to obtain the average decay time of SW emission to investigate changes of fluorophores in different prostate tissue types. The time-resolved SW emission polarization anisotropy was analyzed and used to investigate micro-environment features of cancerous and normal prostate tissue. The anisotropy of the SW emission of cancerous tissue was found to be higher than that of normal tissue. The larger re-orientation of fluorophores in cancerous prostate tissue indicates the higher local viscosity of cancerous prostate tissue. These differences are attributed to larger nuclear size, higher cell density and random structure in cancerous prostate tissues during the evolution of prostate cancer. Stronger intensity of SW emission from cancerous prostate tissue was also observed in comparison with normal prostate tissues in the far-red to NIR spectral and optical imaging measurements. The cancerous region can be distinguished from the surrounding normal tissue by optical imaging using SW emission.

6. 5. References:

1. D. B. Tata, M. Foresti, J. Cordero, P. Tomashefsky, M. A. Alfano and R. R. Alfano, "Fluorescence polarization spectroscopy and time-resolved fluorescence kinetics of native cancerous and normal rat kidney tissues", *Biophys. J.*, 50, 463-46 (1986).
2. G. R. Fleming, J. M. Morris and G. W. Robinson, "Direct observation of rotational diffusion by pico-second spectroscopy", *Chem. Phys.*, 17, 91-100 (1976).
3. R. R. Alfano, D. Tata, J. Cordero, P. Tomashefsky, F. Longo, and M. Alfano, "Laser induced fluorescence spectroscopy from native cancerous and normal tissue", *IEEE J. Quant. Elec.*, 20, 1507-1511 (1984).
4. Y. Pu, W. B. Wang, S. Achilefu, B. B. Das, G. C. Tang, V.Sriramoju, and R. R. Alfano "Time-resolved fluorescence polarization anisotropy and optical imaging of Cybesin in cancerous and normal prostate tissues", *Opt. Commun.*, 274, 260-267 (2007).
5. Y. Pu, W. B. Wang, B. B. Das, S. Achilefu, and R. R. Alfano, "Time-resolved fluorescence polarization dynamics and optical Imaging of Cytate: a prostate cancer receptor-targeted contrast agent", *Appl. Opt.*, 47, 2281-2289 (2008).
6. Kendric C. Smith, "The science of photobiology", 2nd edition, Plenum press, (1989).
7. Donna J. Dean and Brenda J. Korte, "Biomedical Imaging and Bioengineering", *Optics & Photonics News,* October 2003, http://ultra.bu.edu/papers/2003_10_OPN.pdf.
8. G. Zhang, S. G. Demos and R. R. Alfano, "Far-red and NIR spectral wing emission from tissues under 532 and 632 nm photo-excitation", *Laser Life Sci.*, 9, 1-16 (1999).
9. W. B. Wang, S. G. Demos, J. Ali and R. R. Alfano, "Imaging fluorescence objects embedded inside animal tissue using a polarization difference technique", *Opt. Commun.*, 142, 161-166 (1997).

10. R. D. Spencer and G. Weber, "Influence of Brownian rotations and energy transfer upon the measurements of fluorescence lifetime", *J. Chem. Phys*. 52, 1654-1663 (1970).
11. D. V. O'Connor and D. Phillips, "Time-correlated single photon counting", Chapter 1, "Fluorescence, its time dependence and applications", *The royal Institution, London, UK, Copy right@Academic Press,* (1984).
12. R. Cubeddu, D. Comelli, C. D'Andrea, P. Taroni and G. Valentini, "Topical Review: Time-resolved fluorescence imaging in biology and medicine", *J. of Phys. D: Appl. Phys.*, 35, R61-R76 (2002).
13. S. A Tatarkova, A. K. Verma, D. A Berk and C. J Lloyd, "Quantitative fluorescence microscopy of macromolecules in gel and biological tissue", *Phys. Med. Biol.*, 50, 5759–5768 (2005).
14. Armin Shmilovici, "Incomplete tumor volume reduction may improve cancer prognosis", *Med. Hypoth.*, 68, 1236-1239 (2007).
15. D. F. Gleason and G. T. Mellinger, "Prediction of prognosis for prostate adenocarcinoma by combined histological and clinical", *J. Urol*, 111, 58-64 (1974).
16. Y. Pu, W. B. Wang, G. C. Tang, F. Zeng, S. Achilefu, J. H. Vitenson, I. Sawczuk, S. Peters, J. M. Lombardo and R. R. Alfano, "Spectral polarization imaging of human prostate cancer tissue using a near-infrared receptor-targeted contrast agent", *Technol. Cancer Res. Treat.*, 4, 429-436 (2005).
17. Rodolfo Montironi, Adhemar Longatto Filho, Alfredo Santinelli, Roberta Mazzucchelli, Roberto Pomante, Paola Colanzi, Marina Scarpelli, "Nuclear changes in the normal-looking columnar epithelium adjacent to and distant from prostatic intraepithelial neoplasia and prostate cancer", *Virch. Arch*., 437, 625-634 (2000).

18. M. Xu, M. Alrubaue, S. K. Gayen and R. R. Alfano, "Determination of light absorption, scattering and anisotropy factor of a highly scattering medium using backscattered circularly polarized light", Optical interaction with tissue and cells XVIII, Proc. Of SPIE 6435, 64350J1-6 (2007).
19. B. B, Das, Feng Liu and R. R. Alfano, "Time-resolved fluorescence and photon migration studies in biomedical and model random media", *Rep. Prog. Phys*. 60, 227–292 (1997).
20. Rebekah Drezek, Konstantin Sokolov, Urs Utzinger, Iouri Boiko, Anais Malpica, Michele Follen, Rebecca Richards-Kortum, "Understanding the contributions of NADH and collagen to cervical tissue fluorescence spectra: Modeling, measurements, and implications", *J. Biomed. Opt.*, 6(4), 385–396 (2001).
21. C. Morrison, J. Thornhill, E. Gaffney, "The connective tissue framework in the normal prostate, BPH and prostate cancer: analysis by scanning electron microscopy after cellular digestion", *Urol. Res*, 28(5), 304-7 (2000).
22. Yicong Wu and Jiannan Y. Qu, "Combined depth- and time-resolved autofluorescence spectroscopy of epithelial tissue", *Opt. lett.*, 31(12), 1833-1835 (2006).
23. Anita C. Jones, "Biophotonics", http://www.chem.ed.ac.uk/teaching/chem4-5/resources/lectures/moduleE/biophotonicslectureACJ.pdf

Chapter 7

Conclusion and outlook for future research

In this thesis, I presented the experiment and the experimental results of steady state emission spectroscopy, time-resolved polarization-dependent emission spectroscopy and optical spectra polarization imaging to probe prostate cancer. The main focus of the thesis research is to gain knowledge to detect prostate cancer in association with and without receptor-targeted fluorescent contrast agents. The results demonstrated that near-infrared spectroscopy and imaging are promising emerging approaches for future clinical screening diagnosis and other important medical applications.

Both receptor-targeted contrast agents and intrinsic optical biomarker were studied. Optical coefficients (absorption, scattering and reduced scattering coefficients, and anisotropy factor) of cancerous and normal prostate tissues were measured and determined. An optical model that explains the observed scattering properties of biological tissues was studied. Such modeling can provide insight into how the scattering properties are influenced by the contents, sizes and arrangements of the tissue elements. Measurements on the diffusely scattered light have been used to study the distribution of different scatters with different size in tissue. This could have valuable applications in clinical diagnosis since these quantities are important indicators of neoplastic precancerous changes in biological tissues.

Similarly to other clinical spectroscopic and imaging modalities, contrast agents play an important role for prostate cancer detection in combination with spectral polarized technique and time-resolved fluorescence polarization spectroscopy. Optical spectral polarized imaging of Cybesin (Cytate) enhanced lesions showed that preferential adsorption of these optical contrast agents enhances the contrast between cancerous and normal areas in prostate tissue. Receptor-

targeted contrast agents may yield significant differentiation characteristics because of high affinity with cancerous cell. Excellent absorption and emission band of the contrast agents are optimized as discussed in Chapter 5 and chapter 6. There are many advantages for targeted contrast agents in the optical method to make it attractive for clinical applications. Besides being economical and portable, photonic technology can detect optical contrast agents with high sensitivity. There are many biological processes that cannot be easily or directly monitored by existing imaging techniques, because key intrinsic molecules in these processes are not easy to distinguish from each other with the existing technologies. The receptor-targeted contrast agents we studied may be used as highly specific cancer signatures at the cell level. The high sensitivity of the optical methods can then allow the detection and localization of disease before high stages. Advancement in optical imaging and contrast agent developments is mutually beneficial. Furthermore, the combination of absorbing or fluorescent probes with appropriate imaging systems and techniques may create a powerful modality for the detection of early cancers and push the detection limits of the current state-of-the-art. Time-resolved techniques are worth to be explored since it can provide information of the micro-environment of the medium. The works of contrast of intrinsic fluorophores was extended to NIR range by applying both steady-state and time-resolved polarized spectral wing (SW) emission techniques.

In the future, molecular optical imaging will be a growing research field, which aims to probe the malignancy in the cellular and molecular level, rather than the traditional morphological imaging. The synergic efforts in the developments of molecular specific imaging probes (including the chemical dyes and nano-materials such as quantum dots) and the advancements of optical imaging technologies (including the novel instrumentation and imaging algorithm) will lead to a new tool for early disease diagnosis and drug discovery. Although the

barriers of delivering those probes into the designated areas still remain to be understood and overcome, our research on the receptor-targeted contrast agents serves as the first step for molecular imaging. Fluorescence Resonance Energy Transfer (FRET) technique can be applied to quantify the distance from the contrast agents to the targets (cancerous cells), thus may provide a directly evidence of the active target mechanism of the receptor-targeted contrast agents at the cell level.

Although our preliminary results of cancer imaging with receptor-targeted contrast agents are only demonstrated in human tissue and small animals, this technology has great potential for clinical applications. The key issues are the development of novel receptor-targeted contrast agents and their approval from FDA for human studies. The corresponding instrumentation can be readily adapted for preclinical and/or clinical study. NIR light has been shown to penetrate through tissue deeply, thus has unique merit in detecting tumors inside organs such as the human prostate. Considering the prostate imaging systems, a patient-device interface has been proposed. The system can use probe with size as ultrasound imaging system. The excitation lasers are incidence using coherent fibers while the imaging is also output using an optical imaging fiber.

Another interesting prospect is to combine the detection and therapy together. One possible approach is photo-thermal ablation therapy using nanoparticles, in which nanoparticles consisting of dielectric silica (SiO_2) core coated with a thin metal shell, photo-sensitizer-stabilized gold nano-particles and the photo-cytotoxicity of the polymeric nanoparticles. These ceramic-based nanoparticles have a diameter of 100-200 nm and the coating is 10 nm thick. By manipulating the size of the silica core and the thickness of the gold shell, the plasma resonance response can be tuned to determine the absorbing and scattering properties of the particles, so that the nano-shell can be selectively activated. This makes the gold nanoparticles change the

property of the metal, making it absorb light from the near-infrared. After the injections of the nanoparticles, an external laser source of near infrared light is applied through the skin for 3-7 minutes. The gold nanoparticles readily absorb the energy and turn it into heat resulting in an average temperature increase of ~37 °C which induces irreversible cancerous tissue damage. The heating is localized and does not affect healthy tissue adjacent to the tumor. This non-invasive localized thermal ablation technology can be used to replace or supplement chemotherapy. The combination of diagnosis using NIR imaging and treatment using photo-thermal ablation system will be an attractive modality for both clinical diagnosis and therapy in the near future.

Appendix A
Theory of time-resolved fluorescence polarization decay in pico-second range

A. 1. Introduction:

Time-resolved polarized fluorescence spectroscopy is a technique widely used in chemistry and biology as a probe for rotational motions [1]. A fluorescent molecule, absorbing light at time *t*, can by virtue of local forces undergo a rotation within its lifetime of emission. This rotation affects the angle between the polarization vectors of absorption and emission, and is most sensitively detected when linearly polarized light is used to excite the molecule and when a particular component of polarization is observed in emission. A phenomenon was observed in the polarization spectroscopy within pico-second range measurements that the excitation of a isotropic molecular system with a linearly polarized light beam produces apparent changes of the measured decay lifetime for dye in solution [1-3]. This phenomenon leads another field of fluorescence technique: time-resolved polarized fluorescence spectroscopy, which can be used in chemistry and biology to provide information not only the location of bio-molecules but also their biophysical microenvironments [1].

In this appendix, I will investigate and demonstrate the origin of the changes by reviewing the time-resolved fluorescence polarization spectroscopy theory developed by G. Weber *et al* [3]. This theory is mainly based on the assumption that under specified conditions of temperature and viscosity in the nano-second scale, ordinary rate constants describe the equalization of the polarized intensity among the directions in space [3]. I will extend this model to the pico-second regimes to explore the effects of the molecular rotation to the fluorescence polarization spectroscopy. The rotational time and lifetime of the dipole measured by optical streak camera

are analyzed to check the consistency between the experimental data and the calculation value. A FDA approved contrast agent: dye ICG will be used to obtain decay time to compare with the theoretical values. The basis of the different decay rate two polarization components will be discussed iteratively and graphically to compare the parameters obtained from experiment and calculation. The results indicate the model behavior holds at pico-second range and calculated rotational time perfect agree with Einstein-stokes relationships.

A. 2. Theory of fluorescence depolarization

A. 2. 1. Rotation theory of polarized fluorescence in orthogonal system

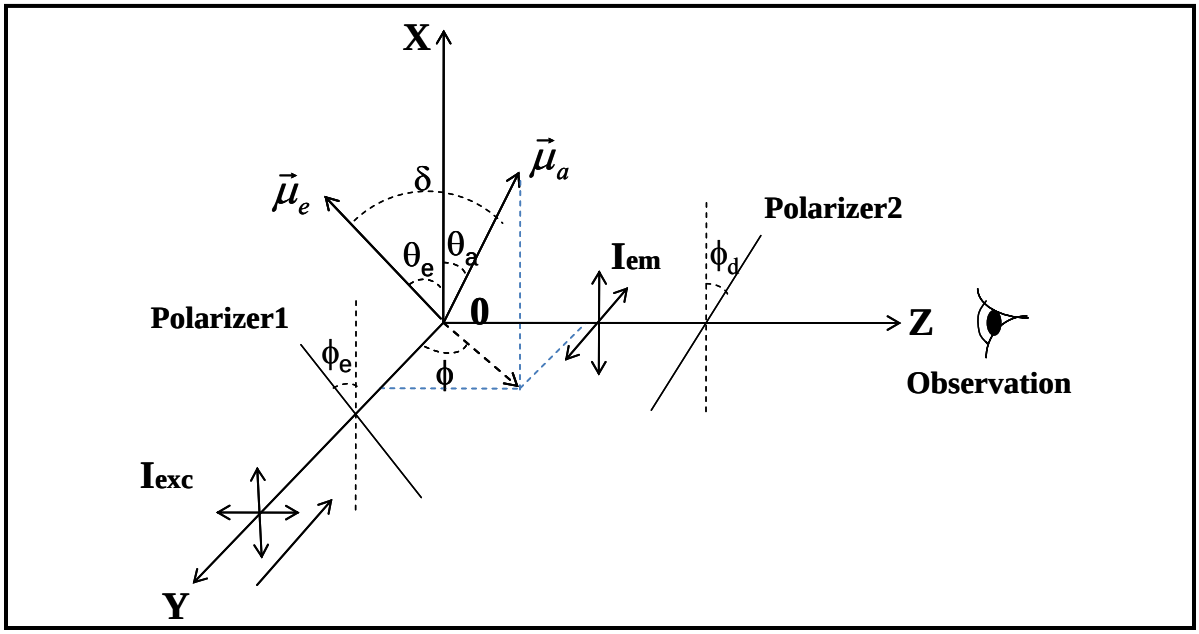

Fig. A-1 The orthogonal co-ordinate system used to study the influence of molecular rotation on the fluorescence decay rate. The fluorescent molecule is place at the origin. The exciting light pulses of an arbitrary linear polarization at angle ϕ_e propagate at the *YO* direction, and the angle ϕ_d define the polarizer introduced in the fluorescence beam. $\vec{\mu}_a$ and $\vec{\mu}_e$ represent the orientation of the absorption and the emission moments, respectively. δ is the angle between the absorption and emission dipoles.

We assume dye molecules placed at the center and along the x-axis of the co-ordinates excited by light pulse of an arbitrary linear polarization propagating at the *YO* direction at time t_0 as shown in Fig. A-1. The emission in all directions of dye molecule can be specified by the intensity from three sets of orthogonal dipoles oriented along the three Cartesian axes. Since any

random oriented dipole can be physically considered as the total effect of three projective sub-dipoles in X, Y and Z axis, we suppose that these three oriented molecular dipoles are the only allowed orientations of molecular dipoles, and that the molecules rotate from one direction to another at fixed rate. Fluorescence intensities from the certain orthogonal dipoles can be expressed by I_x, I_y and I_z, and the instantaneous change rates of the intensities at time t can be described by a set of first-order linear differential equations:

$$\begin{aligned} dI_x/dt &= P_x(t) - (\alpha + 2D_{xy} + 2D_{xz})\, I_x + 2D_{yx}\, I_y + 2D_{zx}\, I_z, \\ dI_y/dt &= P_y(t) + 2D_{xy}\, I_x - (\alpha + 2D_{yx} + 2D_{yz})\, I_y + 2D_{zy}\, I_z, \\ dI_z/dt &= P_z(t) + 2D_{xz}\, I_x + 2D_{yz}\, I_y - (\alpha + 2D_{zy} + 2D_{zx}) I_z, \end{aligned} \qquad \text{(A. 1)}$$

where $P_x(t)$, $P_y(t)$, $P_z(t)$ are functions defining the population of the dipoles corresponding to respective direction excited by the incident pumping light. α is the rate of emission changing, and D_{ij} are the rate describing the fluorescence intensity at direction i transferring to direction j, and i, j are expressions for x, y or z in Cartesian co-ordinate. The change of a dipole from one direction to another may have one of two opposite senses, so factor 2 should be included. In nature condition, the change of the polarization direction happens in two distinct processes: rotation of the emitting molecules or transfer of the excited state from one molecule to another. Experiments can be achieved to exclude one of these two possibilities (in our research, transfer of the excitation among molecules is excluded) so that we may consider the D's only as rates of the molecules' rotations, which simplify equation (A.1) considerably. Furthermore, studies of the fluorescence polarization of molecules in solution show that single rate of rotation is sufficient to characterize the observation in time-resolved spectroscopy [2]. On the other hand, the transfer of energy among randomly oriented molecules at a certain concentration involves a single rate,

independent of the external co-ordinates of the system. Therefore, setting of $D_{ij} = D$ can be use in equation (A. 1):

$$\begin{aligned} dI_x / dt &= P_x(t) - (\alpha + 4D) I_x + 2DI_y + 2DI_z, \\ dI_y / dt &= P_y(t) + 2DI_x - (\alpha + 4D) I_y + 2DI_z, \\ dI_z / dt &= P_z(t) + 2D\, I_x + 2DI_y - (\alpha + 4D) I_z. \end{aligned} \tag{A. 2}$$

Since the excitation beam is a single pulse beam, $P_x(t)$, $P_y(t)$ and $P_z(t)$ should have identical time dependence except for weighting factors κ_x, κ_y and κ_z which have the property of $\kappa_x+\kappa_y+\kappa_z=1$ determined by the degree of polarization of the excitation light. By adding the three equations of equation (A. 2), the total emitted fluorescence intensity observed at a certain rotation rate is given by:

$$dI / dt = d(I_x + I_y + I_z) / dt = P(t) - \alpha(I_x + I_y + I_z) = P(t) - \alpha I \ . \tag{A. 3}$$

Since the excitation pulse is very short, theoretically it is taken as delta function ($P(t)$=0), the total fluorescence intensity can be expressed as:

$$I(t) = I_0 e^{-\alpha t} . \tag{A. 4}$$

It is concluded that the total fluorescence intensity should show a simple exponential decay at rate α after the single short pulse excited. However, the decay of each component I_x, I_y and I_z depends on the rotation constant rate D and the initial distributed state (determined by weighting factors w_x, w_y, w_z) of the excitation $P(t)$. By applying a polarizer in the excitation light path and a polarizer in the emission with an angle to exciting, different weighting factors can be obtained. The depolarization will be observed, providing a way to extracting the rotation rate of the fluorescent molecules from one orthogonal component to another.

To solve equation (A. 2), we can re-write it by moving unknown I_x, I_y and I_z to the left-hand side, we get

$$\begin{vmatrix} d/dt+\alpha+4D & -2D & -2D \\ -2D & d/dt+\alpha+4D & -2D \\ -2D & -2D & d/dt+\alpha+4D \end{vmatrix} \begin{vmatrix} I_x \\ I_y \\ I_z \end{vmatrix} = \begin{vmatrix} w_x P(t) \\ w_y P(t) \\ w_z P(t) \end{vmatrix}, \quad \text{(A. 5)}$$

The solution is:

$$\boldsymbol{I}_i = \frac{\left[\kappa_i\left(\frac{\boldsymbol{d}}{\boldsymbol{dt}}+\alpha\right)+2\boldsymbol{D}\right]\boldsymbol{P}(\boldsymbol{t})}{\left(\frac{\boldsymbol{d}}{\boldsymbol{dt}}+\alpha\right)\left(\frac{\boldsymbol{d}}{\boldsymbol{dt}}+\alpha+6\boldsymbol{D}\right)}, \quad \text{(A. 6)}$$

By multiplying the denominator at both sides, the explicit expression is obtained:

$\frac{d^2 I_i(t)}{dt} + a\frac{dI_i(t)}{dt} + bI_i(t) = (\kappa_i\alpha + 2D)P(t) + \kappa_i\frac{dP(t)}{dt}$, where $a=2\alpha+6D$; $b=\alpha(\alpha+6D)$.

Introducing $P(t)=0$ (since excitation is a single short pulse and ceases after the excitation):

$$\frac{d^2 I_i(t)}{dt} + a\frac{dI_i(t)}{dt} + bI_i(t) = 0 .$$

To solving this homogeneous ordinary differential equation, we need find the roots of its characteristic equation:

$$z^2+(2\alpha+6D)z+\alpha(\alpha+6D)=0.$$

Solving it:

$$\boldsymbol{z} = \frac{-(2\alpha+6\boldsymbol{D}) \pm \sqrt{(2\alpha+6\boldsymbol{D})^2 - 4\alpha(\alpha+6\boldsymbol{D})}}{2} = \frac{-(2\alpha+6\boldsymbol{D}) \pm \sqrt{(4\alpha^2+24\alpha\boldsymbol{D}+36\boldsymbol{D}^2)-(4\alpha^2+24\alpha\boldsymbol{D})}}{2}$$
$$= \frac{-(2\alpha+6\boldsymbol{D}) \pm \sqrt{36\boldsymbol{D}^2}}{2} = \frac{-(2\alpha+6\boldsymbol{D}) \pm 6\boldsymbol{D}}{2}.$$

There exist 2 real roots: $z_1= -\alpha$ $z_2= -(\alpha+6D)$.

Thus the general solution of the ordinary differential equation is:

$$I_i(t)=C_1 e^{-\alpha t} + C_2 e^{-(\alpha+6D)t}.$$

Introducing boundary condition for the above solution and for $dI_i(0)/dt$ from equation (A. 2), which are the following:

$$I_i(0)=C_1 e^{-\alpha 0} + C_2 e^{-(\alpha+6D)0} = C_1 + C_2 \qquad \Rightarrow \quad C_1 = I_i(0) - C_2$$

$$dI_i(0)/dt = -(\alpha+4D)I_i(0)+2[I_0 - I_i(0)]D$$

$$= -\alpha I_i(0)-4DI_i(0)+2DI_0-2D\,I_i(0) = -\alpha I_i(0)-6DI_i(0)+2DI_0$$

where $I_0 = I_x(0)+ I_y(0)+ I_x(0)$, introducing boundary condition into above solution:

$$dI_i(0)/dt = -\alpha C_1 e^{-\alpha 0} - (\alpha+6D)\, C_2 e^{-(\alpha+6D)0} = -\alpha C_1 - (\alpha+6D)\, C_2$$

Combining the two equations for $dI_i(0)/dt$ and substituting $C_1 = I_i(0) - C_2$:

$$-\alpha I_i(0) + \alpha C_2 - \alpha C_2 - 6DC_2 = -\alpha I_i(0) - 6DI_i(0) + 2DI_0$$

$$-\alpha(I_i(0) - C_2) - (\alpha+6D)C_2 = -\alpha I_i(0)-6DI_i(0)+2DI_0$$

It is obtained that: $C_2 = I_i(0) - \frac{1}{3} I_0$, and $C_1 = \frac{1}{3} I_0$.

Introducing C_1 and C_2 into general solution, we get equation (A. 8) in the text

$$I_i(t) = \frac{1}{3} I_0 e^{-\alpha t} + (I_i(0) - \frac{1}{3} I_0) e^{-(\alpha+6D)t}. \qquad \text{(A. 8)}$$

Equation (A. 8) is the description for the decay of any orthogonal component after the excitation of light impulse. The fluorescence decay of one certain direction will not only depend on the fluorescence lifetime of that molecule showing a simple exponential decay, but also on the rotation constant rate D and the initial distributed state of the emission $I_i(0)$ which is actually determined by molecules' orientation distribution in the system and weighting factors κ_i of the excitation $P(t)$.

A. 2. 2. Parallel and perpendicular components of fluorescence excited by a linear polarized light

The distribution of excited molecules absorbing light at the time t_0 is determined by the weighting factor w_i and the orientation distribution function of dipoles. This distribution can be specified by r, the polarization anisotropy which is measured in the emission along direction OY by the excited light polarized along direction OX. The polarization anisotropy is defined by:

$$r = \frac{I_x - I_y}{I_x + I_y + I_z}. \tag{A. 9}$$

Suppose the pumping beam is polarized along OX, since excited molecules is symmetrical about the polarization direction of exciting light, $I_y = I_z$. Since I_i (i=x, y, z) is time-dependent, let $I_x = I_{||}$, $I_y = I_\perp$, equation (A. 9) is then reformed into a simpler but more familiar ways [5, 6],

$$r = \frac{I_{||}(t) - I_\perp(t)}{I_{||}(t) + 2I_\perp(t)}. \tag{A. 10}$$

At time t_0, the weighting factor w_i of the emission light can be obtained in term of r_0 (the value of r at t=0):

$$\begin{aligned} w_x &= \left.\frac{I_x}{I_x + I_y + I_z}\right|_{t=0} = \left.\frac{I_{||}}{I_{||} + 2I_\perp}\right|_{t=0} = \frac{1}{3}\cdot\left.\frac{I_{||} + 2I_\perp + 2(I_{||} - I_\perp)}{I_{||} + 2I_\perp}\right|_{t=0} = \frac{1}{3}(1 + 2r_0) \\ w_y &= w_z = \left.\frac{I_y}{I_x + I_y + I_z}\right|_{t=0} = \left.\frac{I_\perp}{I_{||} + 2I_\perp}\right|_{t=0} = \frac{1}{3}\cdot\left.\frac{I_{||} + 2I_\perp - (I_{||} - I_\perp)}{I_{||} + 2I_\perp}\right|_{t=0} = \frac{1}{3}(1 - r_0) \end{aligned}. \tag{A. 11}$$

Introduce equation (A. 11) into equation (A. 8) to substitute $I_i(0)=w_iI_0$, the free decay of the parallel and perpendicular components of the fluorescence: $I_\perp$ and $I_{||}$, excited by a linear polarized light along OX direction are obtained:

$$\begin{aligned} I_{||}(t) &= \frac{I_0}{3}\exp(-\alpha t)\left(1 + 2r_0\exp(-6Dt)\right) \\ I_\perp(t) &= \frac{I_0}{3}\exp(-\alpha t)\left(1 - r_0\exp(-6Dt)\right) \end{aligned}. \tag{A. 12}$$

Substituting equation (A. 12) into equation (A. 10), the time-resolved fluorescence polarization anisotropy can be written as:

$$r(t) = r_0\exp(-6Dt). \tag{A. 13}$$

The mean decay times of the polarized components $\langle t\rangle_{||}$ and $\langle t\rangle_\perp$ are defined as:

$$\langle t \rangle_{\parallel} = \frac{\int_0^{\infty} tI_{\parallel}(t)dt}{\int_0^{\infty} I_{\parallel}(t)dt}, \text{ and } \langle t \rangle_{\perp} = \frac{\int_0^{\infty} tI_{\perp}(t)dt}{\int_0^{\infty} I_{\perp}(t)dt}. \quad \text{(A. 14)}$$

Introducing equation (A. 12) into equation (A. 14) and performing integration, $\langle t \rangle_{\parallel}$ and $\langle t \rangle_{\perp}$ can be expressed as:

$$\langle t \rangle_{\parallel} = \alpha^{-1} \frac{1 + 2r_0[\alpha/(\alpha + 6D)]^2}{1 + 2r_0[\alpha/(\alpha + 6D)]}, \text{ and } \langle t \rangle_{\perp} = \alpha^{-1} \frac{1 - r_0[\alpha/(\alpha + 6D)]^2}{1 - r_0[\alpha/(\alpha + 6D)]}. \quad \text{(A. 15)}$$

From equation (A. 14), it is concluded that the average decay time of each polarized component is determined by the fluorescence decay rate α of the measured molecules, the rotational constant rate *D* and the initial distributed state of the emission, which can be described by r_0: the polarization anisotropy at t=0.

A. 2. 3. Lifetime, polarization anisotropy and rotation time of fluorescent molecules

Fluorescence is the emission of light due to the electric dipole transition from an excited electronic state to a lower state, usually the ground state. The decay of the fluorescence from excited molecules was schematically studied by A. Jablonskii known as Jablonskii diagram [4]. The fluorescence lifetime τ_F is strongly dependent upon the rate constant of radiate, intersystem crossing, internal conversion and dissociation [4]. The simple decay time measurement has been widely used in understanding the role of specific vibrational mode excitation in the radiative and non-radiative decay of certain compound molecules [4]. The fluorescence lifetime τ_F is usually obtained as the reciprocal of α from fitting the total temporal intensity profiles of fluorescence using equation (A. 3).

The molecule rotation was treated as Brownian motion by G. R. Fleming [1] and G. Porter [2]. The rotational rate *D* is also termed as rotational diffusion constant, and the rotation time of

the dipole is defined. Introducing $\tau_{rot}=(6D)^{-1}$, the time-resolved fluorescence polarization anisotropy shown in equation (6-13) will become [1, 2]:

$$r(t) = r_0 \exp(-6Dt) = r_0 \exp(-\frac{t}{\tau_{rot}}) . \quad \text{(A. 16)}$$

The decay behavior of r(t) is caused by the reorientation of excited molecules due to Brownian Motion [5]. Although Robert Brown is remembered as the discoverer of Brownian motion, it is Albert Einstein that predicted it in theoretical grounds and formulated a correct quantitative of it [6]. In a simple case where the fluorescent molecule undergoes Brownian rotation as an Einstein sphere or oblate, the rotational diffusion constant is determined by Stokes-Einstein relationship as: $D=kT/(6V\eta)$, where k is the Boltzmann constant, T is the absolute temperature, η is viscosity of the solvent, and V is the volume of simple molecule, for a sphere $V=(4/3)\pi a^3$, where a is radius of the sphere [1, 16. Applying this relationship to the fluorescent molecule as an Einstein spherical rotating molecule [1, 2], the rotation time of the dipole may be expressed as:

$$\tau_{rot} = (6D)^{-1} = \frac{\eta V}{kT} = \frac{4\pi\eta a^3}{3kT} . \quad \text{(A. 17)}$$

The parameter T is measurable, k is the Boltzmann constant, and structure and dimensions can be estimated from bond lengths and va der Waals radii [1]. The rotation time should be linearly dependent upon the viscosity of the solvent or the volume of the rotational fluorescent molecule.

The polarization anisotropy r_0 at $t=0$ actually specify the initial orientation of the excited molecules. r_0 is derived from a normalized probability distribution function of dipoles $f(\theta)$ depending on the angle θ between the long axis of the molecule and the major symmetry axis of the system as shown in Fig. A-1 [1]. It is difficult to obtain. This function, however, may be

reproduced with accuracy sufficient for most purposes by a truncated series expansion involving the Legendre polynomial, thus, $r_0$is given by:

$$r_0 = \left(\frac{2 < P_2^2 > + < P_2 >}{1 + 2 < P_2 >} \right) P_2(\cos\delta), \tag{A. 18}$$

where δ is the angle between the absorption and emission dipoles, which is zero at time t_0. $<P_2>$ is the expectation value of the second order Legendre polynomial for the distribution function of dipoles $f(\theta)$, which is given by:

$$< P_2 > \equiv < P_2(\cos\theta) > = \int_0^{\pi} \sin\theta d\theta \, f(\theta) \, P_2(\cos\theta), \tag{A. 19}$$

For our case of fluorescent molecules in solution with low viscosity, the random orientation distribution function $f(\theta)$=1/2 is taken. Using equations (A. 18) and (A. 19), the theoretical value of r_0 is calculated to be 0.4.

Introducing a fluorescence lifetime of a molecules defined as $\tau_F=1/\alpha$, and $\tau_{rot}=(6D)^{-1}$, in to equation (A. 12), the time-dependent fluorescence intensity of the parallel and perpendicular components can be expressed in terms τ_F, τ_{rot} and r_0:

$$I_{\parallel}(t) = \frac{I_0}{3} \exp(-\frac{t}{\tau_F}) \left(1 + 2 r_0 \exp(-\frac{t}{\tau_{rot}}) \right) \qquad I_{\perp}(t) = \frac{I_0}{3} \exp(-\frac{t}{\tau_F}) \left(1 - r_0 \exp(-\frac{t}{\tau_{rot}}) \right). \tag{A. 20}$$

The total fluorescence intensity I(t) can be also reformed as:

$$I(t) = I_{\parallel}(t) + 2\, I_{\perp}(t) = I_0 \exp(-\frac{t}{\tau_f}), \tag{A. 21}$$

From equation (A. 20), three typical conditions related to the fluorescence lifetime τ_F and rotation time τ_{rot} of molecules can be discussed: (1) When $\tau_{rot} \langle\langle \tau_F$, the redistribution of the fluorescence polarization among different polarized components is very quick, and as a result, they differ little from each other right after the emission under the investigated time scale of the

dipole's lifetime [3]. The physical phenomenon is that the fast rotations of the dipoles cause quick depolarization of the fluorescence. (2) When $\tau_{rot} \rangle\rangle \tau_F$, the rotation of diploes are very slow during the lifetime of emission and therefore, the polarization of fluorescence is always observed at the maximum degree of the system [3]. (3) When $\tau_{rot} \approx \tau_F$, the rotation time and fluorescence lifetime of the dipole is on same timescale. The decay time of $I_{\|}(t)$ and $I_{\perp}(t)$ are affected by both re-orientation and fluorescence decay of molecules [3] so that the depolarization evolution can be observed as time dependent *r(t)*. This is the reason that time-resolved fluorescence polarization measurements can be used to investigate the rotation of the molecules.

By introducing τ_{rot} and τ_F, the average decay time of the polarized components $\langle t \rangle_{\|}$ and $\langle t \rangle_{\perp}$ shown in equation (A. 15) can be expressed as:

$$\langle t \rangle_{\|} = \tau_F \frac{1 + 2r_0\left[\tau_{rot}/(\tau_{rot} + \tau_F)\right]^2}{1 + 2r_0\left[\tau_{rot}/(\tau_{rot} + \tau_F)\right]} \qquad \langle t \rangle_{\perp} = \tau_F \frac{1 - r_0\left[\tau_{rot}/(\tau_{rot} + \tau_F)\right]^2}{1 - r_0\left[\tau_{rot}/(\tau_{rot} + \tau_F)\right]}. \quad \text{(A. 22)}$$

A. 3. Study of time-resolved polarization spectroscopy of ICG in picosecond range

A. 3. 1. Time-resolved fluorescence depolarization of ICG solution

To extend the time-resolved polarization theory to picosecond range, we studied the temporal profiles of the polarization-dependent fluorescence emitted from ICG aqueous solution for two polarization directions, parallel and perpendicular to the polarization of the excitation at 800 nm. These data will be used to extract the lifetime and rotation time of ICG in solution and are shown in Fig. A-2(a). The thin-dot and thin-dash line profiles represent the parallel $I_{\|}(t)$ and perpendicular $I_{\perp}(t)$ components, respectively. The obvious differences between parallel and perpendicular components shown by Fig. A-2(a) are: (1) the intensity of $I_{\|}$ is greater than that of $I_{\perp}$ for all decay times. The peak intensity of the parallel component $I_{\|}(0)$ is almost three times stronger than that of the perpendicular component $I_{\perp}(0)$. This indicates the polarization

preservation nature of ICG. (2) There is a distinct difference between the decay slopes of the two polarization components, which can be seen clearly by normalizing the peak of the perpendicular (thin-dashed line) and parallel (thin-solid line) components to the total intensity, which is obtained using equation $I(t)=I_{\perp}(t)+2I_{||}(t)$ shown as the thin-dot line in Fig.2(b).

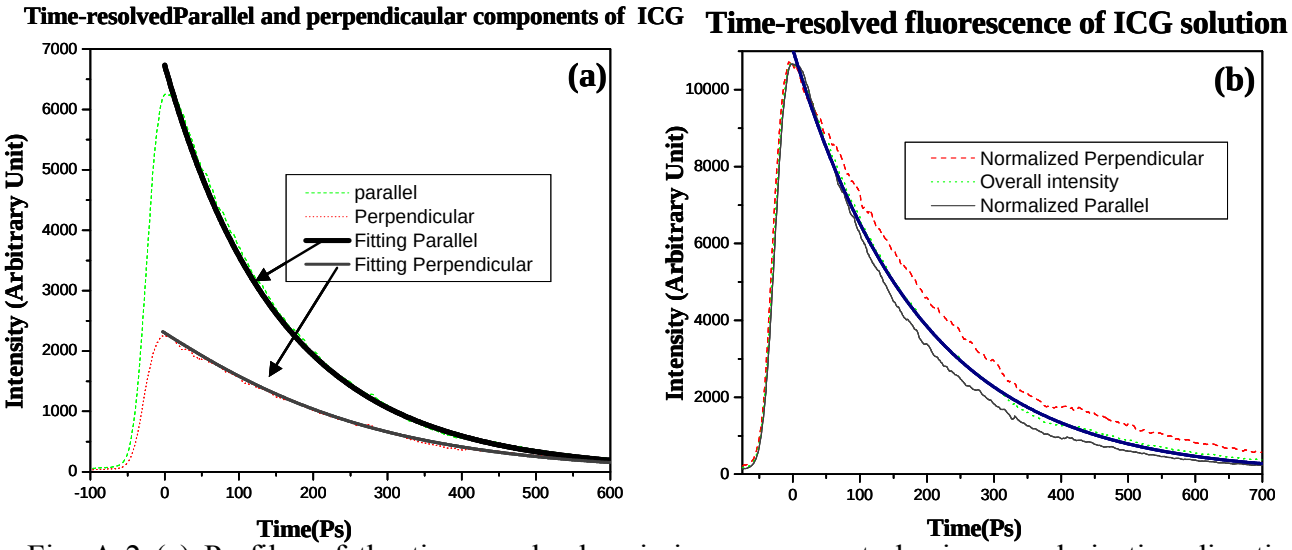

Fig. A-2 (a) Profiles of the time-resolved emission components having a polarization direction parallel (dot line) and perpendicular (dashed line) to the polarization direction of the exciting light. The fitting lines are obtained by using equation (A. 20). (b) Comparison of the decay rate among the normalized perpendicular component (thin-dashed line), the total fluorescence intensity (thin-dot line), and the normalized parallel component (thin-solid line). The fitting curve of temporal total fluorescence intensity (thick line) calculated using equation (A. 21).

This distinct difference was observed in all of previous time-resolved experiments [1-5]. The origin of this deviation was not pointed out and explained. In this study, we will discuss the affect of rotation, initial orientation and the lifetime of the fluorescent molecules to the decay rates of the measured $I_{\perp}(t)$ and $I_{||}(t)$.

The simple time-resolved measurements are widely used in acquiring fluorescence lifetime τ_F by fitting the total temporal fluorescence intensity using equation (A. 21). The fitting curve for the time-resolved fluorescence data indicated in Fig. A-2 (b) is shown by the thick-solid line in

Fig. A-2 (b) gained by equation (6-21). The parameters generated from the fitting are: I_0= 11321.43±216.15 and τ_F =192.46±5.28.

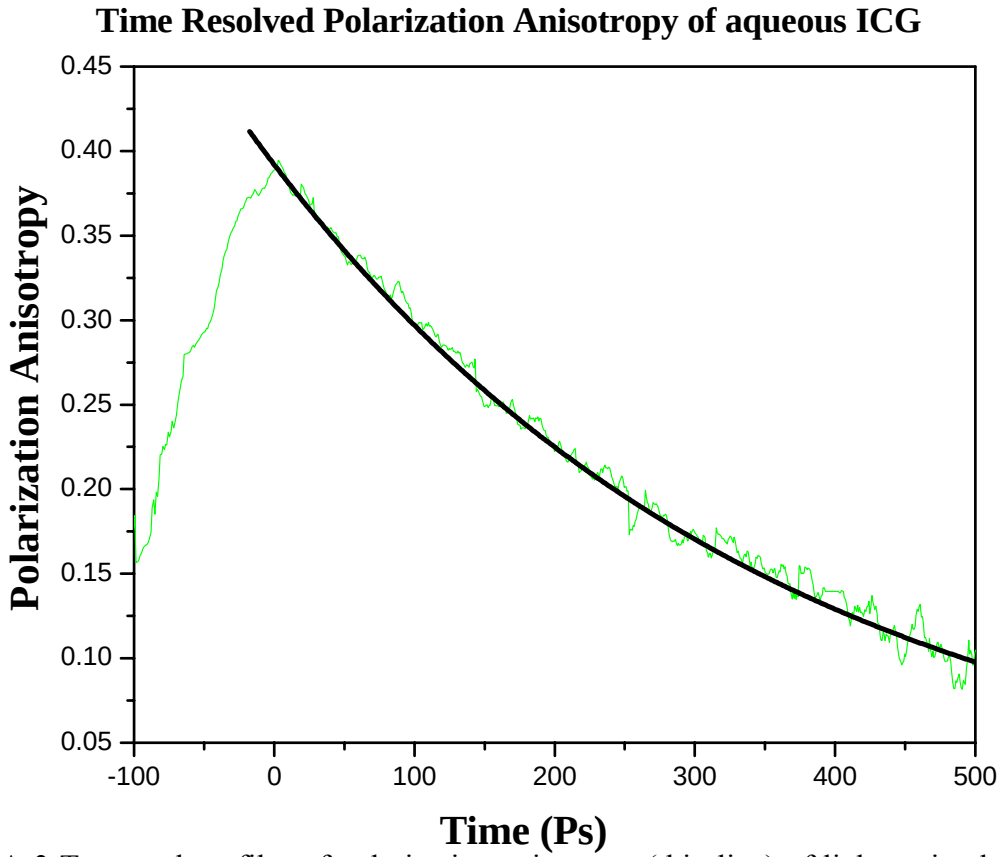

Fig. A-3 Temporal profiles of polarization anisotropy (thin line) of light emitted from ICG in aqueous solution. Time-dependent polarization anisotropy calculated using the measured data shown in Fig. A-2 (a) and equation (A.110). The fitting curve (thick line) calculated using equation (A. 16).

The causes for faster decay rate of parallel component of fluorescent molecule in comparison with perpendicular component in pico-second range are now investigated using the theory iterated in section A. 2 and the time-resolved spectroscopy profiles of ICG. The time-resolved polarization anisotropy can be calculated using equation (A. 10). The thin line in Fig. A-3 displays the time evolution of polarization anisotropy r(t). The decay behavior of r(t) reflects the dipole reorientation of ICG in solvent since the degree of polarization of the fluorescence depends on the rotation time and fluorescence lifetime of the molecules as we discussed in

section A. 2. 3. Polarization anisotropy found in our experiments suggests that rotation time τ_{rot} of ICG molecule is on the same order of magnitude as fluorescence lifetime τ_F.

The polarization anisotropy peak value r_0 and the rotation time τ_{rot} of ICG in solution can be obtained using equation (A. 16) to fit the experimental data of r(t) shown in Fig. A-3. The fitting curve calculated using the experimental data of r(t) and equation (A. 16) is shown by the thick line in Fig. A-3. The fitting results show τ_{rot}=353.37±10.55ps and r_0=0.391±0.0238 (r_0 is very close to the theoretical value of 0.4). This indicates that the transition dipole moments of ICG molecules in aqueous solution are randomly oriented and that the depolarization effects of ICG aqueous solution can be confined to molecular rotations and to the trivial effect of initial randomness [1].

Simple molecule as ICG in low viscosity solution undergoes Brownian rotation. The rotation time of ICG molecules in ~5μM can be calculated using equation (A. 17), and the parameters of $\eta=1.003\times10^{-3}$ Pa·s, T=293 (20°C), $k\approx1.380\times10^{-23}$ and semi-axes as 13 angstrom and 2 angstrom of ICG estimated as a oblate from bond length and van der Waals radii [7, 8]. The calculated rotation time of ICG is $\tau_{rot} \approx 351.02$ps, which is very close to the experimental fitting value. This indicates the experimental circumstance is perfectly matches the condition assumed by Stokes-Einstein relationship [6]. Introducing the values of I_0 and τ_F from fitting, and r_0 and τ_{rot} from theoretical calculation, the curves of the decay parts of $I_\perp(t)$ and $I_\parallel(t)$ are plotted as thick solid lines (each is pointed out in graph, respectively) in Fig. A-2 (a) by using equation (A. 12). The excellent results produce good match of theory and experimental data.

In order to compare the mean decay time of the experimental data with the theoretical calculation, the decay times $\langle t\rangle_\parallel$ and $\langle t\rangle_\perp$ for $I_\parallel(t)$ and $I_\perp(t)$, respectively, can be calculated using equation (A. 22) and values of τ_F =192.46, r_0=0.4 and $\tau_{rot} \approx 351.02$ps. The calculated results are

$\langle t\rangle_{\parallel}$ = 169.79ps and $\langle t\rangle_{\perp}$ = 244.91ps. The experimental values of $\langle t\rangle_{\parallel}$ and $\langle t\rangle_{\perp}$ can be obtained by fitting the time-resolve data of $I_{\parallel}(t)$ and $I_{\perp}(t)$ shown in Fig. A-2 (a) as single exponential decay function. The fitting results gives that $\langle t\rangle_{\parallel}$ =169.35±4.58ps and $\langle t\rangle_{\perp}$=239.15±6.48ps. The theoretical and experimental values of the mean decay times are in good agreement. The results of $\langle t\rangle_{\parallel} \langle \tau_F \langle \langle t\rangle_{\perp}$ indicate that the decay of the parallel component is faster than the total decay, and the decay of the total emission intensity I_{total} is faster than the perpendicular component. In fact, equation (A. 22) clearly shows the property of $\langle t\rangle_{\parallel} \langle \tau_F \langle \langle t\rangle_{\perp}$ while τ_F and τ_{rot} are on the time scale.

In order to schematically show the affect of rotation component (rc(t)) to decay of $I_{\parallel}(t)$ and $I_{\perp}(t)$, Fig. A-4 shows the curves of $rc_{\parallel}(t)$ and $rc_{\perp}(t)$ derived equation (A. 20) and (A. 21) as a function of *t*, that indicate the influence of the rotational component to changes of $I_{\perp}(t)$ and $I_{\parallel}(t)$, as defined by the following equations:

$$rc_{\parallel}(t) = \frac{3I_{\parallel}(t)}{I(t)} = \frac{I_0 \exp(-\frac{t}{\tau_F})\left(1 + 2r_0 \exp(-\frac{t}{\tau_{rot}})\right)}{I_0 \exp(-\frac{t}{\tau_F})} = 1 + 2r_0 \exp(-\frac{t}{\tau_{rot}})$$
$$rc_{\perp}(t) = \frac{3I_{\perp}(t)}{I(t)} = \frac{I_0 \exp(-\frac{t}{\tau_F})\left(1 - r_0 \exp(-\frac{t}{\tau_{rot}})\right)}{I_0 \exp(-\frac{t}{\tau_{rot}})} = 1 - r_0 \exp(-\frac{t}{\tau_{rot}}) \quad \text{(A .23)}$$

The thin-dot lines stand for the experimental data, and the thick-solid lines show the fitting curves from the theoretical calculation. The influence of the rotation to $I_{\perp}(t)$ evidently increases with *t* while that to $I_{\parallel}(t)$ decreases with *t*. Even $I_{\perp}(t)$ and $I_{\parallel}(t)$ emitted from same molecule with same fluorescence lifetime, the influence of the molecules' Brownian rotation causes decay of parallel intensity component faster than the perpendicular component when the fluorescence lifetime τ_F and the rotation time τ_{rot} of the molecule are on same order.

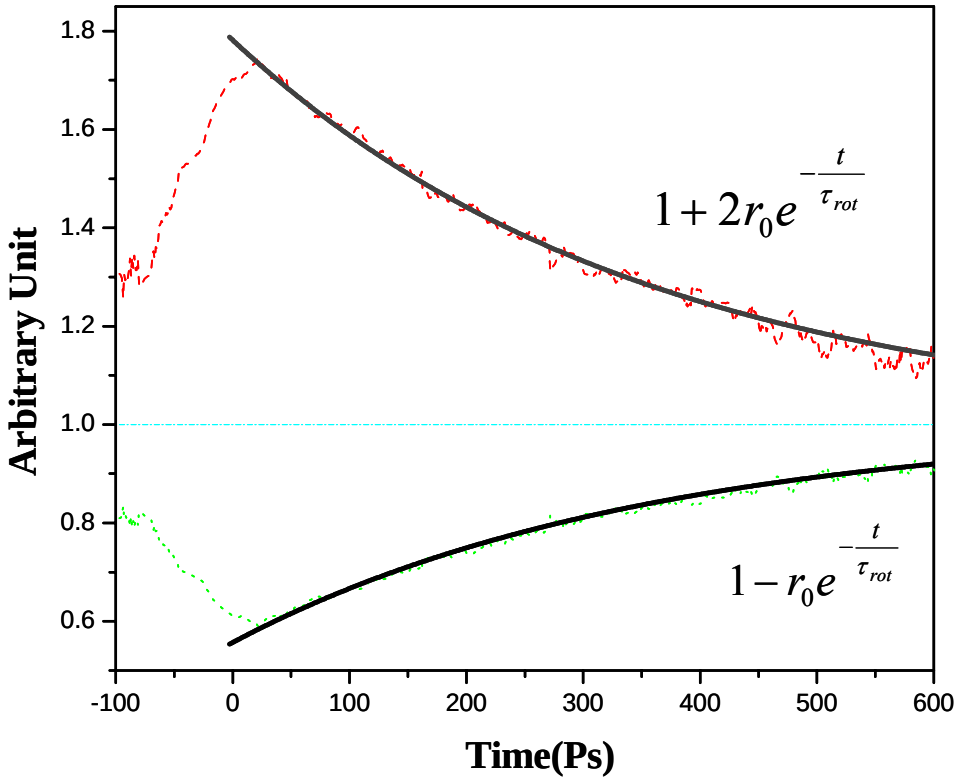

Fig. A-4 The influence of the rotation on the decay rate of ICG. The temporal contributions of rotation to || and ⊥ component are obtained use equation (A. 23) in the text. The thin-dot lines stand for the experimental data, and the thick-solid lines are fitting from the theoretical calculation (each is pointed out in graph, respectively). The trend of the influence of the rotation to $I_{\perp}(t)$ evidently rises up while that to $I_{\parallel}(t)$ drops.

Rotation of the transition dipole, however, is not the only cause of fluorescence depolarization, as intermolecular excitation transfer, effects within the molecule intrinsic to its electronic properties, or relaxation mechanisms can effect angular displacements. However, for a strong absorber emitting from the initially excited electronic state, it is usually safe to assume that intra-molecular depolarization is absent, and if solutions are sufficiently dilute, excitation transfer, including re-absorption of emitted light, can be safely ignored.

For the convenience, all the experimental and calculated parameters for ICG are listed and compared in Table A-1:

Table A-1: Comparison of the experimental and theoretical data of ICG

Type of Data	r_0	τ_{rot}	$\langle t \rangle_{\parallel}$	τ_F	$\langle t \rangle_{\perp}$
Experimental	0.39±0.02	353.4±10.6	169.4±4.6	192.5±5.3	239.2±6.5
Theoretical	0.4	351.0	163.8	----	244.9

A. 4. Summary

We have investigated theoretically and experimentally a phenomenon that when an isotropic fluorescent molecular system is excited by a linearly polarized light beam, the intensity decay of the fluorescence component polarized parallel to the exciting beam is faster than that of the fluorescence component perpendicular to the exciting beam. This phenomenon can be understood with the time-resolve fluorescence depolarization caused by the Brownian rotation of the dipoles. For simple and stable molecule, the effect of Brownian rotation is the main cause of the depolarization.

References:

1. G. R. Fleming, J. M. Morris and G. W. Robinson, "Direct observation of rotational diffusion by pico-second spectroscopy", *Chem. Phys.*, 17, 91-100 (1976).
2. G. Porter, P. J. Sadkowski and C. J. Tredwell, "Pico-second rotational diffusion in kinetic and steady state fluorescence spectroscopy", *Chem. Phys. Lett.*, 49, 416-420, (1977).
3. R. D. Spencer and G. Weber, "Influence of Brownian rotations and energy transfer upon the measurements of fluorescence lifetime". *J. Chem. Phys*. 52, 1654-1663 (1970).
4. D. V. O'Connor and D. Phillips, "Time-correlated single photon counting, Chapter 1, Fluorescence, its time dependence and applications", *The royal Institution, London, UK, Copy right@Academic Press, (1984)*
5. Y. Pu, W. B. Wang, B. B. Das, S. Achilefu, and R. R. Alfano, "Time-resolved fluorescence polarization dynamics and optical Imaging of Cytate: a prostate cancer receptor-targeted contrast agent", *Appl. Opt.*, 47, 2281-2289 (2008).
6. A. Einstein. "Zur Theorie der Brownschen Bewegung", *Ann. Phys.* 19 371, (1906); also translated into English: "Investigations on the theory of the Brownian Movement", Dover, New York, (1956).
7. S. Hell, "Size Matters: How big are molecules", http://www.bbc.co.uk/dna/h2g2/A791246
8. J. E. Bugaj, S. Achilefu, R. B. Dorshow, R. Rajagopalan, "Novel Fluorescent contrast agents for optical imaging of *in vivo* tumors based on a receptor-targeted dye-peptide conjugate platform", *J. Biomed. Opt.*, 6(2), 122-133 (2001).

Appendix B
MATLAB codes for simulation and calculation

Appendix B provides some important MATLAB codes developed for simulation and calculation in this thesis. The purposes and/or the function of each MATLAB code in this work are presented at the beginning of each program.

B. 1. Set of functions for Mie scattering calculation of homogenous spheres

```
function [S11,S12,S33,S34,POL] = Mie_BHSPHERE_S_YP(x, refrel,ang)

%%%%%%%%%%%%%%%%%%%%%%%%%%%%%%%%%%%%%%%%%%%%%%%%%%%%%%%%%%%%%%%%%%%%%%%%%%%%
%function  Mie_BHSPHERE_S_YP CALCULATES, the so-called Mueller Matrix,%
%a 4x4 matrix which relates an input vector of Stokes parameters      %
%(Ii, Qi, Ui, Vi)describing a complex light source and output vector  %
%(Is, Qs, Us, Vs) describing the nature of the transmitted light.     %
%                                                                     %
%ALGORITHM DESCRIBED HERE IS VERSION OF BH FOR HOMOGENEOUS SPHERE     %
% P 477-481 in Bohren and Huffman (1983) ISBN 0-471-05772-X           %
%                                                                     %
% Yang Pu, August 2008                                               %
%%%%%%%%%%%%%%%%%%%%%%%%%%%%%%%%%%%%%%%%%%%%%%%%%%%%%%%%%%%%%%%%%%%%%%%%%%%%

    theta=ang*pi/180;
    amu=cos(theta);
    Nang = length(theta);
    ppi0(1:Nang)=0.0;
    ppi1(1:Nang)=1.0;
    S1(1:2*Nang-1)=complex(0.0,0.0);
    S2=S1;
    Q_sca=0.0;
    [aN, bN]= Mie_BHSPHERE_ab_YP(x, refrel);
    for I=1:length(aN)
        RN=I;
        FN=(2.*RN+1)/(RN.*(RN+1));
        a=aN(I);b=bN(I);
        Q_sca=Q_sca+(2.*RN+1).*(abs(a).*abs(a)+abs(b).*abs(b));
        for J=1:Nang
            JJ=2*Nang-J;
            ppi(J)=ppi1(J);
            tau(J)=RN.*amu(J).*ppi(J)-(RN+1).*ppi0(J);
            P=(-1).^(RN-1);
            S1(J)=S1(J)+FN.*(aN(I).*ppi(J)+bN(I).*tau(J));
            T=(-1).^(RN);
            S2(J)=S2(J)+FN.*(aN(I).*tau(J)+bN(I).*ppi(J));
            if (J==JJ)
               continue
            else
            S1(JJ)=S1(JJ)+FN.*(aN(I).*ppi(J).*P+bN(I).*tau(J).*T);
            S2(JJ)=S2(JJ)+FN.*(aN(I).*tau(J).*T+bN(I).*ppi(J).*P);
            end
```

```
        end
        RN=RN+1;
            for J=1:Nang
               ppi1(J)=((2.*RN-1)/(RN-1))*amu(J).*ppi(J);
               ppi1(J)=ppi1(J)-RN.*ppi0(J)./(RN-1);
               ppi0(J)=ppi(J);
           end
    end
    Q_sca=(2./(x.*x)).*Q_sca;
    Q_ext=(4./(x.*x)).*real(S1(1));
    Q_back=(4./(x.*x)).*abs(S1(2*Nang-1)).*abs(S1(2*Nang-1));

    S11NOR=0.5.*(abs(S2(1)).*abs(S2(1))+abs(S1(1)).*abs(S1(1)));

    for J1=1:2*Nang-1
        AJ=J1;
        SS11=0.5*abs(S2(J1)).*abs(S2(J1));
        SS11=SS11+0.5*abs(S1(J1)).*abs(S1(J1));
        SS12=0.5.*(abs(S2(J1)).*abs(S2(J1))-abs(S1(J1)).*abs(S1(J1)));
        TPOL(J1)=-SS12/SS11;
        SS33=real(S2(J1).*conj(S1(J1)));
        SS34=imag(S2(J1).*conj(S1(J1)));
        TS33(J1)=SS33./SS11;
        TS34(J1)=SS34./SS11;
        TS11(J1)=SS11./S11NOR;
        TS12(J1)=SS12;
        thetaF(J1)=0.5*pi.*(AJ-1)/(Nang-1);
    end
   hal=(length(thetaF)-1)/2;
   dthetaF=thetaF(2)-thetaF(1);
   POL=TPOL(1:hal+1);
   S11=TS11(1:hal+1);
   S12=TS12(1:hal+1);
   S33=TS33(1:hal+1);
   S34=TS34(1:hal+1);


function Q_eff = Mie_BHSPHERE_effic_YP(x, refrel)

%%%%%%%%%%%%%%%%%%%%%%%%%%%%%%%%%%%%%%%%%%%%%%%%%%%%%%%%%%%%%%%%%%%%%%%%%%%%
%function Mie_BHSPHERE_effic_YP CALCULATES SCATTERING MATRIX ELEMENTS %
%AND EFFICIENCIES FOR EXTINCTION AND SCATTERING FOR A GIVEN SIZE      %
%PARAMETER AND RELATIVE REFRACTIVE INDEX                              %
%                                                                     %
%ALGORITHM DESCRIBED HERE IS VERSION OF BH FOR HOMOGENEOUS SPHERE     %
% P 477-481 in Bohren and Huffman (1983) ISBN 0-471-05772-X           %
%                                                                     %
% Yang Pu, August 2008                                               %
%%%%%%%%%%%%%%%%%%%%%%%%%%%%%%%%%%%%%%%%%%%%%%%%%%%%%%%%%%%%%%%%%%%%%%%%%%%%

if x==0                 % To avoid a singularity at x=0
    Q_eff=[0 0 0];
Else

    ang=[0:.5:180];
```

```
theta=ang*pi/180;    %dtheta=theta(2)-theta(1);
amu=cos(theta);
Nang = length(theta);
ppi0(1:Nang)=0.0;
ppi1(1:Nang)=1.0;
S1(1:2*Nang-1)=complex(0.0,0.0);
S2=S1;
Q_sca=0.0;
[aN, bN]= Mie_BHSPHERE_ab_YP(x, refrel);
for I=1:length(aN)
    RN=I;
    FN=(2.*RN+1)/(RN.*(RN+1));
    a=aN(I);b=bN(I);
    Q_sca=Q_sca+(2.*RN+1).*(abs(a).*abs(a)+abs(b).*abs(b));
    for J=1:Nang
        JJ=2*Nang-J;
        ppi(J)=ppi1(J);
        tau(J)=RN.*amu(J).*ppi(J)-(RN+1).*ppi0(J);
        P=(-1).^(RN-1);
        S1(J)=S1(J)+FN.*(aN(I).*ppi(J)+bN(I).*tau(J));
        T=(-1).^(RN);
        S2(J)=S2(J)+FN.*(aN(I).*tau(J)+bN(I).*ppi(J));
        if (J==JJ)
           continue
        else
        S1(JJ)=S1(JJ)+FN.*(aN(I).*ppi(J).*P+bN(I).*tau(J).*T);
        S2(JJ)=S2(JJ)+FN.*(aN(I).*tau(J).*T+bN(I).*ppi(J).*P);
        end
    end
    RN=RN+1;
        for J=1:Nang
           ppi1(J)=((2.*RN-1)/(RN-1))*amu(J).*ppi(J);
           ppi1(J)=ppi1(J)-RN.*ppi0(J)./(RN-1);
           ppi0(J)=ppi(J);
       end
end
Q_sca=(2./(x.*x)).*Q_sca;
Q_ext=(4./(x.*x)).*real(S1(1));
Q_back=(4./(x.*x)).*abs(S1(2*Nang-1)).*abs(S1(2*Nang-1));

S11NOR=0.5.*(abs(S2(1)).*abs(S2(1))+abs(S1(1)).*abs(S1(1)));

for J1=1:2*Nang-1
    AJ=J1;
    SS11=0.5*abs(S2(J1)).*abs(S2(J1));
    SS11=SS11+0.5*abs(S1(J1)).*abs(S1(J1));
    SS12=0.5.*(abs(S2(J1)).*abs(S2(J1))-abs(S1(J1)).*abs(S1(J1)));
    POL=-SS12/SS11;
    SS33=real(S2(J1).*conj(S1(J1)));
    SS34=imag(S2(J1).*conj(S1(J1)));
    TS33(J1)=SS33./SS11;
    TS34(J1)=SS34./SS11;
    TS11(J1)=SS11./S11NOR;
    TS12(J1)=SS12;
    thetaF(J1)=0.5*pi.*(AJ-1)/(Nang-1);
end
```

```
   hal=(length(thetaF)-1)/2;
   dthetaF=thetaF(2)-thetaF(1);
   S11=TS11(1:hal);
   S12=TS12(1:hal);
   S33=TS33(1:hal);
   S34=TS34(1:hal);
   g=sum(S11.*cos(thetaF(1:hal)).*sin(thetaF(1:hal)).*2*pi*dthetaF);
   g=g./(sum(S11.*sin(thetaF(1:hal)).*2*pi*dthetaF));
   Q_eff=[Q_sca;Q_ext;g;Q_back];
end


function [aN, bN]= Mie_BHSPHERE_ab_YP(x, refrel)

%%%%%%%%%%%%%%%%%%%%%%%%%%%%%%%%%%%%%%%%%%%%%%%%%%%%%%%%%%%%%%%%%%%%%%%%%%%%
%function  Mie_SPHERE_ab_YP CALCULATES A MATRIX OF MIE Coefficients   %
%aN, bN SCATTERING MATRIX ELEMENTS A GIVEN SIZE PARAMETER AND RELATIVE%
%REFRACTIVE INDEX                                                     %
%BESSEL FUNCTIONS J(N) AND Y(N) COMPUTED BY DOWNWARD RECURRENCE       %
%                                                                     %
%ALGORITHM DESCRIBED HERE IS VERSION OF BH FOR HOMOGENEOUS SPHERE     %
% P 477-481 in Bohren and Huffman (1983) ISBN 0-471-05772-X           %
%                                                                     %
% Yang Pu, August 2008                                               %
%%%%%%%%%%%%%%%%%%%%%%%%%%%%%%%%%%%%%%%%%%%%%%%%%%%%%%%%%%%%%%%%%%%%%%%%%%%%

y=x*refrel;

%%%%%%%%%%%%%%%%%%%%%%%%%%%%%%%%%%%%%%%%%%%%%%%%%%%%%%%%%%%%%%%%%%%%%%%%%%%%
%    SERIES TERMINATED AFTER NSTOP TERMS                              %
%%%%%%%%%%%%%%%%%%%%%%%%%%%%%%%%%%%%%%%%%%%%%%%%%%%%%%%%%%%%%%%%%%%%%%%%%%%%

nstop=round(2+x+4.*x.^(1/3));
ymod=round(abs(y));
Nmx=max(nstop,ymod)+15;

%%%%%%%%%%%%%%%%%%%%%%%%%%%%%%%%%%%%%%%%%%%%%%%%%%%%%%%%%%%%%%%%%%%%%%%%%%%%
%    LOGRITHMIC DERIVATIVE G(J) CALCULATED BY DOWNWARD RECURRENCE     %
%     BEGINNING WITH INITIAL VALUE 0.0+I*0.0 AT J = NMX               %
%%%%%%%%%%%%%%%%%%%%%%%%%%%%%%%%%%%%%%%%%%%%%%%%%%%%%%%%%%%%%%%%%%%%%%%%%%%%

D(Nmx)=0+0i;
for NN=1:Nmx-1
    RN=Nmx-NN+1;
    k=Nmx-NN;
    D(k)=(RN/y)-1./(D(k+1)+RN/y);
end

%%%%%%%%%%%%%%%%%%%%%%%%%%%%%%%%%%%%%%%%%%%%%%%%%%%%%%%%%%%%%%%%%%%%%%%%%%%%
%    RICCATI-BESSEL FUNCTIONS WITH REAL ARGUMENT X                    %
%    CALCULATED BY UPWARD RECURRENCE                                  %
%%%%%%%%%%%%%%%%%%%%%%%%%%%%%%%%%%%%%%%%%%%%%%%%%%%%%%%%%%%%%%%%%%%%%%%%%%%%

psi0=cos(x); psi1=sin(x); chi0=-sin(x); chi1=cos(x);
apsi0=psi0;
apsi1=psi1;
```

```
xi0=complex(apsi0,-chi0);
xi1=complex(apsi1,-chi1);

Q_sca=0.0;   %N=1;

for N=1:nstop-1    %if  N<nstop
    DN=N; RN=N;
    FN=(2.*RN+1)/(RN.*(RN+1));
    psi=(2.*DN-1)*psi1/x-psi0;
    apsi=psi;
    chi=(2.*RN-1).*chi1/x-chi0;
    xi=complex(apsi,-chi);
    a=(D(N)/refrel+RN/x)*apsi-apsi1;
    a=a./((D(N)/refrel+RN/x).*xi-xi1);
    b=(refrel*D(N)+RN/x)*apsi-apsi1;
    b=b./((refrel.*D(N)+RN/x).*xi-xi1);
    Q_sca=Q_sca+(2.*RN+1).*(abs(a).*abs(a)+abs(b).*abs(b));
    psi0=psi1;
    psi1=psi;
    apsi1=psi1;
    chi0=chi1;
    chi1=chi;
    xi1=complex(apsi1,-chi1);
    aN(N)=a;
    bN(N)=b;
end
    Q_sca=(2./(x.*x)).*Q_sca;
```

B. 2. Set of functions for Mie scattering calculation of normally illuminated infinite cylinder

```
function [T11,T12,T33,T34,Pola] = Mie_BHCYLINDER_T_YP(x, refrel,ang)

%%%%%%%%%%%%%%%%%%%%%%%%%%%%%%%%%%%%%%%%%%%%%%%%%%%%%%%%%%%%%%%%%%%%%%%%%%%%%%%
%function Mie_BHCYLINDER_T_YP CALCULATES the so-called Mueller Matrix,%
%a 4x4 matrix which relates an input vector of Stokes parameters      %
%(Ii, Qi, Ui, Vi)describing a complex light source and output vector  %
%(Is, Qs, Us, Vs) describing the nature of the transmitted light.     %
%                                                                     %
%ALGORITHM DESCRIBED HERE IS VERSION OF BH FOR INFINITE CYLINDER OF   %
%THE INCIDENT LIGHT IS NORMAL TO THE CYLINDER AXIS                    %
% P 204 EQ 8.38-8.39 in Bohren and Huffman (1983) ISBN 0-471-05772-X  %
%                                                                     %
% Yang Pu, August 2008                                               %
%%%%%%%%%%%%%%%%%%%%%%%%%%%%%%%%%%%%%%%%%%%%%%%%%%%%%%%%%%%%%%%%%%%%%%%%%%%%%%%

theta=ang*pi./180;
dtheta=theta(2)-theta(1);
Nab = Mie_BHCYLINDER_ab_YP(x, refrel);
aN=Nab(1,:);
bN=Nab(2,:);

Qscpar=abs(bN(1)).*abs(bN(1));
Qscper=abs(aN(1)).*abs(aN(1));
```

```
T1(1:length(theta))=bN(1);
T2(1:length(theta))=aN(1);

for I=1:length(aN)-1
    RN=I;
    for J=1:length(theta)
        C=cos(RN.*theta(J));
        T1(J)=2.*bN(I+1).*C+T1(J);
        T2(J)=2.*aN(I+1).*C+T2(J);
    end
    Qscpar=Qscpar+2.*abs(bN(I+1)).*abs(bN(I+1));
    Qscper=Qscper+2.*abs(aN(I+1)).*abs(aN(I+1));
end

T11NOR=0.5.*(abs(T1(1))).*(abs(T1(1)));
T11NOR=T11NOR+0.5.*(abs(T2(1))).*(abs(T2(1)));

for J=1:length(theta)
    Tpar=abs(T1(J));
    Tpar=Tpar.*Tpar;
    Tper=abs(T2(J));
    Tper=Tper.*Tper;
    T11(J)=0.5.*(Tpar+Tper);
    T12(J)=0.5.*(Tpar-Tper);
    Pola(J)=T12(J)./T11(J);
    T33(J)=real(T1(J).*conj(T2(J)));
    T34(J)=imag(T1(J).*conj(T2(J)));
    T33(J)=T33(J)./T11(J);
    T34(J)=T34(J)./T11(J);
    T11(J)=T11(J)./T11NOR;
end


function Q_eff = Mie_BHCYLINDER_effic_YP(x, refrel)

%%%%%%%%%%%%%%%%%%%%%%%%%%%%%%%%%%%%%%%%%%%%%%%%%%%%%%%%%%%%%%%%%%%%%%%%%%%%
%function Mie_BHCYLINDER_effic_YP CALCULATE SCATTERING MATRIX LEMENTS %
%AND EFFICIENCIES FOR EXTINCTION AND SCATTERING FOR A GIVEN SIZE      %
%PARAMETER AND RELATIVE REFRACTIVE                                    %
%                                                                     %
%ALGORITHM DESCRIBED HERE IS VERSION OF BH FOR INFINITE CYLINDER OF   %
%THE INCIDENT LIGHT IS NORMAL TO THE CYLINDER AXIS                    %
%P204 EQ 8.36-8.37 in Bohren and Huffman (1983) ISBN 0-471-05772-X    %
%                                                                     %
% Yang Pu, August 2008                                               %
%%%%%%%%%%%%%%%%%%%%%%%%%%%%%%%%%%%%%%%%%%%%%%%%%%%%%%%%%%%%%%%%%%%%%%%%%%%%

if x==0         % To avoid a singularity at x=0
     Q_eff=[0 0 0 0 0];
else            % This is the normal situation

ang=[0:180];
theta=ang*pi./180;
dtheta=theta(2)-theta(1);
Nab = Mie_BHCYLINDER_ab_YP(x, refrel);
aN=Nab(1,:);
```

```
bN=Nab(2,:);

Qscpar=abs(bN(1)).*abs(bN(1));
Qscper=abs(aN(1)).*abs(aN(1));

T1(1:length(theta))=bN(1);
T2(1:length(theta))=aN(1);

for I=1:length(aN)-1
    RN=I;
    for J=1:length(theta)
        C=cos(RN.*theta(J));
        T1(J)=2.*bN(I+1).*C+T1(J);
        T2(J)=2.*aN(I+1).*C+T2(J);
    end
    Qscpar=Qscpar+2.*abs(bN(I+1)).*abs(bN(I+1));
    Qscper=Qscper+2.*abs(aN(I+1)).*abs(aN(I+1));
end

    Qscpar=(2./x).*Qscpar;
    Qscper=(2./x).*Qscper;
    Qexpar=(2./x).*real(T1(1));
    Qexper=(2./x).*real(T2(1));

T11NOR=0.5.*(abs(T1(1))).*(abs(T1(1)));
T11NOR=T11NOR+0.5.*(abs(T2(1))).*(abs(T2(1)));

for J=1:length(theta)
    Tpar=abs(T1(J));
    Tpar=Tpar.*Tpar;
    Tper=abs(T2(J));
    Tper=Tper.*Tper;
    T11(J)=0.5.*(Tpar+Tper);
    T12(J)=0.5.*(Tpar-Tper);
    Pola(J)=T12(J)./T11(J);
    T33(J)=real(T1(J).*conj(T2(J)));
    T34(J)=imag(T1(J).*conj(T2(J)));
    T33(J)=T33(J)./T11(J);
    T34(J)=T34(J)./T11(J);
    T11(J)=T11(J)./T11NOR;
end
   g=sum(T11.*cos(theta).*sin(theta).*2*pi*dtheta);
   g=g./(sum(T11.*sin(theta).*2*pi*dtheta));
   Q_eff=[Qscpar; Qscper; g ;Qexpar;Qexper];
end

function Nab = Mie_BHCYLINDER_ab_YP(x, refrel)

%%%%%%%%%%%%%%%%%%%%%%%%%%%%%%%%%%%%%%%%%%%%%%%%%%%%%%%%%%%%%%%%%%%%%%%%%%%%
%function Mie_BHCYLINDER_ab_YP CALCULATE A MATRIX OF MIE Coefficients %
%aN, bN SCATTERING MATRIX ELEMENTS GIVEN SIZE PARAMETER               %
%AND RELATIVE REFRACTIVE INDEX                                        %
%BESSEL FUNCTIONS J(N) AND Y(N) COMPUTED BY DOWNWARD RECURRENCE       %
%                                                                     %
%ALGORITHM DESCRIBED HERE IS VERSION OF BH FOR INFINITE CYLINDER OF   %
```

```
%THE INCIDENT LIGHT IS NORMAL TO THE CYLINDER AXIS                      %
% P204 EQ 8.36-8.37 in Bohren and Huffman (1983) ISBN 0-471-05772-X    %
%                                                                      %
% Yang Pu, August 2008                                                 %
%%%%%%%%%%%%%%%%%%%%%%%%%%%%%%%%%%%%%%%%%%%%%%%%%%%%%%%%%%%%%%%%%%%%%%%

y=x*refrel;

%%%%%%%%%%%%%%%%%%%%%%%%%%%%%%%%%%%%%%%%%%%%%%%%%%%%%%%%%%%%%%%%%%%%%%%
%    SERIES TERMINATED AFTER NSTOP TERMS                               %
%%%%%%%%%%%%%%%%%%%%%%%%%%%%%%%%%%%%%%%%%%%%%%%%%%%%%%%%%%%%%%%%%%%%%%%

nstop=round(2+x+4.*x.^(1/3));
ymod=round(abs(y));
Nmx=max(nstop,ymod)+15;

%%%%%%%%%%%%%%%%%%%%%%%%%%%%%%%%%%%%%%%%%%%%%%%%%%%%%%%%%%%%%%%%%%%%%%%
%    LOGRITHMIC DERIVATIVE G(J) CALCULATED BY DOWNWARD RECURRENCE      %
%     BEGINNING WITH INITIAL VALUE 0.0+I*0.0 AT J = NMX                %
%%%%%%%%%%%%%%%%%%%%%%%%%%%%%%%%%%%%%%%%%%%%%%%%%%%%%%%%%%%%%%%%%%%%%%%

G(Nmx)=0+0i;
for N=1:Nmx-1
    RN=Nmx-N+1;
    k=Nmx-N;
    G(k)=((RN-2)/y)-1./(G(k+1)+(RN-1)/y);
end

%%%%%%%%%%%%%%%%%%%%%%%%%%%%%%%%%%%%%%%%%%%%%%%%%%%%%%%%%%%%%%%%%%%%%%%
%    BESSEL FUNCTIONS J(N) COMPUTED BY DOWNWARD RECURRENCE             %
%    BEGINNING AT N=NSTOP+NDELTA                                       %
%    BESSEL FUNCTIONS Y(N) COMPUTED BY UPWARD RECURRENCE               %
%    BJ(N+1) = J(N), BY(N+1)=Y(N)                                      %
%%%%%%%%%%%%%%%%%%%%%%%%%%%%%%%%%%%%%%%%%%%%%%%%%%%%%%%%%%%%%%%%%%%%%%%

Ndelta=(101+x)^0.499;
MST=round(Ndelta.*.5+nstop*.5)*2;
F(MST+1)=0.0; F(MST)=10.^-32;

M1=MST-1;
for l1=1:M1
    ML=MST-l1;
    F(ML)=2.*(ML).*F(ML+1)./x-F(ML+2);
end

ALPHA=F(1);
M2=MST-2;

for ll=2:2:M2
    ALPHA=ALPHA+2.*F(ll+1);
end

M3=M2+1;
for n=1:M3
    BJ(n)=F(n)./ALPHA;
```

```
end

BY(1)=BJ(1).*(log(x./2.)+.577215664);
M4=MST/2-1;

for l3=1:M4
    BY(1)=BY(1)-2.*((-1.).^l3)*BJ(2*l3+1)/l3;
end

 BY(1)=0.636619772.*BY(1);
 BY(2)=BJ(2).*BY(1)-0.636619772./x;
 BY(2)=BY(2)./BJ(1);

 Ns=nstop-1;

 for kk=1:Ns
     BY(kk+2)=2*double(kk).*BY(kk+1)./x-BY(kk);
 end

 Nn=nstop+1;

 for n1=1:Nn
     BH(n1)=complex(BJ(n1),BY(n1));
 end

a0=G(1).*BJ(1)./refrel+BJ(2);
a0=a0/(G(1).*BH(1)./refrel+BH(2));
b0=refrel.*G(1).*BJ(1)+BJ(2);
b0=b0./(refrel.*G(1).*BH(1)+BH(2));

for n2=1:nstop
    RN=n2;
    aN(n2)=(G(n2+1)./refrel+RN./x).*BJ(n2+1)-BJ(n2);
    aN(n2)=aN(n2)./((G(n2+1)./refrel+RN./x).*BH(n2+1)-BH(n2));
    bN(n2)=(refrel.*G(n2+1)+RN./x).*BJ(n2+1)-BJ(n2);
    bN(n2)=bN(n2)./((refrel.*G(n2+1)+RN./x).*BH(n2+1)-BH(n2));
end

aN=[a0,aN];
bN=[b0,bN];
Nab =[aN; bN];
```

B. 3. Set of programs for diffusion model

B. 3.1. Matlab code to generate Fig. 2-8 and compute the time-resolved transport of light from an impulse isotropic point source of energy within a homogeneous unbounded absorptive and scattering medium

```
clear all; close all;
```

```
%%%%%%%%%%%%%%%%%%%%%%%%%%%%%%%%%%%%%%%%%%%%%%%%%%%%%%%%%%%%%%%%%%%%%%%%%%%%
% Code to generate Figs. 2-8                                                   %
%%%%%%%%%%%%%%%%%%%%%%%%%%%%%%%%%%%%%%%%%%%%%%%%%%%%%%%%%%%%%%%%%%%%%%%%%%%%

%%%%%%%%%%%%%%%%%%%%%%%%%%%%%%%%%%%%%%%%%%%%%%%%%%%%%%%%%%%%%%%%%%%%%%%%%%%%
% by Y. Pu, Oct. 28, 2008.                                                     %
% Computes the time-resolved fluence rate F(r,t) [W/cm^2]                      %
% in response from an impulse isotropic point source of energy                %
% within a uniform unbounded medium with optical properties of                %
% absorption, reduced scattering, and refractive index.                       %
%                                                                             %
% Uses equations equivalent to the equations published by                     %
% Fishkin et al. Proc. Photo-Opt. Instrum. Eng. 1431:122-35, 1991             %
% Schmitt, Knuettel, Knutson, JOSA 9:1832-1843, 1992,                         %
% Fishkin and Gratton, JOSA 10:127-140, 1993.                                 %
%%%%%%%%%%%%%%%%%%%%%%%%%%%%%%%%%%%%%%%%%%%%%%%%%%%%%%%%%%%%%%%%%%%%%%%%%%%%

%define parameter
CC = 2.997925e10;
mua= 1.0;  % put in absorption cofficient of protate tissue %
mus= 100.0;% put in scattering cofficient of protate tissue %
g= 0.90;   % put in anisotropy factor of protate tissue %
nt= 1.33;
U0=1;

D = 1/( 3*mus*(1 - g)+mua ); % diffusion length [cm] %
c = CC/nt;  % speed of light in medium [cm/s] %
r = [-2:.01:2]; %distance between source and observation point [cm]%
t=[5 100 1000].*1e-12;

for i=1:length(t)
    temp1=exp(-(r.*r)./(4.*c.*D.*t(i)));
    temp2=(4.*pi.*c.*D.*t(i)).^(3/2);
    F(i,:)=c.*U0.*temp1./temp2;
end


figure;

semilogy(r,F(1,:),r,F(2,:),r,F(3,:));
```

B. 3. 2. Matlab code to generate Fig. 2-10 and compute the frequency domain signal F(r,t) at a certain distance in response to a sinusoidally modulated istropic point source S(t) in the medium within a homogeneous unbounded absorptive and scattering medium

```
clear all; close all;

%%%%%%%%%%%%%%%%%%%%%%%%%%%%%%%%%%%%%%%%%%%%%%%%%%%%%%%%%%%%%%%%%%%%%%%%%%%%
% Code to generate Figs. 2-10                                                  %
%%%%%%%%%%%%%%%%%%%%%%%%%%%%%%%%%%%%%%%%%%%%%%%%%%%%%%%%%%%%%%%%%%%%%%%%%%%%

%%%%%%%%%%%%%%%%%%%%%%%%%%%%%%%%%%%%%%%%%%%%%%%%%%%%%%%%%%%%%%%%%%%%%%%%%%%%
% by Y. Pu, Oct. 28, 2008.                                                     %
% Computes the frequency domain fluence rate F(r,t) [W/cm^2]in      %
% response to a sinusoidally modulated istropic point source S(t)[W]%
% within a uniform unbounded medium with optical properties of      %
% absorption, reduced scattering, and refractive index.             %
%                                                                              %
% Uses equations equivalent to the equations published by           %
% Fishkin et al. Proc. Photo-Opt. Instrum. Eng. 1431:122-35, 1991   %
% Schmitt, Knuettel, Knutson, JOSA 9:1832-1843, 1992,               %
% Fishkin and Gratton, JOSA 10:127-140, 1993.                       %
%%%%%%%%%%%%%%%%%%%%%%%%%%%%%%%%%%%%%%%%%%%%%%%%%%%%%%%%%%%%%%%%%%%%%%%%%%%%

%define parameter
CC = 2.997925e10;
mua= 1.0;  % put in absorption cofficient of protate tissue %
mus= 100.0;% put in scattering cofficient of protate tissue %
g= 0.90;   % put in anisotropy factor of protate tissue %
nt= 1.33;
r = 2;     % distance between source and observation point [cm]%
So= 1.0;   % steady-state power of isotropic source point [W] %
Mo= 1.0;   % modulation of source power [-]%
f = 400e6; % modulation frequency [Hz] %
N= 100;    % set number of points in array %
tmax = 2.0/f;
dt = tmax/N;

% Calculate Tss, M, and P. %
c = CC/nt;               % speed of light in medium [cm/s] %
D = 1/( 3*mus*(1 - g) ); % diffusion length [cm]%
delta = sqrt(D/mua);     % 1/e optical penetration depth [cm]%
w = 2.0*pi*f;            % angular frequency [1/s]%

b   = sqrt( sqrt( 1.0 + w*w/(mua*mua*c*c) ) );% temporary variable b%

th  = (w/(mua*c)); % reference angle theta [radians]%

Tss = exp(-r/delta)/(4.0*pi*D*r);% steady-state transport [1/cm^2]%

M   = exp(-r/delta*( b*cos(th/2) -1) );% modulation [-]%

P   = r/delta*b*sin(th/2); % phase lag P [radians]%

for i=1:N+1   % loop %
    t(i) = (i - 1)*dt; % time t %
    S(i) = So*( 1.0 + Mo*sin(w*t(i)));% S(t) %
    F(i)= So*Tss*( 1 + Mo*M*sin(w*t(i) - P) );% F(r,t)%
    Tn(i)=t(i).*1e9;
end
```

```
[AX,H1,H2] = plotyy(Tn,S,Tn,F,'plot');

axis(AX(1),[0 5 -0.5 2.5])
axis(AX(2),[0 5 0 6e-5])

set(get(AX(1),'ylabel'),'String','Source Power S[W]')
set(get(AX(2),'ylabel'),'String','Fluence Rate at r F(r)[W/cm^2]')

xlabel('Time T (ns)')
title('f=400mHZ r=2cm')

set(H1,'LineStyle','--')
set(H2,'LineStyle',':')
```

B. 3.3. Matlab code to generate Figs. 2-11 and compute the frequency domain signal F(r,t) at a certain time in response to a sinusoidally modulated istropic point source S(t) in the medium within a homogeneous unbounded absorptive and scattering medium

```
clear all; close all;

%%%%%%%%%%%%%%%%%%%%%%%%%%%%%%%%%%%%%%%%%%%%%%%%%%%%%%%%%%%%%%%%%%%%%%%%%%%%
% Code to generate Figs. 2-10                                              %
%%%%%%%%%%%%%%%%%%%%%%%%%%%%%%%%%%%%%%%%%%%%%%%%%%%%%%%%%%%%%%%%%%%%%%%%%%%%

%%%%%%%%%%%%%%%%%%%%%%%%%%%%%%%%%%%%%%%%%%%%%%%%%%%%%%%%%%%%%%%%%%%%%%%%%%%%
% by Y. Pu, Oct. 28, 2008.                                                 %
% Computes the frequency domain fluence rate F(r,t) [W/cm^2]in             %
% response to a sinusoidally modulated istropic point source S(t)[W]%
% within a uniform unbounded medium with optical properties of             %
% absorption, reduced scattering, and refractive index.                    %
%                                                                          %
% Uses equations equivalent to the equations published by                  %
% Fishkin et al. Proc. Photo-Opt. Instrum. Eng. 1431:122-35, 1991          %
% Schmitt, Knuettel, Knutson, JOSA 9:1832-1843, 1992,                      %
% Fishkin and Gratton, JOSA 10:127-140, 1993.                              %
%%%%%%%%%%%%%%%%%%%%%%%%%%%%%%%%%%%%%%%%%%%%%%%%%%%%%%%%%%%%%%%%%%%%%%%%%%%%

%define parameter
CC = 2.997925e10;
muac = .1; muan=1;
musc = 100; musn=100.0;
gc  = 0.9;  gn=0.9;
nt = 1.33;
rmax  = 100;% max distance between source and observation point [cm]%
So  = 1.0;  % steady-state power of isotropic source point [W]%
Mo = 1.0;   % modulation of source power [-]%
f = 400e6;  % modulation frequency [Hz] %
N = 200;
```

```
t  = 0;     % time of observation [s] %

%  Calculate Tss, M, and P

dr = rmax/N;% step size [cm]%
c = CC/nt;  % speed of light in medium [cm/s]%
Dc = 1/( 3*musc*(1 - gc) );
Dn = 1/( 3*musn*(1 - gn) );% diffusion length [cm] %
deltac = sqrt(Dc/muac);
deltan = sqrt(Dn/muan);% 1/e optical penetration depth [cm]%
w = 2.0*pi*f; % angular frequency [1/s]%

bc=sqrt( sqrt( 1.0 + w*w/(muac*muac*c*c) ) );
bn=sqrt( sqrt( 1.0 + w*w/(muan*muan*c*c) ) );%temporary variable b [-]%
thc=w/(muac*c));
thn=w/(muan*c));  % reference angle theta [radians]%

for i=1:N+1   % loop %
    r(i) = (i - 1)*dr;  % time t %
    Tssc(i) = exp(-r(i)/deltac)/(4.0*pi*Dc*r(i));
    Mc(i) = exp(-r(i)/deltac*( bc*cos(thc/2) -1) );
    Pc (i)  = r(i)/deltac*bc*sin(thc/2);  % phase lag P [radians]%
    Sc = So*( 1.0 + Mo*sin(w*t) ); % S(t)%
    Mpilc(i)=Mo*Mc(i)*sin(w*t - Pc(i));
    Fc(i) = So*Tssc(i)*( 1 + Mo*Mc(i)*sin(w*t - Pc(i)) );% F(r,t)%
end

for i=1:N+1   % do loop %
    r(i) = (i - 1)*dr;  % time t%
    Tssn(i) = exp(-r(i)/deltan)/(4.0*pi*Dn*r(i));
    Mn(i) = exp(-r(i)/deltan*( bn*cos(thn/2) -1) );
    Pn (i)  = r(i)/deltan*bn*sin(thn/2);  % phase lag P [radians]%
    Sn = So*( 1.0 + Mo*sin(w*t) ); % S(t)%
    Mpiln(i)=Mo*Mn(i)*sin(w*t - Pn(i));
    Fn(i) = So*Tssn(i)*( 1 + Mo*Mn(i)*sin(w*t - Pn(i)) );% F(r,t)%
end

plot(r,Mpilc,r,Mpiln);
legend('prostate cancerous tissue','prostate normal tissue')
axis([0 100 -1 1]);
figure;
semilogy(r,Fc,r,Fn)
legend('prostate cancerous tissue','prostate normal tissue')
axis([.4 14.5 1e-16 2]);
```

B. 4. Matlab code of fractal dimensional model

B. 4.1. Matlabe code to generate Fig. 3-6 and evaluate the g values at 800nm as a function of cutoff diameter d_{max} using fractal dimension model

```
clear all;
close all;
clc
%%%%%%%%%%%%%%%%%%%%%%%%%%%%%%%%%%%%%%%%%%%%%%%%%%%%%%%%%%%%%%%%%%%%%%%%%%%%%%%%
```

```
% Code to generate Fig. 3-6                                                %
%%%%%%%%%%%%%%%%%%%%%%%%%%%%%%%%%%%%%%%%%%%%%%%%%%%%%%%%%%%%%%%%%%%%%%%%

%%%%%%%%%%%%%%%%%%%%%%%%%%%%%%%%%%%%%%%%%%%%%%%%%%%%%%%%%%%%%%%%%%%%%%%%
% by Y. Pu, March 18, 2009.                                                %
% The evaluation of the g values at certain wavelength as a                %
% function of cutoff diameter dmax using fractal dimension model           %
%                                                                          %
% Uses equations (5) and (6) published by Min Xu and R. R. Alfano          %
% Opt. Lett. 30, 3051-3053 (2005).                                         %
% equivalent to the equations of 3.12 and 3.13 in this thesis              %
%%%%%%%%%%%%%%%%%%%%%%%%%%%%%%%%%%%%%%%%%%%%%%%%%%%%%%%%%%%%%%%%%%%%%%%%

klmax=[1:100];Ni=20;
Dfc=3;Dfn=5;lamda=0.8;
n0=1.35;n1=1.46;m=n1/n0;
k=2*pi*n0/lamda;
E2=4.*(m-1).*(m-1).*n0.*n0.*n0.*n0;
nh=1e4;
tempc=E2.*nh.*k.^(Dfc-1)/(2*pi);
tempn=E2.*nh.*k.^(Dfn-1)/(2*pi);
k2=2.*k.*k;
theta=[0:1:180].*pi/180;
u=cos(theta);

for i=1:length(klmax)
    x=linspace(0,klmax(i),Ni);
    for k=1:length(u)
        yc=tempc.*x.^(6-Dfc)./(1+2.*(1-u(k)).*x.^2).^2;
        yn=tempn.*x.^(6-Dfn)./(1+2.*(1-u(k)).*x.^2).^2;
        Sc(i,k)=trapz(x,yc);
        Sn(i,k)=trapz(x,yn);
    end
end

for i=1:length(klmax)
    tempdownc=(1+u.*u).*Sc(i,:)./k2;
    tempupc=tempdownc.*u;
    tempdownc1=trapz(u,tempdownc);
    tempupc1=trapz(u,tempupc);
    gc(i)=tempupc1./tempdownc1;
    tempdownn=(1+u.*u).*Sn(i,:)./k2;
    tempupn=tempdownn.*u;
    tempdownn1=trapz(u,tempdownn);
    tempupn1=trapz(u,tempupn);
    gn(i)=tempupn1./tempdownn1;
end

semilogx(klmax,gc,klmax,gn)
legend('cancer','normal')
```

B. 4.2. Matlabe code to calculate the phase function at certain wavelengths with known d_{min} and cutoff diameter d_{max} using fractal dimension model

```
clear all;
close all;
clc

%%%%%%%%%%%%%%%%%%%%%%%%%%%%%%%%%%%%%%%%%%%%%%%%%%%%%%%%%%%%%%%%%%%%%%%%%%%%
% by Y. Pu, March 18, 2009.                                                    %
% The calculation of phase function by known the dmin and cutoff    %
% diameter dmax using fractal dimension model at certain lamd       %
%                                                                              %
% Uses equations (4) -  (7) published by Min Xu and R. R. Alfano    %
% Opt. Lett. 30, 3051-3053 (2005).                                             %
%%%%%%%%%%%%%%%%%%%%%%%%%%%%%%%%%%%%%%%%%%%%%%%%%%%%%%%%%%%%%%%%%%%%%%%%%%%%

Dfc=1.9;Dfn=4.4;lamda=0.8;
bc=3-Dfc;bn=3-Dfn;
Tv=0.3;
n0=1.35;n1=1.46;m=n1/n0;
lmaxn=2*3.38;lmaxc=0.72*2;
lmin=0;dl=.01;
lmc=[lmin:dl:lmaxc]./2;
lmn=[lmin:dl:lmaxn]./2;

k=2*pi*n0/lamda;
E2=4.*(m-1).*(m-1).*n0.*n0.*n0.*n0;
nhn=0.028;nhc = 0.1955;
tempc=E2.*nhc.*k.^(Dfc-1)/(2*pi);
tempn=E2.*nhn.*k.^(Dfn-1)/(2*pi);
k2=2.*k.*k;
A=[0:1:180];
theta=A.*pi/180;
u=(cos(theta));
su=2.*pi.*sin(theta);

for j=1:length(u)
    yc=tempc.*lmc.^(6-Dfc)./((1+2.*(1-u(j)).*lmc.^2).^2);
    yn=tempn.*lmn.^(6-Dfn)./((1+2.*(1-u(j)).*lmn.^2).^2);
    Sc(j)=(trapz(lmc,yc));
    Sn(j)=(trapz(lmn,yn));
end

pthetan=(1+u.*u).*(Sn)./k2;
tempdown=su.*pthetan;
tempupn=u.*tempdown;
gn=trapz(theta,tempupn)./trapz(theta,tempdown);
pthetac=(1+u.*u).*(Sc)./k2;
tempdowc=su.*pthetac;
tempupc=u.*tempdowc;
gc=trapz(theta,tempupc)./trapz(theta,tempdowc);

figure;

semilogy(A,pthetac,A,pthetan);
legend('cancer','normal')
```

Appendix C
Publications and Presentations

PUBLICATIONS OF THE RELATED TOPICS IN PEER-REVIEWED JOURNALS:

1. Y. Pu, G.C. Tang, W.B. Wang, H. E. Savage and R. R. Alfano, "Native fluorescence spectroscopic evaluation of chemotherapeutic effect on a malignant cell model using Nonnegative Matrix Factorization", submitted to *Technol. Cancer Res. Treat.* (2010).
2. Y. Pu, W. B. Wang, S. Achilefu and R. R. Alfano, "Study of rotational dynamics of receptor-targeted contrast agents in cancerous and normal prostate tissues using time-resolved picosecond emission spectroscopy", submitted to *Appl. Opt.* (2010).
3. E. Jeyasingh, Y. Pu, C.-H. Liu, W. B. Wang and R. R. Alfano, "Diagnostic potential of Stokes Shift Spectroscopy in Breast and Prostate tissues", submitted to *Technol. Cancer Res. Treat.* (2010).
4. E. Jeyasingh, Y. Pu, W. B. Wang, G. C. Tang, R. R. Alfano, "Stokes shift spectroscopy of cancerous and normal prostate tissues", submitted to *Laser Med. Sci.*, (2010).
5. Y. Pu , W.B. Wang , G. C. Tang , R. R. Alfano, "Changes of collagen and NADH in human cancerous and normal prostate tissues studied using fluorescence spectroscopy with selective excitation wavelength", *J. Biomed. Opt.*. 15, 047008-1-5, (2010).
6. Y. Pu, W. B. Wang, B. B. Das, and R. R. Alfano, "Differences of Time-resolved near infrared spectral wing emission and imaging of human cancerous and normal prostate tissues", *Opt. Commun*., 282, 4308–4314 (2009).
7. Y. Pu, W. B. Wang, B. B. Das, S. Achilefu, and R. R. Alfano, "Time-resolved fluorescence polarization dynamics and optical imaging of Cytate: a prostate cancer receptor-targeted contrast agent", *Appl. Opt.*, 47, 2281-2289 (2008).

8. Y. Pu, W. B. Wang, S. Achilefu, B. B. Das, G. C. Tang, V. Sriramoju, and R. R. Alfano, "Time-resolved fluorescence polarization anisotropy and optical imaging of Cybesin in prostate cancerous and normal tissues", *Opt. Commun*., 274, 260-267 (2007).
9. Y. Pu, W. B. Wang, G. C. Tang, F. Zeng, S. Achilefu, J. H. Vitenson (M.D.), I. Sawczuk (M.D.), S. Peters (M.D.), J. M. Lombardo (M.D.), and R. R. Alfano, "Spectral polarization imaging of human prostate cancer tissue using near-infrared receptor-targeted contrast agent", *Technol. Cancer Res. Treat.*, 4, 429-436 (2005).

PUBLICATIONS OF THE RELATED TOPICS IN CONFERENCE PROCEEDING:

1. Yang Pu, Wubao Wang, Guichen Tang, Y. Budansky, M. Sharanov, R. R. Alfano and Min Xu, "Three-dimensional localization of objects in tissue using independent component analysis in backscattering scanning optical polarization imaging", *Optical Biopsy IX, Proc. of SPIE*, in processing (2011).
2. Yang Pu, WubaoWang and Robert R. Alfano, "Time-Resolved fluorescence spectroscopy of contrast agent, ICG, influenced by rotational motion," *Frontiers in Optics (FiO)/Laser Science XXVI (LS)*, JTuA19-1-2 (2010).
3. Yang Pu, WubaoWang, Guichen Tang, Robert R. Alfano, "Changes of NADH and Collagen Contents as Biomarkers in Cancerous Prostate Tissue Analyzed by Selective Excitation Fluorescence," *Biomedical Optics (BIOMED)/ Digital Holography and Three-Dimensional Imaging (DH)*, BCW6-1-3 (2010).
4. Y. Pu, W. B. Wang, S. Achilefu, and R. R. Alfano, "Rotational dynamics and polarization anisotropy of bound and unbound receptor-targeted contrast agents in cancerous and normal prostate tissues studied by time-resolved fluorescence spectroscopy", *Optical Biopsy VIII, Proc. of SPIE*, Vol. 7561, 75610A-1-8 (2010).

5. G. C. Tang, W. B. Wang, Y. Pu, and R. R. Alfano, “Optical Birefringence of Aorta Tissues”, *Optical Biopsy VIII, Proc. of SPIE*, Vol. 7561, 756116-1-9 (2010).
6. Y. Pu, W. B. Wang, B. B. Das, and R. R. Alfano, “Time-resolved fluorescence polarization study of cancer receptor-targeted contrast agents in prostate tissues”, *Conference on Laser and Electro-Optics (CLEO) / International Quantum Electronics Conference (IQEC*), JThE 64, P158 (2009).
7. Y. Pu, W. B. Wang, B. B. Das, and R. R. Alfano, “Time-resolved near infrared spectral wing emission of human native cancerous and normal prostate tissues”, *Proceedings of SPIE*, Vol. 7174, 71741W-1-6 (2009).

PRESENTATIONS:

1. Y. Pu, W. B. Wang and R. R. Alfano, "Time-resolved polarization spectroscopy and near-infrared imaging enhanced by receptor-targeted contrast agents for prostate cancer detection," in *Conference of Optical Biopsy IX*, Oral Invited presentation, on 25 Jan 2011.
2. Yang Pu, WubaoWang and Robert R. Alfano, “Time-Resolved fluorescence spectroscopy of contrast agent, ICG, influenced by rotational motion,” presented in *Frontiers in Optics (FiO)/Laser Science XXVI (LS)*, held in Rochester, on October 24-28, 2010.
3. Yang Pu, WubaoWang, Guichen Tang, Robert R. Alfano, “Changes of NADH and Collagen Contents as Biomarkers in Cancerous Prostate Tissue Analyzed by Selective Excitation Fluorescence,” presented in *Biomedical Optics (BIOMED)/ Digital Holography and Three-Dimensional Imaging (DH) OSA Optics & Photonics Congress*, held in Miami, Florida, on April 11-14, 2010.
4. Y. Pu, W. B. Wang, S. Achilefu, and R. R. Alfano, “Rotational dynamics and polarization anisotropy of bound and unbound receptor-targeted contrast agents in cancerous and normal

prostate tissues studied by time-resolved fluorescence spectroscopy", presented in *Conference of Optical Biopsy VIII of Photonics West: Biomedical Optics (BiOS) 2010 of the Society of Photographic Instrumentation Engineers (SPIE)*, held in San Francisco, California, USA, on 25 January, 2010.

5. G. C. Tang, W. B. Wang, Y. Pu, and R. R. Alfano, "Optical Birefringence of Aorta Tissues", presented in *Conference of Optical Biopsy VIII of Photonics West: Biomedical Optics (BiOS) 2010 of the Society of Photographic Instrumentation Engineers (SPIE)*, held in San Francisco, California, USA, on 25 January, 2010.
6. Y. Pu, W. B. Wang, B. B. Das, and R. R. Alfano, "Time-resolved fluorescence polarization study of cancer receptor-targeted contrast agents in prostate tissues", presented at the 2009 *Conference on Laser and Electro-Optics (CLEO) / International Quantum Electronics Conference (IQEC),* in the Conference Program, JThE 64, held in Baltimore, Maryland, on May 31 - June 5, 2009.
7. Y. Pu, W. B. Wang, B. B. Das, and R. R. Alfano, "Time-resolved near infrared spectral wing emission of human native cancerous and normal prostate tissues", presented in *Conference of Optical Tomography and Spectroscopy of Tissue VIII of Photonics West: Biomedical Optics (BiOS) 2009 of the Society of Photographic Instrumentation Engineers* (*SPIE*), held in San Jose, CA, USA, on 25 January, 2009.

OTHER ACHIEVEMENT:

Presider of session of BWD – Clinical Application of Imaging in Biomedical Optics (BIOMED)/ Digital Holography and Three-Dimensional Imaging (DH), the topic conference of the OSA, Miami, FL, April 11-14, 2010.

Bibliography

Chapter 1

1. American Cancer Society. "Cancer facts and figures"' *American Cancer Society, Atlanta* (2009).
2. Rebecca Ferrini, Steven H. Woolf, "Screening for prostate cancer in American men", http://www.acpm.org/prostate.htm, *American College of Preventive Medicine - Practice Policy Statement.*
3. W. J. Catalona, J. P. Richie, F. R. Ahmann, *et al*. "Comparison of digital rectal examination and serum prostate specific antigen in the early detection of prostate cancer: results of a multi-center clinical trial of 6,630 men", *J. Urol.*, 151, 1283-1290 (1994).
4. D. J. Tindall and P. T. Scardino, "Defeating prostate cancer: crucial direction for research --- except from the report of the Prostate Cancer Progress Review Group (Review)", *Prostate*, 38(2), 166-171 (1999).
5. David A. Benaron, "The future of cancer imaging". *Cancer and Metast. Rev.*, 21, 45–78 (2002).
6. R. R. Anderson and J. A. Parrish, "The optics of human skin", *J. Invest. Dermatol*., 77, 13–19 (1981).
7. J. H. Ali, W. B. Wang, M. Zevallos, R. R. Alfano, "Near infrared spectroscopy and imaging to probe differences in water content in normal and cancer human prostate tissues", *Technol. Cancer Res. Treat.*, 3, 491-497 (2004).
8. T. O. McBride, B. W. Pogue, E. D. Gerety, S. P. Poplack, U. L. Osterberg and K. D. Paulsen, "Spectroscopic diffuse optical tomography for the quantitative assessment of hemoglobin concentration and oxygen saturation in breast tissue", *Appl. Opt.*, 38, 5480-5490 (1999).

9. G. Zhang, S. G. Demos and R. R. Alfano, “Far-red and NIR spectral wing emission from tissues under 532 and 632 nm photo-excitation”, *Laser Life Sci.*, 9, 1-16 (1999); and Y. Pu, W. B. Wang, B. B. Das, and R. R. Alfano, “Differences of time-resolved near infrared spectral wing emission and imaging of human cancerous and normal prostate tissues”, *Opt. Commun.*, 282, 4308–4314 (2009).
10. V. Ntziachristos and B. Chance, “Probing physiology and molecular function using optical imaging: applications to breast cancer”, *Breast Cancer Res.*, 3, 41-46 (2001).
11. D. F. Gleason and G. T. Mellinger, “Prediction of prognosis for prostate adenocarcinoma by combined histological and clinical”, *J. Urol.*, 111, 58-64 (1974).
12. C. Morrison, J. Thornhill and E. Gaffney, “The connective tissue framework in the normal prostate, BPH and prostate cancer: analysis by scanning electron microscopy after cellular digestion”, *Urol. Res*., 28, 304-307 (2000).
13. Rodolfo Montironi, Adhemar Longatto Filho, Alfredo Santinelli, Roberta Mazzucchelli, Roberto Pomante, Paola Colanzi and Marina Scarpelli, “Nuclear changes in the normal-looking columnar epithelium adjacent to and distant from prostatic intraepithelial neoplasia and prostate cancer”, *Virchow Arch*., 437, 625-634 (2000).
14. Y. Pu, W. B. Wang, B. B. Das, S. Achilefu, and R. R. Alfano, “Time-resolved fluorescence polarization dynamics and optical Imaging of Cytate: a prostate cancer receptor-targeted contrast agent”, *Appl. Opt.*, 47, 2281-2289 (2008).
15. J. E. Bugaj, S. Achilefu, R. B. Dorshow and R. Rajagopalan, “Novel fluorescent contrast agents for optical imaging of *in vivo* tumor based on a receptor-targeted dye-peptide conjugate platform”, *J. Biomed. Opt.*, 6(2), 122-133 (2001).

16. V. Ntziachristos, A. G. Yodh, M. Schnall and B. Chance, "Concurrent MRI and diffuse optical tomography of breast after Indocyanine Green enhancement", *Proc. Natl. Acad. Sci. USA*, 97, 2767-2772 (2000).
17. Wubao Wang, Jamal H. Ali, J. H. Vitenson, J. M. Lombardo and R. R. Alfano, "Spectral polarization imaging of human prostate tissues", *Optical Biopsy III, Proceeding of SPIE*, 3917, 75-78 (2000).
18. S. Achilefu, R. B. Dorshow, J. E. Bugaj and R. Rajagopalan, "Novel receptor-targeted fluorescence contrast agent for *in vivo* tumor imaging", *Invest. Radiol.*, 35, 479-485 (2000).
19. G. Zheng, H. Li, K. Yang, D. Blessington, K. Licha, S. Lund-Katz, B. Chance and J. D. Glickson, "Tricarbocyanine cholesteryl laurates labeled LDL: New near infrared fluorescent probes (NIRFs) for monitoring tumors and gene therapy of Familial hypercholesterolemia", *Bioorg. Med. Chem. Lett.*, 12, 1485-1488 (2002).
20. R. Weissleder, C. H. Tung, U. Mahmood and A. Bogdanov, "*In vivo* imaging of tumors with protease-activated near-infrared fluorescent probes", *Nat. Biotechnol.*, 17, 375-378 (1999).
21. J. C. Reubi, B. Waser, J. C. Schaer and R. Markwalder, "Somatostatin receptors in human prostate and prostate cancer", *J. Clin. Endocrinol. Metab*., 80, 2806-2814 (1995).
22. J. Hansson, A. Bjartell, V. Gadaleanu, N. Dizeyi and P. A. Abrahamsson, "Expression of somatostatin receptor subtypes 2 and 4 in human benign prostatic hyperplasia and prostatic cancer." *Prostate*, 53(4), 50-59 (2002).
23. B. Sun, G. Halmos, A. V. Schally, X. Wang and M. Martinez "Presence of receptors for bombesin/gastrin-releasing peptide and mRNA for three receptor subtypes in human prostate cancers", *Prostate* 42(4), 295-303 (2000).

24. Jean Claude Reubi, Sandra Wenger, Jacqueline Schmuckli-Maurer, Jean-Claude Schaer, and Mathias Gugger, "Bombesin receptor subtypes in human cancers: detection with the universal radioligand ^{125}I-[D-TYR^{6}, β-ALA^{11}, PHE^{13}, NLE^{14}] bombesin(6-14)", *Clin. Cancer Res.*, 8, 1139–1146 (2002).

Chapter 2

1. B. B. Das, Feng Liu and R. R. Alfano, "Time-resolved fluorescence and photon migration studies in biomedical and model random media", *Rep. Prog. Phys*. 60, 227–292 (1997).
2. C. F. Bohren and D. R. Huffman, "Absorption and scattering of light by small particles". First edition, New York: John Wiley and Sons, (1983).
3. M. Xu, M. Alrubaue, S. K. Gayen and R. R. Alfano, "Determination of light absorption, scattering and anisotropy factor of a highly scattering medium using backscattered circularly polarized light", *Optical interaction with tissue and cells XVIII, Proc. Of SPIE* 6435, 64350J1-6 (2007).
4. G. Zaccanti, E. Battistelli, P. Bruscaglioni and Q. Wei, "Ananlytic relationships for the statistical moments of scattering point coordinates for photon migration in a scattering medium", *Pure & Appl. Opt*, 3(5), 897-905 (1994).
5. J. H. Lambert, "Photometria, sive de mensura et gradibus luminis, colorum et umbrae" , Augsburg, (1760).
6. A. Beer, "Bestimmung der Absorption des rothen Lichts in farbigen Fl¨ussigketiten", *Ann Physik Chem*, 86(5), 78–88 (1852).
7. B.J. Tromberg, N. Shah, R. Lanning, A. Cerussi, J. Espinoza, T. Pham, L. Svaasand and J. Butler, "Non-invasive in vivo characterization of breast tumors using photon migration spectroscopy", *Neoplasia*, 2, 26-40 (2000).

8. J. H. Ali, W. B. Wang, M. Zevallos, R. R. Alfano, “Near Infrared Spectroscopy and Imaging to Probe Differences in Water Content in Normal and Cancer Human Prostate Tissues”, *Technol. Cancer Res. Treat.*, Volume 3 491-497 (2004).
9. Kendric C. Smith, “The science of photobiology”, 2nd edition, Plenum press, (1989).
10. Donna J. Dean and Brenda J. Korte, “Biomedical Imaging and Bioengineering”, *Optics & Photonics News*, October 2003, http://ultra.bu.edu/papers/2003_10_OPN.pdf.
11. Irene Georgakoudi, Brian C. Jacobson, Markus G. Mu¨ ller, Ellen E. Sheets, Kamran Badizadegan, David L. Carr-Locke, Christopher P. Crum, Charles W. Boone, Ramachandra R. Dasari, Jacques Van Dam and Michael S. Feld, “NAD(P)H and Collagen as *in Vivo* Quantitative Fluorescent Biomarkers of Epithelial Precancerous Changes” *Can. Res.* 62, 682–687 (2002).
12. C. Morrison, J. Thornhill and E. Gaffney, “The connective tissue framework in the normal prostate, BPH and prostate cancer: analysis by scanning electron microscopy after cellular digestion”, *Urol. Res*, 28(5), 304-7 (2000).
13. C. F. Bohren and D. R. Huffman, “Absorption and scattering of light by small particles”, Wiley, New York, (1983).
14. Steven L. Jacques and Scott A. Prahl, "Introduction to tissue optics", http://omlc.ogi.edu/classroom/ece532/index.html
15. J. R. Mourant, T. Fuselier, J. Boyer, T. M. Johnson and I. J. Bigio, “Predictions and measurements of scattering and absorption over broad wavelength ranges in tissue phantoms”, *Appl. Opt*. 36, 949-957 (1997).
16. Wikipedia, “Cell Biology/Introduction/Cell size”, http://en.wikibooks.org/wiki/Cell_Biology/Introduction/Cell_size

17. R. Montironi, R. Mazzucchelli, A. Santinelli, M. Scarpelli, A. Beltran and D. Bostwick, "Incidentally detected prostate cancer in cystoprostatectomies: pathological and morphometric comparison with clinically detected cancer in totally embedded specimens", *Human Pathol.*, 36, 646– 654 (2005).
18. C. Morrison, J. Thornhill, E. Gaffney E, "The connective tissue framework in the normal prostate, BPH and prostate cancer: analysis by scanning electron microscopy after cellular digestion", *Urol. Res*. 28, 304-307 (2000).
19. Wai-Fung Cheong, Scott A. Prahl, and Ashley J. Welch, "A review of the optical properties of biological tissues", *IEEE J. Quant. Elec.*, 26(12), 2166-2184 (1990).
20. J. M. Schmitt and G. Kumar, "Optical Scattering Properties of Soft Tissue: A Discrete Particle Model", *Appl. Opt.*, 37(13), 2788-2797 (1998).
21. Ruikang K. Wang, "Modeling optical properties of soft tissue by fractal distribution of scatterers", *J. Mod. Opt.*, 47(1), 103-120 (2000).
22. M. Xu and R. R. Alfano, "Fractal mechanisms of light scattering in biological tissue and cells", *Opt. Lett*. 30, 3051-3053 (2005).
23. B. C. Wilson and S. L. Jacques, "Optical reflectance and transmittance of tissues: principals and applications", *IEEE J. Quant. Elec.*, 26(12), 2186–2199 (1990).
24. Y. Pu, M. Alrubaiee, W. B. Wang, S. K. Gayen, R. R. Alfano and M. Xu "Determination of optical coefficients and fractal dimensional parameters of cancerous and normal prostate tissues", to be submitted.
25. L. H. Wang and S. L. Jaques, "Monte Carlo modeling of light transport in multi-layered tissues in standard C", Anderson Cancer Center, University of Texas, (1992).

Chapter 3

1. D. F. Gleason and G. T. Mellinger, “Prediction of prognosis for prostate adenocarcinoma by combined histological and clinical”, *J. Urol*, 111, 58-64 (1974).
2. C. Morrison, J. Thornhill and E. Gaffney, “The connective tissue framework in the normal prostate, BPH and prostate cancer: analysis by scanning electron microscopy after cellular digestion”, *Urol. Res*. 28, 304-307 (2000).
3. R. Montironi, A. Filho, A. Santinelli, R. Mazzucchelli, R. Pomante, P. Colanzi and M. Scarpelli, “Nuclear changes in the normal-looking columnar epithelium adjacent to and distant from prostatic intraepithelial neoplasia and prostate cancer. Morphometric analysis in whole-mount sections”, *Virch. Arch*., 437, 625-634 (2000).
4. Martin Chaplin, “Do we underestimate the importance of water in cell biology?”, *Nat. Rev.: Mol. Cell Biol.*, 7, 861-866 (2006).
5. Pavan Atluri, Giorgos C. Karakousis, Paige M Porrett and Larry R. Kaiser, “The Surgical Review: An Integrated Basic and Clinical Science Study Guide: Chapter one: Neurosurgery”, *Lippincott Williams & Wilkins, ISBN 0781756413*, P10-32 (2005).
6. J. H. Ali, W. B. Wang, M. Zevallos and R. R. Alfano, “Near Infrared Spectroscopy and Imaging to Probe Differences in Water Content in Normal and Cancer Human Prostate Tissues”, *Technol. Cancer Res. Treat*., 3, 491-497 (2004).
7. Wai-fung Cheong, Scott A. Prahl, and Ashley J. Welch, “A review of the optical properties of biological tissues”, *IEEE J. Quant. Elec.*, 26(12), 2166-2185 (1990).
8. L. Wang, P. P. Ho, C. Liu, G. Zhang and R. R. Alfano, "Ballistic 2-D imaging through scattering wall using an ultrafast Kerr gate", *Science*, 253, 769-771 (1991).
9. D. A. Benaron, Wai-Fung Cheong and D. K. Stevenson, “Imaging enhanced: tissue optics”, *Science*, 276(5321), 2002–2003 (1997).

10. M. Xu, M. Alrubaue, S. K. Gayen and R. R. Alfano, “Determination of light absorption, scattering and anisotropy factor of a highly scattering medium using backscattered circularly polarized light”, *Optical interaction with tissue and cells XVIII, Proc. of SPIE*, 6435, J1-6 (2007).
11. Ruikang K. Wang, "Modeling optical properties of soft tissue by fractal distribution of scatterers", *J. Mod. Opt.*, 47(1), 103-120 (2000).
12. S. K. Sharma and S. Banerjee, “Volume concentration and size dependence of diffuse reflectance in a fractal soft tissue model,” *Med. Phys.*, 32(6), 1767-1774 (2005).
13. M. Xu and R. R. Alfano, "Fractal mechanisms of light scattering in biological tissue and cells", *Opt. Lett*. 30, 3051-3053 (2005).
14. M. Xu, T. Wu and J. Y. Qu, “Unified Mie and fractal scattering by cells and experimental study on application in optical characterization of cellular and subcellular structures”, *J. Biomed. Opt*., 13, 0240151-9 (2008).
15. R. Drezek, M. Guillaud, T. Collier, I. Boiko, A. Malpica, C. Macaulay, M. Follen and Rebecca Richards-Kortum, “Light scattering from cervical cells throughout neoplastic progression: influence of nuclear morphology, DNA content, and chromatin texture”, *J. Biomed. Opt.*, 8(1) 7–16, (2003).
16. J. R. Mourant, T. M. Johnson, S. Carpenter, A. Guerra, T. Aida and J. P. Freyer, “Polarized angular dependent spectroscopy of epithelial cells and epithelial cell nuclei to determine the size scale of scattering structures”, *J. Biomed. Opt.*, 7(3), 378–387 (2002).
17. Steven L. Jacques and Scott A. Prahl, "Introduction to tissue optics", http://omlc.ogi.edu/classroom/ece532/index.html

18. J. X. Zhu, D. J. Pine and D. A. Weitz, “Internal reflection of diffusive light in random media”, *Phys. Rev. A*, 44, 3948 – 3959 (1991).
19. J. R. Mourant, T. Fuselier, J. Boyer, T. M. Johnson and I. J. Bigio, “Predictions and measurements of scattering and absorption over broad wavelength ranges in tissue phantoms”, *Appl. Opt*., 36, 949-957 (1997).
20. C. F. Bohren and D. R. Huffman, “Absorption and scattering of light by small particles”, Wiley, New York, (1983).
21. Bausch and Lomb, "Refractive index and percent dissolved solids scale, Figure S-5195, 06075", Analytical Systems Division.
22. B. Gelebart, E. Tinet, J. M. Tualle and S. Avrillier, “Phase function simulation in tissue phantoms,” *Pure Appl*. *Opt*., 5, 377–388 *(*1996).
23. J. M. Schmitt and G. Kumar, “Optical Scattering Properties of Soft Tissue: A Discrete Particle Model”, *Appl. Opt.*, 37(13), 2788-2797 (1998).
24. Linhong Kou, Daniel Labrie and Peter Chylek, “Refractive indices of water and ice in the 0.65- to 2.5-gm spectral range”, *Appl. Opt*., 32, 3531--3540 (1993).
25. Ibrahim Ramzy, “Clinical cytopathology and aspiration biopsy”, *The McGraw-Hill Companies* copyright@2001.
26. A. Fischer, S. Bardarov Jr. and Z. Jiang, “Molecular aspects of diagnostic nucleolar and nuclear envelope changes in prostate cancer”, *J. Cell. Biochem.*, 91, 170–184 (2004).
27. M. Varma, M. Lee, P. Tamboli, R. Zarbo, R. Jimenez, P. Salles and M. Amin, “Morphologic criteria for the diagnosis of prostatic adenocarcinoma in needle biopsy specimens: A study of 250 consecutive cases in a routine surgical pathology practice”, *Arch. Pathol. Lab. Med.*, 126, 554-561 (2002).

28. S. Bektas, B. Bahadir, B. Gun, G. Kertis and S. Ozdamar, "The relation between gleason score, and nuclear size and shape factors in prostatic adenocarcinoma", *Turk J Med Sci*, 39(3), 381-387 (2009).

29. R. Montironi, R. Mazzucchelli, A. Santinelli, M. Scarpelli, A. Beltran and D. Bostwick, "Incidentally detected prostate cancer in cystoprostatectomies: pathological and morphometric comparison with clinically detected cancer in totally embedded specimens", *Hum. Pathol.*, 36, 646– 654 (2005).

Chapter 4

1. J. E. Bugaj, S. Achilefu, R. B. Dorshow, R. Rajagopalan, "Novel Fluorescent contrast agents for optical imaging of *in vivo* tumor based on a receptor-targeted dye-peptide conjugate platform", *J. Biomed. Opt.*, 6(2), 122-133 (2001).
2. Jean Claude Reubi, Sandra Wenger, Jacqueline Schmuckli-Maurer, Jean-Claude Schaer, and Mathias Gugger, "Bombesin receptor subtypes in human cancers: detection with the universal radioligand ^{125}I-[D-TYR^{6}, β-ALA^{11}, PHE^{13}, NLE^{14}] bombesin(6-14)", *Clin. Cancer Res.*, 8, 1139–1146 (2002).
3. G. R. Fleming, J. M. Morris and G. W. Robinson, "Direct observation of rotational diffusion by picosecond spectroscopy", *Chem. Phys.*, 17, 91-100 (1976).
4. G. Porter, P. J. Sadkowski and C. J. Tredwell, "Picosecond rotational diffusion in kinetic and steady state fluorescence spectroscopy", *Chem. Phys. Lett.*, 49, 416-420 (1977).
5. R. D. Spencer and G. Weber, "Influence of Brownian rotations and energy transfer upon the measurements of fluorescence lifetime". *J. Chem. Phys*. 52, 1654-1663 (1970).

6. F. Pellegrino, “Energy transfer in the primary stages of the photosynthetic process investigated by picosecond time resolved fluorescence spectroscopy”, A dissertation thesis of the City University of New York, Chapter 9, 270-315 (1981).
7. F. Pellegrino, P. Sekuler and R. R. Alfano, “Picosecond fluorescence kinetics and polarization anisotropy from anthocyanin pigment”, *Photobiol. and Photo Biophys.*, 2, 15-20 (1981).
8. Y. Pu, W. B. Wang, S. Achilefu, B. B. Das, G. C. Tang, V.Sriramoju, and R. R. Alfano “Time-resolved fluorescence polarization anisotropy and optical imaging of in cancerous and normal prostate tissues”, *Opt. Commun*, 274, 260-267 (2007).
9. Y. Pu, W. B. Wang, G. C. Tang, F. Zeng, S. Achilefu, J. H. Vitenson, I. Sawczuk, S. Peters, J. M. Lombardo and R. R. Alfano, “Spectral polarization imaging of human prostate cancer tissue using a near-infrared receptor-targeted contrast agent”, *Technol. Cancer Res. Treat.*, 4 429-436 (2005).
10. D. F. Gleason and G. T. Mellinger, “Prediction of prognosis for prostate adenocarcinoma by combined histological and clinical”, *J. Urol*, 111, 58-64 (1974).
11. D. A. Beysens, G. Forgacs, J. A. Glazier, “Cell sorting is analogous to phase ordering in fluids”, *Proc. Natl. Acad. Sci. USA.*, 97, 9467–9471 (2000).
12. Jean Paul Rieu1 and Yasuji Sawada, “Hydrodynamics and cell motion during the rounding of two dimensional hydra cell aggregates”, *Eur. Phys. J. B*, 27, 167-172 (2002).
13. M. A. Dresner, P. J. Rossman, S. A. Kruse and R. L. Ehman, “MR Elastography of the Prostate”, *ISMRM 99 CDs*, http://cds.ismrm.org/ismrm-1999/PDF2/526.pdf.
14. R. Cubeddu1, D. Comelli, C. D’Andrea, P. Taroni and G. Valentini, “Time-resolved fluorescence imaging in biology and medicine”, *J. Phys. D: Appl. Phys.* 35, R61–R76 (2002).

15. W. B. Wang, S. G. Demos, J. Ali and R. R. Alfano, “Imaging fluorescence objects embedded inside animal tissue using a polarization difference technique”, *Opt. Commun.*, 142, 161-166 (1997).
16. L. Wang, P. P. Ho, C. Liu, G. Zhang and R. R. Alfano, "Ballistic 2-D imaging through scattering wall using an ultrafast Kerr gate," *Science* 253, 769-771 (1991).

Chapter 5

1. J. C. Reubi, B. Waser, J. C. Schaer and R. Markwalder, “Somatostatin receptors in human prostate and prostate Cancer”, *J. Clin. Endocrinol. Metab*., 80, 2806-2814 (1995).
2. S. P. Rohrer, E. T. Birzin, R. T. Mosley and S. C. Berk *et al*, “Rapid identification of subtype-selective agonists of somatostatin receptor through combined chemistry”, *Science*, 282, 737-740 (1998).
3. J. E. Bugaj, S. Achilefu, R. B. Dorshow and R. Rajagopalan, “Novel fluorescent contrast agents for optical imaging of *in vivo* tumor based on a receptor-targeted dye-peptide conjugate platform”, *J. Biomed. Opt.*, 6(2), 122-133 (2001).
4. G. R. Fleming, J. M. Morris and G. W. Robinson, “Direct observation of rotational diffusion by picosecond spectroscopy”, *Chem. Phys.*, 17, 91-100 (1976).
5. G. Porter, P. J. Sadkowski and C. J. Tredwell, “Picosecond rotational diffusion in kinetic and steady state fluorescence spectroscopy”, *Chem. Phys. Lett.*, 49, 416-420 (1977).
6. R. D. Spencer and G. Weber, “Influence of Brownian rotations and energy transfer upon the measurements of fluorescence lifetime”. *J. Chem. Phys*. 52, 1654-1663 (1970).
7. A. V. Schally, “Oncological applications of somatostatin analogs”, *Can. Res., 48(24 Pt 1)*, 6977-6985 (1988).

8. L. J. Hofland and S. W. J. Lamberts, “Somatostatin subtype expression in human tumors”, *Ann. of Oncol.*, 12(2), 31-36 (2001).
9. E. Thodou, G. Kontogeorgos, D. Theodossiou, M. Pateraki, “Mapping of somatostatin receptor types in GH or/and PRL producing pituitary adenomas”, *J. Clin. Pathol* 59(3), 274–279 (2006).
10. Hansson J, Bjartell A, Gadaleanu V, Dizeyi N, Abrahamsson PA, “Expression of somatostatin receptor subtypes 2 and 4 in human benign prostatic hyperplasia and prostatic cancer”, *Prostate*, 53(1), 50-59 (2002).
11. Y. Pu, W. B. Wang, G. C. Tang, F. Zeng, S. Achilefu, J. H. Vitenson, I. Sawczuk, S. Peters, J. M. Lombardo and R. R. Alfano, “Spectral polarization imaging of human prostate cancer tissue using a near-infrared receptor-targeted contrast agent”, *Technol. Cancer Res. Treat.*, 4, 429-436 (2005).
12. Y. Pu, W. B. Wang, S. Achilefu, B. B. Das, G. C. Tang, V.Sriramoju, and R. R. Alfano “Time-resolved fluorescence polarization anisotropy and optical imaging of Cytate in cancerous and normal prostate tissues”, *Opt. Commun.*, 274, 260-267 (2007).
13. Wubao Wang, Jamal H. Ali, R. R. Alfano, J. H. Vitenson and J. M. Lombardo, “Spectral Polarization Imaging of Human Rectum-Membrane-Prostate Tissues”, *IEEE J. Quant. Elec.*, 9, 288-293 (2003).
14. Armin Shmilovici, “Incomplete tumor volume reduction may improve cancer prognosis”, *Med. Hypoth.*, 68, 1236-1239 (2007).
15. W. B. Wang, S. G. Demos, J. Ali and R. R. Alfano, “Imaging fluorescence objects embedded inside animal tissue using a polarization difference technique”, *Opt. Commun*., 142, 161-166 (1997).

16. F. Pellegrino, “Energy transfer in the primary stages of the photosynthetic process investigated by picosecond time resolved fluorescence spectroscopy”, *A dissertation thesis of the City University of New York, Chapter 9*, 270-315 (1981).
17. D. A. Beysens, G. Forgacs, J. A. Glazier, “Cell sorting is analogous to phase ordering in fluids”, *Proc. Natl. Acad. Sci. USA.*, 97, 9467–9471 (2000).
18. M. A. Dresner, P. J. Rossman, S. A. Kruse and R. L. Ehman, “MR Elastography of the Prostate”, *ISMRM 99 CDs*, http://cds.ismrm.org/ismrm-1999/PDF2/526.pdf.
19. T. S. Deisboeck, Y. Mansury, C. Guiot, P.G. Degiorgis, P. Giorgio and P.P. Delsanto, “Insights from a novel tumor model: indications for a quantitative link between tumor growth and invasion”, *Med. Hypoth.*, 65(4), 785-790 (2005).
20. D. F. Gleason and G. T. Mellinger, “Prediction of prognosis for prostatic adenocarcinoma by combined histological grading and clinical staging”, *J. Urol*, 111, 58-64 (1974).
21. H. P. M. de Oliveira and M. H. Gehlen, “Time resolved fluorescence anisotropy of basic dyes bound to poly (methacrylic acid) in solution”, *J. Braz. Chem. Soc*., 14(5), 738-743 (2003).
22. L. Wang, P. P. Ho, C. Liu, G. Zhang and R. R. Alfano, “Ballistic 2-D imaging through scattering wall using an ultrafast Kerr Gate”, *Science*, 253, 769-771 (1991).

Chapter 6

1. D. B. Tata, M. Foresti, J. Cordero, P. Tomashefsky, M. A. Alfano and R. R. Alfano, “Fluorescence polarization spectroscopy and time-resolved fluorescence kinetics of native cancerous and normal rat kidney tissues”, *Biophys. J.*, 50, 463-46 (1986).
2. G. R. Fleming, J. M. Morris and G. W. Robinson, “Direct observation of rotational diffusion by pico-second spectroscopy”, *Chem. Phys.*, 17, 91-100 (1976).

3. R. R. Alfano, D. Tata, J. Cordero, P. Tomashefsky, F. Longo, and M. Alfano, "Laser induced fluorescence spectroscopy from native cancerous and normal tissue", *IEEE J. Quant. Elec.*, 20, 1507-1511 (1984).
4. Y. Pu, W. B. Wang, S. Achilefu, B. B. Das, G. C. Tang, V.Sriramoju, and R. R. Alfano "Time-resolved fluorescence polarization anisotropy and optical imaging of Cybesin in cancerous and normal prostate tissues", *Opt. Commun*., 274, 260-267 (2007).
5. Y. Pu, W. B. Wang, B. B. Das, S. Achilefu, and R. R. Alfano, "Time-resolved fluorescence polarization dynamics and optical Imaging of Cytate: a prostate cancer receptor-targeted contrast agent", *Appl. Opt.*, 47, 2281-2289 (2008).
6. Kendric C. Smith, "The science of photobiology", 2nd edition, Plenum press, (1989).
7. Donna J. Dean and Brenda J. Korte, "Biomedical Imaging and Bioengineering", *Optics & Photonics News*, October 2003, http://ultra.bu.edu/papers/2003_10_OPN.pdf.
8. G. Zhang, S. G. Demos and R. R. Alfano, "Far-red and NIR spectral wing emission from tissues under 532 and 632 nm photo-excitation", *Laser Life Sci.*, 9, 1-16 (1999).
9. W. B. Wang, S. G. Demos, J. Ali and R. R. Alfano, "Imaging fluorescence objects embedded inside animal tissue using a polarization difference technique", *Opt. Commun*., 142, 161-166 (1997).
10. R. D. Spencer and G. Weber, "Influence of Brownian rotations and energy transfer upon the measurements of fluorescence lifetime", *J. Chem. Phys*. 52, 1654-1663 (1970).
11. D. V. O'Connor and D. Phillips, "Time-correlated single photon counting", Chapter 1, "Fluorescence, its time dependence and applications", *The royal Institution, London, UK, Copy right@Academic Press*, (1984).

12. R. Cubeddu, D. Comelli, C. D'Andrea, P. Taroni and G. Valentini, "Topical Review: Time-resolved fluorescence imaging in biology and medicine", *J. of Phys. D: Appl. Phys.*, 35, R61-R76 (2002).
13. S. A Tatarkova, A. K. Verma, D. A Berk and C. J Lloyd, "Quantitative fluorescence microscopy of macromolecules in gel and biological tissue", *Phys. Med. Biol.*, 50, 5759–5768 (2005).
14. Armin Shmilovici, "Incomplete tumor volume reduction may improve cancer prognosis", *Med. Hypoth.*, 68, 1236-1239 (2007).
15. D. F. Gleason and G. T. Mellinger, "Prediction of prognosis for prostate adenocarcinoma by combined histological and clinical", *J. Urol*, 111, 58-64 (1974).
16. Y. Pu, W. B. Wang, G. C. Tang, F. Zeng, S. Achilefu, J. H. Vitenson, I. Sawczuk, S. Peters, J. M. Lombardo and R. R. Alfano, "Spectral polarization imaging of human prostate cancer tissue using a near-infrared receptor-targeted contrast agent", *Technol. Cancer Res. Treat.*, 4, 429-436 (2005).
17. Rodolfo Montironi, Adhemar Longatto Filho, Alfredo Santinelli, Roberta Mazzucchelli, Roberto Pomante, Paola Colanzi, Marina Scarpelli, "Nuclear changes in the normal-looking columnar epithelium adjacent to and distant from prostatic intraepithelial neoplasia and prostate cancer", *Virch. Arch.*, 437, 625-634 (2000).
18. M. Xu, M. Alrubaue, S. K. Gayen and R. R. Alfano, "Determination of light absorption, scattering and anisotropy factor of a highly scattering medium using backscattered circularly polarized light", Optical interaction with tissue and cells XVIII, Proc. Of SPIE 6435, 64350J1-6 (2007).

19. B. B. Das, Feng Liu and R. R. Alfano, “Time-resolved fluorescence and photon migration studies in biomedical and model random media”, *Rep. Prog. Phys*. 60, 227–292 (1997).
20. Rebekah Drezek, Konstantin Sokolov, Urs Utzinger, Iouri Boiko, Anais Malpica, Michele Follen, Rebecca Richards-Kortum, “Understanding the contributions of NADH and collagen to cervical tissue fluorescence spectra: Modeling, measurements, and implications”, *J. Biomed. Opt.*, 6(4), 385–396 (2001).
21. C. Morrison, J. Thornhill, E. Gaffney, “The connective tissue framework in the normal prostate, BPH and prostate cancer: analysis by scanning electron microscopy after cellular digestion”, *Urol. Res*, 28(5), 304-7 (2000).
22. Yicong Wu and Jiannan Y. Qu, “Combined depth- and time-resolved autofluorescence spectroscopy of epithelial tissue”, *Opt. lett.*, 31(12), 1833-1835 (2006).
23. Anita C. Jones, “Biophotonics”, http://www.chem.ed.ac.uk/teaching/chem4-5/resources/lectures/moduleE/biophotonicslectureACJ.pdf